Vasyl Harik *Editor*

Trends in Nanoscale Mechanics

Mechanics of Carbon Nanotubes, Graphene, Nanocomposites and Molecular Dynamics

Springer

Trends in Nanoscale Mechanics

Vasyl Harik
Editor

Trends in Nanoscale Mechanics

Mechanics of Carbon Nanotubes, Graphene, Nanocomposites and Molecular Dynamics

Springer

Editor
Vasyl Harik
Nanodesigns Consulting
Wilmington, DE
USA

ISBN 978-94-017-9262-2 ISBN 978-94-017-9263-9 (eBook)
DOI 10.1007/978-94-017-9263-9

Library of Congress Control Number: 2014946185

Springer Dordrecht Heidelberg New York London

© Springer Science+Business Media Dordrecht 2014
This work is subject to copyright. All rights are reserved by the Publisher, whether the whole or part of the material is concerned, specifically the rights of translation, reprinting, reuse of illustrations, recitation, broadcasting, reproduction on microfilms or in any other physical way, and transmission or information storage and retrieval, electronic adaptation, computer software, or by similar or dissimilar methodology now known or hereafter developed. Exempted from this legal reservation are brief excerpts in connection with reviews or scholarly analysis or material supplied specifically for the purpose of being entered and executed on a computer system, for exclusive use by the purchaser of the work. Duplication of this publication or parts thereof is permitted only under the provisions of the Copyright Law of the Publisher's location, in its current version, and permission for use must always be obtained from Springer. Permissions for use may be obtained through RightsLink at the Copyright Clearance Center. Violations are liable to prosecution under the respective Copyright Law.
The use of general descriptive names, registered names, trademarks, service marks, etc. in this publication does not imply, even in the absence of a specific statement, that such names are exempt from the relevant protective laws and regulations and therefore free for general use.
While the advice and information in this book are believed to be true and accurate at the date of publication, neither the authors nor the editors nor the publisher can accept any legal responsibility for any errors or omissions that may be made. The publisher makes no warranty, express or implied, with respect to the material contained herein.

Printed on acid-free paper

Springer is part of Springer Science+Business Media (www.springer.com)

This book is dedicated to
my dear family and friends,
Staff Scientists of ICASE,[1] *NIA*
and NASA as well as
my friends in academia and industry.

---

[1] Our team of ICASE Staff Scientists has received the 2002 NASA Public Service Group Achievement Award for outstanding research. ICASE has also helped to form a new National Institute of Aerospace (Hampton, VA).

Foreword

Nanoscale mechanics is an exciting new field of fundamental sciences that encompasses *Nanomechanics*, *Mechanics of Nanocomposites*, relevant areas of *Micromechanics* as well as other disciplines (e.g., *Molecular Mechanics*, *Molecular Dynamics*, *Design of MEMS/NEMS*, *Multiphysics*, and *Biomechanics*). This approach defines a broad scope of related disciplines that contribute to a coherent conceptual framework for the analysis of mechanical aspects in the behavior of nanoscale material systems. *This book is written for graduate and undergraduate students, Post Docs, and other researchers in academia and industry*. In this volume, leading experts in their respective fields share own perspectives and the most recent research concerning the still emerging nanoscale sciences. This edited volume consists of two parts dedicated to *Nanoscale Mechanics* and *Molecular Dynamics* reviewed in three chapters and an editorial review as well as *Modeling and Analysis of Nanocomposites, Graphene, and Biomedical Problems*, which are also described in three chapters and an editorial review.

Research on *Nanomechanics* of nanostructures is represented by Professor Boris I. Yakobson of Rice University and his student, Professor Trajan Dumitrica of University of Minnesota, as well as Dr. Vasyl Harik of Nanodesigns Consulting (Wilmington, Delaware) and two researchers from Taiwan, Dr. W.H. Chen and Dr. H.C. Cheng. The state-of-the-art research on nanocomposite materials is represented by Professor Catalin Picu of Rensselaer Polytechnic Institute. This edited volume includes six chapters, two editorial reviews of recent research and a short review of trends in recent publications on nanoscale mechanics.

The first three chapters introduce various models and new effects in the still emerging field of *Mechanics of Carbon Nanotubes* starting with an editorial review and classification of carbon nanotubes into *four classes (i.e.,thin and thick lattice shells, long high-aspect-ratio nanotubes, and beam-like carbon nanotube crystals of small radii).* In Chapter "Mechanics of Carbon Nanotubes," a nanoscale analog of Newton's friction law and *the effect of spatial exclusion of electrons (ESEE)* at nanoscale interfaces are also presented. Chapter "Mechanics of Carbon Nanotubes" reviews numerous results of molecular dynamics simulations of carbon nanotubes and other nanostructures. The third chapter addresses the mechanical behavior of carbon nanotubes and the dislocation dynamics in graphite lattice.

The three chapters on *Mechanics of Carbon Nanotubes* are seamlessly followed by two chapters on nanostructured materials: graphene and nanocomposites. After an editorial review of various nanostructures, chapter "Nanomechanics of Graphene Sheets: Registry Matrix Analysis and Interfacial Sliding" presents new *Registry Matrix Analysis* for interfacial sliding of graphene sheets in layered stacking as well as planar cases of *the SEE effect* and the nanoscale analog of Newton's friction law. In chapter "Molecular Mechanics of Polymer Nanocomposites," Dr. Picu shows how to deduce elastic properties of nanocomposites directly from their molecular structure. He addresses intriguing aspects of the recent breakthroughs in understanding the behavior of nanostructures and nanostructured materials as well as how to enhance macroscopic properties of nanocomposites.

Nanostructured materials exhibit extraordinary properties suitable for traditional and novel applications. However, nanotechnology of carbon nanotubes and their safety have not been fully examined to ensure stable and safe nanotechnology development (see chapter "Carbon Nanotubes and Safety: Classification of Carbon Nanotubes, Size Effects and Potential Toxicity of the High-Aspect Ratio Nanotubes"). While many questions in the fundamental science of nanostructured materials are being answered, the numerous mysteries of nanoscale effects remain unsolved. Safety of nanotechnology is one of the key challenges.

In summary, the volume of invited papers covers a wide range of issues pertinent to the development of a fundamental understanding of nanoscale effects in the mechanical behavior of nanoscale material systems. Particular attention has been given to the emerging trends in mechanics of carbon nanotubes, nanocomposites, as well as nanoscale analysis of biological systems. A broad selection of topics and methods has been provided to highlight *Molecular Dynamics*, *Molecular Mechanics*, *Monte Carlo methods*, length-scale analyses and multiscale approaches.

Wilmington, Delaware V.M. Harik

Preface

This volume on *Mechanics of Carbon Nanotubes*, mechanics of graphene and nanocomposites, molecular dynamics simulations of carbon nanotubes and low-dimensional carbon allotropes grew out of the state-of-the-art research carried out at several research laboratories in the United States and Taiwan. A recent discovery of ***a nanoscale analog of the Pauli principle*** involving ***an effect of the spatial exclusion of π-electrons*** or the so-called ***SEE effect*** has prompted *Nanodesigns Consulting* staff to share the new research findings of our technical reports with the wider scientific community. Another recent development of the new ***Matrix Registry Analysis*** for modeling and analysis of nanoscale interfacial sliding along the atomic scale registry potentials and the energetically favorable atomic lattice paths has allowed the Nanodesigns Consulting staff to analyze the nanoscale controllability of graphene-based configurations for nanoscale electronic applications. These new developments should stimulate further scientific research and discovery involving nanoscale sciences.

This edited volume follows the first volume of *Trends in Nanoscale Mechanics* (2003), which grew out of discussions held at the NASA Langley Research Center (LaRC), talks and events shared by many researchers. A team of NASA and NASA contract scientists of the ICASE Institute was at the forefront of these scientific activities as the new NASA programs in Nanotechnology, Nanostructured Materials, and Multifunctional Materials and Structures were being established. The goal of these interactions was to foster collaborations between academic researchers and a university-based ICASE institute, which has pioneered world-class computational, theoretical, and experimental research in disciplines that are important to NASA. In 2002, a team of ICASE staff scientists and supporting staff have received the NASA Public Service Group Achievement Award for their outstanding work.

Nanodesigns Consulting itself is a 2004 NASA spin-off from the NASA Langley Research Center. It was formed to serve the research needs of the new NASA founded URETI Institute (http://bimat.org), which was based at Princeton University. This URETI Institute still provides new publications that are available to the public. The American Society of Mechanical Engineers (ASME) has invited the editor of this volume to present a short course on new and novel research at its

Annual Congress in 2012. This volume highlights some material from the 2012 ASME Short Course entitled *New Trends in Nanoscale Mechanics*. This new short course is based on the technical reports published by Nanodesigns Press (Wilmington, Delaware) of Nanodesigns Consulting. The editor has also authored a 2011 monograph entitled *Mechanics of Carbon Nanotubes*. New results from the technical reports concerning nanoscale mechanics of graphene sheets, nanotechnology of carbon nanotubes and safety, as well as mechanics of nanodesigns are briefly reviewed in this volume. Results of our technical reports on Nanodesign Standards are beyond the scope of this volume except the well-known nanoscale homogenization criterion and classification of carbon nanotubes. This volume also presents new research results of world-class researchers from Rensselaer Polytechnic Institute, Rice University and Taiwan.

The editor gratefully acknowledges resources of Nanodesigns Consulting along with the help and support of Springer staff and Nanodesigns Press.

Wilmington, Delaware Vasyl Harik

Contents

Part I Nanoscale Mechanics and Molecular Dynamics

Part II Modeling and Analysis of Graphene, Nanocomposites and Biomedical Problems

Contributors

Wen-Hwa Chen Department of Power Mechanical Engineering, National Tsing Hua University, Hsinchu, Taiwan, ROC

Hsien-Chie Cheng Department of Aerospace and Systems Engineering, Feng Chia University, Taichung, Taiwan, ROC

Traian Dumitrică Department of Mechanical Engineering and Materials Science, and Center for Nanoscale Science and Technology, Rice University, Houston, TX, USA; Now at University of Minnesota, Minneapolis, USA

Vasyl Harik Nanodesigns Consulting, Wilmington, DE, USA

R. Catalin Picu Department of Mechanical, Aerospace and Nuclear Engineering, Rensselaer Polytechnic Institute, Troy, NY, USA

Boris I. Yakobson Department of Mechanical Engineering and Materials Science, and Center for Nanoscale Science and Technology, Rice University, Houston, TX, USA

Part I

Nanoscale Mechanics and Molecular Dynamics

New Trends in Nanoscale Mechanics of Carbon Nanotubes

Editor's Notes

Vasyl Harik

Abstract Editor's notes provide a few examples of the nanoscale modeling and novel applications of carbon nanotubes in nanotechnology, e.g., the carbon nanotube based AFM probes, nanodevices and nanocomposites in order to introduce and motivate reviews presented in chapters "Mechanics of Carbon Nanotubes," "Molecular Modeling and Simulation of Physical Properties and Behavior of Low-Dimensional Carbon Allotropes" and "Nanomechanics: Physics Between Engineering and Chemistry" on the still emerging field of nanomechanics.

Introduction

Advances in the development of conceptual framework of nanomechanics are illustrated in this volume starting with chapter on *Mechanics of Carbon Nanotubes* by reviewing and re-evaluating some of the key models and the associated concepts, which are discussed in chapters "Mechanics of Carbon Nanotubes," "Molecular Modeling and Simulation of Physical Properties and Behavior of Low-Dimensional

---

An erratum for this chapter can be found at DOI 10.1007/978-94-017-9263-9_10.

Dr. V. Harik, Scientist at Nanodesigns Consulting, a former ICASE Staff Scientist at the NASA Langley Research Center (Hampton, VA), author of a monograph and a short course entitled "*Mechanics of Carbon Nanotubes*" © (2001) presented at the ASME Annual Congress (2001 and 2004) and a co-editor of two Kluwer volumes: "*Trends in Nanoscale Mechanics*" (2003) and "*Micromechanics and Nanoscale Effects*" (2004).

Nanodesigns Consulting is a 2004 spin-off from the NASA Langley Research Center, Hampton, Virginia. Its Staff consulted for the Princeton-based NASA-funded URETI Institute for Nanostructured Bio-inspired Materials (http://bimat.org), National Institute of Aerospace (Hampton, VA), University Space Research Association (USRA) and NASA NAIC (Atlanta, GA).

V. Harik (✉)
Nanodesigns Consulting, P.O. Box 5303, Wilmington, DE 19808-5303, USA
e-mail: Harik@nanodesignconsult.com

V. Harik (ed.), *Trends in Nanoscale Mechanics*, DOI 10.1007/978-94-017-9263-9_1

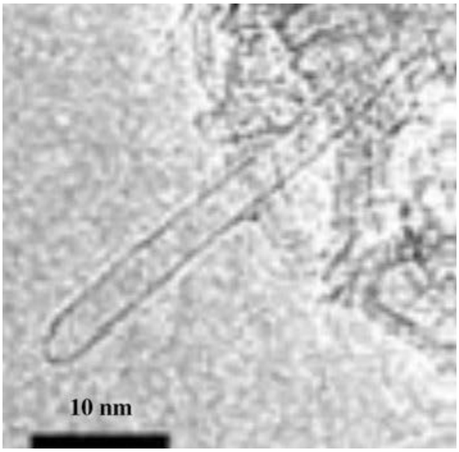

Fig. 1 TEM image of a single wall carbon nanotube (after [2])

Carbon Allotropes" and "Nanomechanics: Physics Between Engineering and Chemistry" in the context of more recent research [1–17]. From the historical and epistemological perspectives it is useful to note some of the key contributions to the understanding of the mechanical behavior of carbon nanotubes:

- **1991**—S. Iijima (NEC Labs) has discovered multiwall carbon nanotubes.
- **1993**—S. Iijima and T. Ichihashi (NEC Labs) have discovered the single wall carbon nanotubes (SWNT) and used the concept of 'a shell' (see Fig. 1).
- **1993/94**—R.S. Ruoff and J. Tersoff's team at IBM has done first theoretical modeling of carbon nanotubes and carbon nanotube crystals.
- **1996**—M.M.J. Treacy, T.W. Ebbesen and J.M. Gibson have carried out the first experimental testing of carbon nanotubes with the atomic force microscope (AFM).
- **1996**—B.I. Yakobson, C.J. Brabec and J. Bernholc have performed molecular dynamics (MD) simulations of the axial buckling and twisting of carbon nanotubes. They have successfully used the shell-based model.
- **1997**—C.M. Lieber and his team at Harvard have done experimental testing of vibrating carbon nanotubes similar to the AFM experiments.
- **1998**—Many scientists have tested, modeled and analyzed single wall carbon nanotubes (e.g., Ajayan, Brenner, Dai, Halicioglu, Lordi, Ru, Ruoff, Sinnott, Schadler, Wagner, White and others).
- **2001**—V.M. Harik (ICASE Institute, NASA Langley Research Center) has introduced classification of carbon nanotubes into four classes[1] (i.e., *thin and thick lattice shells, long high-aspect-ratio nanotubes and the beam-like carbon nanotube crystals of very small radii*).

---

[1] In 2001 V.H. Crespi [3] and his group at Penn State University and V.M. Harik at NASA Langley Research Center have independently predicted degeneration of C_{NT} lattice shells into the thin nano-beams around the critical value of the normalized C_{NT} radius, $R_{NT}/a \approx 1$, Crespi had predicted breaking of "the symmetry of *sp*3 bonds in tubular geometries" in the smallest nanotubes. Also see V.M. Harik, Solid State Communications, **120**(7–8), 331–335 (2001).

Figure 1 is showing a TEM image of a single wall carbon nanotube (SWNT), which is representative of experimental images in Iijima and Ichihashi experiments in 1993 at NEC Labs in Japan. It is important to note from the experimental and theoretical points of view that the C_{NT} lattice structure shown in Fig. 1 is also representative of the whole class of SWNTs having similar geometric parameters, which belong to the specific range of structural parameters of SWNTs having similar deformation response (see chapter "Mechanics of Carbon Nanotubes"). The 2001 classification of carbon nanotubes is essential for the characterization of mechanical behavior of C_{NT} shells and evaluation of ranges of applicability for various equivalent-continuum models for SWNTs (see chapter "Mechanics of Carbon Nanotubes"), and carbon nanotube based nanocomposites (Fig. 2).

The structure of carbon nanotubes and the C_{NT} based materials have multiple length scales (see chapter "Mechanics of Carbon Nanotubes"), which affect their structure-property relationships and their multiscale modeling both in different classes of C_{NT} lattice shells and in nanocomposites. Figure 2 illustrates different scales

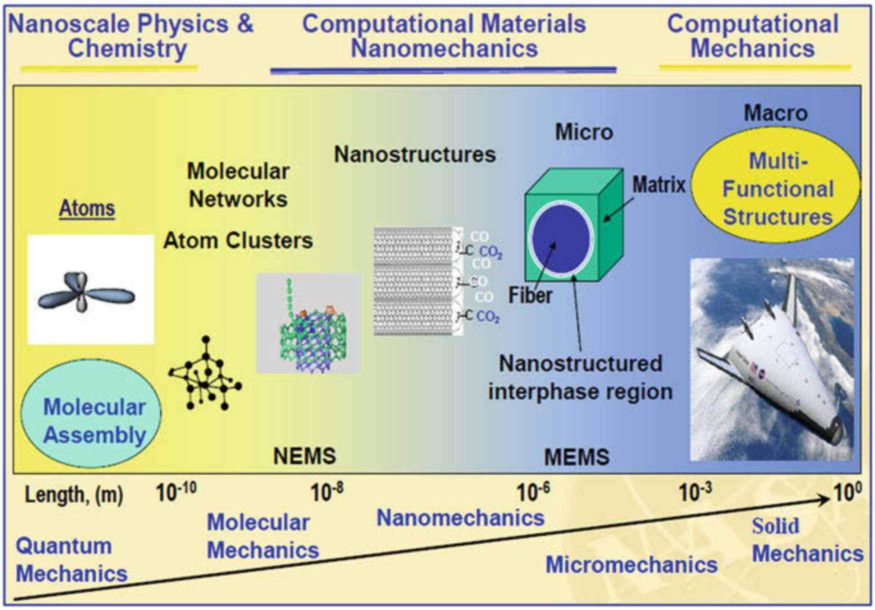

Fig. 2 Schematics of the length scales involved in the mechanics of carbon nanotubes and nanostructured materials (e.g., nanocomposites, nanotube-modified polymers and multifunctional membranes) and other areas of sciences (from the NASA LaRC Nanotechnology database). Figure 2 was developed in 2000–2001 during the establishment of new Nanotechnology and Multifunctional Materials and Structures Programs at the NASA Langley Research Center (Hampton, Virginia) and the ICASE Institute (i.e., Institute for Computer Applications in Science and Engineering or ICASE), which was transformed in 2002 into National Institute of Aerospace near the NASA Langley Research Center (NASA LaRC, Hampton, Virginia) with the assistance of its supporting staff and some of its staff scientists

in the structure of nanostructured materials. macromechanical material properties of the C_{NT}/polymer nanocomposites depend on their microscopic and nanoscale structure (see chapter "Molecular Mechanics of Polymer Nanocomposites"). The structure-property relationships in nanocomposites are different at different length scales. The content of many concepts and definitions including that of a representative volume elements either change or have to be adjusted at the nanoscale level. While on macroscopic level electromagnetic field effects are a matter of choice, at nanoscale level various field effects influence mechanical interactions (e.g., van der Waals' force, atomic lattice registry potentials, stiction, and the so called effect of the spatial exclusion of electrons (ESEE),[2] see chapter "Mechanics of Carbon Nanotubes").

Carbon Nanotube Based AFM Probes

Atomic force microscopy (AFM) allows one to characterize submicron details in the profiles of micro-channels (Fig. 3). The profile obtained by using a multi wall carbon nanotube (MWNT) probe visibly has finer details due to the smaller size of a MWNT. Resolution of the nanoscale probes (e.g., carbon nanotube based AFM probes) also depends on the size and the aspect ratio of carbon nanotubes (see chapter "Mechanics of Carbon Nanotubes"). Design of AFM probes (Fig. 3) can be optimized by selecting either SWNTs or MWNTs belonging to different classes of carbon nanotubes described in chapter "Mechanics of Carbon Nanotubes".

Resolution of nanoscale details of the submicron surface roughness in the 6 μm wide silicon micro-channel shown in Fig. 3 has benefited from the thin size of the MWNT based AFM probe (Fig. 4). The accuracy of the AFM line scan profiles shown in Fig. 5 is obviously affected by the difference in the size of a silicon probe and the MWNT probe, which is better suited for nanoscale characterization. The MWNT and SWNT AFM probes of high aspect ratio can easily deform and buckle (see chapter "Mechanics of Carbon Nanotubes"). Deformation of such AFM probes is a part of characterization of the deep nanoscale channels shown in Fig. 5.

---

[2] A new study of the so called effect of the spatial exclusion of electrons (ESEE) or the SEE effect is presented in V.M. Harik, *Mechanics of Carbon Nanotubes*, Nanodesigns Press, Newark, Delaware, 2011 (see www.amazon.com and www.nanodesignconsult.com).

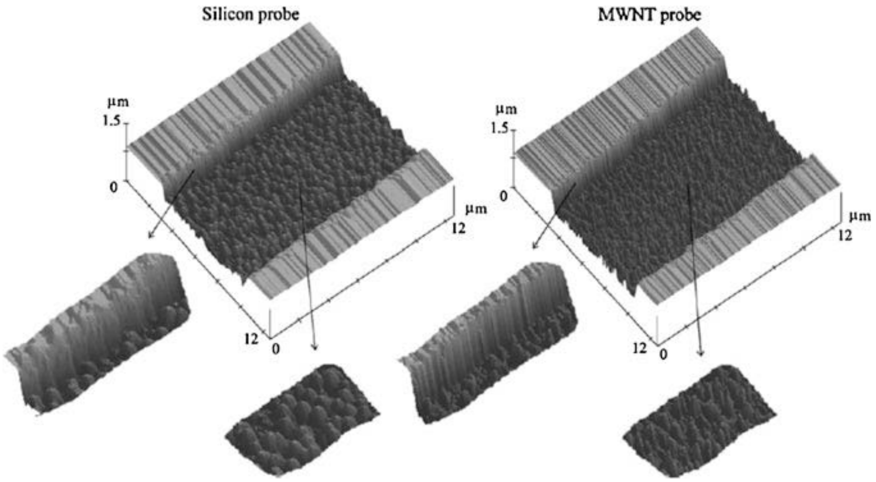

Fig. 3 3D profiles of a 6 µm wide micro-channel obtained by using a silicon probe and a MWNT probe (after [4]). Insets show submicron details along the left edge and in the middle of a micro-channel having nanoscale roughness

Fig. 4 An SEM image of a MWNT based AFM probe, which is aligned with respect to the surface of the apex of the silicon tip (after [4]). Note the periodic dark spots of weaker regions

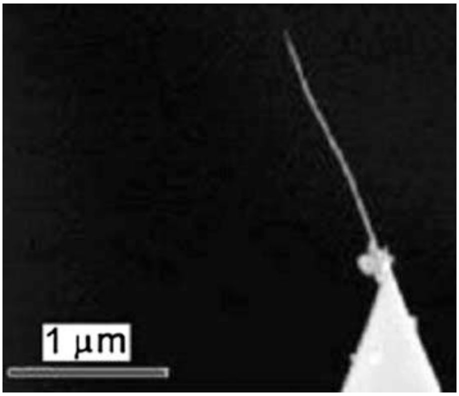

Deformation of Carbon Nanotubes

Deformation of carbon nanotube based AFM probes (Fig. 4) involves a variety of vibration modes (Fig. 6) and buckling modes (Fig. 7). Chapter "Mechanics of Carbon Nanotubes" reviews basic models for the high aspect ratio carbon nanotubes. Chapters "Nanomechanics: Physics Between Engineering and Chemistry" and "Molecular Modeling and Simulation of Physical Properties and Behavior of Low-Dimensional Carbon Allotropes" present examples of the molecular dynamic (MD) simulations for different types of deformation of carbon nanotubes. Figures 6 and 7 illustrate molecular mechanics simulations.

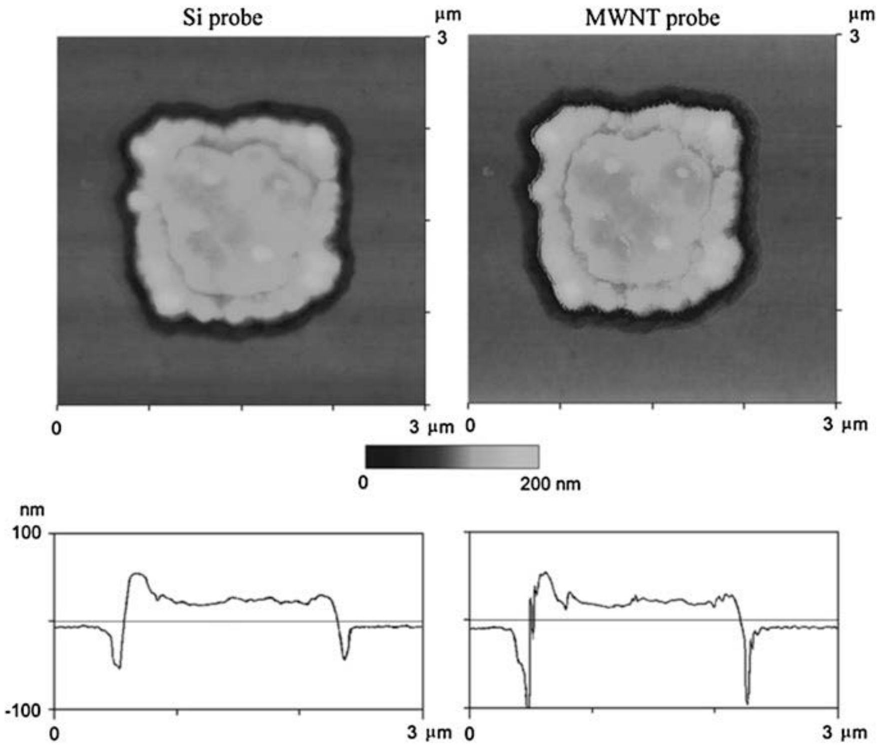

Fig. 5 AFM images and the line scan profiles of and a MWNT based AFM probe (after [4])

Axial Buckling of Carbon Nanotubes with Defects

Axial buckling of carbon nanotubes occurs in many important applications. The buckling of nanotubes depends on their geometric parameters and the atomic lattice structure as shown in chapters "Mechanics of Carbon Nanotubes" and "Molecular Modeling and Simulation of Physical Properties and Behavior of Low-Dimensional Carbon Allotropes". The buckling and vibration modes illustrated in Figs. 6 and 7 are applicable to the deformation of carbon nanotubes belonging to only one class of high aspect ratio carbon nanotubes. Carbon nanotubes belonging to other classes (see chapter "Mechanics of Carbon Nanotubes") have different buckling modes. Defects in the atomic lattice structure of carbon nanotubes affect their buckling behavior (see Figs. 8 and 9).

The buckling deformation of atomic lattices shown in Figs. 8 and 9 involves greatly distorted sections of armchair and zig-zag carbon nanotubes, which cannot be easily represented by the so called equivalent continuum models (see chapter "Mechanics

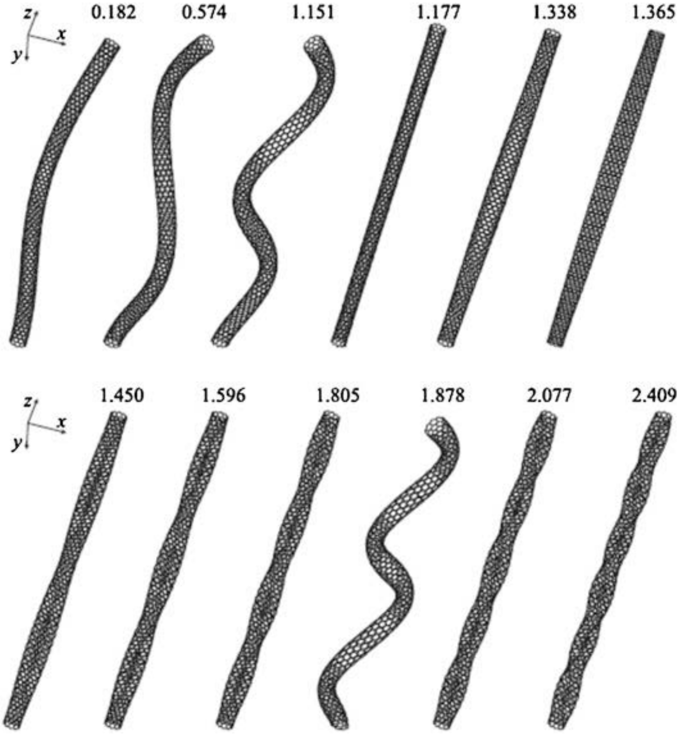

Fig. 6 Lower frequencies (THz) and the corresponding eigenmodes of a vibrating high aspect ratio carbon nanotube (after [5]). For the limitations of the shell and beam models see chapter "Mechanics of Carbon Nanotubes"

of Carbon Nanotubes"), because these sections of carbon nanotube lattices do not satisfy the nanoscale homogenization criterion (see chapter "Mechanics of Carbon Nanotubes"). This criterion states that the length of carbon nanotubes represented by any continuum model should be an order of magnitude larger than the size of one carbon ring in their atomic lattice. The length of carbon nanotubes also affects its buckling modes (see Figs. 10 and 11). A more detailed review of the role of geometric parameters on the mechanical behavior of SWNT atomic lattices including the length and the aspect ratio of carbon nanotubes is presented in chapter "Mechanics of Carbon Nanotubes" and in the 2011 monograph by the editor.

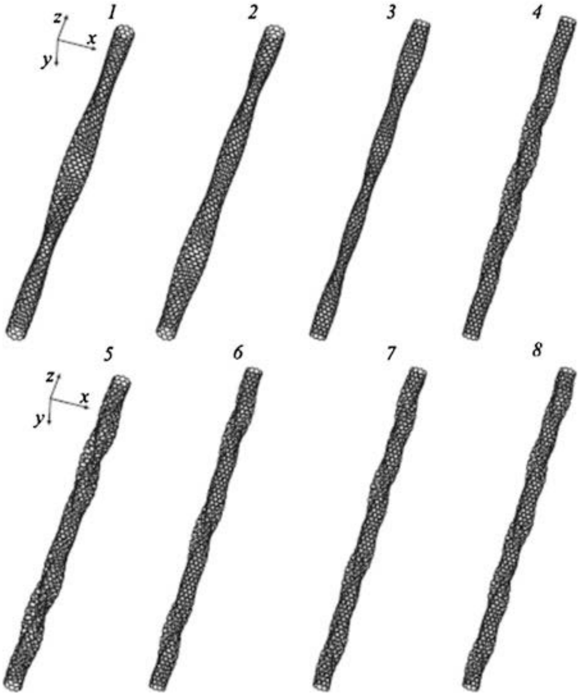

Fig. 7 Buckling modes of a high aspect ratio carbon nanotube corresponding to the buckling bifurcation points (after [5]). For the limitations of the shell and beam models see chapter "Mechanics of Carbon Nanotubes"

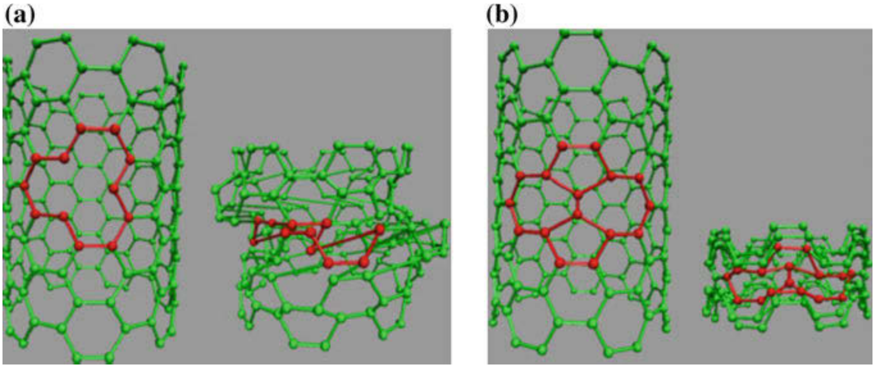

Fig. 8 Buckling behavior of armchair SWCNT with single vacancy (**a**) and Stone–Wales (**b**) defects (after [6])

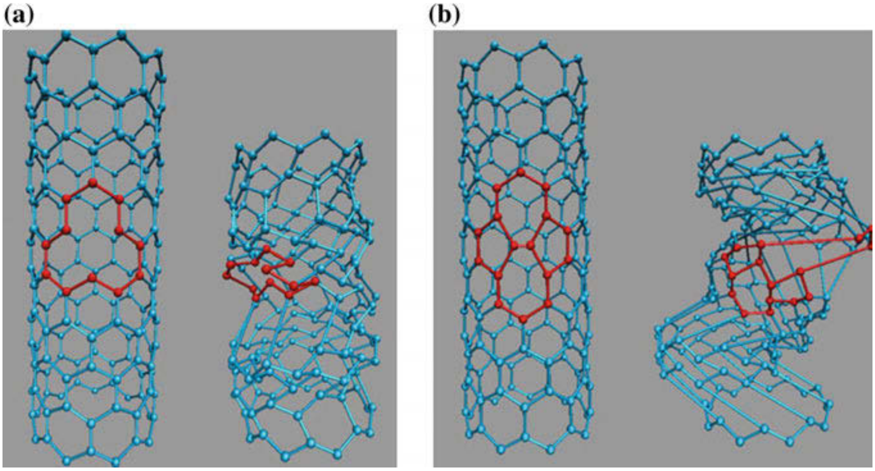

Fig. 9 Buckling behavior of zig-zag SWCNT with a single vacancy (**a**) and the Stone-Wales defects (**b**) (after [6])

Fig. 10 Influence of the carbon nanotube length on its buckling modes for a zig-zag (6, 0) SWNT (after [6])

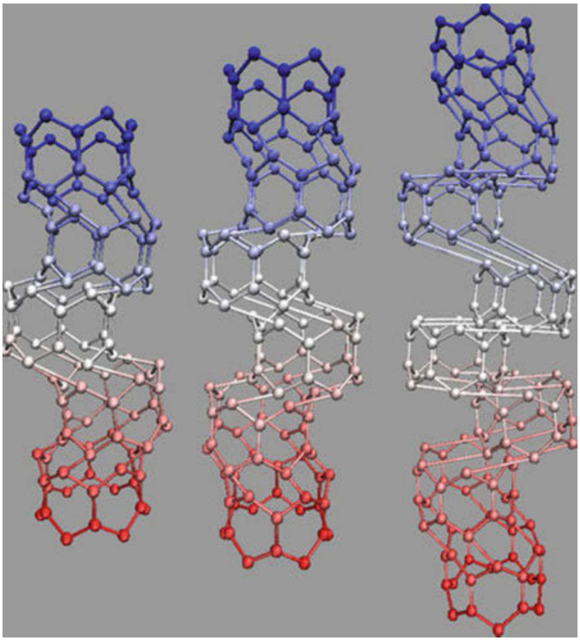

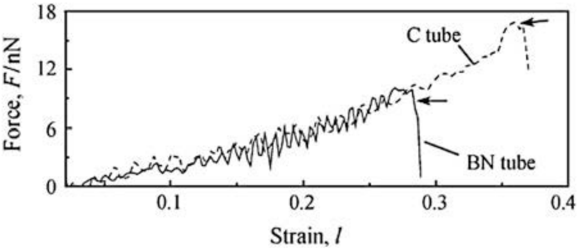

Fig. 11 Variations of the force for radially compressed and buckling boron (BN) and carbon nanotubes (after [7])

Radial Deformation of Carbon and Boron Nanotubes

Radial deformation of carbon nanotubes is very important in the design of nanoscale devices[3] and in the study of the effects of van der Waals forces on the deformation of SWNT atomic lattices (see chapter "Mechanics of Carbon Nanotubes"). Examples of radial deformation of boron nanotubes are shown in Fig. 12. The illustrated stages in the radial compression of nanotubes composed of either carbon or boron atoms are important for the understanding of nanodevices (Fig. 13) and the formation of carbon nano-ribbons.

Carbon Nanotube Based Nanodevices

Nanoscale devices can be made of carbon nanotubes, SWNT and MWNT, such as AFM probes (Fig. 4), two carbon nanotubes (Fig. 14) or a material system involving carbon nanotubes as one of its parts (Fig. 13). Chapter "Mechanics of Carbon Nanotubes" presents a review of scaling laws for SWNTs and their classification into four classes, which can be used for the optimization of AFM probes. Nanodevices based on two SWNTs (Fig. 14) or on MWNTs involve interfacial sliding affected by the lattice registry interlocking, the SEE effect (see chapter "Mechanics of Carbon Nanotubes", [11]) and registry potentials [11] as well as generation of phonons (see chapter "Mechanics of Carbon Nanotubes") [11, 12] and *excitons* (Fig. 15).

In carbon nanotubes higher Coulomb interactions may result in the generation of *excitons* (Fig. 15, i.e., a strongly bound electron-hole pair [10]). The size of excitons

---

[3] V.M. Harik, *New Trends in Nanoscale Mechanics © 2012*, Lecture notes for a short course, 2012 Annual Congress—IMECE, American Society of Mechanical Engineers (ASME), Houston, Texas, November 11, 2012 (Nanodesigns Press, Newark, Delaware, 2012).

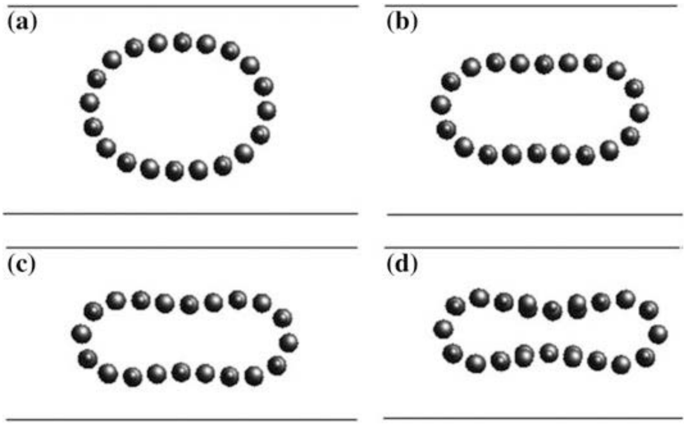

Fig. 12 The compressive deformation of boron nanotube (BN): **a** 9 %; **b** 17 %; **c** 27 %; and **d** 30 % (after [7])

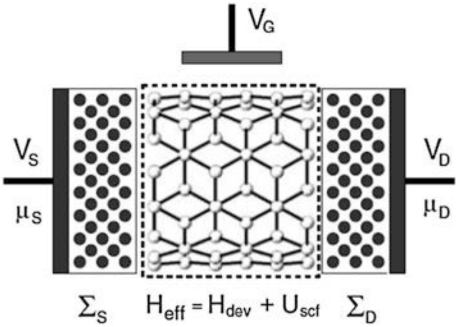

Fig. 13 A sketch of a typical device geometry for a SWNT connected to metallic contacts such as gold in [111]-orientation. Here H_{eff} corresponds to the effective device Hamiltonian including the Hamiltonian of the isolated device H_{dev}, and the self-consistent potential U_{scf}. The self-energy matrices $\Sigma_{S,D}$ are introduced to account for the device-contact couplings. V_S, V_D, and V_G are the source, drain, and gate terminal potentials, respectively (after [8]). V.M. Harik, *New Trends in Nanoscale Mechanics © 2012*, Lecture notes for a short course, 2012 Annual Congress—IMECE, American Society of Mechanical Engineers (ASME), Houston, Texas, November 11, 2012 (Nanodesigns Press, Newark, Delaware, 2012)

distributed at a chiral angle along circumference of SWNT shown in Fig. 15 is slightly larger than the diameter of SWNT. Interfacial sliding of the adjacent lattice shells in the multi wall carbon nanotubes can generate various lattice *phonons* [12], which have been discussed in chapter "Mechanics of Carbon Nanotubes" along with the nanoscale analog of Newton's friction law [11, 13, 14]. The process of closing of the carbon nanotube is illustrated in Fig. 16 by the molecular dynamic simulations [17].

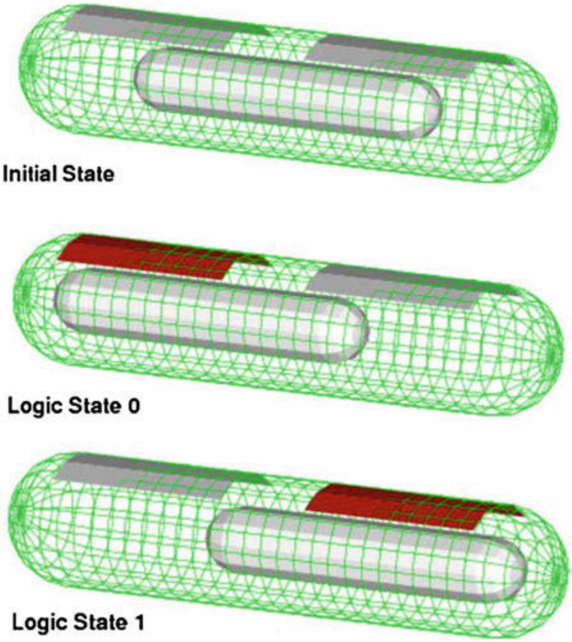

Fig. 14 Positions of the inner tube at different logic states in SRAM configuration (after [9])

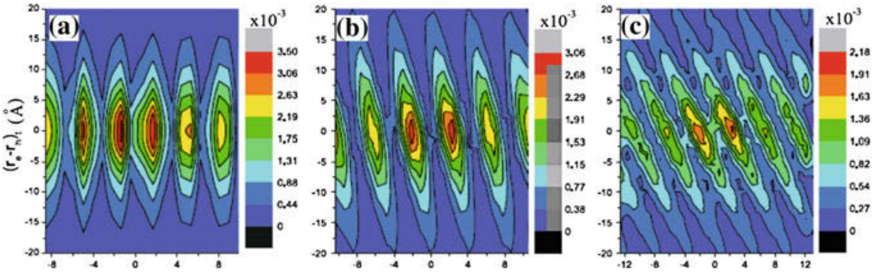

Fig. 15 Real space probability distribution $|\phi(\mathbf{r}_e, \mathbf{r}_h)|^2$ of the electron ($\mathbf{r}_e$) with respect to the hole ($\mathbf{r}_h$) for the lowest energy singlet exciton in various SWNTs. Here electron and hole are both at even sites, respectively. In order to make the distribution more visually, the structure of SWNTs is an unrolled graphene plane. **a** (8, 0) tube, **b** (8, 1) tube, **c** (8, 4) tube but only considering the summation from the lowest q_1 and q_2 subbands (after [10])

Chapters "Mechanics of Carbon Nanotubes" and "Molecular Modeling and Simulation of Physical Properties and Behavior of Low-Dimensional Carbon Allotropes" present molecular dynamics simulations of carbon nanotubes and other fullerenes with the results similar to those in the latest publications (see Fig. 17 [1]). It should be noted that the buckling shape modes simulated for a (5, 5) armchair carbon nanotube in Fig. 17 are noticeably affected by the thick lattice shell structure

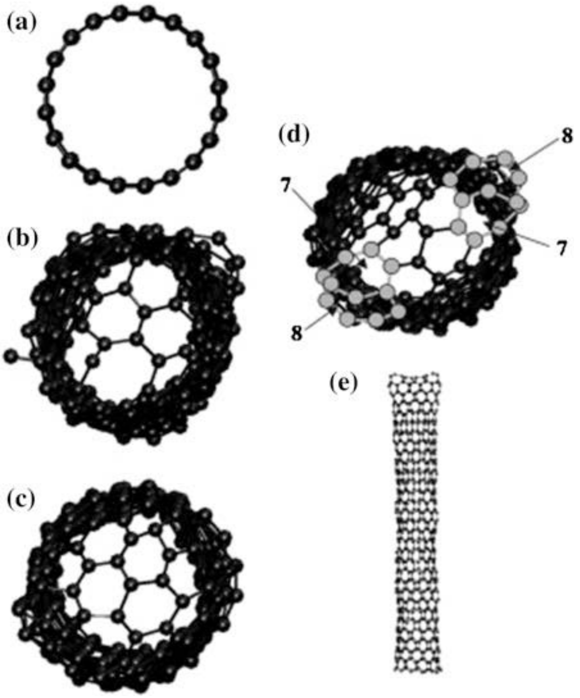

Fig. 16 Snapshots of the molecular dynamics simulations of the closing process of the (10, 0) SWCNT with 21 atomic layers taken with the simulation times of **a** 0 ps, **b** 10 ps, **c** 20 ps, and **d** 200 ps. Side view of (**d**) is shown in (**e**). The atoms in (**d**) with bright contrast are illustrated to show defects (after [17])

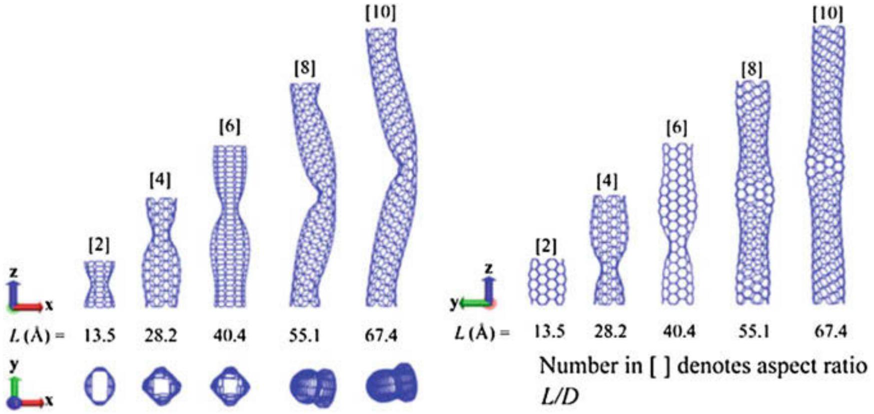

Fig. 17 Snapshots of the molecular dynamics simulations of buckling shape modes for a (5, 5) armchair carbon nanotube (with the thick lattice shell) shown for various aspect ratios from three different viewpoints [1]

of this nanotube with the relatively small radius according to the classification of carbon nanotubes (see chapter "Mechanics of Carbon Nanotubes"). The simulation results [1] show the buckling shape modes for various aspect ratios of a specific carbon nanotube. This (5, 5) armchair carbon nanotube demonstrates the beam-like buckling mode at the aspect ratio of 8, which is below the 1/10 threshold separating the beam and shell buckling modes (see chapter "Mechanics of Carbon Nanotubes" for more details).

Nanomechanics of Graphene Sheets

Nanomechanics of graphene sheets is very important for the design of graphene-based nanoscale devices and graphene-based electronics. The structure of carbon nanotubes has been often illustrated by rolling up a graphene sheet cut at different angles as shown in Fig. 15. The atomic structure of graphene lattice sheets[4] will be further discussed in chapter "Nanomechanics: Physics Between Engineering and Chemistry". Ranges of applicability of different estimates for the effective thickness of graphene sheets rolled into carbon nanotubes varying between 0.66 and 3.4 Å are discussed in chapter "Mechanics of Carbon Nanotubes" along with their dependence on the balance between the elastic interactions and *van der Waals* forces [11]. The nanoscale analog of Newton's friction law used for MWNT in chapter "Mechanics of Carbon Nanotubes" can be also used for the analysis of interfacial sliding of graphene sheets as will be shown in chapter "Nanomechanics: Physics Between Engineering and Chemistry". The onset of the interfacial registry between a carbon atom 'asperity' in one graphene sheet and a carbon ring potential barrier through a C–C bond of the adjacent graphene sheet is associated with the initiation of the so called *effect of the spatial exclusion of electrons (SEE)* during interaction between the spatially-distributed $\pi - \pi$ electrons along the adjacent graphene sheets [11].

Nanotube/Polymer Interfaces in Nanocomposites

The nanotube/polymer interface plays an important role in the stress transfer in nanocomposites. The strength of interfacial adhesion depends on the surface area of the SWNT/polymer interface, its roughness, interlocking of asperities and molecular bonding of the nanoscale interface [11, 13, 14]. An example of a fracture surface with some features of the nanotube/polymer interface (segments of carbon

---

[4] Nanoscale mechanics of graphene sheets and flakes has been reviewed in chapter "Nanomechanics of Graphene Sheets: Registry Matrix Analysis and Interfacial Sliding" and in Ref. [10], which includes a Chapter on electronic energy barriers in graphene, deformed Fermi cones, material properties, interfacial sliding and nanoscale friction, lattice waves, i.e., *phonons*, etc.

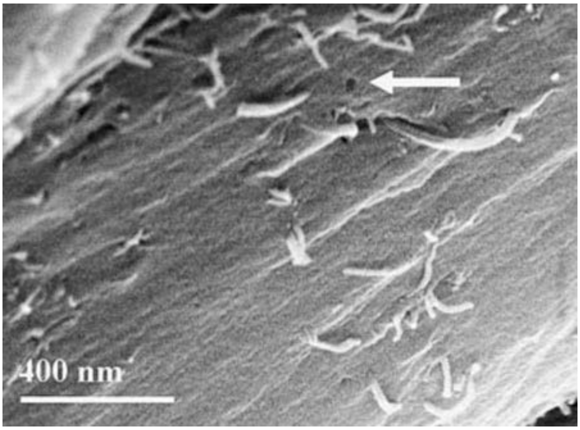

Fig. 18 An image of a fracture surface of a carbon nanotube based polymer nanocomposite showing segments of carbon nanotubes and an empty hole after a carbon nanotube was pulled out (the hole is marked by a white arrow, after [15])

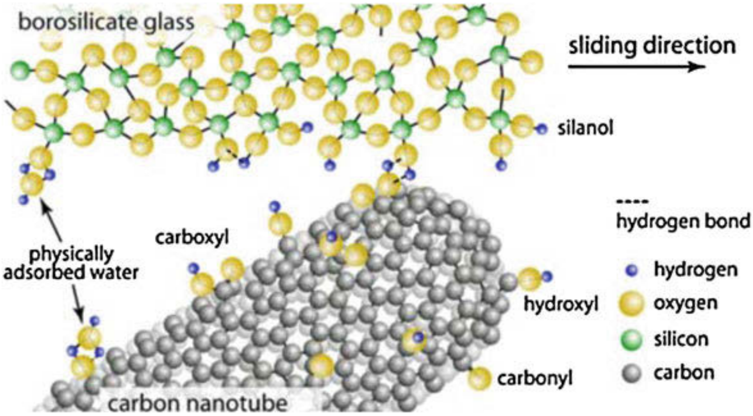

Fig. 19 Molecular model of the nanoscale interface between the borosilicate glass and a carbon nanotube (after [16])

nanotubes pulled-out of polymer and an empty hole) is shown in Fig. 18. The nanoscale modeling of the pull-out process of a carbon nanotube out of polymer or glass materials (Fig. 19) can be quite complex as discussed in chapter "Mechanics of Carbon Nanotubes". Interfacial sliding of a nanotube depends on the interfacial interactions and the atomic lattice structure of nanoscale interfaces (see chapter "Mechanics of Carbon Nanotubes" [11, 13, 14]).

References

1. C.M. Wang, A.N. Roy Chowdhury, S.J.A. Koh, Y.Y. Zhang, in *Modeling of Carbon Nanotubes, Graphene and Their Composites,* ed. by K.I. Tserpes, N. Silvestre. Springer Ser. Mater. Sci. **188**, 239–273 (2014)
2. H. Dai, Chapter 3, ed. by M.S. Dresselhaus, G. Dresselhaus, Ph. Avouris *Carbon Nanotubes* (Springer, 2000), pp. 29–52
3. D. Stojkovic, P. Zhang, V.H. Crespi, Phys. Rev. Lett. **87**(12), 125502 (2001)
4. B. Bhushan, T. Kasai, C.V. Nguyen, M. Meyyappan, Microsyst. Technol. **10**, 633–639 (2004)
5. B.D. Annin, S.N. Korobeynikov, A.V. Babichev, J. Appl. Industrial Math. **3**(3), (2009)
6. A.R. Ranjbartoreh, G. Wang, Nano. Res. Lett. **6**, 28 (2011)
7. H.-J. Shen, Front. Mater. Sci. China **3**(2), 201–204 (2009)
8. S. Xiao, D.R. Andersen, W. Yang, Nano. Res. Lett. **3**, 416–420 (2008)
9. D. Kienle, A.W. Ghosh, J. Comput. Electron. **4**, 97–100 (2005)
10. Y. Lu, H. Liu, B. Gu, Eur. Phys. J. B **74**, 499–506 (2010)
11. V.M. Harik, *Mechanics of Carbon Nanotubes* (Nanodesigns Press, Newark, Delaware, 2011)
12. M.S. Dresselhaus, P.C. Eklund, Adv. Phys. **49**(6), 705 (2000)
13. S.J.V. Frankland, A. Caglar, D.W. Brenner, M. Griebel, J. Phys. Chem. B **106**(12), 3046–8 (2002)
14. S.J.V. Frankland, V.M. Harik, Surf. Sci. Lett. **525**, L103 (2003)
15. C.S. Grimmer, C.K.H. Dharan, J. Mater. Sci. **43**, 4487–4492 (2008)
16. P.L. Dickrell, S.K. Pal, G.R. Bourne, C. Muratore, A.A. Voevodin, P.M. Ajayan, L.S. Schadler, W.G. Sawyer, Tribol. Lett. **24**(1), 85 (2006)
17. S.S. Han, H.M. Lee, Met. Mater. Int. **9**(2), 99 (2003)

Further Readings

18. B.I. Yakobson, T. Dimitrica, Chapter 1, in *Trends in Nanoscale Mechanics*, ed. by V.M. Harik, M. Salas (Kluwer Academic Publishers, The Netherlands, 2003), pp. 3–33
19. B.N.J. Persson, *Sliding Friction: Physical Principles and Applications* (Springer, Berlin, 1998)
20. B.N.J. Persson, Surf. Sci. Reports **33**, 83 (1999)
21. Q.Y. Li, K-S. Kim, Proc. R. Soc. A **464**, 1319 (2008)

Mechanics of Carbon Nanotubes

A Review of Basic Models and New Nanoscale Effects

Vasyl Harik

Abstract This chapter reviews basic models and new effects in the still emerging field of *Nanoscale Mechanics* and one of its essential parts: *Mechanics of Carbon Nanotubes*. Experiments with carbon nanotubes, theoretical models and modeling (i.e., molecular dynamics simulations), classification of carbon nanotubes into *four classes (i.e., thin and thick lattice shells*, *long high-aspect-ratio nanotubes and beam-like carbon nanotube crystals of small radii)* have been reviewed. Classification of carbon nanotubes is important for the safety of nanotechnology and evaluation of health effects. Interfacial sliding of the adjacent lattice shells in the multi wall carbon nanotubes (MWNT) has been discussed along with a nanoscale analog of the Newton's friction law and *the effect of spatial exclusion of electrons (ESEE)* at the interface, which effectively can be viewed as a nanoscale analog of the *Pauli's exclusion principle*. Examples of lattice waves, i.e., *phonons*, in carbon nanotubes have been presented. Ranges of applicability of estimates for the effective thickness of carbon nanotubes varying between 0.66 and 3.4 Å have been examined along with their dependence on the balance between the elastic interactions and van der Waals forces.

Dr. V. Harik, former ICASE Staff Scientist at the NASA Langley Research Center (Hampton, VA), Principal Scientist at Nanodesigns Consulting, author of a monograph and a short course entitled "*Mechanics of Carbon Nanotubes*" © (2001) presented at the Annual ASME Congress (2001 and 2004) and a co-editor of Kluwer volumes: "*Trends in Nanoscale Mechanics*" (2003) and "*Micromechanics and Nanoscale Effects*" (2004).

Nanodesigns Consulting is a 2004 spin-off from the NASA Langley Research Center, Hampton, Virginia. Its Staff consulted for the Princeton-based NASA-funded URETI Institute for Nanostructured Bio-inspired Materials (http://bimat.org), National Institute of Aerospace (Hampton, VA), University Space Research Association (USRA) and NASA NAIC (Atlanta).

V. Harik (✉)
Nanodesigns Consulting, P.O. Box 5303, Wilmington, DE 19808-5303, USA
e-mail: Harik@nanodesignconsult.com

V. Harik (ed.), *Trends in Nanoscale Mechanics*, DOI 10.1007/978-94-017-9263-9_2

A Historical Perspective

After the discovery of multiwall carbon nanotubes in 1991 by S. Iijima and single wall carbon nanotubes in 1993 by Iijima and Ichihashi of NEC laboratories in Japan [1, 2], first theoretical modeling of carbon nanotubes and carbon nanotube crystals was carried out at the IBM Watson Research Center in 1993 [3, 4]. First vibration experiments with carbon nanotubes were carried out in 1996 [5, 6] at the time of first molecular dynamics (MD) simulations of buckling of carbon nanotubes [7, 8]. The nomenclature for the physical description of carbon nanotubes and their chirality (e.g., armchair and zig-zag) has been proposed in 1992 [9]. Classification of carbon nanotubes into four classes[1] of *thin and thick lattice shells, long high-aspect-ratio nanotubes and beam-like carbon nanotube crystals of small radii* (Fig. 1) has been developed in 2001 [10, 11][2] at the NASA Langley Research Center in Hampton, Virginia.[3]

Length Scales in the Structure of Carbon Nanotubes

The atomic structure of carbon nanotubes (C_{NT}) consists of six carbon atoms arranged in hexagonal carbon rings (Fig. 2). The key length-scale parameters that describe the atomic structure of C_{NT} lattices include the length of the covalent σ-bond, $l_{C\text{–}C}$, 1.41–1.44 Å, the size of a carbon ring, $a = 2.46$ Å, the radius, R_{NT}, of C_{NT} lattices (~ 0.2–2 nm, for the single wall nanotubes, and ~ 35 nm for the multi wall nanotubes) or the diameter, d_{NT}, and their length, L_{NT}, varying between few nanometers and 100 s of microns (even a few centimeters).

The length scale associated with the length of the C–C bond, $l_{C\text{–}C}$, is important for the evaluation of relative deformation of C–C bonds in the elastic interactions, dynamics vibrations and structural deformations, as well as for the scaling analysis of the energy distribution of covalent electrons and the out-of-plane π-electrons [12]. The C–C bonds can be stretched from its minimum size of 1.41 Å in the graphene sheets to longer lengths of about 1.62 Å in the carbon nanotubes of smaller radii [12]. The length scale associated with the size of a carbon ring, a, is

---

[1] Classification of new types of materials is important in any field of science, especially, for the highly promising carbon nanotubes, which can be separated into four distinct classes associated with quite distinct geometric parameters and some similarities with ***asbestos*** though.

[2] This research results have been first published at NASA and its ICASE Institute; see Harik, V.M., 2001. *Ranges of applicability for the continuum-beam model in the constitutive analys is of carbon nanotubes: nanotubes or nano-beams?* (NASA/CR-2001-211013, NASA Langley Research Center), Hampton, Virginia, USA. Harik, V.M., 2001. *Mechanics of carbon nanotubes* © 2001. ASME Education Institute (Notes for a Short Course, a 2002 CD and a 2001 video), American Society of Mechanical Engineers, New York, NY.

[3] For more historical perspectives and some epistemological notes about the concepts of emerging *Nanoscale Mechanics* see author's footnotes for the references cited in this chapter.

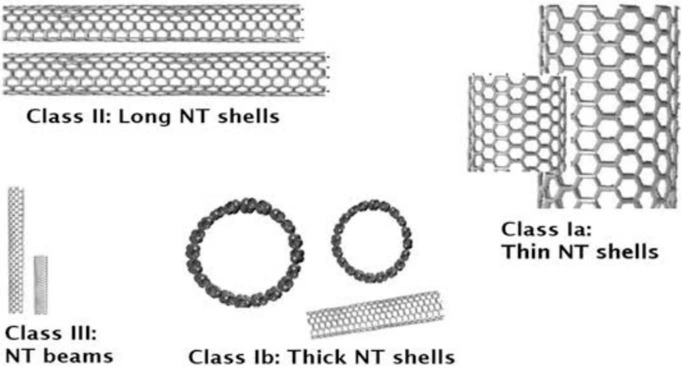

Fig. 1 Classification of carbon nanotubes (NT or C_{NT}) into four classes (after [12]): *the thin* C_{NT} *shells* (Class Ia), *the thick* C_{NT} *shells* (Class Ib), *the long* C_{NT} *shells* (Class II, i.e., the high aspect ratio C_{NT} shells) and *the* C_{NT} *nano-beams and* C_{NT} *nanocrystals* (Class III)

essential for nanoscale homogenization[4] [11, 12] and analysis of relative deformation of graphene sheets (Fig. 2) and segments of carbon nanotubes (Fig. 3 and Table 1).

The diameter-to-length aspect ratio, d_{NT}/L_{NT}, of the carbon nanotube lattice (Fig. 3) is an important structural parameter in many applications such as in the nanotube based AFM probes and in the buckling process of C_{NT} lattices [10–12]. The ratio of the radius, R_{NT}, to the carbon ring size, a, i.e., R_{NT}/a, or the normalized circumference, $2\pi R_{NT}/a$, are important in the evaluation of radial deformation of carbon nanotubes and the radial buckling of C_{NT} lattices [7–11]. Separation and collapse of the adjacent length scales result in different classes of C_{NT} lattices (Fig. 1): *thin nanotubes, thick nanotubes, nano-beams of small radii and the high aspect ratio nanotubes* [10–12].

Nanoscale Homogenization Criterion

The material properties of different classes of carbon nanotubes and their C_{NT} lattices become unique and independent of their size or the number of atomic unit layers shown in Fig. 3, for instance, when the C_{NT} atomic structure satisfies a nanoscale criterion for the unique averaging (or *homogenization*) of the material properties over a nanoscale volume or an extended surface:

---

[4] Nanoscale homogenization itself and nanoscale homogenization criteria [11, 12], in particular, are very important for the application of continuum concepts (e.g., continuous surface or a properly-defined number of representative volume elements for the volume-averaging for the uniquely-defined material properties of any material having a discrete atomic lattice structure) to the C_{NT} lattice structures (for more details, see the next part of this chapter).

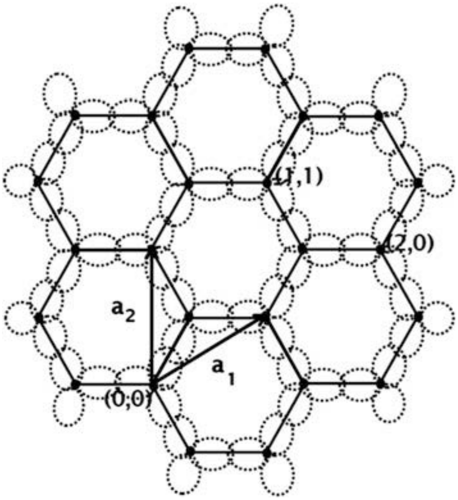

Fig. 2 Atomic lattice structure of a graphene flake (Nanoscale mechanics of graphene sheets and flakes has been presented in Ref. [12], which includes a chapter on electronic energy barriers in graphene, deformed Fermi cones, material and mechanical properties, interfacial sliding and nanoscale friction, lattice waves, i.e., *phonons*, etc.) and that of carbon nanotubes with the hexagonal carbon rings of carbon atoms and a schematic of the electron distribution in the C–C bonds. The (n, m) lattice structure is based on the unit vectors a_1 and a_2

Fig. 3 Schematic of a carbon ring with the length of the C–C bond, $l_{C\text{–}C} = 1.41\text{–}1.42$ Å, and the size of 2.46 Å, and the atomic lattice structure of an armchair (10, 10) carbon nanotube of diameter, $d_{NT} = 13.6$ Å, and the length, $L_{NT} = 52.5$ Å, which represent the four length scales involved

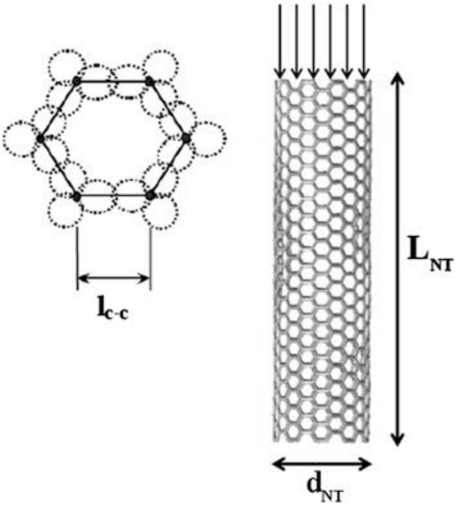

Table 1 The length scales in the structure of single wall carbon nanotubes

Parameters	Typical values	Ranges of values[a]
C–C bond length, l_{C-C}	1.41–1.42 Å	1.41–1.62 Å
Carbon ring size, a	2.46 Å	~2.22–2.70 Å
Effective thickness, h_{NT}	0.66–3.4 Å	Load path dependent
Diameter, d_{NT}	~1 nm	4–50 Å
Length, L_{NT} Length, L_{NT}	~20–100 nm 100 nm–1 μm–3 cm	Vary in AFM/NEMS Vary in nanocomposites

[a] Ranges of values of the C–C bond length, l_{C-C} are associated with the bond stretching in the C_{NT} lattices of small radii. The carbon ring size, a, may vary under the tensile and compressive loading and the C_{NT} lattice corrugation. The effective thickness, h_{NT}, depends on the type of loads and the load path through thermodynamic states of the deformation process (for details see [12])

$$L_{NT} \gg a, \tag{1}$$

or $L_{NT}/a >> 1$, where the length of a C_{NT} lattice, L_{NT}, should be considerably greater than the size of a carbon ring, $a = 2.46$ Å, its smallest structural element [10–12]. The inequality in the homogenization criterion (1) means roughly an order of magnitude difference, i.e., $L_{NT}/a \approx 10$. It turns out that the molecular structure of the fullerene C60, i.e., the Buckminster buckyball with $a \approx 2.46$ Å, represents the smallest stable nanostructure [12], the surface of which satisfies the aforementioned homogenization criterion (1) due to Harik [10–12].

Classification of Carbon Nanotubes

Carbon nanotubes with large values of radius, R_{NT}, have small curvature, i.e., $1/R_{NT} << 1$, and atomic lattices with elastic properties similar to the graphene sheets [12]. This class of *thin* C_{NT} *lattice shells* (Fig. 1) satisfies, the following criterion for the ratio of the effective thickness, h_{NT}, of C_{NT} lattices to their radius, R_{NT}: $h_{NT}/R_{NT} << 1$ [10, 11]. The two adjacent length scales: R_{NT} and the effective thickness, h_{NT} (or the bond length, l_{C-C}) are well separated, and the bond length, l_{C-C}. plays virtually no role in the global deformation response for small strains.

Deformation of single wall carbon nanotubes having large values of radius, $R_{NT} = \frac{a}{2\pi}\sqrt{n^2 + m^2 + nm}$, can depend on their chirality defined by the (n, m) pair and the following scaling condition for the class of *thin* C_{NT} *lattices* (Fig. 1):

$$h_{NT} \ll \frac{a}{2\pi}\sqrt{n^2 + m^2 + nm} \tag{2a}$$

or

$$\frac{h_{NT}}{R_{NT}} = \frac{2\pi h_{NT}}{l_{C-C}\sqrt{3(n^2+m^2+nm)}} \ll 1. \tag{2b}$$

The advantage of this form is evident when single carbon rings are deformed in the (n, m) C_{NT} lattices, and the nanoscale homogenization criterion (1) for the carbon rings is more difficult to apply. Carbon nanotubes satisfying the scaling conditions (2a, b) deform as thin lattice shells.

Since the effective C_{NT} thickness, h_{NT}, can be estimated as a half of the C–C bond length, 0.72 Å [10–12], the presence of the carbon ring size, a, the effective C_{NT} thickness, h_{NT}, and the C–C bond length, $l_{C\text{–}C}$, in the new thin lattice-shell conditions (2a, b) can be avoided by presenting them in the following form, which is solely based on the (n, m) nomenclature for the C_{NT} lattices:

$$\frac{\pi}{\sqrt{3(n^2+m^2+nm)}} \ll 1 \tag{3}$$

The (10, 10) C_{NT} lattice (R_{NT} = 6.8 Å, Fig. 3) satisfies the thin lattice-shell conditions (2a, b) and (3). It is so happens that the (10, 10) C_{NT} lattice shown in Fig. 3 is the smallest armchair nanotube, which fulfills this condition for the class of *thin* C_{NT} *shells* [10–12]. The C_{NT} lattices of larger radii (both with the armchair and the zig-zag chirality) also satisfy the conditions (2a, 2b) and (3). The class of *thick* C_{NT} *lattices* [10–12] satisfies, a related condition for the radius, R_{NT}, of carbon nanotubes and the effective C_{NT} thickness, h_{NT} (see Table 2):

Table 2 Values of the effective C_{NT} lattice thickness, h_{NT} estimates for carbon nanotubes

Types of analysis used in nanoscale analysis	C_{NT} thickness estimates, h_{NT} Å	Authors of the C_{NT} thickness estimates
Molecular dynamics (MD) simulations	0.66	Yakobson et al. [7, 8]
Scaling analysis[a] of bonds in carbon rings	0.71–72	Harik [11, 12]
Tight-binding method (atomic scale)	0.74	Zhou et al. [13]
Local density approximation	0.75	Tu and Ou-Yang [14]
Continuum shell theory	0.75	Panatano et al. [15]
Ab inito computations	0.665	Wang et al. [16]
Continuum ring theory	0.617	Vodenitcharova and Zhang [20]
Atomic potential based analysis	0.62–0.87	Huang et al. [80]
Continuum modeling	0.87	Goupalov [21]
Ab inito computations	0.89	Kudin et al. [17]
Continuum hollow cylinder	0.98	Sears and Batra [22, 23, 34]
C_{NT} bundle-based crystal	3.42	Tersoff and Ruoff [4]
Molecular dynamics (MD) simulations	~3.4	Avouris et al. [18]

[a] The effective C_{NT} lattice thickness, h_{NT} can be estimated as a half of the length of the C–C bonds, $l_{C\text{–}C}$ = 1.41–1.44 Å via a spherical approximation for the distribution of σ-electrons in the elastic load-transferring bonds [10–12]

$$\frac{h_{NT}}{R_{NT}} = \frac{2\pi h_{NT}}{a\sqrt{n^2 + m^2 + nm}} > 1/10 \tag{4}$$

Carbon nanotubes of small radii $R_{NT} < 6$ Å or $R_{NT}/a < 2$, satisfy this condition for the class of *thick* C_{NT} *lattices*. These radii are close to the radii of C_{NT} *nano-beams* [12], which have smaller number of the circumscribed carbon rings along their circumference and much greater curvature (Fig. 1). Long high-aspect-ratio carbon nanotubes (class II, Fig. 1) have C_{NT} *lattice shells* of the length, L_{NT}, such that $d_{NT}/L_{NT} < 1/10$, and considerable surface with the surface effects proportional to their surface area: $\pi d_{NT} L_{NT}$ or $a\sqrt{n^2 + m^2 + nm} L_{NT}$.

The length scale and the size effects associated with the $\mathrm{C_{NT}}$ lattice length, L_{NT}, which influence the global deformation of carbon nanotubes and their material properties (for short $\mathrm{C_{NT}}$ lattices), are represented in both the aspect ratio, d_{NT}/L_{NT} and the homogenization ratio, L_{NT}/a, or the minimum homogenization length, L_H. At the length scale level associated with the $\mathrm{C_{NT}}$ radius, R_{NT}, the mechanical material properties of carbon nanotubes are influenced not only by their chirality, but also by the thickness-to-radius ratio, h_{NT}/R_{NT}. For the $\mathrm{C_{NT}}$ nano-beams [12], the curvature effects and the degree of bond stretching are also important due the structural properties of carbon nanotubes having small radius.

Effective Thickness of Carbon Nanotubes

The value of the effective $\mathrm{C_{NT}}$ lattice thickness, h_{NT}, is affected by the degree of the balance the elastic C–C bond interactions associated with the approximation: $h_{NT} \approx l_{\mathrm{C-C}}/2$ [11, 12], Table 2, and the van der Waals forces associated with the experimental graphene value of $h_{NT} \approx 3.4$ Å. The value of the effective lattice thickness, h_{NT}, in a particular deformation response of the $\mathrm{C_{NT}}$ lattice (e.g., axial buckling with $h_{NT} \approx l_{C-C}/2$, or other types of deformations with h_{NT} such that $l_{\mathrm{C-C}}/2 < h_{NT} < 3.4$ Å, Fig. 3) is associated with the specific change in the potential energy, U, of the considered atomic lattice (Table 2).

In a physical setting, the balance between the elastic C–C bond interactions and the van der Waals forces in a deformation response of the $\mathrm{C_{NT}}$ atomic lattices associated with a particular loading path, can be described by the following approximation equation [12]:

$$\sum_{i=1}^{n_C} \frac{1}{V_{\mathrm{C-C},i}} \left| \left(\frac{\partial^2 U}{\partial \varepsilon^2}\right)_{\varepsilon=0,i} \right|_{\mathrm{C-C}} = \frac{h_C}{h_0} \sum_{i=1}^{n_{vdW}} \frac{1}{V_{vdW,i}} \left| \left(\frac{\partial^2 U}{\partial \varepsilon^2}\right)_{\varepsilon=0,i} \right|_{vdW}, \tag{5}$$

where n_C is the number of carbon atoms in the $\mathrm{C_{NT}}$ lattice, all of which are obviously associated with the C–C bond interactions, n_{vdW} is the number of atoms affected by the van der Waals interactions because of their displacement in radial direction, and the proportionality coefficients, h_C and h_0, characterize the discrete and the homogenized contributions of the C–C bond interactions to the value of the effective thickness, h_{NT}, of $\mathrm{C_{NT}}$ lattice: $h_{NT} = h_0\, h_{vdW}$, with $h_{vdW} = 3.4$ Å, $0 < h_0 \leq 1$, and $h_C > 1$, for most axial deformations, and $h_C = 0$ and $h_0 \approx 1$, for the $\mathrm{C_{NT}}$ lattices with large diameters subjected to the predominately surface forces proportional to the surface area of the carbon rings, N_{vdW}, under significant van der Waals forces, as in the case of graphene sheets under the transverse loading [12]:

$$h_0 = \frac{1}{2} l_{\mathrm{C-C}}/h_{vdW} + \frac{l_{\mathrm{C-C}}}{2\pi R_{NT}} \frac{\frac{3}{2} a N_{vdW}}{L_{NT}} \left(1 - \frac{1}{2} l_{\mathrm{C-C}}/h_{vdW}\right), \tag{6}$$

Note that $h_C = h_0$, when the elastic forces (i.e., the C–C bond interactions) and the van der Waals forces exactly balance each other during the deformation response of a $\mathrm{C_{NT}}$ lattice and the corresponding loading path.

The value of the effective thickness, h_{NT}, of $\mathrm{C_{NT}}$ lattice shells can be estimated by the number of carbon rings, N_{vdW}, subjected predominately to the van der Waals forces [12]:

$$h_{NT} = \frac{1}{2} l_{\mathrm{C-C}} + \frac{l_{\mathrm{C-C}}}{2\pi R_{NT}} \frac{3 a N_{vdW}}{2 L_{NT}} \left(h_{vdW} - \frac{1}{2} l_{\mathrm{C-C}}\right), \tag{7a}$$

or by the number of carbon rings, $N_{\mathrm{C-C}}$, mostly involved in the elastic C–C interactions [12]:

$$h_{NT} = h_{vdW} - \frac{l_{\mathrm{C-C}}}{2\pi R_{NT}} \frac{3 a N_{\mathrm{C-C}}}{2 L_{NT}} \left(h_{vdW} - \frac{1}{2} l_{\mathrm{C-C}}\right). \tag{7b}$$

The value of the effective $\mathrm{C_{NT}}$ thickness, h_{NT}, in a particular deformation response is such that $l_{\mathrm{C-C}}/2 \leq h_{NT} < 3.4$ Å [12].

Deformation of Carbon Nanotubes

Since the discovery of carbon nanotubes in 1991 by S. Iijima and his NEC lab [1, 2], the mechanical response of single wall nanotubes (SWNT) had been evaluated via atomistic and molecular dynamics (MD) simulations [3, 4, 7, 12–19] and experimental testing [5, 6]. In these studies, the multi-cylinder crystal model [4], the continuum shell theory [7, 8, 11, 12, 15, 17, 20–25] and the continuum beam model [5, 6, 10–12] were used to examined the mechanical deformation of carbon nanotubes and deduce their Young's modulus (Table 3).

In 1999, Govindjee and Sackman [25] had considered an elastic multi-sheet model to show the explicit dependence of material properties on the system size when a continuum cross-section assumption is made for a multi-shell system subjected to bending. The continuum assumption was shown to hold when more than 201 shells are present in the macromechanical system considered. In 2001, it

Table 3 Young's modulus of single wall carbon nanotubes in early experiments

Methods used in a study	Predicted values	Authors of predictions
Molecular dynamics (MD)	5.5 TPa[a]	Yakobson et al. [7, 8]
AFM (Fig. 5) vibration experiments	1.5–5 TPa	Treacy et al. [5]
AFM bending experiments	1.3 TPa	Wong et al. [6]
AFM tensile experiments	0.32–1.5 TPa	Yu et al. [81]

[a] Molecular Dynamics (MD) predictions [7, 8] of Young's modulus are associated with the value of 0.66 Å for the effective thickness, h_{NT}, of carbon nanotubes

was shown that nanoscale scaling analysis and the length scales associated with the geometric parameters of C_{NT} atomic lattice structure can define a set of restrictions on the assumptions that are used in the Euler beam model [10, 11].

Ru [24] proposed an intrinsic bending stiffness for carbon nanotubes in order to decouple the bending C_{NT} shell stiffness from their ill-defined effective thickness, h_{NT}, and to ensure a consistent use of the classical shell theory [26]. Soon after it was shown [10, 11] that the thickness of carbon nanotubes may have no direct effect on the buckling behavior of C_{NT} atomic lattices for two classes of C_{NT} structures (e. g., C_{NT} *nanocrystals* or C_{NT} *nano-beams*, Fig. 1) and most continuum models are applicable only within a certain range of the length scale parameters.

Extensive atomistic and MD simulations of carbon nanotubes remain computationally expensive. As a result, the continuum models that are appropriately tailored for a particular molecular structure and specific loading conditions may be useful for the qualitative analysis of constitutive behavior of carbon nanotube lattice shells. Since the mechanics of C_{NT} response is likely to depend on the C_{NT} lattice structure, a blend of nanoscale scaling analysis [10, 11] and the continuum mechanics models based on atomic potentials [27–29], whenever possible, seems appropriate for the development of a methodology for the inter-scale extension of continuum models to the nanoscale level for various nanostructures including carbon nanotubes and for optimization of the nanotube-based AFM probes for the atomic force microscopy [12]. It has been shown [10–12] that each theoretical and experimental prediction for the most types of C_{NT} deformation can be extended to a full class of carbon nanotubes (Fig. 1) through *the laws of similitude*.

Axial Buckling of Carbon Nanotubes

Axial buckling of carbon nanotubes is especially important for the optimization and design of AFM probes. Yakobson et al. [7, 8] presented molecular dynamics (MD) simulations of carbon nanotubes under axial buckling and demonstrated a shell-like buckling deformation response. Due to the lack of established characterization methods for the mechanical properties of such nanoscale structures, an analogy with macroscopic continuum beams and shells, which had some geometric similarities with the carbon nanotubes and their global behavior, was used. Such analogy

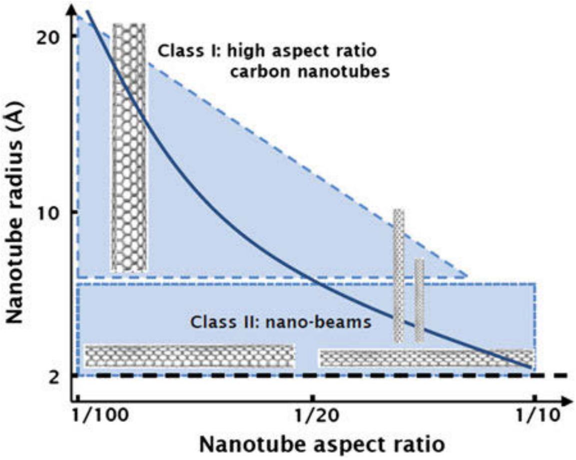

Fig. 4 A parametric map for the two classes of the high aspect ratio carbon nanotubes: *long* C_{NT} *shells* (class I) and the $\mathrm{C_{NT}}$ nanocrystals *of* small radii, i.e., the C_{NT} *nano-beams* (class II). The thick line ($\sim 1/(10d_{NT}/L_{NT})$) represents a boundary for the optimal material structure of the high aspect ratio $\mathrm{C_{NT}}$ lattices (after [10–12])

provided estimates for the $\mathrm{C_{NT}}$ Young's modulus, E_{NT}, which may reach as high as 1,000 GPa. Such simple models provide an attractive tool for the data reduction and the analysis of structure–property relationships for nanostructured materials and carbon nanotubes, in particular.

A macromechanical model "may serve as a useful guide, but its relevance for a covalent bonded system of only a few atoms in diameter is far from obvious" [7, 8]. The MD buckling strain predictions of 0.05 % indicate hyperelastic rather than elastic behavior of $\mathrm{C_{NT}}$ lattice shells. To ensure the robustness of data reduction schemes that are based on continuum mechanics, a careful analysis of continuum approximations used in macromechanical models and possible limitations of this approach at the nanoscale level is required [10–12].

The aspect ratio, d_{NT}/L_{NT}, of the $\mathrm{C_{NT}}$ lattice structures, or its equivalent, R_{NT}/L_{NT}, is the main non-dimensional length scale parameter governing the nanoscale critical buckling (Fig. 4) and the buckling strain, ε_{cr}, of the high aspect ratio carbon nanotubes (Fig. 1):

$$\varepsilon_{cr} = 4\pi^2 \frac{R_{NT}^2}{L_{NT}^2}\left[\left(1+\frac{h_{NT}}{2R_{NT}}\right)^2-\left(1-\frac{h_{NT}}{2R_{NT}}\right)^2\right], \tag{8}$$

where h_{NT} is the equivalent thickness of the thick or thin $\mathrm{C_{NT}}$ lattice shells. Note that the $\mathrm{C_{NT}}$ buckling strain, ε_{cr}, also depends on the thickness-to-radius ratio, h_{NT}/R_{NT}, of high aspect ratio carbon nanotubes, but only in the second order effects.

The explicit dependence of the critical buckling strain, ε_{cr}, on the helicity of the atomic lattices of carbon nanotubes can be estimated by

$$\varepsilon_{cr} = 4\pi^2 \left(\frac{a\sqrt{n^2+nm+m^2}/\pi + h_{NT}}{2L_{NT}} \right)^2 - 4\pi^2 \left(\frac{a\sqrt{n^2+nm+m^2}/\pi - h_{NT}}{2L_{NT}} \right)^2, \tag{9a}$$

where L_{NT} is aN_a or $a\sqrt{3}N_a$ for the armchair and zig-zag carbon nanotubes, respectively; N_a is the number of carbon rings along the C_{NT} length, L_{NT}. Since the effective C_{NT} thickness, h_{NT}, can be estimated as a half of the C–C bond length, 0.72 Å [10–12], the nanoscale analog of the Euler formula (9a, b) for the critical buckling strain of the (n, m) C_{NT} lattice shell can be written as

$$\varepsilon_{cr} = 4\pi^2 \left[\left(\frac{a\sqrt{n^2+nm+m^2}/2\pi + l_{\mathrm{C-C}}}{4L_{NT}} \right)^2 - \left(\frac{a\sqrt{n^2+nm+m^2}/2\pi - l_{\mathrm{C-C}}}{4L_{NT}} \right)^2 \right], \tag{9b}$$

where the C–C bond length is about 1.41–1.62 Å, as it can be shorter or elongated. Under extensive elongation of the C–C bonds, the approximation: $h_{NT} \approx l_{C\text{-}C}/2$, has its limitations, which are also affected by the balance between the elastic C–C bond interactions and the van der Waals forces [12]. Applicability of any continuum model for carbon nanotubes has its limitations, i.e., *a*, the size of carbon ring.

The Model Applicability Map

Ranges of applicability of the nanoscale analogs (9a, b) of the Euler formula (8) for the axial buckling of the high aspect ratio carbon nanotubes are defined by the carbon ring size, *a*, on one side of the model applicability map (Fig. 4) and by the values of the C_{NT} lattice aspect ratio, i.e., the so called shell-beam transition border line $\sim 1/(10d_{NT}/L_{NT})$, beyond which geometric parameters define the class of *thin* C_{NT} *shells* [12]. The key non-dimensional parameters that govern the materials map for the beam-like carbon nanotubes (i.e., the class of the high aspect ratio C_{NT} lattices and the class of nano-beams, Fig. 1), include the aspect ratio, d_{NT}/L_{NT}, the homogenization ratio: L_{NT}/a, and the normalized radius, R_{NT}/a (Fig. 4) [10–12].

Examples of the atomic lattices of the C_{NT} *nano-beams* include [12, 30]:

- the (2, 2) $C_{\mathbf{NT16}}$ nanocrystals;
- the (3, 3) $C_{\mathbf{NT24}}$ nanocrystals;
- the (3, 0) $C_{\mathbf{NT12}}$ nanocrystals;
- the (4, 0) $C_{\mathbf{NT16}}$ nanocrystals;
- the (6, 0) $C_{\mathbf{NT16}}$ nanocrystals.

The atomic lattice structure of the C_{NT} *nano-beams* has characteristic bond stretching due to the curvature, the small radii and considerable corrugation [12, 30].

Materials maps for the class of beam-like C_{NT} nanocrystals (or the C_{NT} *nano-beams*) indicate that the unique material properties of the corresponding C_{NT} lattices have the mechanical properties and the associated deformation response of the beam-like structures. Ranges of applicability for the equivalent-continuum beam models [10–12, 31] span two different groups of geometric parameters (Fig. 6) that define two different classes of C_{NT} lattices with small and large values of radii (Fig. 1). It has been shown that these carbon nanotubes have the same buckling behavior [10–12], although other mechanical properties (e.g., transverse stiffness) may diverge due to different structural characteristics [12, 32, 33].

The Thin Shell Effects in the Buckling of Carbon Nanotubes

The global mechanical behavior of the carbon lattice can be analyzed by representing the discrete molecular structure with an equivalent shell [7, 8, 12, 15, 21–24, 27–29, 34]. This representation can be used to define a homogeneous equivalent-continuum[5] by equating the energies of the two corresponding systems [7, 8]. The global shell-like response of a short C_{NT} lattice of 1 nm in diameter was first shown by Yakobson et al. [7, 8] by the molecular dynamics (MD) simulations. Equivalence between the potential energy of the C_{NT} lattice and its elastic strain energy represented by the continuum shell model [26] was used to obtain the value of the axial and flexural bending stiffness, $C = E_{NT}h_{NT} = 59.36$ eV/atom, and $D = E_{NT}\,(h_{NT})^3/12(1 - v^2) = 2.886$ eV Å^2/atom. For the Poisson's ratio, v, of 0.19, these two equations yield the Young's modulus, $E_{NT} = 5.5$ TPa, and the equivalent C_{NT} thickness, $h_{NT} = 0.66$ Å [7, 8, 32, 33]. Other authors have obtained similar values of 5.1 TPa and 0.74 Å, or 4.8 TPa and 0.75 Å (see Table 2) [12].

Carbon nanotubes of the radii $R_{NT} > 6$ Å or $R_{NT}/a > 2$, have larger radii than the C_{NT} *nano-beams* (Fig. 4) and the greater number of the circumscribed carbon rings along their circumference, i.e., more than 12, which corresponds to the C_{NT} *lattice shells* larger than the (12, 0) zig-zag carbon nanotube, e.g., the (15, 0) zig-zag C_{NT} *lattice shell*. Carbon nanotubes with many circumscribed carbon rings are quite different from the C_{NT} *nano-beams* (Fig. 1) [12]. The C_{NT} *lattice shells* of large diameters, $d_{NT} > 12$ Å, have much smaller intra-tubular van der Waals forces and small curvature effects. The highly-concentrated intra-tubular van der Waals forces and significant curvature effects in the C_{NT} *nano-beams* represent volumetric as opposed to the surface effects [4, 12].

The buckling strain, ε_{cr}, for the class of thin C_{NT} lattices (Fig. 1) having (m, n) chirality can be estimated by the following formulae for the nanoscale critical buckling strain, ε_{cr} [12]:

---

[5] V.M. Harik et al. 2002. *Applicability of the Continuum-shell Theories to the Mechanics of Carbon Nanotubes*. (NASA/CR-2002-211460/ICASE Report No. 2002–2007, ICASE Institute) NASA Langley Research Center, Hampton, Virginia. In this NASA report model applicability map [12] for the continuum shell models has been presented.

$$\varepsilon_{cr} = \frac{2\pi}{\sqrt{(1-\nu^2)}} \frac{h_{NT}/a}{\sqrt{3(n^2+m^2+nm)}}, \tag{10a}$$

or

$$\varepsilon_{cr} = \frac{2\pi}{\sqrt{(1-\nu^2)}} \frac{h_{NT}/l_{\mathrm{C-C}}}{\sqrt{n^2+m^2+nm}}, \tag{10b}$$

which represent the nanoscale analogs of the following formula: (see footnote 5)

$$\varepsilon_{cr} = \frac{1}{\sqrt{3(1-\nu^2)}} \left(\frac{h_{NT}}{R_{NT}}\right),$$

where ν is the Poisson's ratio [12] of atomic $\mathrm{C_{NT}}$ lattices shells (Fig. 5).

Formulae (10a, b) are valid when the nanoscale homogenization criterion (1), the scaling condition for the class of thin shells: $h_{NT}/R_{NT} << 1$, or the new nanoscale thin lattice-shell conditions (2a, b) and (3) for the (n, m) $\mathrm{C_{NT}}$ lattices are fulfilled. The role of van der Waals forces is discussed in more details in a new book *Mechanics of Carbon Nanotubes* [12]. Formulae (10a, b) and their counterparts for the nanoscale buckling provide good estimates for the axial buckling of carbon nanotubes as was shown by Harik [10–12] for different classes of atomic lattices and verified with the molecular dynamics (MD) data [12]. Each theoretical and experimental prediction is applicable and extendable within one class of carbon nanotubes [10–12] or a class of single shells in multi wall carbon nanotubes (with the role of van der Waals forces taken into account [12]).

Interfacial Sliding of Shells in Multi Wall Carbon Nanotubes

At the nanoscale level fundamental origins of sliding friction involve the surface-to-surface interactions such as the interlocking and registry effects [35–41] between the $\mathrm{C_{NT}}$ lattice structures (Fig. 5) and the morphology of asperity distribution, the sliding induced excitation of atomic lattice vibrations [42], interaction of phonons [43, 44] propagating along the sliding surfaces [45, 46], electrostatic interactions, electron motion and the electron interactions akin to the π–π bonding interactions [12]. These interfacial friction mechanisms have been studied to some extent by a quartz-crystal microbalance, scanning force microscopy and the nanotube pullout, AFM and TEM experiments (Fig. 6), as well as theoretical modeling including MD simulations [12].

Fig. 5 Atomic lattice of a single wall (10, 10) carbon nanotube with the C_{NT} length $L_{NT} = 52.5$ Å and diameter, $d_{NT} = 13.6$ Å, and a schematic of a multi wall carbon nanotube (after [12])

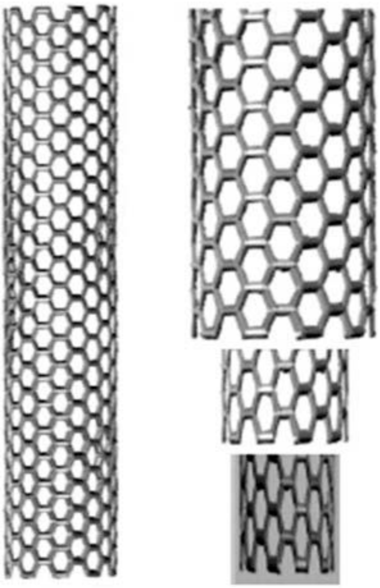

Fig. 6 TEM images of multi wall carbon nanotubes with different inner and outer diameters with five, two and seven cylindrical lattice shells reported by Iijima in 1991 (after [1])

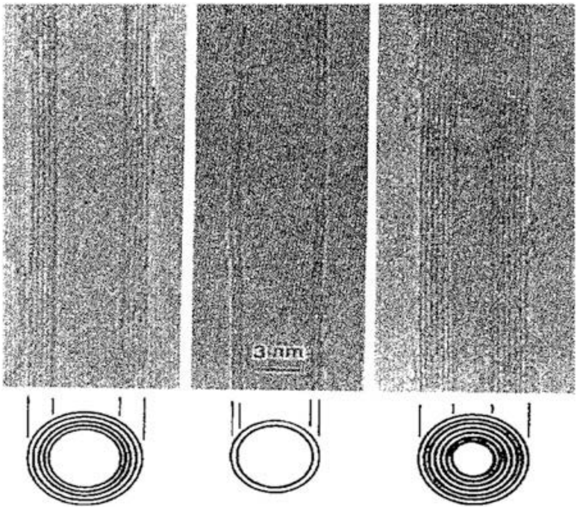

Nanoscale Analogs of the Newton's Friction Law

Nanoscale friction between adjacent C_{NT} lattice shells in multi wall carbon nanotubes (Fig. 5) can be described at the length-scale longer than the size of carbon rings, a, by a nanoscale analog of the Newton's friction law [12, 39–41] as follows. The average shear stress, $<\tau_{rz}>$, for planar sliding interactions can be defined as $<\tau_{rz}> \approx <f>_{pull}/A_{ss}$, where $<f>_{pull}$ is the average force applied to the C_{NT} lattice and

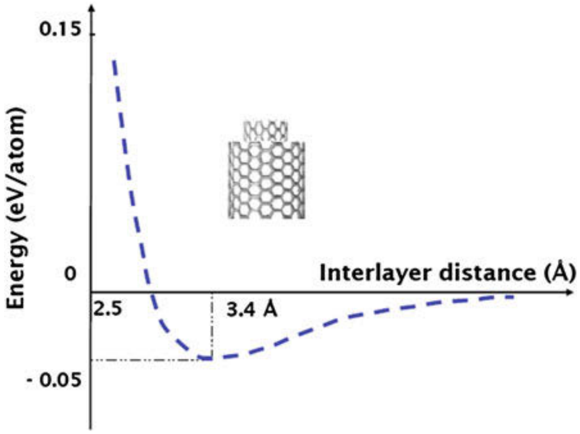

Fig. 7 Energy of interfacial interactions due to the van der Waals forces between adjacent lattices in a multi wall carbon nanotube (with the graphene-based equilibrium distance of 3.4 Å)

A_{ss} is the common interfacial area of steady sliding between the inner and the outer C_{NT} lattices. The average strain rate, $<\dot{\gamma}>$, can be estimated by $< \dot{\gamma} > \approx \frac{\partial < V_z >}{\partial r}$, where $<V_z>$ is the average C_{NT} velocity in the axial z-direction and r is the radial distance. Then, a nanoscale analog of the Newton's law for steady C_{NT} sliding is given by [1, 12, 39–41, 47]

$$< \tau_{rz} > = \mu_{eff} \frac{\partial < V_z >}{\partial r}, \tag{11}$$

where μ_{eff} is an effective viscosity for the C_{NT}/C_{NT} interfacial sliding and the strain rate can be approximated as $\frac{\partial < V_z >}{\partial r} \approx \frac{< V_z >}{h_{VdW}}$ with the change in sliding velocity across the interfacial separation,h_{VdW}, estimated as the average C_{NT} velocity, $<V_z>$. The average surface separation, h_{vdW}, is caused by the van der Waals forces, which can be described by the Lennard-Jones potential:

$$U_{LJ}(r) = \varepsilon\left(\frac{r_0^2}{r^{12}} - \frac{r_0^2}{r^6}\right),$$

where ε is the depth of the potential well and r_0 is the distance between two C_{NT} lattices at which the potential, U_{LJ}, is zero (Fig. 7).

In order to complete the description of the interface model, the effective viscosity, μ_{eff}, should be described. The C_{NT} velocity, $<V_{NT}> = <V_z>$, is, on average, linearly related to the average applied force, $<f>$ [39–41], and the slope, χ_{eff}, can be determined. The resulting force-velocity dependence: $< f > = \chi_{eff} < V_{NT} >$ is a nanoscale analog of the friction law in equation (11). Then, the complete interfacial friction model [12, 39–41] for the sliding process is given by

$$< f >_{pull} = f_0 + \chi_{eff} < V_{NT} >, \tag{12}$$

where f_0 is the critical force associated with the onset of interfacial sliding of the inner carbon nanotube [12, 39–41].

The applied force, <*f*>, is related to the shear stress in Eq. (11) by the force balance: $<f> \; = \; <\tau_{rz}> A_{ss}$. Therefore, the viscosity coefficient, χ_{eff}, can be related to the effective viscosity μ_{eff} by

$$\mu_{eff} = \chi_{eff} \frac{h_{vdW}}{R_{NT}} \left[2\pi(1 + \frac{h_{NT}}{2R_{NT}})L_{NT} \right]^{-1} \tag{13}$$

and the complete interfacial friction model (12) takes the following form [12]:

$$<f>_{pull} = f_0 + 2\pi\mu_{eff} \left[\frac{h_{vdW}}{R_{NT}} \right]^{-1} (1 + \frac{h_{NT}}{2R_{NT}})L_{NT} < V_{NT} > , \tag{14}$$

The magnitude of the critical force f_0 is on order of *pico-Newtons*, the value of coefficient χ_{eff} may vary in the range of (pN ps)/Å units and the average C_{NT} velocity, $<V_z>$, is on order of Å/ps or 100 s of m/s at the nanoscale level. The effective viscosity μ_{eff}, which characterizes the viscosity of the spatially distributed π-electrons, is associated with the transient interlocking of π-electrons in the spatial energy map shown on Fig. 8b for a quasi-static case. The viscosity of π-electrons is on the order of fractions of centi-Poise for the noted range of velocities [12].

Effect of the Spatial Exclusion of Electrons (SEE)

Variations in the interfacial frictional forces and the picosecond spikes in the axial velocity, V_{NT}, of a sliding carbon nanotube lattice shell within a multi wall carbon nanotube are associated with the interfacial registry effects, registry barriers and the

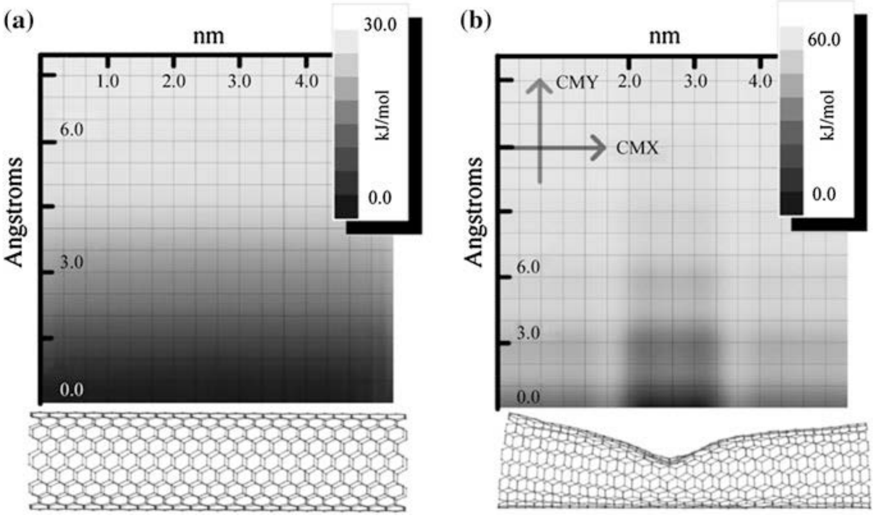

Fig. 8 A function representing the 2-D vdW energy (kJ/moL) varying with the distance from the outer surface for a (**a**) straight and (**b**) buckled single wall carbon nanotube (after [77])

accompanied generation of lattice waves, *phonons*, in the sliding carbon nanotube subjected to semi-constant force [12]. The onset of the interfacial registry between a carbon atom 'asperity' and a carbon ring potential barrier through a C–C bond is associated with the initiation of the so called *effect of the spatial exclusion of electrons (SEE)*[6] in the repulsive interaction between the spatially-distributed π–π electrons [12]. After a carbon atom passes over a C–C bond and the thermodynamically unstable potential maximum, the C_{NT} lattice relaxes into and oscillates around a more favorable position within the potential well of a lattice-asperity registry under the ambient registry potential akin to the capillary effect. The local spatial energy map of π-electrons is affected by the transient interlocking of π-electrons, which is similar to the quasi-static interlocking illustrated by the energy map shown in Fig. 8b.

This sliding behavior of a carbon nanotube is also associated with the release of the lattice waves, i.e., *phonons* (see Fig. 9) [12] during sharp yet short peaks in the interfacial registry interlocking and the associated sharp but small drops in the $\mathrm{C_{NT}}$ sliding velocity, $\mathrm{V_{NT}}$. This stick-slip phenomenon of the nanoscale friction is caused by the emergence of various registry-dependent interlocking of the atomic lattice barriers, which are sensitive and directly connected to the $\mathrm{C_{NT}}$ lattice sliding path,[7] its carbon rings, as well as to the influence of lattice oscillations [12]:

Phonons in the Atomic Lattice Shells

At the nanoscale level, oscillations of the graphene lattice (Fig. 9) are inherent in most physical settings due to thermodynamic motion of carbon atoms. Lattice waves, i.e., *phonons*, in the atomic lattice structure of carbon nanotubes occur continuously due to the thermal vibrations, nanoscale mechanical deformation with complex loading path or complex sequence of thermodynamic equilibrium states (e.g., buckling [1, 8, 10–12, 48–54]) and during the taping mode of the carbon

---

[6] V.M. Harik, New Trends in Mechanics of Carbon Nanotubes and Applications, Technical Report TR-2012-2, Nanodesigns Consulting, Newark, Delaware, 2012.

[7] Initiation of the so called *SEE effect* is associated with the need of at least one π-electron to overcome the registry potential of an opposing C–C bond and the associated Coulomb repulsion within the so called *spatial exclusion zone* (SEZ) for electrons. The size of *the spatial exclusion zone* depends on the local atomic lattice configuration (e.g., orientation of C–C bonds), the registry potential barriers, the nanoscale Coulomb repulsion proportional to $1/r^2$, and the nanoscale repulsion proportional to $-1/r^{12}$. The combined effect results in the so called *SEE effect.* The nanoscale analog of Pauli exclusion-repulsion for electrons stems from the quantum Pauli principle for the identical electrons, i.e. particles with the spin ½ (*fermions*); the two identical particles cannot occupy the same energy state, as their combined wave function, ψ, is anti-symmetric. The nanoscale analog of Pauli repulsion and the quantum Pauli principle for the electrons both affect the precise dimensions of the spatial exclusion zone for interfacial electrons.

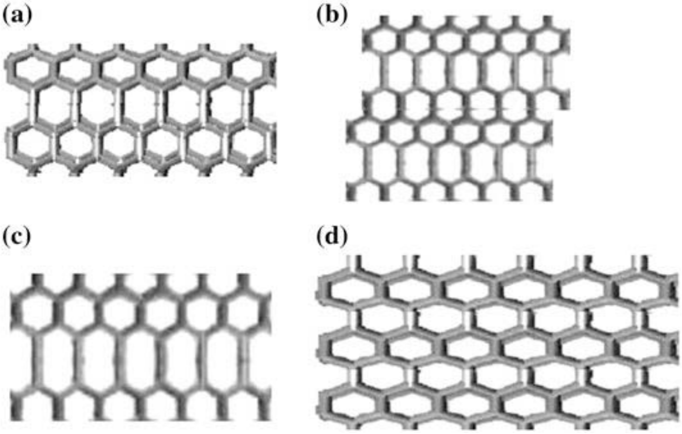

Fig. 9 Schematics of the longitudinal lattice waves (**a**), (**b**), (**c**) and (**d**) (i.e., longitudinal phonons) and tensile lattice deformations of the graphene sheets: local stretching (**c**) and the global or uniform tensile deformation (**d**)

nanotube based AFM probes (Fig. 5). Distribution of the low energy *border value (BV) phonons* of stochastic lattice waves [12] emerging at low temperatures in stochastic oscillations with the border value amplitudes depends on the energy of thermal vibrations. Probability and the dominant mode of these phonons are directly connected to the configuration of specific atomic lattice structures [12], for example, the curvature of atomic lattice in carbon nanotubes, Fig. 9 illustrates a few examples of *phonons* in a portion of graphene lattices of various sizes.

At the nanoscale level the generated lattice waves and the induced mechanical stresses, σ_{ij}, can produce various types of deformations (Fig. 9). The nanoscale mechanical stresses can be described by the following formula [39–41]:

$$\sigma_{ij,n} = -\frac{1}{\Lambda_n}\left(M_n V_{n,i} V_{n,j} + \sum_{m=1}^{N} F_{nm,i} r_{nm,j}\right), \tag{15}$$

where M_n is the mass of the nth-atom, Λ_n is the volume of the nth-atom, $V_{\mathrm{n,i}}$ and $V_{n,j}$ are the ith and jth-components of the velocity vector of the nth-atom ($i, j = 1, 2$ and 3), $F_{nm,i}$ is the ith-component of the force interaction between the nth-atom and mth-atom (i.e., the inter-atomic potential gradient) and $r_{\mathrm{nm,j}}$ is the jth-component of the difference between the position vectors of the nth-atom and mth-atom. Note that the velocity contributions to the values of thermodynamic stress components (15) include the intrinsic dynamic effects into the nanoscale mechanical stresses, containing the velocity-dependent thermal effects associated with *phonons*.

Fig. 10 The atomic force microscope (AFM) probe with the high aspect-ratio carbon nanotube tip (the orientation of the tip attachment is not completely vertical due to the orientation of the faces of the pyramidal tip)

Applications of Carbon Nanotubes

Since the discovery of carbon nanotubes in 1991 by S. Iijima and his lab,[8] these fullerenes have become one of the most popular types of nanostructured materials and particles used in novel applications and studied by academic and industrial researchers[9] and students. Examples of nanotube-based applications in nanotechnology include: *nanoscale probes, sensors and resonators, the atomic force microscope (AFM) probes* [48–54] (Fig. 10)*, nanotube-enhanced polymer membranes and multifunctional nanocomposites* [12]. Carbon nanotubes or their fragments and graphene flakes are claimed to be found in women's mascara, the fireplace ash, in the steel of Damascus swords, and soon to be found in advanced solar panels, fuel cells and batteries.

The Carbon Nanotube Based AFM Probes

Atomic force microscopes (AFM) are important instruments for the nanoscale characterization of material properties of various nanostructures, nanocrystals and molecules. Carbon nanotubes, both single wall carbon nanotubes and multi wall carbon nanotubes (Fig. 5) have been used as a high aspect ratio tip in the pyramidal AFM probes. Because of the smaller diameters (~ 1–2 nm and ~ 50–70 nm*)* of the available single wall and multi wall carbon nanotubes, respectively, resolution of the nanotube-based AFM probes is much higher as opposed to the pyramidal tip with diameters between 1 and 50 μm.

---

[8] S. Iijima was awarded the 1996 Nobel Prize in Chemistry for "discovering fullerenes", which also include carbon nanotubes.

[9] V.M. Harik, *Mechanics of Carbon Nanotubes* © (2001), a short course, the Annual ASME Congress (2001, 2004) and the 2002 Nanosystems Conference (Berkeley, Califormia).

Table 4 Typical length scales in the material structure of nanocomposites

Carbon nanotubes	Polymers	Polymer composites
Carbon ring (2.46 Å)	(CH_2) zig-zag (∼3 Å)	Fiber/matrix interphase (1–3 μm)
Diameter (∼1 nm)	Crystalline unit (∼7 Å)	Carbon fiber (20 μm)
Length (10 nm–cm)	Length of chains (∼300 nm)	Fiber length (1–10 m)

AFM probes allow characterization of nanoscale surface profiles and the degree of roughness (Table 4), corrugation of atomic lattices, surface adhesion and friction, surface sliding and stiction, adhesion of single molecules and groups of atoms to the atomic lattices, the pullout and pull-off processes at the nanoscale, interfacial friction and atomic scale sliding or rolling of nanostructures, vibrational and material properties of carbon nanotubes (including nanoscale buckling [10–12, 50–52] [55–57]) as well as various manipulation processes [12, 48, 49] [48–54].

Carbon Nanotube Based Nanocomposites

Carbon nanotube based polymer nanocomposites [54–66] represent one of the highly promising multifunctional materials, which are sensitive to the electromagnetic field effects [12, 67, 68]. Typical length scales in the material structure of carbon nanotubes as compared to the polymeric structure of a crystalline polyethylene (PE) polymer (Fig. 11) and the polymer matrix composites reinforced by the carbon fibers [69, 70] are shown in Table 4. Carbon nanotube based *nanocomposites* or the nanotube-modified polymers have unique structural length scales, which are different from the hierarchical length scales associated with the microstructure of typical composites. One of the important characteristics of nanocomposites is the high ratio of interfacial surface to the volume of reinforcing carbon nanotubes or graphene flakes.

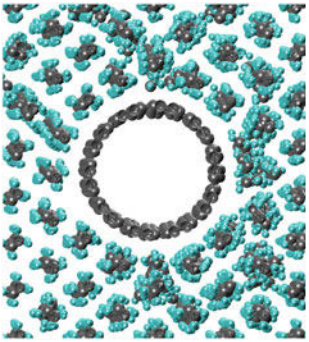

Fig. 11 Molecular lattice structure of the crystalline part of the polyethylene (PE) polymer with the $(CH_2)_n$ zig-zag chains surrounding the armchair (10, 10) carbon nanotube, $d_{NT} = 13.6$ Å [78]

Another distinction of nanocomposites [53–66] is the small size of the representative volume element (RVE) or a unit cell (Fig. 11) in nanoscale homogenization [10–12, 39–41] or property averaging [12]. Intratubular space in carbon nanotubes contributes to their high porosity, however, it is not taken into account in the calculations of their volume fraction in nanocomposites. The C_{NT} volume fraction, V_{NT}, includes entire C_{NT} cross-section:

$$V_{NT} = \pi(R_{NT} + h_{NT}/2)^2/A_{RVE}$$

where $h_{NT} < h_{vdW}$ and h_{vdW} is the equilibrium van der Waals spacing between the C_{NT} lattice and the matrix, and A_{RVE} is the cross-sectional area of the unit cell. The value of effective C_{NT} thickness, h_{NT}, and the van der Waals separation distance, h_{vdW}, depend on the loading and the nature of the C_{NT}/polymer interfacial interactions. Therefore, the macroscopic volume fraction relation in micromechanics:

$$V_{NT} + V_m = 1$$

and Tsai's *rules of mixtures* [71] in micromechanics of composite materials for the longitudinal (E_1) and transverse (E_2) Young's moduli of a nanocomposite should be modified at nanoscale [12]:

$$V_{NT} + V_m = 1 - V_{vdW}, \tag{16a}$$

$$E_1 = E_{NT}V_{NT} + E_mV_m + E_{1\mathrm{int}}V_{vdW}, \tag{16b}$$

$$\frac{1}{E_2} = \frac{V_{NT}}{E_{2NT}} + \frac{V_m}{E_m} + \frac{V_{vdW}}{E_{2\mathrm{int}}}, \tag{16c}$$

so *the van der Waals volume fraction*, V_{vdW}, is included along with the matrix volume fraction, V_m, Young's moduli of the matrix, E_m, and the van der Waals interface, E_{int}, and some of the nanoscale effects (Table 5) are accounted for.

Material properties of nanotube-based nanocomposites depend on the structure-property relations and dependencies, which are different across the hierarchical length scales. In order to link a particular macroscopic material property with the nanoscale material characteristics or structural elements, an appropriate multi-scale "tree root" diagram is needed (Table 5). Dependence of the Young's modulus, E, on the material characteristics at different length scales is illustrated for the polymer composites based on the single wall and multi wall carbon nanotubes (SWNTs and MWNTs) and on traditional carbon fibers (Table 5).

One of the first experiments characterizing the interfacial shear strength and the interfacial shear modulus has been carried out by Wagner and his group in 1998 [58–67, 71–73] by examining carbon nanotubes pulled out of a polymer matrix. Frankland et al. [39–41] carried out MD simulations to numerically evaluate the

Table 5 The structure-property relations for the Young's modulus in nanocomposites[a]

The length scales	Nanocomposites	Polymer composites
Macroscopic	Entanglement, NT coil size	Volume fraction, E_m
Microscopic	NT bundles, clustering	Carbon fibers (size, E)
Submicron	SWNT versus MWNT effects	Interphase/interface
Nanoscale	NT/polymer interphase, polymer molecular weight	Crosslink density, interface structure
Atomic	NT/polymer bonding, molecular aromaticity	Polymer structure, molecular weight, etc.

[a] The structure-property relations reflect the scale-based connections in the structure-property diagram, which links material properties with the material structure in the multiscale tree-root diagram for the structure-property relations [12]

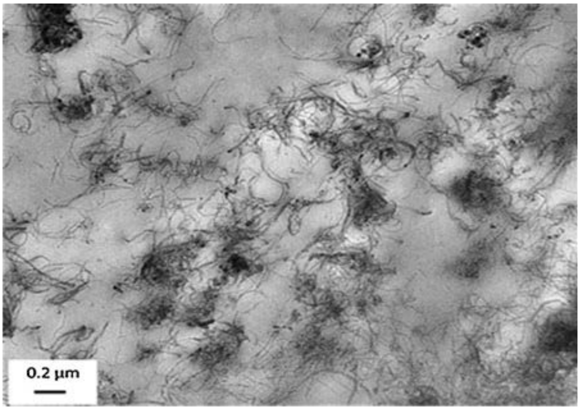

Fig. 12 TEM image of a carbon nanotube polyethylene nanocomposite with 3.5 wt% of multi wall carbon nanotubes wrapped with 10 wt% of polyethylene-polyethylene oxide (after [79])

interfacial debonding force of about 0.1 nN between a carbon nanotube and polymer matrix in polyethylene nanocomposites. An example of a carbon nanotube based polyethylene nanocomposite is shown in Fig. 12.

Frankland and Harik [39–41] have confirmed earlier theoretical results for the critical debonding force, developed an MD-based modeling procedure to examine interfacial sliding of carbon nanotubes in the pull-out experiments and presented an interfacial friction model based on a nanoscale analog of the *Newton's friction law*. A nanoscale friction model [39–41], which is similar to the new interfacial model described by the Eq. (14), and the associated friction law have been used to simulate interfacial sliding of carbon nanotubes in a nanocomposite during a pull-out experiment. The axial displacement of a carbon nanotube and its sliding under an increasing axial force has been shown to be periodic as in the stick-slip processes [42, 74, 75] with the period of nanotube sliding equal to the size of carbon rings, a.

Conclusions

This chapter has presented a review of the basic models for carbon nanotubes in terms of the (n, m) nomenclature for the chirality of lattice structures and novel nanoscale effects such as *the effect of spatial exclusion of electrons (ESEE)*, which can be considered as a nanoscale analog of *the Pauli's exclusion principle* for electrons. An example of a spatial energy map for the spatially distributed π-electrons is included to illustrate a quasi-static spatial interlocking of the distributed π-electrons, which contributes to the viscosity of π-electrons. A nanoscale analog of the Newton's friction law has been introduced in a model for the interfacial friction between adjacent lattice shells in the multi walled carbon nanotubes involving a periodic stick-slip phenomenon.[10] Interfacial lattice interlocking and the lattice registry effects also contribute to the effective viscosity of the spatially distributed π-electrons.

The ranges of applicability for different models for elastic deformation of carbon nanotubes within a particular class of carbon nanotubes have been discussed in the context of classification of their atomic lattices into *four classes (i.e., thin and thick lattice shells, long high-aspect-ratio nanotubes and beam-like carbon nanotube crystals of small radii)*. Applicability of different estimates for the effective thickness of carbon nanotubes varying between 0.66 Å (for axial buckling) and 3.4 Å (for transverse deformation dominated by van der Waals' forces) have been reviewed in the context of the balance between the elastic C–C bonds interactions and *van der Waals'* forces. The effect of van der Waals' interface in nanocomposites has been discussed for *the nanoscale rules of mixtures* and the nanotube/polymer interfacial sliding.

References

1. S. Iijima, Helical microtubules of graphitic carbon. Nature, **354**, 56 (1991) (Note that in 1991 S. Iijima has first referred to carbon nanotubes as 'microtubules' of graphitic carbon, which he and his colleague later changed to nanotubes in 1993 [2]. From the epistemological point of view this change from 'microtubules' to nanotubes indicates one of the first origins of the nanoscale concepts for new nanostructures, i.e., one of the first nanoparticles. Note that Buckminster ball, i.e., molecule C60, or the buckyball, was discovered in 1985 by R. Smalley.)
2. S. Iijima, T. Ichihashi, Single-shell (Note that in 1993 S. Iijima and T. Ichihachi have first proposed to consider carbon nanotubes as an atomic lattice 'shell'. The concept of a 'shell' was later used by B. Yakobson and his colleagues in their analysis of the carbon nanotube

---

[10] In the late 15th century Leonardo da Vinci had identified the three important parts of friction as follows. "Friction is divided into three parts: these are simple, compound and disordered." Simple friction is due to the motion and dragging; the compound friction is "between two immovable things" and the irregular friction is associated with the "corners of different sides." For more details see the notebooks of Leonardo da Vinci [76].

buckling [7, 8]. This was important from the epistemological point of view and for the development of new models for carbon nanotubes.) carbon nanotubes of low diameters. Nature, **363**, 603 (1993)

3. R.S. Ruoff, J. Tersoff, D.C. Lorents, S. Subramoney, B. Chan, Radial deformation of carbon nanotubes by van der Waals' forces. Nature, **364**, 514–516 (1993)
4. J. Tersoff, R.S. Ruoff, Structural properties of a carbon nanotube crystal, (Note that in 1993 J. Tersoff and R. S. Ruoff have first recognized the importance of the carbon nanotube crystals (or bundles), which are important for the manufacturing of centimeter long carbon nanotubes based fibers more than fifteen years later.) Phys. Rev. Lett. **73**, 676 (1994)
5. M.M.J. Treacy, T.W. Ebbesen, J.M. Gibson, Exceptionally high Young's modulus observed for individual carbon nanotubes. Nature **381**, 680 (1996)
6. E.W. Wong, P.E. Sheehan, C.M. Lieber, Nanobeam mechanics: (Note that in 1997 C. Lieber and his colleagues have introduced the concept of nanobeams (as opposed to nanowires, for example) and an area in *Nanoscale Mechanics: Nanobeam Mechanics or Mechanics of Nanobeams*) elasticity, strength, and toughness of nanorods and nanotubes. Science, **277**, 1971 (1997)
7. B.I. Yakobson, C.J. Brabec, J. Bernholc, Nanomechanics (Note that in 1996 B. Yakobson and his colleagues were among the first scientists, who have proposed to use a new term *Nanomechanics*, which has heralded the emerging field of *Nanoscale Mechanics*. They have also used the term "carbon tubes" for carbon nanotubes while they have utilized the concepts of macroscopic shell theory in the analysis of carbon nanotube buckling.) of carbon tubes: instabilities beyond linear response. Phys. Rev. Lett. **76**, 2511 (1996)
8. B.I. Yakobson, T. Dimitrica, Chapter 1, in *Trends in Nanoscale Mechanics,* ed. by V.M. Harik, M. Salas (Kluwer Academic Publishers, Dordrecht, 2003), pp. 3–33
9. R. Saito, M. Fujita, G. Dresselhaus, M.S. Dresselhaus, Electronic-structure of chiral graphene tubules. (Note that in 1992 (and 1991) the use of terms of "tubules" and "microtubules" for carbon nanotubes was present as an alternative term during the early stages of the emerging *Nanoscale Materials Science and Nanoscale Science of Nanostructured Materials.* The cited paper has also introduced the nomenclature for the physical description of carbon nanotubes and their chirality.) Appl. Phys. Lett. **60**, 18, 2204–2206 (1992)
10. V.M. Harik, Ranges of applicability (Note that this paper was among the first addressing the ranges of applicability (and limitations) of continuum models to carbon nanotubes. Also note the criticism of the use of multiple macroscopic shells in the analysis of continuum cross-sectional area by S.J. Frankland, V.M. Harik, Analysis of carbon nanotube pull-out from a polymer matrix. Mat. Res. Soc. Symp. Proc. **733 E**, T6.2.1 (2002). In 1997 in their paper [13], B. I. Yakobson and R. Smaley expressed their hope that continuum mechanics can be applied at the level of "a few atoms", which was rather optimistic as was later demonstrated in the aforementioned papers.) for the continuum beam model in the mechanics of carbon nanotubes and nanorods. Solid State Commun. **120** (7–8), 331–335 (2001)
11. V.M. Harik, Mechanics of carbon nanotubes: (Note that in 2001 [10], and in 2002, a particular area of *Nanoscale Mechanics: Mechanics of Carbon Nanotubes* was defined and its key basic concepts were outlined in a first nationally-distributed short course by V.M. Harik: *Mechanics of Carbon Nanotubes* © 2001 (a Short Curse of ASME Education Institute, American Society of Mechanical Engineers (ASME), New York).) applicability of the continuum-beam models. Comput. Mater. Sci. **24**(3), 328–342 (2002)
12. V.M. Harik, *Mechanics of Carbon Nanotubes* (Nanodesigns Press, Newark, 2011)
13. X. Zhou, J.J. Zhou, Z.C. Ou-Yang, Phys. Rev. B, **62**, 13692 (2000)
14. Z.C. Tu, Z.C. Ou-Yang, Phys. Rev. B, **65**, 233407–233414 (2002)
15. A. Pantano, M.C. Boyce, D.M. Parks, Phys. Rev. Lett. **91**, 145504 (2004)
16. A. Pantano, D.M. Parks, M.C. Boyce, J. Mech. Phys. Solids **52**, 789–821 (2004)
17. S.V. Goupalov, Phys. Rev. B, **71**, 085420 (2005)
18. P. Avouris, T. Hertel, R. Martel, T. Schmidt, H.R. Shea, R.E. Walkup, Appl. Surf. Sci. **141**, 20 (1999)
19. T. Halicioglu, Stress calculations for carbon nanotubes. Thin Solid Films, **312**, 11 (1998)
20. L. Wang, Q. Zheng, J.Z. Liu, Q. Jiang, Phys. Rev. Lett. **95**, 105501 (2005)

21. Y. Huang, J. Wu, K.C. Hwang, Phys. Rev. B, **74**(24), 24541 (2006)
22. K.N. Kudin, C.E. Scuseria, B.I. Yakobson, Phys. Rev. B, **64**, 235406 (2001)
23. A. Sears, R.C. Batra, Phys. Rev. B. **69**, 235406 (2004)
24. C.Q. Ru, Effective bending stiffness of carbon nanotubes. Phys. Rev. B, **62**(15), 9973 (2000)
25. S. Govindjee, J.L. Sackman, Solid State Commun. **110**, 227, 1999
26. S.P. Timoshenko, J.M. Gere, *Theory of Elastic Stability* (McGraw-Hill, New York, 1961)
27. M. Arroyo, T. Belytschko, J. Mech. Phys. Solids, **50**, 1941 (2002)
28. M. Arroyo, T. Belytschko, Mech. Mater. **35**(3–6), 193–215 (2003)
29. M. Arroyo, T. Belytschko, Phys. Rev. **B**, No. 69, Paper N 115415 (2004)
30. D. Stojkovic, P. Zhang, V.H. Crespi, Phys. Rev. Lett. **87**(12), 125502 (2001) (In 2001 V. H. Crespi [33] and his group at the Penn State University and V. M. Harik [34] at NASA Langley Research Center have independently predicted degeneration of C_{NT} lattice shells into nano-beams around the critical value of the normalized C_{NT} radius, $R_{NT}/a \approx 1$, Crespi predicted "breaking the symmetry of *sp*3 bonds in tubular geometries" in the smallest nanotubes.)
31. V.M. Harik, *Ranges of Applicability for the Continuum-Beam Model in the Constitutive Analysis of Carbon Nanotubes: Nanotubes or Nano-beams?* NASA/CR-2001-211013, NASA Langley Research Center, Hampton, Virginia (2001)
32. B.I. Yakobson, R.E. Smalley, (In 1997 B.I. Yakobson and R. Smaley after a very successful paper on the origins of Nanomechanics [7, 8] have expressed rather optimistic hopes that the concepts of macroscopic continuum mechanics can be applied to nanostructures at the scale of "a few atoms", which was later corrected by the nanoscale homogenization criterion as often happens in an emerging new science.) Am. Sci. **85**, 324 (1997)
33. C.Y. Li, T.-W. Chou, Int. J. Solids Struct. **40**, 2487–2499 (2003)
34. R.C. Batra, S.S. Gupta, ASME J. Appl. Mech. **75**, 061010 (2008)
35. A.N. Kolmogorov, V.H. Crespi, Phys. Rev. Lett. **85**(22), 4727 (2000)
36. K. Liao, S. Li, Appl. Phys. Lett. **79**(25), 4225 (2001)
37. A.N. Kolmogorov, V.H. Crespi, Phys. Rev. B **71**, 235415 (2005)
38. N. Marom, J. Bernstein, J. Garel, A. Tkatchenko, E. Joselevich, L. Kronik, O. Hod, Phys. Rev. Lett. **105**, 046801 (2010)
39. S.J.V. Frankland, V.M. Harik, Surf. Sci. Lett. **525**, L103 (2003)
40. S.J.V. Frankland, V.M. Harik, Mat. Res. Soc. Symp. Proc. **733 E**, T6.2.1 (2002). (This research on the nanoscale friction modeling was supported in part by NASA and the Princeton University based NASA URETI Institute for the Bio-inspired Nanostructured Multifunctional Materials (see the Princeton University based web site: http://bimat.org, award No. NCC-1-02037 by the NASA Langley Research Center, Hampton, Virginia).)
41. S.J.V. Frankland, A. Caglar, D.W. Brenner, M. Griebel, J. Phys. Chem. B **106**(12), 3046–3048 (2002)
42. Q.Y. Li, K-S. Kim, Proc. R. Soc. A **464**, 1319 (2008)
43. M.S. Dresselhaus, P.C. Eklund, Adv. Phys. **49**(6), 705 (2000)
44. A.N. Cleland, *Foundations of Nanomechanics* (Springer, Berlin, 2003)
45. P. Tangney, M.L. Cohen, S.G. Louie, Phys. Rev. Lett. **97**(19), 195901 (2006)
46. X.H. Zhang, G.E. Santoro, U. Tartaglino, E. Tosatti, Phys. Rev. Lett. **102**(12), 125502 (2009)
47. V.M. Harik, R.A. Cairncross, Mech. Mater. **32**, 807 (2000)
48. M.F. Yu, B.I. Yakobson, R.S. Ruoff, J. Phys. Chem. **104**, 8764 (2000)
49. J. Buchoux, J.-P. Aime, R. Boisgard, C.V. Nguyen, L. Buchaillot, S. Marsaudon, Nanotechnology **20**, 475701 (2009)
50. H. Dai, Nature **384**, 147 (1996)
51. K. Jensen, C. Girit, W. Mickelson, A. Zettl, Phys. Rev. Lett. **96** (21), 215503 (2006)
52. R. Stevens et al., Appl. Phys. Lett. **77**, 3453 (2000)
53. H. Nishijima, Appl. Phys. Lett. **74**, 4061 (1999)
54. J.H. Hafner, C.L. Cheung, T. Oosterkamp, C.M. Lieber, J. Phys. Chem. **105**, 743 (2001)
55. A. Garg, S.B. Sinnott, Chem. Phys. Lett. 295, 273–278 (1998)
56. I.-L. Chang, B.-C. Chiang, J. Appl. Phys. **106**, 114313 (2009)

57. C.Y. Li, T.-W. Chou, Mech. Mater. **36**(11), 1047–1055 (2004)
58. L.S. Schadler, S.C. Giannaris, P.M. Ajayan, Appl. Phys. Lett. **73**, 3842 (1998)
59. S.B. Sinnott, O.A. Shenderova, C.T. White, D.W. Brenner, Carbon, **36**(1–2), 1–9 (1998)
60. H.D. Wagner, O. Lourie, Y. Feldman, R. Tenne, Appl. Phys. Lett. **72**, 188 (1998)
61. P.M. Ajayan, L.S. Schadler, S.C. Giannaris, A. Rubio, Adv. Mater. **12**, 750 (2000)
62. C.Y. Li, Chou, J. Nanosci. Nanotechnol. **3**(5), 423–430 (2000)
63. S.B. Sinnott, J. Nanosci. Nanotechnol. **2**(2), 113–123 (2002)
64. S.J.V. Frankland, V.M. Harik, G.M. Odegard, D.W. Brenner, T.S. Gates, Compos. Sci. Technol. **63**(11), 1655–1661 (2003)
65. Y. Hu, I. Jang, S.B. Sinnott, Compos. Sci. Technol. **63**(11), 1663–1669 (2003)
66. Z. Qunaies, C. Park, K.E. Wise, E.J. Siochi, J.S. Harrison, Compos. Sci. Technol. **63**(11), 1637–1646 (2003)
67. D. Srivastava, C. Wei, K. Cho, Appl. Mech. Rev. **56**(2), 215–230 (2003)
68. A.N. Cleland, M.L. Roukes, Nature, **320**, 160–161 (1998)
69. V.M. Harik, L.-S. Luo (eds.), *Micromechanics and Nanoscale Effects* (Kluwer Academic Publishers, The Netherlands, 2004)
70. T.W. Chou, *Microstructural Design of Fiber Composites* (Cambridge University Press, Cambridge, 1992)
71. E.T. Thostenson, C. Li, T.-W. Chou, Compos. Sci. Tech. **65**, 491–516 (2005)
72. R.C. Picu, A. Sarvestani, M.S. Ozmusul, Chapter 3, in V.M. Harik, M.D. Salas (eds.) *Trends in Nanoscale Mechanics* (Kluwer Academic Publishers, The Netherlands, 2003), pp. 61–87
73. Y. Hu, O.A. Shenderova, Z. Hu, C.W. Padgett, D.W. Brenner, Rep. Prog. Phys. **69**, 1847 (2006)
74. B.N.J. Persson, *Sliding Friction: Physical Principles and Applications* (Springer, Berlin, 1998)
75. B.N.J. Persson, Surf. Sci. Reports **33**, 83 (1999)
76. E. MacCurdy (ed.), *The Notebooks of Leonardo da Vinci* (Konecky and Konecky printing, Duckworth, London, 1906)
77. S. Gorantla, S. Avdoshenko, F. Börrnert, A. Bachmatiuk, M. Dimitrakopoulou, F. Schäffel, R. Schönfelder, J. Thomas, T. Gemming, J. H. Warner, G. Cuniberti, J. Eckert, B. Büchner, M. H. Rümmeli, Enhanced π–π Interactions Between a C60 Fullerene and a Buckle Bend on a Double-Walled Carbon Nanotube. Nano. Res. **3**, 92–97 (2010)
78. S.J. Frankland, V.M. Harik, Analysis of carbon nanotube pull-out from a polymer matrix. Mat. Res. Soc. Symp. Proc. **733 E**, T6.2.1 (2002)
79. C. Semaan, G. Pecastaings, M. Schappacher, A. Soum, Polym. Bull. **68**, 465–481 (2012)
80. T. Vodenitcharova, L.C. Zhang, Phys. Rev. B, **68**, 165401 (2003)
81. M.-F. Yu, B.S. Files, S. Arepalli, R.S. Ruoff, Phys. Rev. Lett. **84**, 5552 (2000)

Molecular Modeling and Simulation of Physical Properties and Behavior of Low-Dimensional Carbon Allotropes

Carbon Nanotubes, Deformation and Fracture

Wen-Hwa Chen and Hsien-Chie Cheng

Abstract This chapter presents theoretical foundations and results of molecular modeling and simulation of carbon nanotubes, evaluation of their static and dynamic mechanicalproperties, radial buckling and deformation of the single wall carbon nanotubes (SWCNTs), their radial breathing vibrations, thermal effects and vibration modes. A review ofmolecular simulationsof buckyballs and other low dimensionalfullerenes is presented along with the fracture evolution for defective armchair SWCNTs.

Introduction

Nanotechnology has become one of the most fast growing fields in science and engineering over the last decade. Up to date, explosive-growing research efforts in material science and engineering have been devoted to exploration and development of low-dimensional allotropes of carbon such asfullerenes, nanotubes, nanorods and graphene sheets, ever since the discovery of carbon nanotubes (CNTs) [1]. Mainly because of their many extraordinary biological, chemical and physical properties due to nanosize with minor defects as well as distinct size-dependent quantum effects, they are potential for diversified industrial applications from such

---

"Learn matters of foreign lands and don't shun those of your own." T. Shevchenko (1814–1861), a great poet and educator of Eastern Europe. In 2014 we celebrate 200th anniversary of his birth.

W.-H. Chen (✉)
Department of Power Mechanical Engineering, National Tsing Hua University,
Hsinchu 30013, Taiwan, ROC

H.-C. Cheng
Department of Aerospace and Systems Engineering, Feng Chia University,
Taichung 40724, Taiwan, ROC

V. Harik (ed.), *Trends in Nanoscale Mechanics*, DOI 10.1007/978-94-017-9263-9_3

as fiber-reinforcement composites, nanoelectronics, solar energy harvesting, bio-imaging, biosensors, drug delivery, field emission panel display to electromechanical sensors etc. For instance, there has been a great interest in using low-dimensional carbon nanostructures for thin film transistors, conducting electrodes and interconnects in next-generation integrated circuit (IC) devices due to that the feature size of IC technology would soon come down to or below 16 nm in near future. In order for successful manipulation of the nanostructures for a desired device response and so realization of their engineering potential, it is rather essential to have full knowledge of their fundamental characteristics and behaviors. Moreover, nanostructures in practice are generally subjected to many environmental stressing conditions, such as heat, pressure or humidity. These external conditions, in particular temperature, can result in not only the deformations of the nanostructures but also the variation of their material properties, which eventually affect the performance of the associated application devices. In addition to the external conditions, low-dimensional carbon allotropes would also essentially change with their size, chirality and layer number. However, accurate prediction of the material properties of the nanostructures and those dependences using theoretical and experimental approaches remains a great deal of difficulty or challenge due to their nanoscale dimension.

To date, various experimental methods using high-resolution microscopes, including scanning electron microscopy (SEM), transmission electron microscope (TEM), scanning probe microscopy (SPM), atomic force microscope (AFM), X-ray diffraction, Raman spectroscopy and nanoindentation, were developed. With the techniques, extensive studies on the thermodynamic and thermal-mechanical properties of low-dimensional carbon allotropes, in particular CNTs, were attempted (see [2–6]). However, there are some implied limitations in the experimental approaches even though they turn out to be effective and straightforward in exploring the material properties of the nanostructures. For instance, owing to the limited capability of the experimental characterization techniques, conducting experiments at the scale to explore their material properties is generally very difficult, not to mention to address their size, chirality and temperature dependence. In addition, high measurement variation and even structural uncertainty of the nanostructures such as defects, which are difficult to be experimentally inspected, tend to lead to wide-dispersion experimental data. The restriction in specimen size can barely give tentative conclusions and thus provide a restricted insight from experimental results. Besides, it becomes more and more cost-ineffective and technically challenging as the specimen size gets smaller and smaller. Hence, there is an indispensable need of a more efficient and cost-effective means for characterizing the material properties of the nanostructures.

To supplement laboratory assessment, it is now possible to carry out computer modeling using such as first principles calculation andmolecular dynamics (MD) simulation due to the rapid development of powerful computers nowadays. To assess the mechanical or thermodynamic properties, presently the most successful and effective theoretical model is first-principles calculation or first-principles quantum-mechanical simulation [7]. It is, however, to find that the approach is limited to a very small system size (less than a few hundred atoms) and short simulation time (less than 10 picoseconds (ps) time scale). By contrast, MD or molecular mechanics (MM) methods are a powerful alternative because they are much more efficient and less computation-intensive. They allow simulation of a much larger system because of the neglect of the motion of electrons. In addition, their effectiveness is strongly dependent on a suitable potential function to evaluate the interactions between particles. By the approach, many studies can be found in literature in the predictions of thermodynamic and thermal-mechanical properties of low-dimensional carbon allotropes (see [8–14]). Classical MD simulation can only generate a micro-canonical ensemble (NVE), in which the total number of particles (N) and the volume (V) and energy (E) of the system are conserved, rather than a canonical ensemble such as those often encountered in experiments, where temperature (T) instead of energy is conserved. To perform canonical ensemble (NVT) or constant temperature MD simulation, several extended MD algorithms have been extensively proposed, such as velocity-rescaling algorithm [15, 16], Andersen thermostat [17], Berendsen thermostat [18] and Nosé-Hoover (NH) thermostat [19, 20], which is presently termed the standard NH thermostat method. In the standard NH thermostat method, a thermal reservoir represented by an additional, virtual variable s and effective mass Q is defined, which acts as an external system on the physical system. As a result, an extended Lagrangiansystem of particles and the variable s are formed. Heat exchange between the physical and external systems can regulate the temperature of the system. The effective mass governs the coupling of these two systems, and thus, affects the oscillation of the system temperature. In essence, the method allows fluctuation in the total energy of the physical system. However, the results made by the standard NH thermostat are not guaranteed to cover all of the available phase space [21, 22]. To resolve the drawback, some other extended NH thermostat methods were introduced, including NH chain (NHC) thermostat [23], "massive" NHC (MNHC) thermostat [24], the generalized Gaussian moment thermostat (GGMT) for a superior performance in equilibrium calculations and the Nosé-Poincaré thermostat [25] by way of a Poincaré-time transformation [26] for correcting the deficiency of angular momentum non-conservation in the standard NH thermostat method. Tuckerman et al. [26] have provided a rigorous statistical foundation for general non-Hamiltonian systems. With this foundation, the standard NH and NHC thermostat methods have been proved that through the use of a particular thermal reservoir, including potential and kinetic energies, the calculated partition function of the extended system is equivalent to that of the physical system in the canonical ensemble except for a constant factor, which means the calculated quantities are equal to those in a canonical ensemble. These thermostat methods incorporated with MD simulation have gained considerable success on a variety of studies of the temperature-dependent thermodynamic and mechanical properties of low-dimensional carbon allotropes. For example, through constant temperature MD simulation, László [27] found that the formation temperature of C_{60} fullerene in various gases is about 4,000 K. Raravikar et al. [28] exploited the velocity-rescaling algorithm to calculate the axial and radial coefficients of thermal expansion (CTEs) of single-walled CNTs (SWCNTs). Raravikar et al. [28] and Schelling and Keblinski [29] applied the velocity-rescaling method to explore the thermal effects on the CTE of CNTs. Kwon et al. [30] employed the standard NH thermostat method to calculate the CTE of SWCNTs and $C_{60.}$

From the equations of motion for the standard NH thermostat, the system reaches equilibrium if the system's kinetic energy is equal to $3Nk_BT/2$, where k_B is the Boltzmann's constant and T the externally set temperature. The relation between the system's kinetic energy and temperature is calculated based on the ideal monatomic gas model, where the intermolecular interactions are neglected [31]. However, unlike diluted gases, the interatomic interactions in a tightly bound system, such as molecules, crystals and solids, are not negligible [31]. It was reported that when dealing with such system but without taking into account the potential energy of atoms so as the effect of phonons during the correlation of the physical system energy to temperature, the temperature of the physical system would be significantly underestimated. This would result in potentially feeding back an extra amount of energy into the physical system through feedback control of the external system. Based on solid state physics [31], this will further generate, such as, large fluctuation in system energy at high temperature, thereby leading to poor system stability, reduced solution accuracy and early rupture of atomic bonds etc., and also giving an inaccurate estimate of the thermal behaviors and properties of solids/molecules. Premature atomic bond breaking problems [32] were often reported when performed through quasi-steady state MD simulation with an NH thermostat. This perhaps explains why in many previous studies [27, 33], transient rather than quasi-steady state modeling was carried out to investigate the high-temperature material properties of carbon fullerenes. Accordingly, a more robust and effective extended NH thermostat method for constant temperature MD simulation of solid system is needed.

Despite the powerful capability and great efficiency of microcomputers today, MD simulation is still limited to a relatively small-scale model where atoms are less than 10^6–10^8 and duration less than 10^{-6}–10^{-9} s. Long calculating time is generally essential for sampling high-frequency modes. Unfortunately, there present great difficulties in isolating each frequency mode due to a trivial gap among the high-frequency models. To deal with the issues, there is a crucial demand of more effective modeling techniques. A recent progress in computational methods based on equivalent continuum modeling (ECM) has allowed an effective and efficient characterization and simulation of the mechanical properties and behaviors of a larger scale of nano-structured systems in a longer time span. In principle, the ECM approaches transform chemical bonds between atoms in MM into a continuum model using finite element (FE) methods such as a shell, spring, truss, or beam element, thereby greatly improving computational efficiency while still maintaining solution accuracy. The approaches have been extensively applied in predicting the thermal-mechanical properties of low-dimensional carbon allotropes. For example, Odegard et al. [34] utilized an equivalent plate and truss model, based on computational chemistry and solid mechanics, to simulate the mechanical properties of SWCNTs and graphite. Yakobson et al. [35], Harik [36] and Wang et al. [37] proposed equivalent elastic shell models to examine the axial buckling of carbon nanotubes. Sohi and Naghdabadi [38] assessed the torsional buckling behaviors of CNTs filled withfullerenes using a multi-layered shell model. Wu et al. [39] predicted the elastic modulus of CNTs via tensile/vibrational analysis through an equivalent spring model. Li and Chou [40, 41] proposed a molecular structural mechanics (MSM) approach based on an equivalent round beam element to investigate the Young's and shear modulus and vibrational and buckling behaviors of S/MWCNTs. The beam model could offer a better description of the bonding energy of CNTs. However, its round beam assumption for simulating the covalent bonds in CNTs would potentially result in an overestimate of CNT's mechanical properties and behaviors. Furthermore, a modification of the classical MSM model was proposed by Kasti [42] for simulating the mechanical properties of zigzag CNTs. However, there are certain technical insufficiencies and shortcomings in the conventional ECM approaches. For example, they are incapable of handling the surface and temperature effects, thereby potentially leading to an inaccurate prediction of the corresponding mechanical properties. Thus, a more effective and reliable ECM approach is demanded. In this chapter, an advanced ECM model is introduced to alleviate the disadvantages of the conventional ECM approaches.

In this chapter, the static and dynamic thermal-mechanical properties and behaviors of several low-dimensional carbon allotropes, as well as their phase transformation and fracture behaviors, are extensively reported using the presently proposed MSM model and constant temperature MD model. The proposed MSM model is simply a modification of the classical MSM model, which is thus termed the modified MSM (MMSM) model. Furthermore, for facilitating MD simulation of the temperature-dependent material properties and behaviors of the carbon nanostructures in a wide temperature range from low (below Debye temperature) to high temperature (near phase change point), a novel NVT thermostat model is proposed. The proposed NVT model is a modification of the standard NH thermostat incorporated with classical MD simulation, derived by considering the contribution of phonons by virtue of the vibrational energy of lattice and the zero-point energy based on the Debye theory. The equivalence of the thermostat method and the canonical ensemble is also proved. Besides, the influences of temperature, layer number, chirality, and size on the physical properties and behaviors are also addressed. The effectiveness of the proposed theoretical models is demonstrated through comparison with the MD results derived using the conventional thermostat methods, such as the standard NH, NHC, and MNHC thermostats, and also the literature experimental and theoretical data.

The rest of the chapter is divided into four sections. Firstly, a brief introduction of the molecular structures of low-dimensional carbon allotropes is done. Secondly, in addition to the classical MD method, the theoretical background and derivations behind the proposed MMSM model and modified NH thermostat method are introduced. Thirdly, the static and dynamic thermal-mechanical properties and behaviors of various CNTs, such as Young's modulus, radial elastic properties, radial deformations, vibrational behaviors, and radial breathing modes (RBMs) and frequencies, and their temperature dependences are investigated using the presently proposed constant temperature MD simulation and MMSM model as well as the classical MSM model. Lastly, the influences of various types of atomistic defects on mechanical properties and fracture behaviors of SWCNTs are explored through the classical MD simulation. Moreover, the phase transformation behaviors of carbonfullerenes at atmospheric pressure and their thermal-mechanical properties at temperature below Debye temperature are also reported using the proposed constant temperature MD simulation model.

Molecular Structures

Allotropes of carbon are organic compounds that exist in forms with different chemical structures, such as diamond, graphene sheet, CNT and fullerene. Two examples of low-dimensional carbon allotropes are discussed herein, namely fullerenes and CNTs. They are formed by the basic structural element of graphene, and are all sp^2-hybridized, in which three C–C bonds are formed with adjacent carbon atoms.

Carbon Fullerenes

Fullerenes, alternatively called Buckminster fullerenes or simplybuckyballs, are the smallest fullerene molecule, which were named after the architect Richard Buckminster Fuller who developed a geodesic dome with great structural stability. Fullerenes are essentially composed of a number of hexagonal carbon rings (benzene) which are linked to each other or to some pentagonal carbon rings. The relationship between the number of carbon atoms (n_c) in a fullerene and hexagon carbon rings (n_h) is given by: $n_h = (n_c/2) - 10$, where the number of pentagonal carbon rings are at all times set to 12. The smallest family member is C_{20}; however, fullerene C_{20} is not a common structure. The most common structure is C_{60}, which is a soccer-ball-shaped cage, made of 20 hexagons and 12 pentagons with a carbon atom at the vertices of each polygon and a bond along each polygon edge. The stable and highly symmetric structure of C_{60} has two bond lengths: the so-called "double bond" between two hexagons and "single bond" between a hexagon and a pentagon. In essence, the former is shorter than the latter, and its average bond length is 1.4 angstroms. Ever since the discovery of C_{60} in 1985 by Kroto et al. [43], fullerenes have been the subject of intense research by many scientists worldwide.

C_{60} fullerenes can be discovered in nature and more surprisingly, also in outer space, spotted in 2010 in cosmic dust cloud. Other common higher fullerenes are C_{70} and C_{80} structure. Besides C_{60}, C_{70}, consisting of 70 carbon atoms, can be also produced in nature. It is a cage-like fused-ring atomistic structure which resembles a rugby ball, composed of 25 hexagons and 12 pentagons, with a carbon atom at the vertices of each polygon and a bond along each polygon edge. C_{80}, consisting of 80

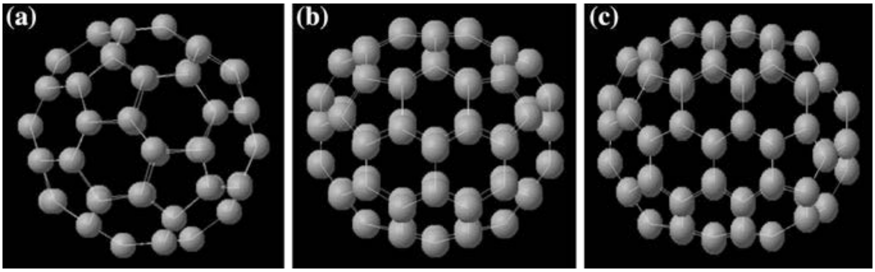

Fig. 1 Molecular structure of three kinds of buckyballs. **a** C_{60}, **b** C_{70}, **c** C_{80}

carbon atoms, is an equilibrium combination of the rhombic triacontahedron and pentagonal dodecahedron, made of 30 hexagons and 12 pentagons, and consists of full isometric pentagonal symmetry. The molecular structure of C_{60}, C_{70} and C_{80} are illustrated in Fig. 1.

Carbon Nanotubes (CNTs)

CNTs are a cylindrical carbon allotrope or buckytube. A CNT structure can be considered as a result of a number of rolled-up graphene sheets, and can be deemed an atypical variation of typical graphite. Thus, the bonding structure between carbon atoms in a CNT system is similar to that of graphite. According to the roll-up directions, the geometry of nanotubes can be uniquely determined. Prior to the wrapping of graphene sheet and the establishment of the geometry of CNTs, the chiral vector (the roll up directions) of original hexagonal lattice in graphene sheet must be determined. As shown in Fig. 2a, the chiral vector $\vec{C}_v$ in a graphene sheet is defined [44] as

$$\vec{C}_v = n_1\vec{a}_1 + n_2\vec{a}_2, \tag{1}$$

where $\vec{a}_1$ and $\vec{a}_2$ are the two primitive vectors with 60° for graphene hexagonal lattice and n_1 and n_2 arbitrary integral variables. Along the chiral vector, the graphene sheet is rolled up to a cylinder, thereby forming a CNT. Based on the roll-up directions, different CNT structures can be produced: $n_2 = 0$ for a zigzag CNT, $n_1 = n_2$ for an armchair CNT, and a chiral CNT, otherwise. In other words, three major types of CNTs can be defined based on the chiral angle θ, i.e., zigzag ($\theta = 0^\circ$), chiral ($0^\circ < \theta < 30^\circ$), and armchair ($\theta = 30^\circ$). The diameter d (Å) and chiral angle θ of CNTs can be derived from simple geometry as

$$d = 0.783\sqrt{n_1^2 + n_1n_2 + n_2^2}, \tag{2}$$

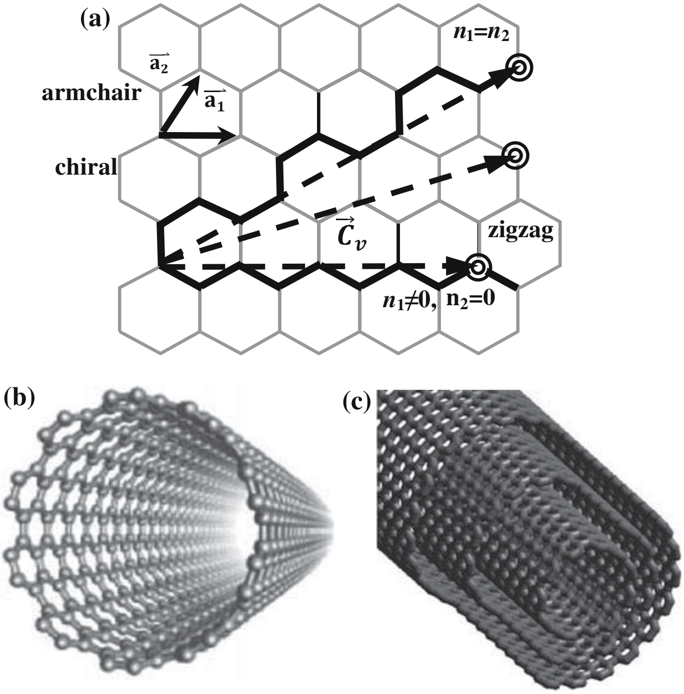

Fig. 2 Molecular structure of CNTs. **a** Chiral vector, **b** SWCNT, **c** MWCNT

$$\theta = \sin^{-1}\left[\frac{\sqrt{3}n_2}{2\left(n_1^2 + n_1 n_2 + n_2^2\right)}\right]. \tag{3}$$

CNTs can be either metallic or semi-conducting depending on their chirality, where it mainly determines the density, lattice structure, material strength, and conductance of CNTs. Based on the structure of CNTs, it can be rapidly divided into two typical categories: SWCNTs and MWCNTs. Unlike SWCNTs, MWCNTs are established by more than one rolled-up graphene sheets with an interplanar spacing of 0.34 nm. The structures of SWCNT and MWCNT are shown in Fig. 2b, c.

Theoretical Modeling

MD and ECM approaches are mainly applied in the study for exploring the physical properties and behaviors of the two low-dimensional carbon allotropes. In the session, the theoretical background and mathematical derivations of the classical

MD methods together with the potential function applied for simulating the C–C bond interactions or bonding energy are first presented, followed by a brief introduction of the standard and modified NH thermostat method [45] for constant temperature MD simulation. The former is herein termed the classical MD methods while the latter the modified MD method. Unlike the modified MD method that employs the modified NH thermostat algorithm, the classical MD methods using different existing thermostat algorithms follow classical statistical mechanics, thereby being incapable of accurately reproducing quantum predictions or capturing quantum effects, particularly at temperature below Debye temperature. In other words, they should be quantumly corrected because of the neglect of the quantum effects [46]. At last, two ECM approaches, namely the classical MSM [40, 41] and modified MSM (MMSM) are briefly introduced [47].

Molecular Dynamics (MD)

Hamiltonian Dynamics

MD is based on Hamiltonian dynamics [48]. Consider a general physical system with N atoms and the total energy of system E, including kinetic energy $\sum_{i=1}^{N} \frac{1}{2} m_i \dot{\vec{r}}_i^2$ and potential energy $U(\vec{r}_1, \vec{r}_{12}, \ldots., \vec{r}_{1N})$. The Lagrange function $L(\vec{r}_1, \vec{r}_2, \ldots, \vec{r}_N, \dot{\vec{r}}_1, \dot{\vec{r}}_2, \ldots, \dot{\vec{r}}_N, t)$ is

$$L\left(\vec{r}_1, \vec{r}_2, \ldots, \vec{r}_N, \dot{\vec{r}}_1, \dot{\vec{r}}_2, \ldots, \dot{\vec{r}}_N, t\right) = -U(\vec{r}_1, \vec{r}_2, \ldots., \vec{r}_N) + \sum_{i=1}^{N} \frac{1}{2} m_i \dot{\vec{r}}_i^2, \tag{4}$$

where m_i, $\vec{r}_i$ and $\dot{\vec{r}}_i$ are the mass, position and velocity of atom i. Replacing the velocity $\dot{\vec{r}}_i$ with the momentum $\vec{p}_i$ yields the following generalized momentum,

$$\vec{p}_i \equiv \frac{\partial L\left(\vec{r}_1, \vec{r}_2, \ldots, \vec{r}_N, \dot{\vec{r}}_1, \dot{\vec{r}}_2, \ldots, \dot{\vec{r}}_N, t\right)}{\partial \dot{\vec{r}}_i}, \tag{5}$$

and the Hamiltonian function $H(\vec{r}_1, \vec{r}_2, \ldots, \vec{r}_N, \vec{p}_1, \vec{p}_2, \ldots, \vec{p}_N, t)$ of the system is

$$H(\vec{r}_1, \vec{r}_2, \ldots, \vec{r}_N, \vec{p}_1, \vec{p}_2, \ldots, \vec{p}_N, t) = \sum_{i=1}^{N} \dot{\vec{r}}_i \vec{p}_i - L\left(\vec{r}_1, \vec{r}_2, \ldots, \vec{r}_N, \dot{\vec{r}}_1, \dot{\vec{r}}_2, \ldots, \dot{\vec{r}}_N, t\right). \tag{6}$$

The total differential of Hamiltonian function H can be expressed as:

$$dH = \sum_{i=0}^{N}\left(\frac{\partial H}{\partial \vec{r}_i}\right)d\vec{r}_i + \sum_{i=0}^{N}\left(\frac{\partial H}{\partial \vec{p}_i}\right)d\vec{p}_i + \frac{\partial H}{\partial t}dt = \sum_{i=0}^{N}\left(-\frac{\partial \vec{p}_i}{\partial t}\right)d\vec{r}_i + \sum_{i=0}^{N}\left(\frac{\partial \vec{r}_i}{\partial t}\right)d\vec{p}_i, \tag{7}$$

and the Hamilton's equations of motion can be found as

$$\frac{\partial H}{\partial \vec{r}_i} = -\frac{\partial \vec{p}_i}{\partial t} \quad (i = 1, 2, \ldots, N), \tag{8}$$

and

$$\frac{\partial H}{\partial \vec{p}_i} = \frac{\partial \vec{r}_i}{\partial t} \quad (i = 1, 2, \ldots, N). \tag{9}$$

By substituting Eqs. (4) and (5) into Eq. (6), the Hamiltonian function can be rewritten as:

$$H(\vec{r}_1, \vec{r}_2, \ldots, \vec{r}_N, \vec{p}_1, \vec{p}_2, \ldots, \vec{p}_N, t) = \sum_{i=1}^{N}\frac{\vec{p}_i^{\,2}}{2m_i} + U(\vec{r}_1, \vec{r}_2, \ldots, \vec{r}_N) = E. \tag{10}$$

Further substituting Eq. (10) into the Hamilton's equations of motion (Eqs. (8) and (9)) yields the equations of motion of the physical system,

$$\frac{\partial \vec{p}_i}{\partial t} = -\frac{\partial U(\vec{r}_1, \vec{r}_2, \ldots, \vec{r}_N)}{} \quad (i = 1, 2, \ldots, N), \tag{11}$$

and

$$\frac{\partial \vec{r}_i}{\partial t} = \frac{\vec{p}_i}{m_i}. \qquad (i = 1, 2, \ldots, N) \tag{12}$$

In MD, it is generally assumed that there is no loss in the mass of each atom; hence, Eq. (11) can be shown as

$$m_i \frac{\partial^2 \overrightarrow{r}_i}{\partial t^2} = -\frac{\partial U(\vec{r}_1, \vec{r}_2, \ldots, \vec{r}_N)}{} \quad (i = 1, 2, \ldots, N). \tag{13}$$

According to the Newton's second law $\left(F_i = m_i \frac{\partial^2 \vec{r}_i}{\partial t^2}\right)$ and Eq. (13), the conservative force can be represented by the negative gradient of some potential function U. MD method is based on the equations of motion of the physical system, i.e., Eqs. (11) and (12), calculating the positions and velocities of atoms versus time.

Potential Function

In MD simulation, an analytical or empirical potential function is applied to evaluate the atomistic interaction or bonding energy, and the formulation of MD is then defined by assessing the spatial gradient of the specified potential function. In order to derive accurate physical material properties, selection of an appropriate potential function is rather crucial. To describe the covalent bonds, i.e., σ-bonds, of carbon atoms, the pair potential approximation is not technically sufficient. The potential energy induced by the bond angle variation should be included, and a many-body potential is also required. The Tersoff-Brenner potential is one of the widely-used three body potentials for the covalent chemical bond, such as silicon and carbon. This potential is first made by Tersoff [49] for simulation of solid silicon. Later on, Brenner [50] extended the Tersoff potential for carbon and hydrocarbon system. This potential has become very popular in studying the physical properties of carbon allotropes. The total covalent potential of a physical system is denoted as the sum of individual covalent bond energy,

$$U_{\text{cov}} = f_c\left(r_{ij}\right)\left\{V_R\left(r_{ij}\right) - b_{ij}V_A\left(r_{ij}\right)\right\}, \tag{14}$$

where $f_c\left(r_{ij}\right)$ is the cutoff function of Tersoff-Brenner potential. The cutoff function can be defined as

$$f_c\left(r_{ij}\right) = \left\{\begin{array}{ll} 1 & r_{ij} < \bar{R} - \bar{D} \\ \frac{1}{2} - \frac{1}{2}\sin\left[\frac{\pi}{2\bar{D}}\left(r_{ij} - \bar{R}\right)\right] & \bar{R} - \bar{D} < r_{ij} < \bar{R} + \bar{D} \\ 0 & r_{ij} > \bar{R} + \bar{D} \end{array}\right\}, \tag{15}$$

where r_{ij} is the distance between atom i and j, $\bar{D}$ the half width and $\bar{R}$ the cutoff length. Generally, the cutoff function is a simple decaying function showing the weighting of covalent bonds centered at $r_{ij} = \bar{R}$. If r_{ij} is smaller than "$\bar{R} - \bar{D}$", the potential energy should be considered, and the weighting becomes one. When it is in between "$\bar{R} - \bar{D}$" and "$\bar{R} + \bar{D}$", the weighting varies from 1 to 0. When it becomes larger than "$\bar{R} + \bar{D}$", the potential energy can be ignored and the weighting is equal to zero. The $V_R\left(r_{ij}\right)$ and $V_A\left(r_{ij}\right)$ in Eq. (14) are the repulsive and attractive interactions. Those two parts of interactions can be described as a Morse type potential [51],

$$V_R\left(r_{ij}\right) = \frac{D_e}{S-1}\exp\left\{-\beta\sqrt{2S}\left(r_{ij} - R_e\right)\right\}, \tag{16}$$

and

$$V_A\left(r_{ij}\right) = \frac{D_e S}{S-1}\exp\left\{-\beta\sqrt{2/S}\left(r_{ij} - R_e\right)\right\}, \tag{17}$$

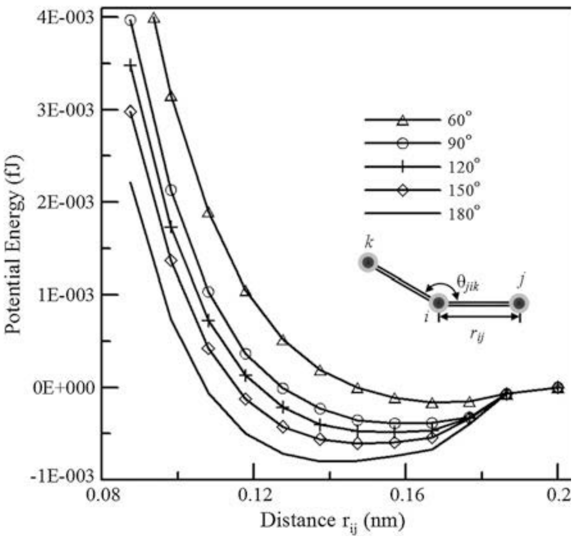

Fig. 3 Tersoff-Brenner potential versus distance at different bonding angles

where D_e and R_e are the dissociation energy and equilibrium bond length of materials, and S and β the coefficients of materials. Furthermore, b_{ij} in Eq. (14) denotes the modification of the covalent bonding energy depending on θ_{ijk} (as shown in Fig. 3). It is expressed as

$$b_{ij} = \left(1 + a^n \left\{ \sum_{k(\neq i,j)} g\left(\theta_{ijk}\right) \right\}^n \right)^{-\delta}, \tag{18}$$

where

$$g\left(\theta_{ijk}\right) = 1 + \mathrm{c}^2/\mathrm{d}^2 - \mathrm{c}^2/\left(\mathrm{d}^2 + \left(\mathrm{h} - \cos\theta_{ijk}\right)^2\right). \tag{19}$$

In Eq. (19), a, n, δ, c, d and h are also the coefficients of materials. For a carbon system, the parameters used in the Tersoff-Brenner potential have been used by Maruyama [52], and the Tersoff-Brenner potential versus distance r_{ij} with different bonding angle θ_{ijk} are illustrated in Fig. 3. It should be noted that according to Brenner [50], the non-bonding interactions such as van der Waals (vdW) forces were not considered in the potential form.

However, for some carbon allotropes, the atomistic interactions across layers are modeled with the vdW potential. A widely-used pair potential, Lennard-Jones 12-6 potential function [53], Battezzatti et al. [54] is used to describe the vdW atomistic interactions. The Lennard-Jones 12-6 potentialfunction can be written as follows,

Fig. 4 Lennard-Jones potential versus distance between two atoms

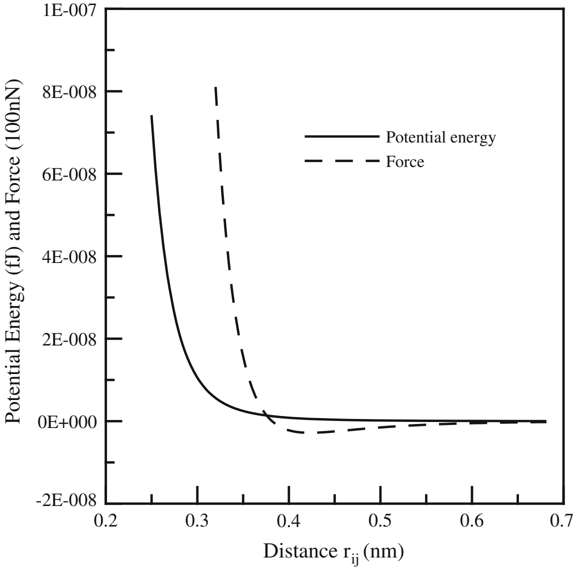

$$U_{vdw}\left(r_{ij}\right) = 4\varepsilon_0\left[\left(\frac{r_0}{r_{ij}}\right)^{12} - \left(\frac{r_0}{r_{ij}}\right)^{6}\right], \tag{20}$$

where ϵ_0 is the energy at minimal U_{vdw} and r_0 the distance between two atoms at which U_{vdw} is zero. For carbon atoms, $\epsilon_0 = 3.8791 \times 10^{-10}$ fJ and $r_0 = 0.34$ nm. The first derivative of U_{vdw} gives the vdW atomistic force function,

$$F_{vdw}\left(r_{ij}\right) = -\frac{dU_{vdw}}{dr_{ij}} = 24\frac{\varepsilon_0}{r_0}\left[2\left(\frac{r_0}{r_{ij}}\right)^{13} - \left(\frac{r_0}{r_{ij}}\right)^{7}\right]. \tag{21}$$

The relationship of both the Lennard-Jones pair potential and pair force and the inter-atomistic distance is illustrated in Fig. 4. In this investigation, the Tersoff-Benner potential is used to describe the covalent bond in fullerene, the inlayer covalent bonds of CNTs, graphite and diamond, while the interactions across layers are described with the Lennard-Jones potential.

Verlet Algorithm

By virtue of a finite-difference method, the position after a time interval Δt can be predicted according to the equations of motion for each atom. There are two numerical schemes, such as the leapfrog method [55] and Verlet method [56], are widely used in MD simulation. For the leapfrog formula, there is a need of the coordinate at next time step in order to calculate the velocity at current time. By contrast, the Verlet method is a more straightforward and efficient algorithm, and is therefore used in the investigation. With this method and the force between atoms, the position and velocity of atoms can be then calculated through MD simulation. Based on the calculated position and velocity of atoms, the thermodynamic and thermal-mechanical properties can be further estimated according to mechanics theories, such as static physics.

Thermostat Algorithms

The Standard Nosé-Hoover (NH) Thermostat Method

The standard NH thermostat [19–21] is formulated based on the idea of thermal reservoir (an external system) to control the system temperature. Consider a physical system in a fixed volume *V*. The NH thermostat introduces an additional degree of freedom *s* that denotes the thermal reservoir of the physical system to form an extended system. As a result, the thermal reservoir is considered an integral part of the physical system. The interaction between the physical and external systems is expressed via the scaling of the velocities of the particles,

$$\vec{v}_i = s\dot{\vec{r}}_i \quad (i = 1, 2, \ldots, N), \tag{22}$$

where $\dot{\vec{r}}_i = d\vec{r}_i/d\tau$ and τ is the virtual time in the extended system. The relation between the real time t and the virtual time τ is

$$d\tau = sdt. \tag{23}$$

The Hamiltonian function of the extended system can be expressed in the following form,

$$H_{Nos'e} = U(\vec{r}_1, \vec{r}_2, \ldots, \vec{r}_N) + \sum_i^N \frac{\vec{\pi}_i^2}{2m_i s^2} + 3N\kappa_B T \ln s + \frac{\pi_s^2}{2Q}, \tag{24}$$

where $\sum_i^N \vec{\pi}_i^2/2m_i s^2$ is the kinetic energy of the physical system, $3N\kappa_B T\ln s$ and $\pi_s^2/2Q$ the potential and kinetic energyof the external system, respectively, $\vec{\pi}_i$ the momentum of particle i of the physical system in terms of the virtual time τ and equal to $m_i s^2\dot{\vec{r}}$, κ_B Boltzmann's constant, T the externally set temperature, Q the effective mass of the external system, which determines the time scale and affects the temperature fluctuation, and π_s the momentum of the external degree of freedom s in terms of the virtual time τ and equal to $Q\dot{s}$.

Based on the Hamiltonian equations of motion, the scaling relations of the momenta between t and τ are

$$\vec{p}_i = \frac{\vec{\pi}_i}{s}, \tag{25}$$

and

$$p_s = \frac{\pi_s}{s}, \tag{26}$$

where p_s is the momentum of external degree of freedom s in terms of the real time t. As a result, the equations of motion of particles at time t are

$$\frac{d\vec{r}_i}{dt} = \frac{\vec{p}_i}{m_i} \qquad (i = 1, 2, \ldots, N), \tag{27}$$

$$\frac{d\vec{p}_i}{dt} = -\frac{\partial U}{\partial \vec{r}_i} - \vec{p}_i \frac{p_\eta}{Q} \quad (i = 1, 2, \ldots, N), \tag{28}$$

$$\frac{d\eta}{dt} = \frac{p_\eta}{Q}, \tag{29}$$

and

$$\frac{dp_\eta}{dt} = 2\left[\sum_{i=1}^{N} \frac{\vec{p}_i^2}{2m_i} - \frac{3}{2} N \kappa_B T\right]. \tag{30}$$

where η and p_η are two parameters used in replace of s and p_s, respectively, and their relations are denoted by

$$\eta = \ln s, \tag{31}$$

and

$$p_\eta = s p_s. \tag{32}$$

Comparing Eq. (28) with Eq. (11), the changing rate of the momentum $\vec{p}_i$ is influenced not only by the interaction force between atoms (i.e., $-\partial U / \partial \vec{r}_i$) but also by the parameter p_η and $\vec{p}_i$ itself. Equation (30) reveals that the changing rate of p_η is determined by the difference between the kinetic energy of the physical system and the total potential energy associated with the externally set temperature. According to the ideal gas law, the instantaneous system temperature T_s can be related to the kinetic energy of the physical system,

$$\sum_{i=1}^{N} \frac{\vec{p}_i^2}{2m_i} = \frac{3}{2} N \kappa_B T_s. \tag{33}$$

The equation does not consider the potential between atoms. As addressed earlier, without considering the factor in the formula, the standard NH thermostat would potentially underestimate the system temperature, and so feedback excessive energy to the physical system. This will become even more evident and critical when dealing with a tightly bound system, such as solids, crystals, and molecules.

Solid State Physics

Solid state physics [31, 57] is a branch of condensed matter physics concerned with understanding the physical properties of matter in solid state by way of techniques such as electromagnetism, quantum mechanics and crystallography. The theory has been widely applied to calculate the mechanical, thermal, electrical, magnetic and optical properties of solids. Unlike dilute gas, the interaction between atoms in solids cannot be neglected. In solid state physics, crystalline lattice is treated as a mass-and-spring system, and each atom in the lattice stays in a potential well whose minimum is at a lattice point. As the atom is perturbed from equilibrium, an induced net force would tend to restore it back to the balanced position. Consider a non-translation and non-rotation system with N particles, the energy of all possible states can be express as [31, 57]:

$$E = \sum_{i=1}^{\alpha} \hbar\omega_i \left(n_i + \frac{1}{2} \right) + U_b, \tag{34}$$

where $\hbar = h/2\pi$ and h is the Planck's constant, α and U_b the number of independent harmonic oscillators and the potential energy when all particles are in equilibrium state, and the vibrational frequency $\omega_i = \sqrt{\bar{\bar{k}}_i/\mu_i}$, where $\bar{\bar{k}}_i$ and μ_i are the effective force constant and reduced mass. The effective force constant and reduced mass are difficult to be estimated; as a result, all possible energy states should be calculated through other methods. With the energy of all possible states, the partition function can be described as

$$Z(N, V, T) = e^{-U_b/\kappa_B T} \prod_{i=1}^{\alpha} \left(e^{-\hbar\omega_i/2\kappa_B T} / 1 - e^{-\hbar\omega_i/\kappa_B T} \right). \tag{35}$$

Furthermore, based on the partition function, the total energy can be denoted as

$$E = \kappa_B T^2 \frac{\partial \ln Z}{\partial T} = U_b + \sum_{i=1}^{\alpha} \left[\frac{\hbar\omega_i}{2\kappa_B T} + \ln\left(1 - e^{-\hbar\omega_i/\kappa_B T} \right) \right]. \tag{36}$$

Since it is not straightforward to calculate the summation function, the density-of-state function $g(\omega)$, giving the number of states at frequency ω, is introduced. Accordingly, Eq. (36) can be rewritten as

$$E = U_b + \int_0^{\infty} \left[\frac{\hbar\omega}{2\kappa_B T} + \ln\left(1 - e^{-\hbar\omega/\kappa_B T}\right) \right] g(\omega) d\omega, \tag{37}$$

where

$$\int_0^{\infty} g(\omega) d\omega = 3N. \tag{38}$$

Equation (37) also can be further estimated from quantum statistics under the assumption of the quanta of lattice vibrations, i.e., phonons, which are considered as ideal Bose-Einstein gas. In order to calculate the quantity of total energy, the well-known Debye approximation [57] is used to compute the $g(\omega)$ function. In the Debye approximation, the sound velocity c_s is considered as constant for each polarization type. The relation is defined as $\omega = c_s \left|\vec{K}\right|$, where $\vec{K}$ is the wave vector. The density-of-state function $g(\omega)$ becomes

$$g(\omega) = V\omega^2 / 2\pi^2 c_s^3. \tag{39}$$

For an N-particle system, the total number of acoustic phonon modes is 3 N. A cutoff frequency ω_D, i.e., Debye frequency, can be determined form Eqs. (38) and (39) as

$$\omega_D = \sqrt[3]{18\pi^2 N c_s^3 / V}. \tag{40}$$

Substituting the cutoff frequency ω_D and the density-of-state function $g(\omega)$ into Eq. (37) yields,

$$E = U_b + \int_0^{\omega_D} \left[\frac{\hbar\omega}{2\kappa_B T} + \ln\left(1 - e^{-\hbar\omega/\kappa_B T}\right) \right] \left(9N\omega^2 / \omega_D^3\right) d\omega. \tag{41}$$

After integration, the total energy E can be written as

$$E = U_0 + 3N\kappa_B T \bar{D}(x), \tag{42}$$

where U_0 is the zero-point energy, x a dimensionless temperature $x = \theta_D / T$, where θ_D the Debye temperature $\theta_D = \hbar\omega_D / \kappa_B$, and $\bar{D}(x)$ the Debye function defined as

$$\bar{D}(x) = \frac{3}{x^3} \int_0^{x} \frac{y^3}{e^y - 1} dy. \tag{43}$$

Equation (42) reveals the relation between the total energy and temperature for a crystal.

The Modified NH Thermostat Method

The effect of the potential energy of atoms in a solid on the calculation of the system temperature is addressed through the concept of phonons, the quanta of vibrational energy. Since MD, grounded on classical dynamics, cannot deal with phonon particles, the total phonon energy is, instead, calculated based on the ideal Bose-Einstein gas model [31] and the externally set temperature. The calculated phonon energy is then added into the thermal base (i.e., the external system) in order to correct the feedback energy from the external system to the physical one. Based on the energy interaction between the physical and the external system, the energy state of the physical system would be eventually consistent with that of the external system, and also with that at the externally set temperature. Accordingly, the properties of the physical system at the energy state can be assessed. As mentioned earlier, quantum statistics remains unable to calculate the total phonon energy because of the unknown phonon density-of-state function $g(\omega)$. Thus, the well-known Debye approximation is used in the work to give an estimate of the function.

The ideal gas relation in Eq. (32) is replaced by the relation of the vibrational energy of lattice and the zero-point energy and temperature, which is derived based on the Debye theory. Consequently, both the kinetic and potential energies of atoms or the effect of phonons are taken into account in the calculation of the system temperature. According to the Debye theory, the relation of energy and temperature can be described as

$$U(\vec{r}_1, \vec{r}_2, \ldots, \vec{r}_N) + \sum_{i}^{N} \frac{\vec{p}_i^2}{2m_i} = U_0 + 3N\kappa_B T\bar{D}(x). \tag{44}$$

Substituting the right-hand side term of Eq. (32), i.e., $\sum_{i=1}^{N} \frac{\vec{p}_i^2}{2m_i} - \frac{3}{2}N\kappa_B T$, by the relation of Eq. (44) gives the modified NH thermostat equations of motion,

$$\frac{dp_\eta}{dt} = 2\left[U(\vec{r}_1, \vec{r}_2, \ldots, \vec{r}_N) - U_0 + \sum_{i}^{N} \frac{\vec{p}_i^2}{2m_i} - 3N\kappa_B T_s\bar{D}(x)\right], \tag{45}$$

and Eq. (27)–(29). The effectiveness of the proposed modified NH thermostat method remains indecisive unless the calculated partition function of the extended system is proved to be comparable to that of the physical system in a canonical ensemble. Note that the effective mass Q is determined by the following form [58],

$$Q = 3N\kappa_B T_s \tau^2, \tag{46}$$

where τ is a characteristic time scale. It was demonstrated that for a non-Hamiltonian system constructed from the modified NH thermostat, the total energy and momentum conservation laws shall be satisfied as the sum of the external forces are equal to zero [59]. Moreover, it was also theoretically proved by Chen et al. [45]

that the partition function of the extended system based on the modified NH thermostat is proportional to that of the physical system in the canonical ensemble, suggesting that the averages of any statistic quantities are exactly those in canonical ensemble [19].

Atomistic Stress

The Cauchytype ofstress measure in continuum mechanics is inadequate for use in the discrete atomic system because its physical responses are all discrete. The virial theorem [60] was often used to estimate the pressure of gas atoms or the homogeneous bulk stress. If the stress state is homogeneous in the entire volume, the virial stress can be effective. In order to compute the stress around a single atom, Basinski et al. [61] proposed the BDT stress to estimate the local stress, in which the stress measure would be valid for individual atom through the concept of effective atom volume as

$$\Omega_i = \frac{4\pi}{3} a_i^3, \tag{47}$$

where

$$a_i = \frac{1}{2} \frac{\sum_{j \neq i} r_{ij}^{-1}}{\sum_{j \neq i} r_{ij}^{-2}}, \tag{48}$$

and Ω_i is the effective volume of atom i. In essence, both virial and BDT stress are simply a volume-average-based stress measure. For the type of stress measure, the idea of the so-called volume would be vague for atomic ensembles with irregular atom arrangement. In addition, the stress measure is very difficult to satisfy the conservation of linear momentum.

The issue was also dealt with by Shen and Atluri [62] through a proposed model transferring the discrete atomistic force field into an equivalent continuum system using the smoothed particle hydrodynamics (SPH) technique. In the model, the force density $\tilde{g}(r)$ at point r can be computed from the discrete atomistic force field by the SPH method:

$$\tilde{g}(r) = \sum_i f_i W(r - r_i, \bar{h}), \tag{49}$$

where f_i is the force on atom i, $W(r, \bar{h})$ the smooth kernel function, $\bar{h}$ the smoothing length, and r_i the position of atom i. Typically, the followingGaussian function is chosen as the smooth kernel function,

$$W(r,\bar{h}) = \frac{1}{\left(\sqrt{\pi}\bar{h}\right)^d} exp\left(-\frac{x^2}{\bar{h}^2}\right), \tag{50}$$

where d is the number of spatial dimensions. As $\bar{h}$ approaches to zero, the kernel function becomes a delta function. An appropriate selection of $\bar{h}$ would make the Gaussian kernel function drop rapidly so that only a small number of atoms would contribute to the force density. By the smooth kernel function, the relationship between the atomistic force and stress fields can be obtained by analyzing the force state of the infinitesimal parallelepiped at point r. With an appropriate choice of the smoothing length $\bar{h}$, the Cauchy stress in the atomistic level at point r falls into the following simple form:

$$\sigma(r) = \frac{1}{2}\sum_i \sum_{j \neq i} r_{ij} \otimes f_{ij} \int_0^1 W\left(r + \left(r_{ij}c - r_j\right)\right) dc. \tag{51}$$

It has been well demonstrated that the Shen and Atluri's stress would be much easier to implement and also more effective for a crystalline solid with homogeneous deformations and defects. By contrast to those of the volume-average-based ones, the calculated results based on the stress measure turn out to be more consistent with the bulk value. Consequently, the stress definition is used herein.

The Classical MSM Model

The classical MSM model proposed by Li and Chou [40, 41] introduces a nonlinear rod element and an equivalent round beam to simulate the bonding force and vdW interaction between any two carbon atoms in CNTs, respectively. In other words, the model assumes that there is an equivalent bond bending rigidity in both the major and minor principal centroidal axes of the cross section of the covalent bond because of the round beam assumption. The bending rigidity of the equivalent round beam is principally derived from the bond-angle variation energy. The general potential energy expression V_t for a covalent bond system was given by Cornell et al. [63],

$$V_t = \sum V_r + \sum V_\theta + \sum V_\varphi + \sum V_\omega + \sum V_{vdW}, \tag{52}$$

where V_r, V_θ, V_φ, V_ω, and V_{vdW} are the bond-stretching energy, bond-angle variation energy, dihedral-angle torsion energy, inversion energy and vdW interaction energy, respectively. The potential energy in MM is schematically demonstrated in Fig. 5. The electrostatic interaction is herein neglected because CNTs are a neutral system. In addition, many previous studies (e.g., [63, 64]) claimed that the inversion energy is considered trivial for axial mechanical properties and behaviors of CNTs,

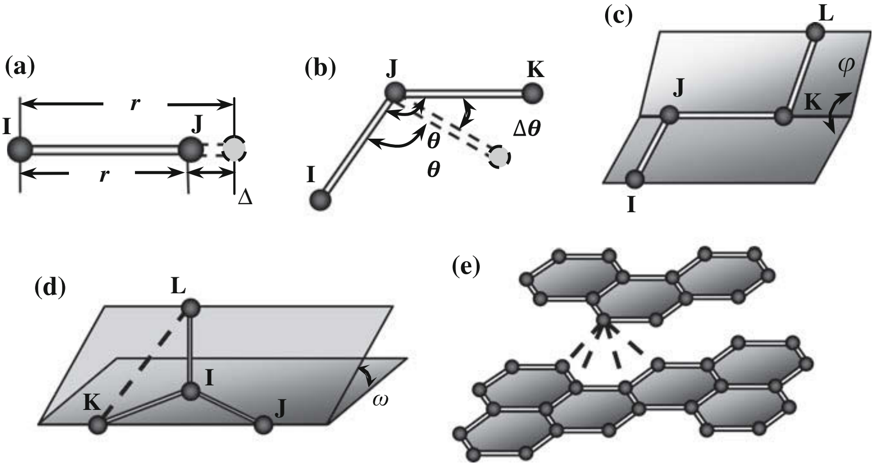

Fig. 5 Potential energy in MM. **a** V_r, **b** V_q, **c** V_φ, **d** V_ω, **e** V_{vdw}

as compared to the other energy terms. However, it will be proved later on that the energy would play a significant role in the calculation of the radial mechanical properties.

In summary, the total potential energy for a covalent bond structure, such as a CNT, is dominated by the first three terms of Eq. (52). Based on the harmonic expressions under the assumption of small deformation, the simple expressions for these energy terms can be written as

$$V_r = \frac{1}{2}K_r(r - r_0)^2 = \frac{1}{2}K_r(\Delta r)^2, \tag{53}$$

$$V_\theta = \frac{1}{2}K_\theta(\theta - \theta_0)^2 = \frac{1}{2}K_\theta(\Delta\theta)^2, \tag{54}$$

and

$$V_\varphi = \frac{1}{2}K_\varphi(\Delta\varphi)^2, \tag{55}$$

where K_r, K_θ and K_φ denote the bond-stretching, bond-angle variation and torsional-resistance force constant, and Δr, $\Delta\theta$ and $\Delta\varphi$ are the bond-stretching, bond-angle and bond-twisting-angle variation, respectively. In principle, the bond-angle variation force constant is the sectional bending rigidity about the major principal axis of the covalent bond for a graphene sheet.

To explore the stiffness and geometric parameters of the equivalent beam, including Young's modulus E, shear modulus G, length L, sectional area A, moment of inertia I, and polar moment of inertia J, their relationships with the force constants in MM need to be first determined. The stiffness and geometric

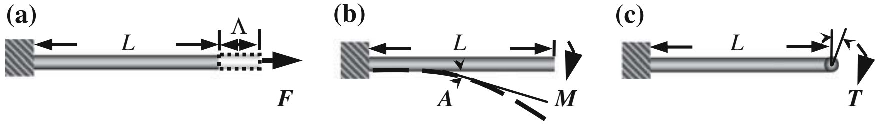

Fig. 6 Deformation of a beam element. **a** Tension. **b** Bending. **c** Torsion

parameters of the equivalent beam can be evaluated from the relationship between the potential energy of the covalent bond due to atomic interactions and the strain energy of the equivalent beam as a result of structural deformation. According to structural mechanics, the strain energies of a uniform beam subjected to a pure axial force F (Fig. 6a), a pure bending moment M (Fig. 6b) and a pure torsion T (Fig. 6c) can be expressed, respectively, as

$$U_A = \frac{1}{2}\int_0^L \frac{F^2}{EA}dL = \frac{1}{2}\frac{F^2L}{EA} = \frac{1}{2}\frac{EA}{L}(\Delta L)^2, \tag{56}$$

$$U_M = \frac{1}{2}\int_0^L \frac{M^2}{EI}dL = \frac{1}{2}\frac{M^2L}{EI} = \frac{1}{2}\frac{EI}{L}(\theta_B)^2, \tag{57}$$

and

$$U_T = \frac{1}{2}\int_0^L \frac{T^2}{GJ}dL = \frac{1}{2}\frac{T^2L}{GJ} = \frac{1}{2}\frac{GJ}{L}(\Delta\beta)^2, \tag{58}$$

where ΔL, θ_B and $\Delta\beta$ are the axial stretching deformation, the angle of rotation at the end of the beam and the relative rotation between the two ends of the beam, respectively. In Eqs. (53)–(58), both V_r and U_A represent the stretching energy, both V_θ and U_M indicate the bending energy, and both V_φ and U_T stand for the torsional energy. Accordingly, Δr is reasonably assumed to be equal to ΔL, $\Delta\theta$ is equal to θ_B, and $\Delta\varphi$ is equal to $\Delta\beta$. Therefore, relating Eqs. (53)–(55) to (56)–(58), respectively, yields the following direct relationship between the structural mechanics parameters and MM force field constants,

$$K_r = \frac{EA}{L}, K_\theta = \frac{EI}{L} \text{ and } K_\varphi = \frac{GJ}{L}. \tag{59}$$

Since the force constants K_r, K_θ and K_φ, as well as the bond length L can be directly derived from the second generation force field [63], the stiffness and geometric parameters E, G, A, I, and J of the equivalent beam can be also determined. For modeling the in-layer or inter-layer vdW interaction, a non-linear spring element is used based on the vdW interaction function from Eq. (20).

Modified MSM (MMSM) Model

The round-beam assumption in the classical MSM model is theoretically sound since the sectional bending rigidity of the covalent bond in the minor principal centroidal axis should be closely related to the weak inversion energy rather than the bond-angle variation energy according to MM [47]. As the minor-axis bending rigidity of the covalent bond would primarily determine the radial stiffness properties of CNTs, the inaccurate modeling of the sectional bending rigidity in the minor axis of the covalent bond would lead to a poor estimate of the associated radial mechanical properties and behaviors. Therefore, Chen et al. [47] introduced an MMSM model to ease the technical deficiency.

Figure 7a displays two of the hexagons in a graphene sheet, which is considered as a frame structure in the MMSM model. Point O in the figure is defined as the origin of the local Cartesian coordinate system for the beam (covalent bond) OA. Assume that there is a force F_x parallel to the X axis at point B of the beam OB, thus resulting in a bond-angle variation between the beam OA and OB or a moment M_z directed along the Z axis. Since this moment would fully contribute to the bond-angle variation energy between the covalent bond OA and OB, the relation between the sectional bending rigidity of the continuum pseudo-rectangular beam element about the Z axis (the major axis) and the bond-angle variation force constant is described as,

$$K_\theta = \frac{EI_z}{L}. \tag{60}$$

Assuming that another force F_z parallel to the Z axis is applied at the point O, as shown in Fig. 7b, which would induce a moment M_y directed along the Y axis. The force would induce the inversion energy V_ω between the atom O and the plane A−B−C. Thus, roughly one third of the inversion energy would contribute to the bending energy (U_{M_y}) of the covalent bond OA because of the moment M_y,

$$U_{M_y} = \frac{1}{3} V_\omega = \frac{1}{6} K_\omega \theta_y^2, \tag{61}$$

where K_ω is the inversion force constant, which is 1.1 kcal/mol based on Cornell et al. [63], and θ_y is the bending angle of the beam OA along the Y axis. Further combining Eq. (57) with Eq. (61) yields

$$K_\omega = \frac{3EI_y'}{L}. \tag{62}$$

By relating Eq. (60)–(62), the relation of the moment of inertia about the minor (I_y') and major (I_z) principal centroidal axes can be derived,

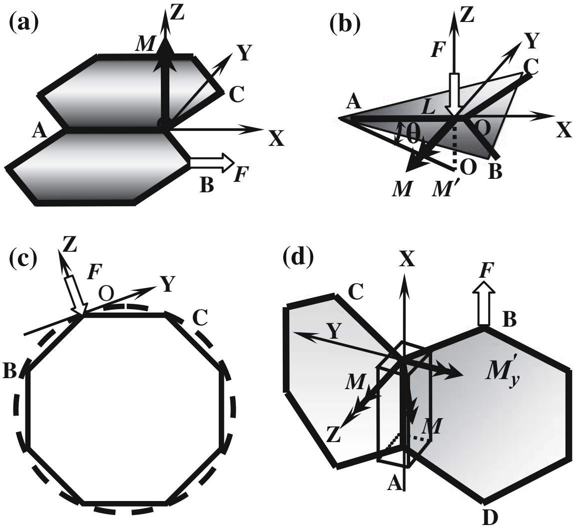

Fig. 7 Schematic of induced bond-angle variation and inversion energy in acovalent bond of a graphene sheet and CNT. **a** Bond-angle variation energy in a graphene sheet, **b** inversion energy in a graphene sheet, **c** top view of a zigzag SWCNT, **d** bond-angle variation energy in a zigzag SWCNT

$$I_y' = \frac{K_\omega}{3K_\theta} I_z = 0.0058 I_Z = \check{k}_1 I_z. \tag{63}$$

Based on Cornell et al. [63], the bond-angle variation force constant K_θ is 63 kcal/mol. From Eq. (4–61), it is evident that the I_y' is much smaller than I_z, implying that the round beam assumption in the classical MSM model is clearly not conservative.

There is a need of slight modification of the above derivation for an SWCNT since it is a rolled-up graphene sheet rather than a plane one [47]. Figure 7c, d show the top view of an SWCNT, where the circular dot line is the “virtual” tube wall of the SWCNT, and the black segment lines are the actual tube wall (i.e., a polygon), and two of the hexagons in a zigzag SWCNT, respectively. It is clear to see that unlike the graphene sheet, shown in Fig. 7a, there exhibits an angle between these two hexagons (see Fig. 7c); as a result, Eqs. (4–58), which is derived from a graphene sheet, would no longer hold for a CNT. Note that as shown in Fig. 5c, the force F_z applied at the point O would also induce a bending moment M_y on the beam OA, and then contribute to the corresponding inversion energy V_ω and also the moment of inertia along the Y-axis, just similar to the case of the graphene sheet shown in Fig. 7b. Further consider that a force F_x is acted on the beam OB at point B in the X direction, as shown in Fig. 7d, which creates a bending moment M on the beam OA. As shown in the figure, the moment M can be then separated into two components, M_y' and M_z, directed along the Y and Z axis, respectively,

$$M_y' = \frac{E\left(I_y''\right)}{L}\theta, \tag{64}$$

and

$$M_z = \frac{E(I_z)}{L}\theta, \tag{65}$$

where I_y'' is the moment of inertial of beam OA directed along the Y axis due to the bond-angle variation energy V_θ. The relation between I_y'' and I_z can be written by comparing the above two equations,

$$I_y'' = \check{k}_2 I_z. \tag{66}$$

According to Eq. (59), the corresponding bending energy terms associated with these two moment components can be calculated and the bond-angle variation energy V_θ between the covalent bond OA and OB should be equal to the sum of the above two terms, i.e.,

$$V_\theta = \frac{M_y'^2 L}{2EI_y''} + \frac{M_z^2 L}{2EI_z}. \tag{67}$$

Thus, the following relation, similar to Eq. (60), can be obtained,

$$K_\theta = \frac{E\left(I_y'' + I_z\right)}{L}, \tag{68}$$

and then I_y'' can be derived by solving Eqs. (66) and (68). Since the inversion energy and bond-angle variation energy both contribute to the energy of the beam OA, the moment of inertia of this beam along the Y axis (I_y) can be calculated by the sum of I_y' and I_y'' as

$$I_y = I_y' + I_y'' = \left(\check{k}_1 + \check{k}_2\right) I_z. \tag{69}$$

Further combining Eqs. (63), (66), (68), and (69) yields the following relations,

$$I_y = \frac{\check{k}_1 + \check{k}_2}{1 + \check{k}_2} I = k_y I, \tag{70}$$

and

$$I_z = \frac{1}{1 + \check{k}_2} I = k_z I. \tag{71}$$

From Eq. (70) to (71), the modified moment of inertia I_y and I_z are obtained. It should be noted that for a decreasing radius, k_y would come close to k_z while for an increasing radius, k_y and $\check{k}_2$ approach to zero and k_z advances to unity. This suggests that the bending energy would be dominated by the bond-angle variation energy as the radius becomes smaller. On the other hand, as the radius becomes larger than about 1.5 nm, $\check{k}_1$ tends to be greater than $\check{k}_2$, suggesting that both the inversion energy and bond-angle variation energy would have a considerable impact on the bending energy.

Static and Dynamic Mechanical Properties of CNTs

The static and dynamic mechanical properties and behaviors of CNTs, including axial Young's modulus, shear modulus, Poisson's ratio, radial elastic properties, radial buckling, radial deformations, vibrational behaviors, and radial breathing modes (RBMs) and frequencies, are presented using three simulation approaches, namely the constant temperature MD simulation incorporating the modified NH thermostat method, classical MSM and MMSM modeling. In these two MSM models, temperature effects are considered by using the predicted temperature-dependent bond length and angle through the constant temperature MD simulation and temperature-dependent force constants through the Badger's rule [65].

Elastic Properties of SWCNTs

The radial elastic modulus [66] is defined as the ratio of radial stress to radial strain, similar to the axial Young's modulus,

$$E_r = \frac{\sigma_r}{\varepsilon_r} = \frac{F/A}{\delta/D}, \tag{72}$$

where δ is the radial displacement, D the diameter of the SWCNT, F the normal force acting on the top of an SWCNT, and A the area on which F is applied, as shown in Fig. 8a. The definition of the area A is based on the assumption of Li and Chou [67, 68], in which it is the triangular area shown in Fig. 8b. The calculated radial elastic moduli by the MMSM model are illustrated in Fig. 8a, together with those calculated from the classical MSM model [67, 68]. It ranges from 30 to 0.3 GPa for the armchair CNTs with an increasing radius from 0.48 to 2.38 nm, and 62 to 0.4 GPa for the zigzag SWCNTs as their radius increases from 0.39 to 2.35 nm. It is clear to see that the radial stiffness of the zigzag type is larger than that of the armchair type, probably because of the difference of the structural arrangement of atoms. Furthermore, the radial elastic moduli tend to decrease

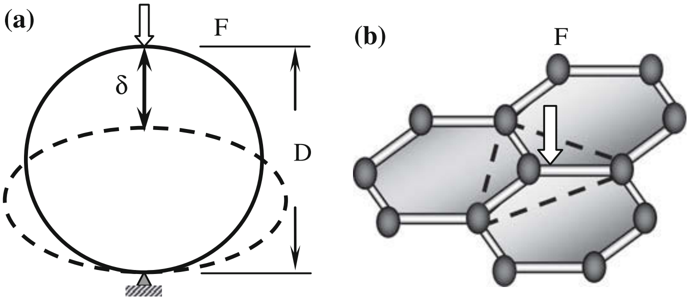

Fig. 8 Definition of the radial modulus and acting force area on an SWCNT. **a** Radial modulus. **b** Acting force area

significantly with an increasing of tube radius. The calculated radial elastic modulus from the classical MSM model at the same radius interval is in the range of 256–7.2 GPa for the zigzag type and 117–4.0 GPa for the armchair type. Clearly, there is a great deviation in the MMSM results from the classical MSM ones, and more importantly, the difference would decrease with an increasing radius. Moreover, the radial elastic modulus of the SWCNTs is remarkably lower than the associated axial one (about 1.0 TPa). Presently, there are very limited experimental data on the radial elastic modulus of SWCNTs available; accordingly, the reported numerical/experimental data of the radial modulus of multi-walled CNTs (MWCNTs) are used for an indirect validation of the MMSM model. The validation can be still considered effective mainly because they would hold a similar radial elastic stiffness due to the weak vdW interaction between CNT layers in an MWCNT. For instance, Shen et al. [66] performed nanoindentation tests to investigate the radial elastic modulus of MWCNTs using a scanning probe microscope, and found that the associated radial elastic modulus increases from 9.7 to 80.0 GPa with an increasing compressive stress. Yu et al. [4] characterized the radial elastic modulus of MWCNTs also using nanoindentation tests with a tapping-mode atomic force microscope. They reported the effective radial elastic modulus ranges from 0.3 to 4.0 GPa at different cross-sections. Muthaswami et al. [69] showed that the measured radial elastic modulus of MWCNTs using ultrasonic force microscopy is in the range of 16.0–23.0 GPa. Beside experimental characterization, Wang et al. [70] performed MD simulation to characterize the radial elastic modulus of SWCNTs and found that it is in the range of 2.0–0.1 GPa as their radius increases from 0.5 to 4.0 nm. It is apparent to see from the above reported experimental and numerical data and the present results that the classical MSM model tends to overestimate the radial elastic stiffness of the SWCNTs in contrast to the MMSM model.

The Poisson's ratio, axial Young's modulus and shear modulus of SWCNTs are subsequently examined using the MMSM model. Theoretically, the Poisson's ratio v of a continuum material is defined as the negative ratio of lateral strain ε_l to axial strain ε_a,

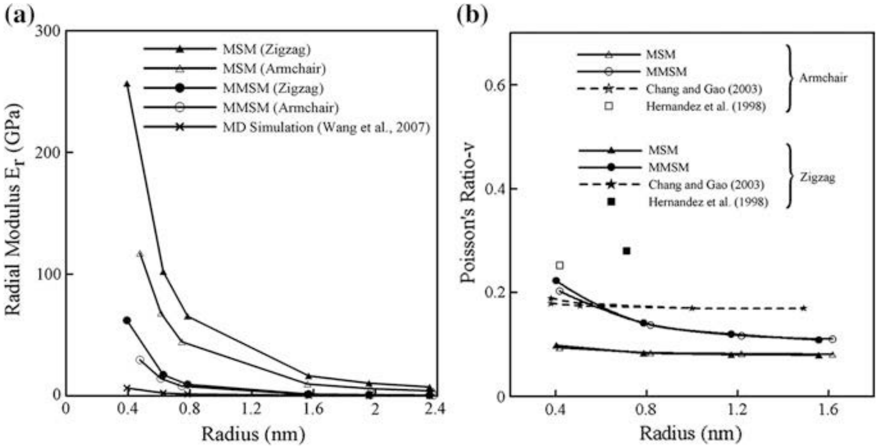

Fig. 9 Radial modulus and Poisson's ratio versus SWCNT radius [47]. **a** Radial modulus. **b** Poisson's ratio

$$v = -\frac{\varepsilon_l}{\varepsilon_a}. \tag{73}$$

The calculated results are shown in Fig. 9b, where the Poisson's ratio of the SWCNTs tends to decrease with an increasing radius. Furthermore, as the radius increases from 0.4 to 1.6 nm, the calculated Poisson's ratios using the MMSM (i.e., 0.20–0.10 for the armchair type and 0.22–0.10 for the zigzag type) are all larger than those of the classical MSM (0.08–0.06 for both the armchair and zigzag types). This suggests that the MMSM yields significantly lower radial tube stiffness for the SWCNTs than the classical MSM. Most importantly, the results obtained from the MMSM are much more consistent with the literature published data calculated using various approaches than those of the classical MSM model. For example, Hernandez et al. [10] reported the Poisson's ratio 0.25 for the armchair SWCNT with a radius of 0.41 nm, and 0.28 for the zigzag with a radius 0.75 nm using the tight-binding method. Chang and Gao [64] made an estimate of the Poisson's ratio of SWCNTs using the MM model and found that it is in the range of 0.18–0.16 for the armchair type and 0.20–0.16 for the zigzag with a radius ranging from about 0.25 to 1.0 nm.

The axial Young's modulus of a continuum material can be defined as the ratio of axial stress σ_a to axial strain ε_a,

$$E = \frac{\sigma_a}{\varepsilon_a}. \tag{74}$$

The calculated axial Young's modulus of SWCNTs using the MMSM model is presented in Fig. 10, together with the literature published results of Popov et al. [71] using a lattice-dynamical model, Chen et al. [72] using MD simulation, and

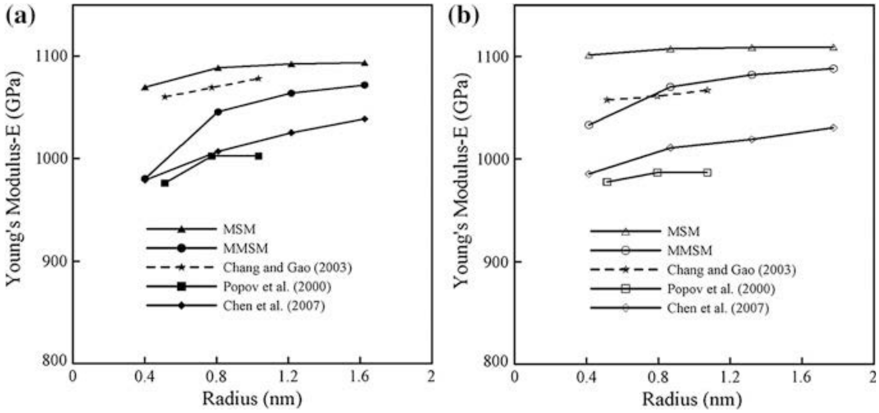

Fig. 10 Axial Young's modulus versus SWCNT radius [47]. **a** Zigzag. **b** Armchair

Chang and Gao [64] using an MM model. The simulation results show an inconsiderable discrepancy in the axial Young's modulus between the MMSM (i.e., 1,030–1,083 GPa for the armchair SWCNTs and 961–1,056 GPa for the zigzag) and classical MSM model (i.e., 1,096–1,104 GPa for the armchair and 1,054–1,078 GPa for the zigzag). The maximum distinction between these two modeling results is less than about 8 %, suggesting that unlike the radial elastic stiffness and Poisson's ratio, the modification of the covalent bond's cross-sectional bending rigidity may not notably impact on the axial Young's modulus of SWCNTs. Moreover, it is also found that the present MMSM results are slightly more comparable to the published data than the classical MSM ones, in which the latter tends to give a stiffer axial Young's modulus than the former.

The shear modulus of a continuum material can be defined as, according to the continuum assumption,

$$G = \frac{TL}{\theta J}, \tag{75}$$

where θ is the torsional angle, J the cross-sectional polar moment of inertia, T the applied torque, and L the tube's length.

The calculated shear moduli of the SWCNTs are presented in Fig. 11a, b, associated with the zigzag and armchair type, together with the literature data [72, 71]. The results show that there is only about 8–17 % discrepancies in the calculated shear modulus between the MMSM (i.e., 183–426 GPa for the armchair type and 220–425 GPa for the zigzag) and classical MSM model (i.e., 224–477 GPa for the armchair type and 265–466 GPa for the zigzag). Furthermore, by comparing the MMSM and MSM results with the literature published data of Popov et al. [71] and Chen et al. [72], a very good consistency can be found. This indicates that the correction in the cross-sectional bending rigidity of the covalent bond would have a little impact on the shear modulus of SWCNTs. In summary, the correction would

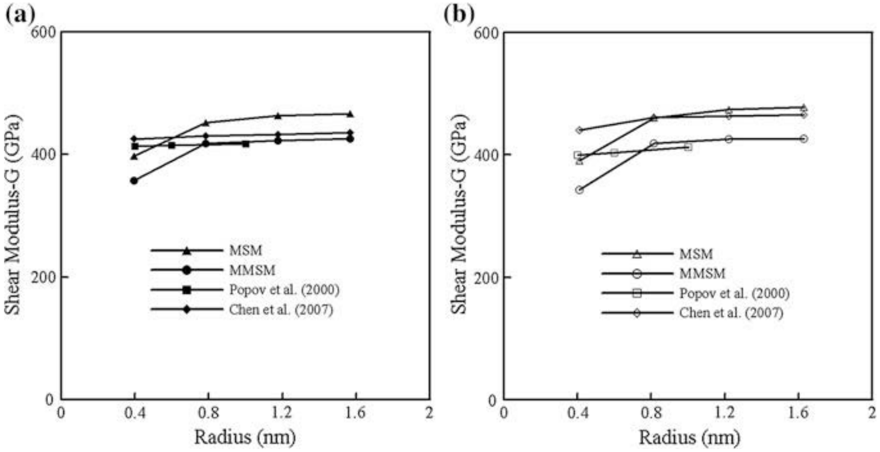

Fig. 11 Shear modulus versus the radius of SWCNTs [47]. **a** Zigzag. **b** Armchair

affect more the radial elastic stiffness and Poisson's ratio than the axial Young's and shear modulus of SWCNTs.

Radial Buckling and Deformation of SWCNTs

The radial buckling and deformations of SWCNTs are strongly associated with their radial stiffness. Figure 12 shows that the vdW atomistic interactions may lead to the radial buckling of SWCNTs. In addition, as the radius of SWCNTs increases up to a critical value, radial buckling would potentially occur because of the weakening of the associated stiffness. The radial buckling is defined as the collapse of a tube in the radial direction due to its instability before attaining the ultimate strength of the material. The critical buckling load P_{cr} of SWCNTs in the radial direction can be derived from the elastic instability analysis based on the following equation for elastic instability,

$$[K_0 + \lambda \bar{K}_1]\psi = 0, \tag{76}$$

where ψ is the eigenvector or buckling-mode shape, K_0 the linear stiffness matrix and $\bar{K}_1$ the geometric stiffness matrix. The scalar factor λ at which buckling occurs is designated "λ_{cr}", and the critical buckling load $P_{cr} = \lambda_{cr} P$, where P is the normalized external load. The vdW interactions between any two neighboring atoms are considered to be the external loads, and the critical scalar factor λ_{cr} can be calculated from linear buckling analysis usingfinite element (FE) methods. The approach to unity for λ_{cr} indicates that the vdW atomistic interactions considered here are close to the critical buckling load of the structure.

The calculated critical scalar factor λ_{cr} of the armchair and zigzag SWCNTs is shown in Fig. 13, as a function of their radius. Note that as λ_{cr} becomes larger than

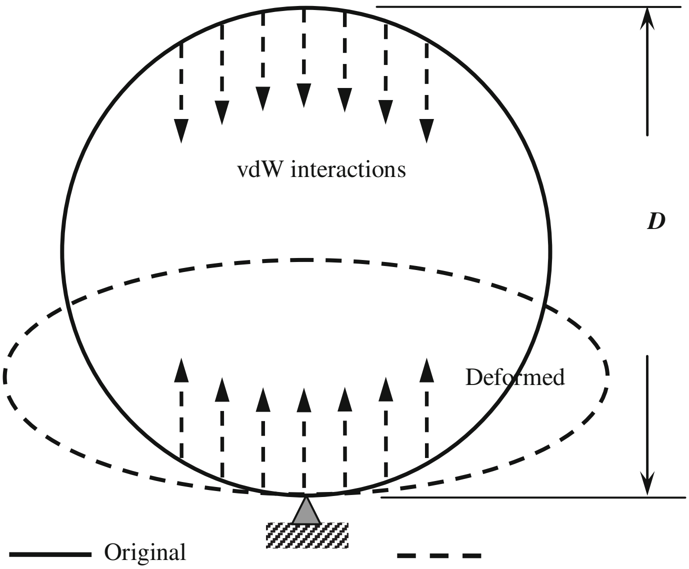

Fig. 12 Radial buckling of an SWCNT due to vdW atomistic interactions

1.0, the SWCNTs tend to collapse simply under the vdW atomistic interactions. A monotonic decrease of the critical scalar factor λ_{cr} can be observed in the figure as the radius of the SWCNTs increases, implying that the SWCNTs with a larger radius would collapse more easily due to the vdW interactions. Most importantly, the calculated results from the MMSM model are substantially lower than those of the classical MSM model.

The radial deformation of two vertically adjacent SWCNTs due to the vdW atomistic interactions is also examined to further demonstrate the effectiveness of the MMSM model. An example of the radial deformation (δ) of two vertically overlapped SWCNTs with an equal diameter (D) of 2.0 nm is presented in Fig. 14. According to Abrams and Hanein [7], radial deformation rate is defined as the ratio of δ to D. The calculated radial deformation rate of the SWCNT by using the MMSM and classical MSM model are listed in Table 4.1, in addition to the literature experimental data [2, 7]. The respective radial deformation rate obtained from these two models is about 8.3 and 1.95 %. Clearly, the MMSM model can yield a much larger radial deformation rate than the classical MSM. By further comparing them with the Ruoff et al.'s study (i.e., 7.5 %) and the Abrams and Hanein's work (i.e., 5.0 %), it is found that the result obtained from the present MMSM model is clearly much closer to the experimental data (Table 1).

Fig. 13 Critical radial scalar factor λ_{cr} versus the radius of SWCNTs [47]

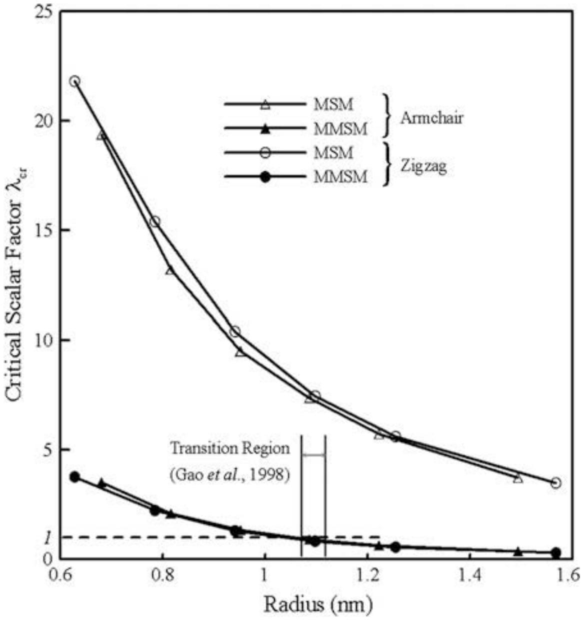

Fig. 14 Radial deformation of two vertically overlapped SWCNTs

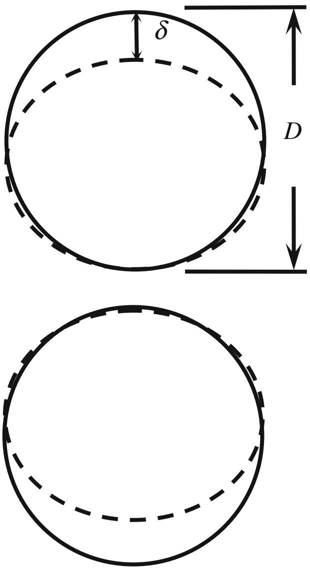

Radial Breathing Vibration of S/DWCNTs

Well identification of the structural geometry of CNTs, such as tube's diameter or chirality, is of great interest and importance for engineering applications. Among

Table 1 Radial deformation rate of two vertically overlapped SWCNTs with D = 2.0 nm

	MSM	MMSM	Ruoff et al. [2]	Abrams and Hanein [7]
Deformation rate (%)	1.95	8.30	7.50	5.00

the experimental techniques, Raman spectroscopy is widely recognized **as** one of the most powerful non-destructive techniques for the particular purpose because of better sensitivity and lower cost. In essence, CNTs reveal several characteristic Raman modes, e.g., the low Raman shift value, also termed the radial breathing mode (RBM), and the other higher Raman shift values, such as the D mode, induced by disorder, and the tangential band, G band, giving some information on metallic or semiconducting properties of CNTs. The RBM is the most studied presently, which is caused by radial vibration, where all the carbon atoms in a CNT move in the radial direction synchronously. This is very unique to CNTs and could not be detectable in other carbon systems. In the previous studies, the RBM has been extensively extended to its dependence on the conformational and electronic properties of CNTs. For instance, through the relation $\omega_{RBM} = \zeta/D + \xi$ [73–76], the RBM frequency ω_{RBM} can be correlated to the CNTs' diameter D, where the parameter ζ and ξ are determined from Raman spectroscopy. Furthermore, even though the RBM modes and vibrations have been extensively investigated in literature, most previous calculations of CNT's geometry and electronic properties based on their RBM frequencies assumed that all atoms would move axisymmetrically and synchronously along the axial direction, and meanwhile, vibrate symmetrically about the middle plane of the CNTs. They are alternatively termed the standard RBM modes. This is, however, not quite true and accurate. It was demonstrated by Dobardžić et al. [76] and Damnjanović et al. [77] through a symmetry-based calculation or a dynamic model that the RBM modes of SWCNTs would not be always radial since its longitudinal and circumferential components are both diameter- and chirality-dependent. The non-radial RBMcomponents would generally create non-axisymmetric and even asymmetric RBM vibration. Even for pure radial vibration, the possibility of the existence of a number of RBM-like modes, such as hourglass and broadening modes, in a small frequency spectrum could not be excluded. Having an inaccurate or even false identification of both the RBM and RBM-like modes in Raman spectroscopy experiment would lead to a poor estimate of the conformational properties of CNTs. Thus, it is essential to have a clear and thorough comprehension of their characteristics.

To investigate the RBM frequencies and shapes of CNTs at different temperatures, MMSM models associated with several CNTs with a different diameter, aspect ratio (i.e., length/diameter ratio, L/D ratio) and chirality are constructed. Further by modal analysis, the associated mode frequencies f and mode shapes are obtained. The Hertz (Hz) is adopted for convenience despite that the commonly used unit of RBM frequency ω in Raman experiment would be cm^{-1}. The relation between them is $f = c\omega$, where $c = 3.0 \times 10^{10}$ cm/s.

RBM Frequencies

The calculated RBM frequencies of the zigzag/armchair SWCNTs and DWCNTs as a function of their diameter are shown in Fig. 15. Their length is equal to 2.84 nm for the zigzag and 2.46 nm for the armchair. Note that the SWCNTs and DWCNTs hold an identical outer-diameter. The figure reveals that the RBM frequencies are very sensitive and inversely-proportional to the diameter, where they decrease with an increasing diameter, and roughly become stable as the diameter exceeds 3 nm. In specific, the calculated RBM frequencies of the zigzag SWCNTs, i.e., (10, 0), (15, 0), (20, 0), (25, 0), (30, 0) and (40, 0), and DWCNTs are in the range of 7.87–2.08 and 5.40–2.26 THz, respectively, while those of the armchair ones, namely (5, 5), (7, 7), (9, 9), (11, 11), (15, 15), (18, 18) and (23, 23), are 5.86–1.57 and 3.93–1.73 THz. Furthermore, the results of the DWCNTs are slightly larger than those of the SWCNTs by about 2–8 % for the zigzag type and 6–10 % for the armchair. This turns out that the additional layer in a DWCNT would have little impact on the associated RBM frequency. Besides, even though the diameter of these two types of CNTs (zigzag and armchair) is slightly different, the RBM frequencies of the zigzag CNTs are likely to be greater than those of the armchair, regardless of the number of layers. This implies that the zigzag CNTs tends to surpass the armchair ones in the radial stiffness. By comparing with the experimental data obtained by Jorio et al. [74] using Raman spectroscopy measurement, a very good consistency in both the result trend and value is achieved between the present results and the experimental observations. Moreover, the calculated RBM frequencies of the zigzag CNTs are much closer to the data from the experiment [74], indicating that the test vehicle used in the experiment might be a zigzag type. Since the wall number of CNTs is insensitive to their RBM frequency, it remains uncertain in how many layers of CNTs were actually in the CNTs used in the experiment. The calculated RBM frequencies of the SWCNTs with a different chirality, i.e., (9, 1), (8, 3), (7, 5), (10, 2), (9, 4) and (8, 6), are presented in Fig. 15b. It shows that the RBM frequencies are also sensitive to the chirality of the SWCNTs, where they are roughly in the range of 9.3–7.3 THz. Furthermore, a good consistency in the RBM frequency between the MMSM approach and the Raman spectroscopy measurement [78] can be observed. In addition, a larger diameter would yield a smaller RBM frequency, and the result trend is very similar to that shown in Fig. 4.8a for the zigzag and armchair S/DWCNTs.

The corresponding RBM mode shapes of the armchair and zigzag S/DWCNTs are shown in Fig. 16. The solid circle denotes the original configuration of the CNTs while the dotted circle shows the vibrational mode shape. As can be seen in Fig. 16a, b for the zigzag and armchair SWCNTs, respectively, only the zigzag SWCNT would exhibit purely axisymmetric RBM mode shape or radial vibration, i.e., all atoms move axisymmetrically along the radial direction synchronously, mainly because of its axisymmetric atomic structure. By contrast, the armchair SWCNT presents a nearly axisymmetric (i.e., polygon) RBM mode shape. Furthermore, the RBM mode shapes of the DWCNTs are illustrated in Fig. 16c, d. The outer layer in the DWCNTs undergoes radial vibration while the inner wall stays a

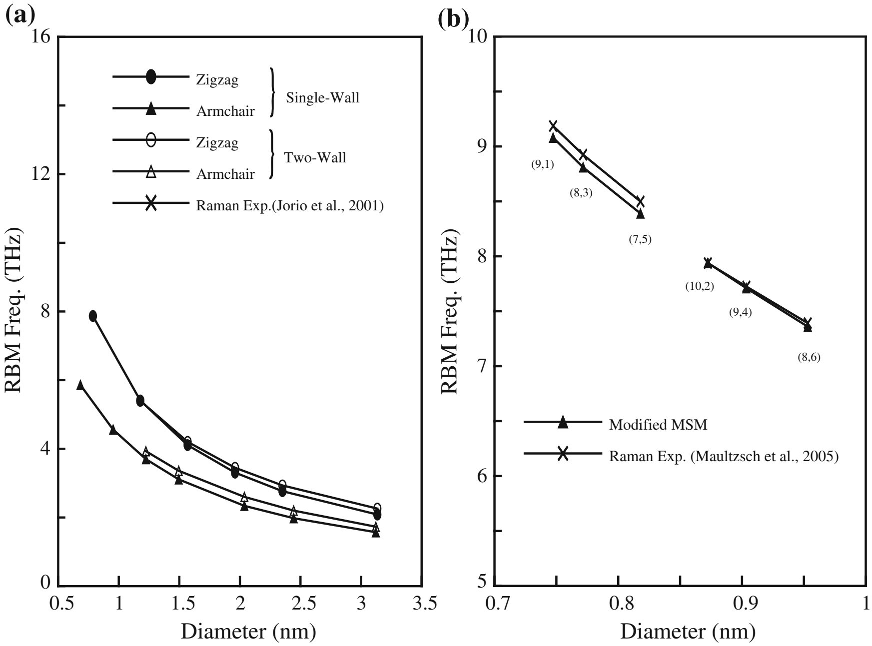

Fig. 15 RBM frequencies of CNTs versus diameter [79]. **a** Armchair/zigzag S/DWCNTs. **b** Chiral SWCNTs

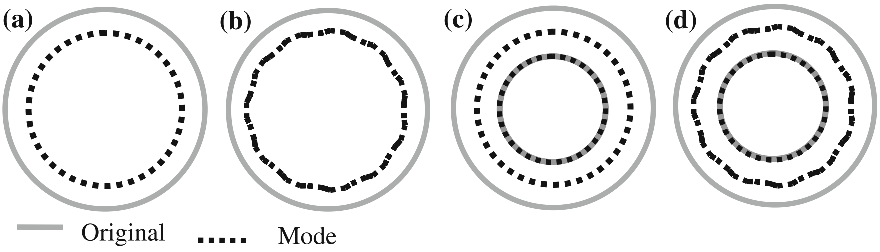

Fig. 16 RBM mode shapes of zigzag/armchair S/DWCNTs

stationary mode. By contrast, we find that for a (8, 3) chiral SWCNT, there is an asymmetric and non-radial RBM mode shape, which is accordingly termed RBM-like vibration.

Effect of Aspect Ratio

According to the preceding results, the key factor affecting the vibrational mode shape of f CNTs would be their atomic arrangement. Accordingly, the influences of the geometric properties of CNTs on the RBM frequency are explored. Several zigzag SWCNTs with two diameters (*D*), namely 1.26 and 1.41 nm, and different L/D ratios ranging from 0.2 to 2.6 are discussed using the MMSM model. The associated calculated diameter-dependent RBM or RBM-like frequencies are shown in Fig. 17a, b. It is demonstrated that the RBM and RBM-like frequencies all slightly decrease with an increasing L/D ratio, and in addition, a larger diameter SWCNT would yield a smaller RBM or RBM-like frequency. More specifically, as the L/D ratio is less than around 1.25, two vibrational modes are found, including the standard RBM and RBM-like (i.e., RBM-Like-1) mode shown in Fig. 18a, b, respectively. The difference in the mode frequency between the two modes is only about 1 %. In specific, Fig. 18b is an hourglass mode, where the upper part of the SWCNTs is expanding while the lower part contracting. In other words, they do not symmetrically undergo dynamic deformation with respect to the middle cross-sectional plane of the SWCNTs even though they do vibrate axisymmetrically along the axial axis of the SWCNTs.

Since the difference between RBM-like mode frequencies may be insignificant, the actual RBM mode frequency would be difficult to be simply confirmed by Raman experiments. On the other hand, as the L/D ratio becomes larger than around 1.25,

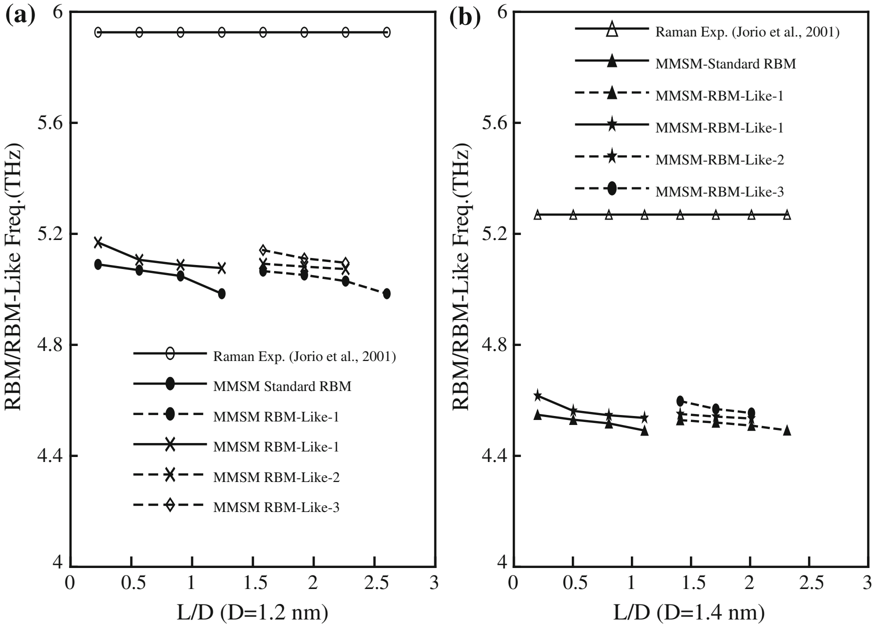

Fig. 17 RBM/RBM-like frequencies of zig-zag SWCNTs versus L/D ratio [79]. **a** D = 1.26 nm. **b** D = 1.41 nm

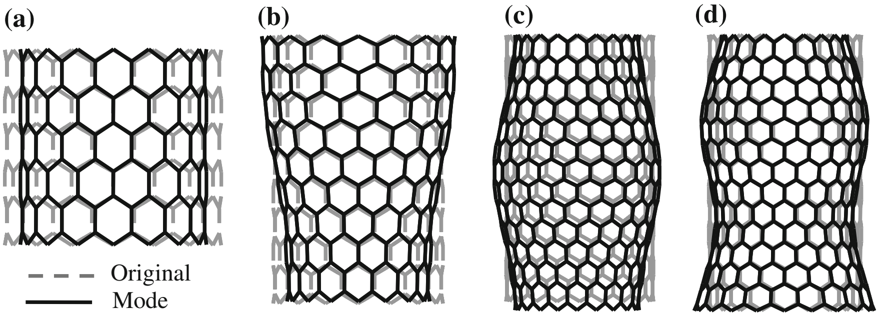

Fig. 18 RBM/RBM-like mode shape of a zig-zag SWCNT [79]. **a** RBM. **b** RBM-like-1. **c** RBM-like-2. **d** RBM-like-3

another two RBM-like modes are derived and shown in Fig. 18c, d, while the standard RBM modes are not found. In the RBM-like modes, atoms in the SWCNTs are not simultaneously moving along the same radial direction. The calculated results are quite comparable to the Raman spectroscopy experimental data [74] across the specific L/D ratio range. However, the CNT test vehicles used in the Raman experiments usually have an L/D ratio greater than 1.25. The present simulation results also indicate that the standard RBMsmay not exist in the current frequency range, and the identified mode would no longer be the standard RBM vibration.

Thermal Effects on Vibrational Behaviors of SWCNTs

In the section, thermal effectson the vibrational behaviors of SWCNTs, such as natural frequency, mode shape as well as dynamic Young's modulus, are extensively studied using the MMSM modeling [47, 79]. The temperature-dependent bond length and angle are determined through the Badger's rule and constant temperature MD simulation. For comparison, the vibrational behaviors of SWCNTs are alternatively determined directly using the constant temperature MD simulation that incorporates the modified NH thermostat model [45] for the system temperature control. To calculate the natural frequencies and mode shapes of SWCNTs, both Fast Fourier Transform (FFT) and Inverse Fast Fourier Transform are adopted. In the MD simulation, the Tersoff-Brenner potential [50] for modeling the covalent bonds between carbon atom pairs, a time step of $\Delta t = 5 \times 10^{-16}$ seconds and a number of equilibrating time steps 2×10^4 are used. In addition, a random sampling method is performed to take a sample out of every 1,000 time steps from 2×10^6 time steps.

Bond length and angle

The temperature-dependent bond length and angle of a (5, 5) armchair and a (9, 0) zigzag SWCNT at temperature of 100–2,000 K are first examined using the constant temperature MD simulation, and the results are, respectively, presented in Fig. 19a, b.

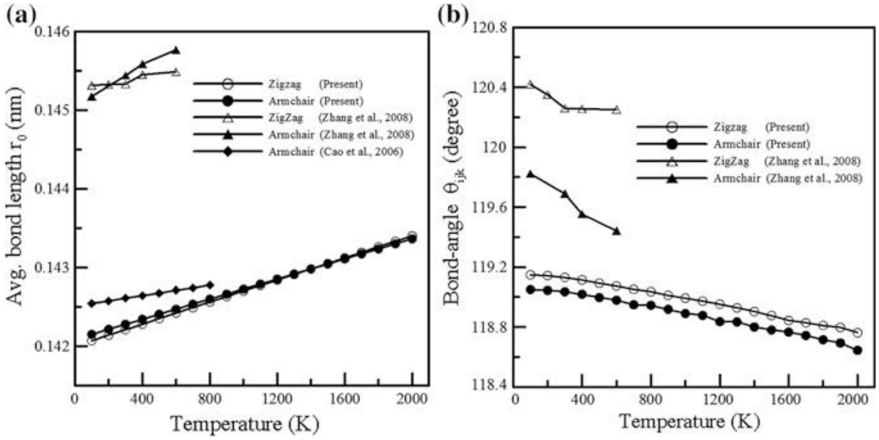

Fig. 19 Thermal effects on the bond length and angle of SWCNTs [106]. **a** Bond length. **b** Bond angle

The figure shows that the bond length would increase with increasing temperature while the bond angle would decrease. Based on the ideal gas law, it is not surprising to see the result trend because more kinetic energy is added to the CNT system via the particles' momenta, thereby increasing the bonding length. On the other hand, the decrease of the bond angle with an increasing temperature is mainly because of the thermal expansion of the CNTs. The trend of the present results calculated from the constant temperature MD simulation are well consistent with the literature data [80], and the difference between them is as much as only about 1–3 %.

The temperature dependence of the carbon-carbon bond length r and bond angle θ has been theoretically derived using, such as, the Helmholtz free energy together with the local harmonic model, or an empirical temperature-dependent potential function together with MD simulation (see, e.g., [80–82]). The results of Zhang et al. [80] are also illustrated in Fig. 19 for comparison. It is found that the present results are closely in line with these published data [80, 82], where the maximum difference between them is less than about 2.3 %. Furthermore, by contrast to the previous studies where the temperature dependence less than 800 K was investigated, the present modeling can reliably extend the temperature correlations up to 2,000 K.

Mode Frequencies and Shapes

By the abovestudy, the temperature-dependent first two thermal natural frequencies associated with the (9, 0) and (17, 0) zigzag and (5, 5) and (10, 10) armchair SWCNTs with several different L/D ratios at 300 K can be estimated using the constant temperature MD and MMSM models, and the calculated results are shown in Tables 2 and 3. Note that the variation of the L/D ratio of the CNTs is achieved by

Table 2 Mode frequencies (THz) and types with different L/D ratios for armchair SWCNTs [106]

(5, 5)	L/D = 3.62			L/D = 5.62			L/D = 7.26		
Mode	MD	MMSM	Type	MD	MMSM	Type	MD	MMSM	Type
1	0.3898	0.4147	A	0.1853	0.1931	A	0.1076	0.1103	A
2	1.2494	1.3126	B	0.8370	0.8761	C	0.5838	0.5876	D
(10, 10)	L/D = 1.82			L/D = 2.72			L/D = 3.63		
1	0.3700	0.3848	B	0.2879	0.2919	B	0.1996	0.2066	A
2	0.6310	0.6721	A	0.3299	0.3450	A	0.2659	0.2698	B

Table 3 Mode frequencies (THz) and types with different L/D ratios for zigzag SWCNTs [106]

(9, 0)	L/D = 3.43			L/D = 5.27			L/D = 7.10		
Mode	MD	MMSM	Type	MD	MMSM	Type	MD	MMSM	Type
1	0.4000	0.4205	A	0.1865	0.1895	A	0.1058	0.1065	A
2	1.1961	1.1900	B	0.9150	0.9149	C	0.5810	0.5845	D
(17, 0)	L/D = 1.80			L/D = 2.77			L/D = 3.73		
1	0.3780	0.3889	B	0.2821	0.2937	B	0.1897	0.1947	A
2	0.6240	0.6658	A	0.3181	0.3310	A	0.2560	0.2715	B

changing their length but fixing their diameter. In addition, the diameter of the (5, 5) and (10,10) armchair SWCNTs is similar to that of the (9, 0) and (17, 0) zigzag, respectively, and that of the (10, 10) and (17, 0) SWCNTs is nearly two times that of the (5, 5) and (9, 0), respectively. The corresponding vibrationalmode shapes of the mode types shown in Tables 2 and 3 are illustrated in Fig. 20, where Type A is a beam-like flexural mode, Type B a radial mode, Type C a torsional mode, and Type D also a beam-like flexural mode. The tables demonstrate that the calculated normal modes of the SWCNTs at all these L/D ratios using these two approaches are very comparable. Obviously, there exists a gap in the calculated natural frequencies between these two approaches, in which the MD results are somewhat less than those of the MMSM. This could be due to that the dihedral-angle torsion was included in the MMSM model rather than in the MD simulation using the Tersoff-Benner potential, as a result leading to a higher stiffness and frequency.

In addition, the natural frequencies would decrease significantly with the increase of the L/D ratio, and the associated mode shape would also vary with the L/D ratio except the first mode of the (5, 5) armchair and (9, 0) zigzag SWCNTs, where it remains a beam-like flexural mode throughout the range of the L/D ratio. More specifically, the second mode of both the (5, 5) armchair and (9, 0) zigzag SWCNTs would change from a radial mode (Type B) to a flexural (Type D) across the L/D ratio range. By contrast, the first mode of the (10, 10) armchair and (17, 0) zigzag SWCNTs tends to vary from a radial mode (Type B) to a flexural one (Type A) as the L/D ratio increases from 1.82 to 3.63, while their second mode from a flexural mode (Type A) to a radial one (Type B). Clearly, the first and second mode

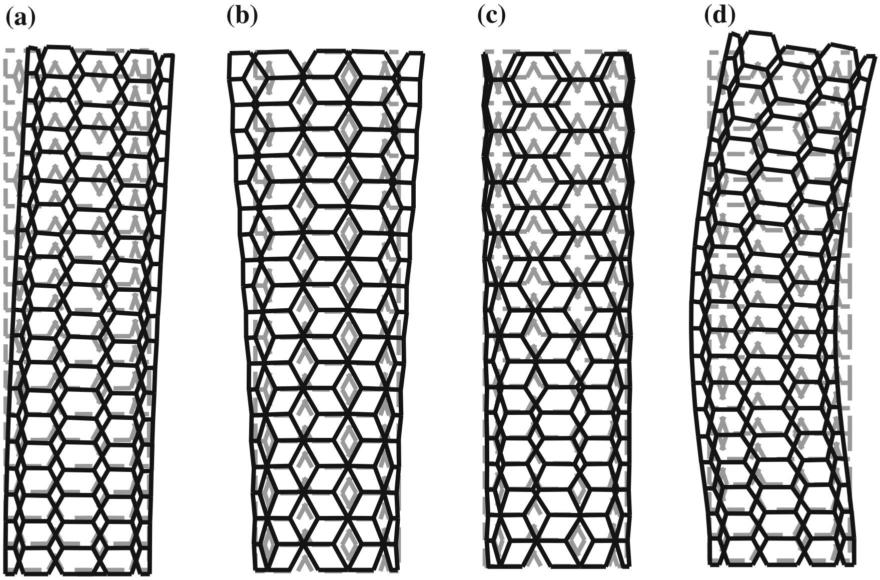

Fig. 20 Vibrational mode shapes of a (5, 5) SWCNT with L/D = 3.62 [106]. **a** Type A. **b** Type B. **c** Type C. **d** Type D

(Type A and Type B) are swapped as the L/D ratio increases from 1.82 to 3.63, or more accurately speaking, as the length increases from 2.4 to 4.9 nm for these two SWCNTs.

It can be seen that under a similar L/D ratio, e.g., the L/D = 3.62 case for the (5,5) armchair SWCNT and the L/D = 3.63 case for the (10, 10), the first two natural frequencies of the (5, 5) would considerably outperform those of the (10, 10). But, under a similar L/D ratio, (see, e.g., L/D = 1.82 for the (10, 10) armchair SWCNT and L/D = 1.80 for the (17, 0) zigzag), there is a very comparable frequency value in the first two modes between the armchair and zigzag SWCNTS. Likewise, an analogous result can be also detected in the examples of L/D = 2.72 for the (10, 10) armchair SWCNT and L/D = 2.77 for the (17, 0) zigzag.

Furthermore, the temperature-dependent first two mode frequencies associated with the armchair and zigzag SWCNTs of an L/D ratio of 5.62 and 5.27 are presented in Fig. 21. According to Tables 2 and 3, the first mode (i.e., mode 1) of these two SWCNTs is a flexural mode (i.e., Type A) while the second mode (i.e., mode 2) is a torsional mode (i.e., Type C). As the temperature increases from 100 to 1,500 K, the predicted first natural frequency for mode 1 of the armchair SWCNT would decrease from 0.1860 to 0.1800 THz (about 3.23 % drops) by the constant temperature MD simulation and from 0.1932 to 0.1907 THz (about 1.31 % drops) by the MMSM model. In addition, that of the zigzag SWCNTs would reduce from 0.1870 to 0.1810 THz (about 3.21 % drops) by the MD simulation and from 0.1897 to 0.1872 THz (about 1.28 % drops) by the MMSM. Likewise, there is a similar trend for mode 2 (i.e., Type C). The results reveal that the mode frequencies of the

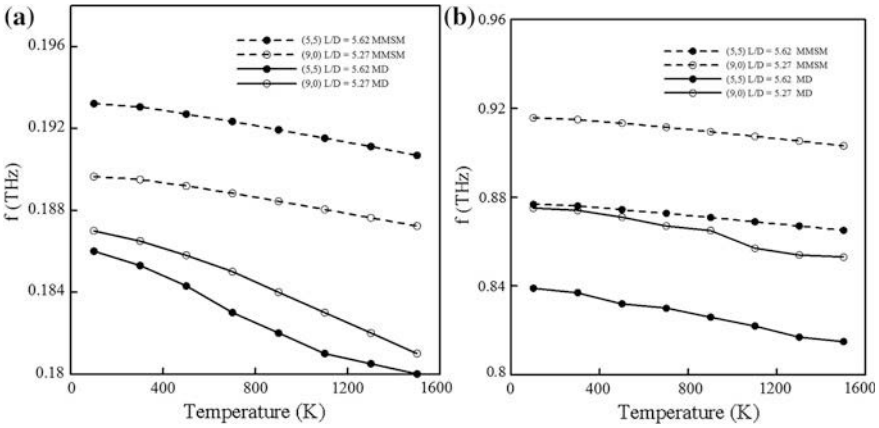

Fig. 21 First two mode frequencies of SWCNTs versus temperature [106]. **a** Mode 1 (Type A). **b** Mode 2 (Type C)

SWCNTs would drop with an increasing temperature despite that the temperature dependence is not considerable in the temperature range (i.e., 100–1,500 K). Also due to the dihedral-angle torsional stiffness considered in the MMSM model, the MD model would have a larger reduction in the mode frequencies as temperature increases.

In order to validate the modeled results, the ratio of the first two calculated flexural mode frequencies of the (5, 5) armchair SWCNTs with the L/D ratio of 7.26, i.e., Type A and Type D, using the constant temperature MD and MMSM models is assessed. The result is shown in Fig. 22a. It demonstrates that there are maximally about 0.5 % differences for these two modeled results as the temperature

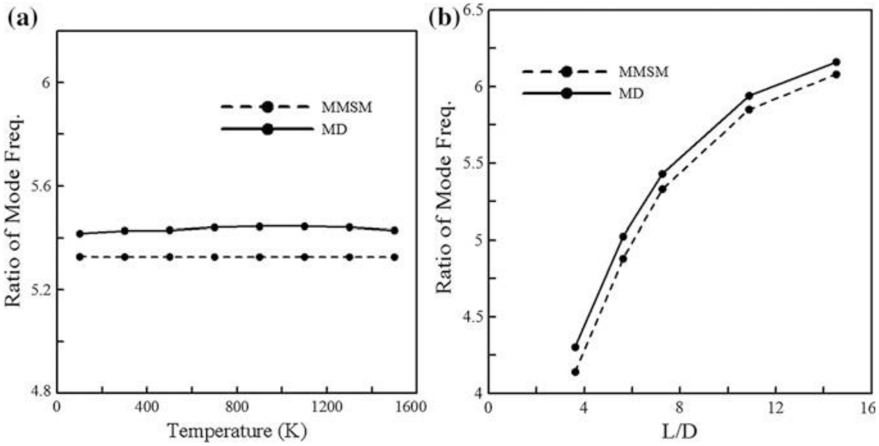

Fig. 22 Ratio of the first two flexural mode frequencies of a (5, 5) armchair SWCNT [106]. **a** Effect of temperature (L/D = 7.26). **b** Effect of L/D ratio (T = 300 K)

increases from 100 to 1,500 K, suggesting that the frequency ratio would be temperature-independent. The frequency ratio as a function of the L/D ratio of the (5,5) armchair SWCNTs at 300 K is further plotted in Fig. 22b. It is shown that the two approaches yield not only a very similar result but also a consistent trend. Moreover, the calculated frequency ratio tends to greatly enhance with an increasing L/D ratio, or more precisely, length (*L*) as the diameter (*D*) of the SWCNTs is fixed, indicating that there is a great dependence of the frequency ratio on the L/D ratio. Besides, the frequency ratio tends to converge to 6.1–6.2 as the L/D ratio becomes significantly large. The result agrees well with the published experimental data [83], where the converged frequency ratio approaches 6.2 as the L/D ratio is around 431.

Dynamic Young's Modulus

SWCNTscan be regarded as continuous beams. Based on the beam vibration theory [84], the effective Young's modulus *E* of the beams can be derived from the associated natural frequencies,

$$\omega_i = \frac{\Gamma_i^2}{L^2}\sqrt{\frac{EI}{\rho A}}, \tag{77}$$

where ω_i and Γ_i are the natural frequency and constant of the *i*-th natural mode, respectively, and L, I, ρ and A the length, moment of inertia, density and cross-sectional area of the beams. By the relation, the dynamic Young's modulus of the SWCNTs can be, for example, calculated from its first flexural mode. Further assume that an SWCNT is a hollow circular tube, and its natural frequencies can be denoted as

$$\omega_j = \frac{\Gamma_j^2}{4L^2}\sqrt{D_{in}^2 + D_{out}^2}\sqrt{\frac{E}{\rho}}, \tag{78}$$

where D_{in} and D_{out} are the inner and outer diameter of an SWCNT.

The dynamic Young's modulus of (5, 5), (9, 0), (10, 10) and (17, 0) SWCNTs of the same length (i.e., 4.9 nm) but a different radius are illustrated in Fig. 23a, as a function of temperature. On the other hand, the dynamic Young's modulus of the (9, 0) SWCNTs at a different length (i.e., 2.4, 3.7 and 4.9 nm) are shown in Fig. 23b, as a function of temperature. Note that the calculations are made simply based on their first flexural mode, i.e., Type A shown in Fig. 20, together with Eq. (4–8). The results in Fig. 23 demonstrate that that the dynamic Young's modulus of the SWCNTs would have a slight decrease with an increasing temperature. The discrepancies in the calculated dynamic Young's modulus between 300 and 1,500 K are only about 5 and 2 %, associated with the constant temperature MD simulation and

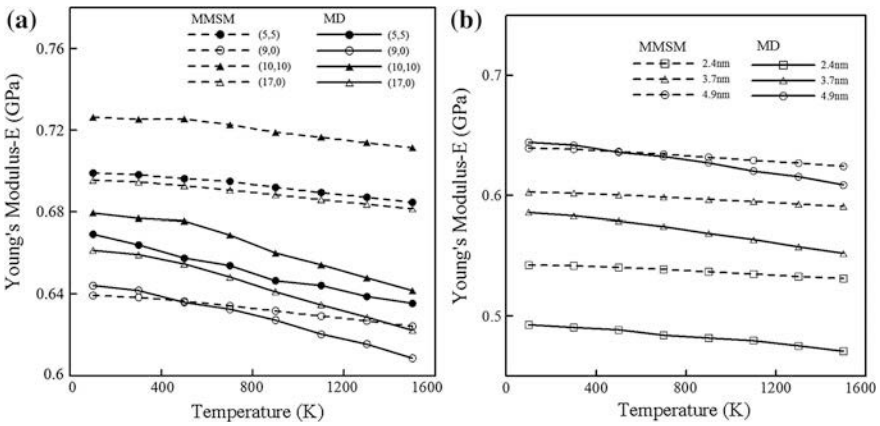

Fig. 23 Dynamic Young's modulus of SWCNTs versus temperature [106]. **a** Radius effect. **b** Length effect

MMSM modeling. Furthermore, it is observed that the dynamic Young's modulus would be raised with the increase of the length. The result trend can be found in many previous literatures (see, e.g., [40, 41, 47, 64, 85]). It can be probably due to the surface or boundary effect [72]. More specifically, because of the surface or boundary effect, an SWCNT in an unstrained state tends to deform into a new relaxed, stabilized configuration, i.e., a concave shape [72], for stress relief, thus leading to a decrease of the overall strength or stiffness of the SWCNT structure. The surface or boundary effect and so the stress relief phenomenon would become more apparent as the L/D ratio of SWCNTs becomes smaller. Under the same radius, a shorter SWCNT would yield a smaller L/D ratio and thus a higher surface or boundary effect and then a lesser Young's modulus. It is also found that the dynamic Young's modulus would increase with an increasing tube radius. The result trend could be explained by the inherent geometry of the CNT structure, in which a CNT of a small radius would present a polygon cross section rather than a circular one. Because of the imperfect shape or structure, structural stiffness and so Young's modulus are likely reduced. Moreover, the degree of the temperature effect on the dynamic Young's modulus of the SWCNTs tends to be size- and geometry-independent. The calculated dynamic Young's modulus of the SWCNTs, i.e., about 0.5–0.7 TPa, is similar to the first principles calculation result (i.e., 0.764 TPa) [86], but much less than the static Young's modulus calculated using both MD simulation and the classical MSM model under an uniaxial tensile test, such as 0.97–1.05 TPa [9], 0.94–1.02 TPa [64], 0.92–0.98 TPa [72] and 0.98–1.15 TPa [87]. The result trend is in a good agreement with that of many bulk materials, in which the dynamic Young's modulus calculated from vibrational analysis would be generally smaller than the static one obtained from uniaxial tensile/compressive tests.

Besides, as shown in Fig. 23b, there is an increasing gap in the calculated dynamic Young's modulus as the length of the SWCNT decreases. This is probably because a shorter SWCNT tends to be more influenced by the boundary or end effect than a longer one, and unfortunately, the effect is not taken into account in the classical MSM and MMSM modeling. The problem can be solved by using the atomistic-continuum modeling (ACM) approach proposed by Cheng et al. [87], which incorporates atomistic modeling by virtue of MD simulation for simulating the initial unstrained equilibrium state, and equivalent-continuum modeling by way of FE approximations for modeling the subsequent static/dynamic behaviors.

RBM Frequency

The temperature dependences of the average bond length and angle of a (6, 6) and (10, 10) armchair SWCNT and a (11, 0) and (17, 0) zigzag SWCNT can be, likewise, evaluated using the constant temperature MD simulation incorporating the modified NH thermostat method. Note that the associated diameter of the SWCNTs is 0.82, 1.49, 0.86, and 1.33 nm. The derived results turn out to be similar to those shown in Fig. 19, in which the increase of temperature would increase the bond length but decrease the bond angle. By the temperature-dependent relation of the bond length and angle together with the Badger's rule, the RBM frequencies of these armchair and zigzag SWCNTs as a function of temperature can be calculated and illustrated in Fig. 24. It is found that they all slightly drop with the increase of temperature. As the temperature is raised from 300 to 900 K, the RBM frequencies of the zigzag SWCNTs would decrease by about 0.7–0.8 % and by about 0.65–0.75 % for the armchair. The results are in good agreement with the literature experimental data of

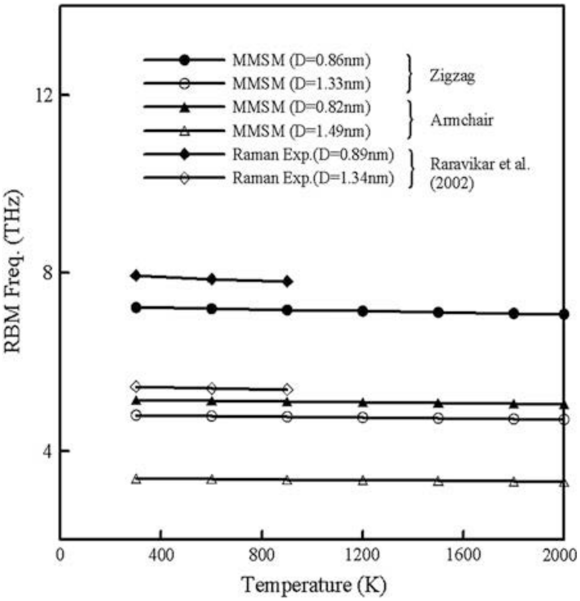

Fig. 24 RBM frequencies of SWCNTs versus temperature [79]

Raravikar et al. [28] using a Raman measurement technique, i.e., about 1.2–1.7 % drops under the same temperature range. As the temperature increases from 300 to 2,000 K, the RBM frequencies continue to reduce inconsequentially by about 2 % for both the zigzag and armchair SWCNTs. The lessening of the RBM frequencies with temperature could be mainly attributed to that the force constants, such as the bond-stretching and bond-angle variation, would decrease with an increasing temperature. The insignificant temperature effect on the RBM frequencies suggests that the radial stiffness of the SWCNTs, most affecting the RBM frequencies, would have a little influence on the associated force constants.

Computational Efficiency

The computational performance of these two theoretical models is compared on the same problem. The problem is solved on the same computer (CPU: Intel® Core (TM)2 Quad CPU Q9400 with 2.66 GHz; RAM:3.21 Gb). In the MD simulation, a total of 2×10^6 time steps are needed in order to find the low mode frequency through FFT. For the different scale of the SWCNTs that possess a different number of carbon atoms, as shown in Tables 2 and 3, the required elapsed time of these MD calculations ranges from 10.5 to 51 h. Furthermore, in order to find the lower frequencies, more than 2×10^6 time steps are needed, thereby requiring more calculation time. On the other hand, for the MMSM, the temperature-dependent bond length and angle are first estimated using MD simulation. The calculation requires only about 2×10^4 time steps of MD simulation, which takes only about 0. 5–5 h elapsed time. By the calculated temperature-dependent bond length and angle, FE modal analysis is then performed to compute the mode frequencies and shapes of the SWCNTs, which requires only about 0.2 h elapsed time. In sum, the total required elapsed time of the MMSM model is about 0.7–5.2 h. It is found that the MMSM model is about 10 times faster than the MD model.

Fracture, Thermo-Mechanical and Phase Transformation Behavior of Carbon Allotropes

According to previous experimental measurements, structural or atomistic defects such as vacancy and topological defects can be often observed in CNTs during the fabrication process. Thus, a systematic investigation of the effects of atomistic defects on the mechanical properties andfracture behaviors of SWCNTs is attempted using MD simulation. The predicted local stress distribution using the smoothed particle hydrodynamics (SPH) technique [62] is correlated with the fracture evolution. The effects of the number, type (namely the vacancy and Stone-Wales defects), location or distribution of defects are further examined. Besides, the thermal-mechanical properties and phase transformation behaviors of carbon fullerenes (buckyballs) at atmospheric pressure are also reported through constant temperature MD simulation using the modified NH thermostat method.

Fracture Behavior of SWCNTs

This session attempts to explore the effects of atomistic defects on the mechanical properties of the SWCNTs, including stress-strain relationship, elastic modulus, ultimate strength and strain, and fracture evolution through uniaxial MD tension test simulation. According to mechanics of materials, when a CNT is subjected to an axial deformation, the resultant force F in the axial direction can be estimated by summing the interatomic forces of the atoms at the end side of the CNT. The associated axial stress σ can be then obtained by dividing the F by the cross-sectional area defined as $A = C \times 0.34$ (nm^2), where C is the circumference. On the other hand, the corresponding tensile strain ε can be computed by $(L - L_0)/L_{0,}$ in which L_0 and L are the initial (undeformed) and elongated (deformed) length, respectively. From the stress-strain relationship, both the ultimate strength and strain can be extracted. Besides, from the slope of the stress-strain curve at an infinitesimal strain, the axial elastic modulus of the CNT can be also calculated. Finally, the fracture evolution of the defective CNTs under uniaxial tension can be also observed through the simulation.

Atomistic Defects in CNT

Two types of atomistic defects are considered in the investigation, namely vacancy defect and Stone-Wales defect. The Stone-Wales defect, as shown in Fig. 25a, is a crystallographic defect, where it is a 90° rotation of two carbon atoms in a hexagonal network with respect to the midpoint of the bond, thereby creating two pentagons and two heptagons. Unlike the vacancy defect, the defect is created as a

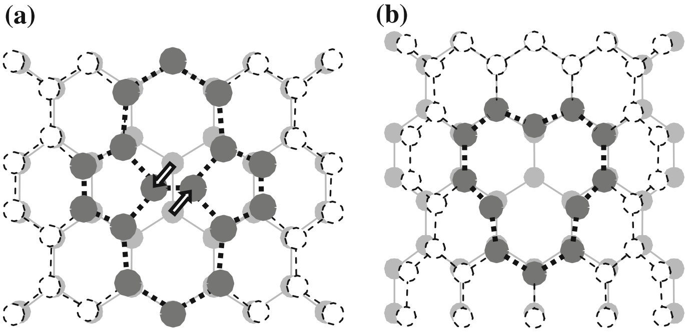

Fig. 25 Type of atomistic defect in a CNT. **a** Stone-wales defect. **b** Monovacancy defect

result of the translation of atoms and dislocation of bonds. The defect is generally developed under local strain for shear stress relaxation process in crystal, by moving atoms from one location to other, thus varying the bond topology (see, e.g., [88]). On the other hand, the vacancy defect is attained by eliminating one or more atoms as well as the corresponding bonds from a CNT. If there is only a one-atom vacancy, it is termed a monovacancy defect, while it is called a divacancy defect if there is a vacancy of two adjacent atoms. Figure 25b presents an example of a CNT structure with a monovacancy defect, where the center atom (i.e., atom 1 in the figure) as well as the three adjacent bonds is removed from the CNT.

Effects of Atomistic Defects

The study first addresses the effects of atomistic vacancy defect on the mechanical properties of an armchair SWCNT with a radius and length of 0.76 and 11.99 nm, respectively. Atomistic vacancy defect is developed by randomly eliminating certain atoms from the tube based on a specified defect rate or percentage. The defect rate or percentage is defined as the number of removed atoms divided by the total number of atoms in the system. In practice, the defect rate in a graphene layer is roughly 0.3 atom/nm^2, which is equal to 0.71 % atom amount, according to Hashimoto et al. [89]. Correspondingly, five different defect rates are considered in the investigation, namely 0 % (i.e., defect-free), 0.3, 0.6, 1.0, and 2.0 %. The deformations or configurations of the defective SWCNTs under 0, 0.3 and 2.0 % defect rate at the free relaxation state are shown in Fig. 26, together with the calculated atomistic-level axial normal stress distributions using the Shen and Atluri's stress model [87].

It is possible to see that the defective SWCNTs would no longer hold a straight tube, suggesting that the tubes are subjected to bending deformations. According to the stress distributions of the defective SWCNTs, both compressive and tensile stresses can be observed due to the multiple bending and local buckling. In addition, an increasing defect rate tends to induce a larger flexural deformation in the SWCNT at the free relaxation state, thereby having an increasing compressive and tensile flexural stress. Notably, the SWCNT with 2.0 % defect rate would hold the most significant flexural deformation, as shown in Fig. 26c. The curvature of the defective tube is neither constant, indicating multiple bending or/and local buckling deformations occurring across the tube. In other words, the atomistic vacancies would create not only global bending but also local buckling deformations. The flexural deformations strongly depend on the location of the atom vacancy and also defect rate. Moreover, the atomistic vacancies would also induce stress concentration, leading to non-uniform stress distribution across the tubes, where stress gradient becomes more considerable as vacancy defect rates is higher. As shown in Fig. 26c, the maximum tensile and compressive flexural stress tends to take place around the atomistic vacancies located on the tensile and compressive tube surface of the flexural SWCNTs, respectively. Note that the stresses are further considered as a preload for subsequent MD simulation.

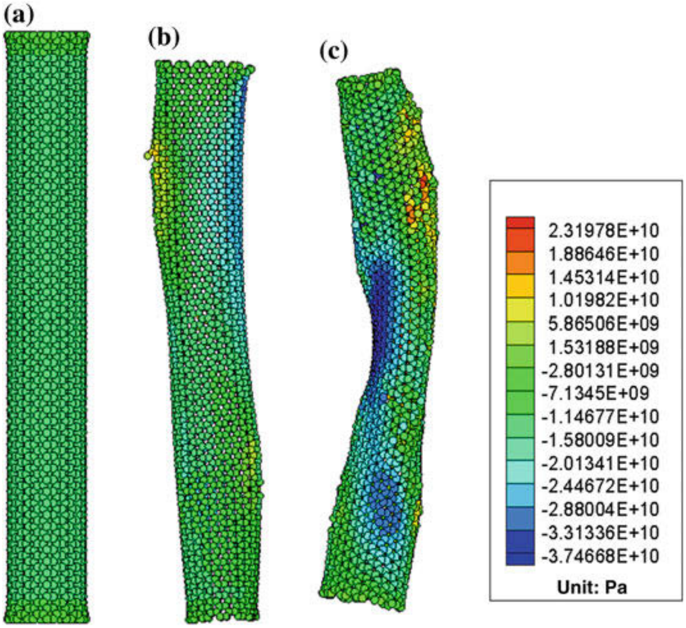

Fig. 26 Effects of atomistic vacancy defects for SWCNTs at the free relaxation state [107]. **a** 0 %, **b** 0.3 %, **c** 2.0 %

It should be noted that the location of atomistic vacancy defect on the tube is uncertain or random. To minimize the uncertainty when examining the effects of the defect rates, ten simulation trials are performed for each specific defect-rate test, each of which involves a different random vacancy-defect distribution pattern. The arithmetic mean value of these ten simulation results are presented together with the associated standard deviation. First of all, the calculated elastic moduli under those defect rates are shown in Fig. 27a. The figure demonstrates that the average elastic modulus associated with 0.3, 0.6, 1.0, and 2.0 % defect rate is 859.0, 812.0, 766.0 and 670.0 GPa. The results reveal that the axial elastic modulus decreases with an increasing defect rate. By contrast to the elastic modulus of the defect-free SWCNT, i.e., about 900.0 GPa, the corresponding reduction is about 4.6, 9.8, 14.9 and 25.6 %. It is found that the results are consistent with those of Mielke et al. [90] using MM calculations. It is also essential to note that the standard deviation of the estimated average elastic moduli tends to increase with an increasing defect rate. Furthermore, the ultimate strength of the defective SWCNTs at these four different defect rates is presented in Fig. 27b. The average ultimate strength is 84.0, 80.0, 77.0 and 69.0 GPa, associated with the defect rate of 0.3, 0.6, 1.0, and 2.0 %. As compared to the defect-free SWCNT (i.e., 97 GPa), these defective SWCNTs comprise about 13.4, 17.5, 20.6 and 28.9 % reductions in the ultimate strength. The standard deviation of these ultimate strengths would also rise with an increasing defect rate, similar to the result trend of the elastic modulus aforementioned.

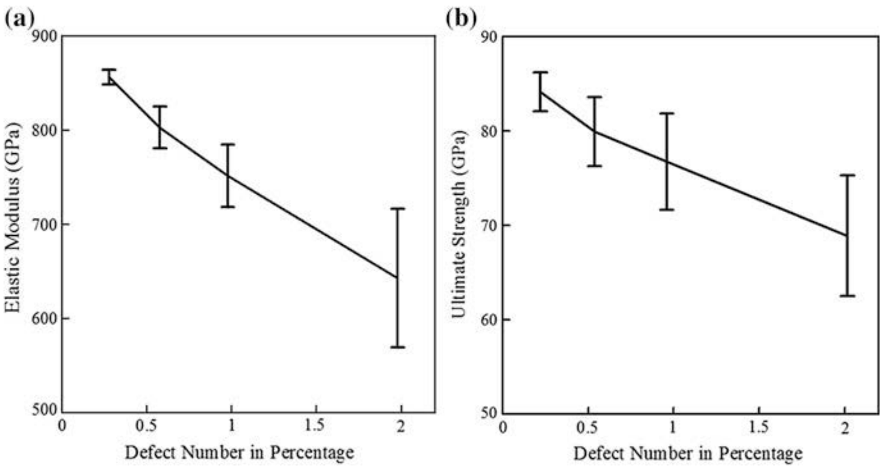

Fig. 27 Elastic modulus and ultimate strength at different defect rates [107]. **a** Elastic modulus. **b** Ultimate strength

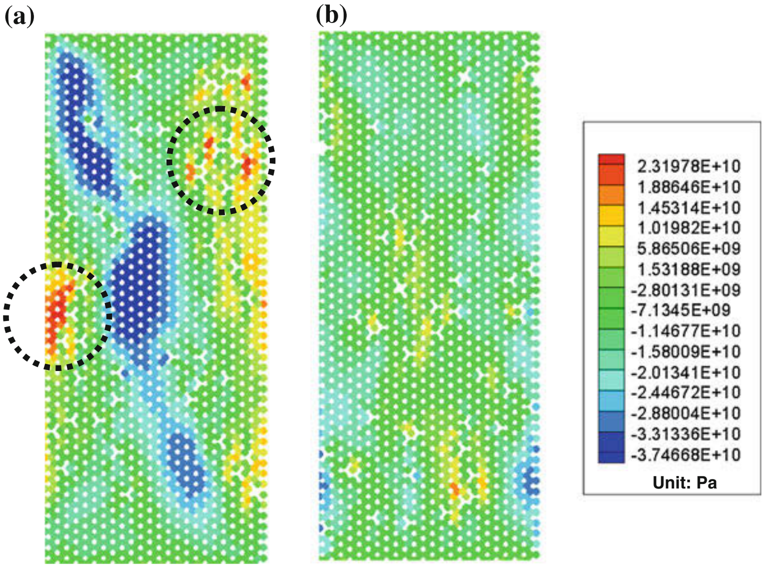

Fig. 28 Stress distribution of an armchair SWCNT with an identical defect rate but a different defect layout [107]. **a** Lower elastic modulus. **b** Higher elastic modulus

Furthermore, two armchair SWCNTs, as shown in Fig. 28, consisting of an identical defect rate 2 % but with a different atom-vacancy distribution pattern would result in a different elastic modulus, i.e., 609 and 733 GPa, respectively. For the lower elastic modulus case, it is found that there is a more significant aggregation of the atomistic vacancies created, thus forming several more substantial stress concentration portions and further causing the reduction of the elastic modulus and ultimate strength. This turns out that a higher defect rate would present a more wide-ranging defect distribution, and so create a larger standard deviation in the calculated mechanical properties.

The size dependence of the armchair SWCNT with one atomistic divacancy defect on the mechanical properties is further examined. The defect is located at the middle of the SWCNTs. The stress-strain relationships of the defective SWCNTs at a different tube radius and length are shown in Fig. 29. It is noted that the length of the tubes is fixed to 3.815 nm when varying the tube radius, while the radius is set to 0.766 nm when changing the tube length. In the investigation, three different tube radii are considered, i.e., 0.766, 1.534, and 2.308 nm. As can be seen in the figure, there is a very comparable ultimate strengths for these three defective SWCNTs, suggesting that the tube radius would have an insignificant impact on the ultimate strength of the defective SWCNTs. On the other hand, the associated ultimate strain would show a much larger dependence on the tube radius, where it is 0.299, 0.284 and 0.268 corresponding to these three defective SWCNTs, indicating the ultimate strain would reduce as the tube radius increases. However, from the slope of these stress-strain curves, it is found that a larger radius tends to hold a greater elastic modulus. The result trend is highly consistent with the literature data for the defect-free cases, such as Lu [9], Li and Chou [40, 41], and Chen et al. [72] using an empirical model, MSM approach and MD simulation, respectively. Furthermore, Fig. 29b reveals that the tube length would have a little influence on its elastic modulus, ultimate strength and ultimate strain as it changes from 3.815 to 11.991 nm. Besides, the tube length of the defective armchair SWCNTs would be less dependent on their mechanical properties than the tube radius.

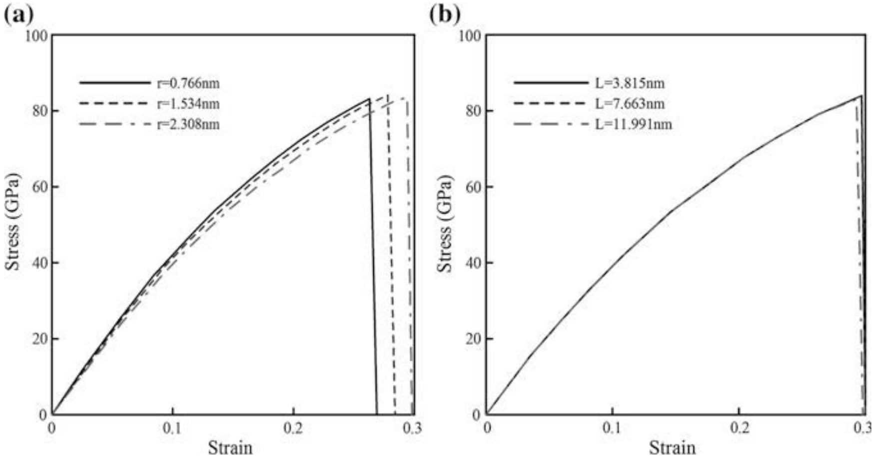

Fig. 29 Stress-strain relationship of the armchair SWCNTs with a divacancy defect at a different tube radius and length [107]. **a** Radius effect. **b** Length effect

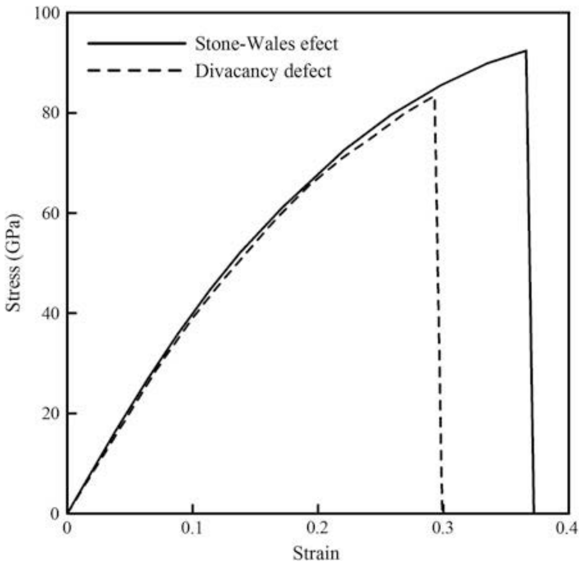

Fig. 30 Stress-strain relationship of the armchair SWCNTs with a divacancy and Stone-wales defect [107]

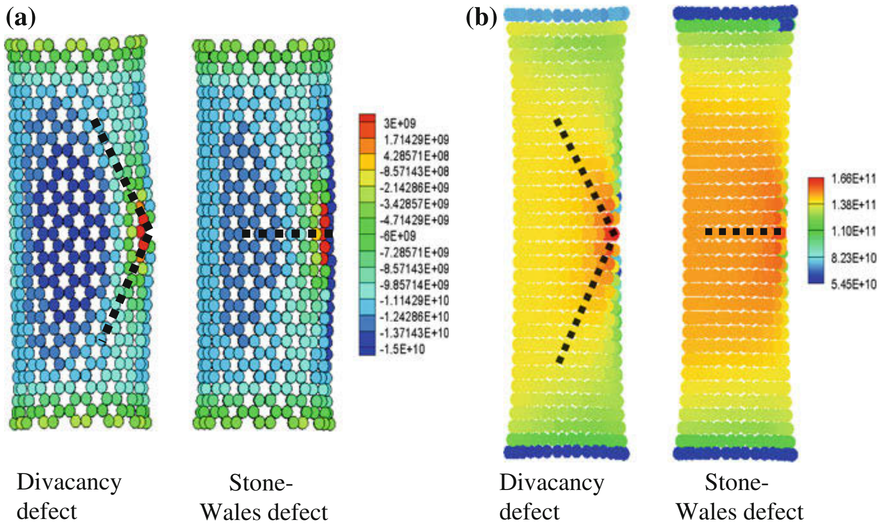

Fig. 31 Snapshots of stress distributions of defective armchair SWCNTs at the free relaxation state and before the onset of crack propagation [107]. **a** At free relaxation state. **b** Before the onset of crack propagation

The stress-strain relationship of the armchair SWCNT with a single Stone-Wales defect is shown in Fig. 30, together with theta divacancy defect. The tube radius and length of the SWCNT are 0.766 and 3.815 nm. The figure shows that the ultimate strength and associated ultimate strain of the armchair SWCNT with a single Stone-Wales defect (Fig. 31) are all greater than those with a single divacancy defect. Specifically, the ultimate strength and strain of the former are 93 and 0.37 GPa, which are about 11 and 23 % larger than those of the latter. The reason can be that the Stone-Wales defect is developed simply by way of the "pyracylene" transformation or atom rearrangement without removing any atom or bond, thus retaining better integrity in atomistic structure and having a less effect on the mechanical properties of SWCNTs.

Evolution of Fracture

The fracture evolutions of defective armchair SWCNTs with one or three divacancy defects and one Stone-Wales defect, respectively, are further examined. It is found that the SWCNTs with or without defects would show a sudden facture failure once the strain attains a critical value (i.e., the ultimate strain), at which the associated stress exhibits an abrupt drop down to zero. This concludes that the SWCNTs tend to be very brittle as the strain reaches the ultimate value. The observation is rather consistent with that of Yu et al. [91], Belytschko et al. [92] and Tserpes et al. [93], regardless of with or without atomistic defects. First of all, snapshots of the atomistic-level axial normal stress distribution of the defective armchair SWCNTs at the free relaxation state and right before the onset of crack propagation are shown in Fig. 31.

The fracture evolutions of the armchair SWCNTs with a single divacancy defect and that with a single Stone-Wales defect under uniaxial tensile test are shown in Fig. 32. These two defective SWCNTs would involve a different crack propagation path even though they have a comparable defect location and rate. According to the fraction evolutions, crack would initiate from the atomistic defect, and then quickly propagate in the direction of high tensile stress concentration zone. More specifically, for the SWCNT with a divacancy defect, crack starts to propagate along the 45° direction, and then tends to turn into the 0° direction due to atom rearrangement, leading to the redistribution of the atomistic stress. In contrast, for the SWCNT with a Stone-Wales defect, crack also propagates along its high tensile stress concentration region. As shown in Fig. 33b, the region is located in the 0° direction at the atomistic defect. Besides, the crack once initiated would continue to propagate till a full fracture occurs, implying that SWCNTs are a very brittle material, and thus, would undergo a brittle fracture as the strain exceeds the ultimate value, which is 0.3 for the SWCNT with a vacancy-defect and 0.37 for that with a Stone-Wales defect.

Fracture evolution may be dependent on some essential factors, such as location, distribution pattern and number of atomistic defects. Accordingly, further investigation is undertaken to examine the fracture evolution of the armchair SWCNT having more than one divacancy defect. Besides the divacancy defect located at the middle of the SWCNT, two other divacancy defects are also developed, which are resided in between the top end of the SWCNT and the first divacancy defect. The

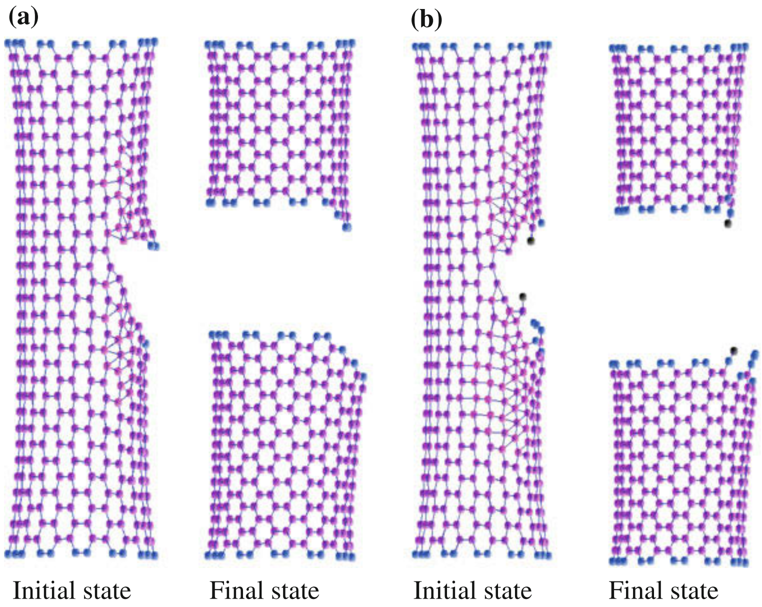

Fig. 32 Fracture evolutions of defective armchair SWCNTs [107]. **a** With a divacancy defect. **b** With a stone-wales defect

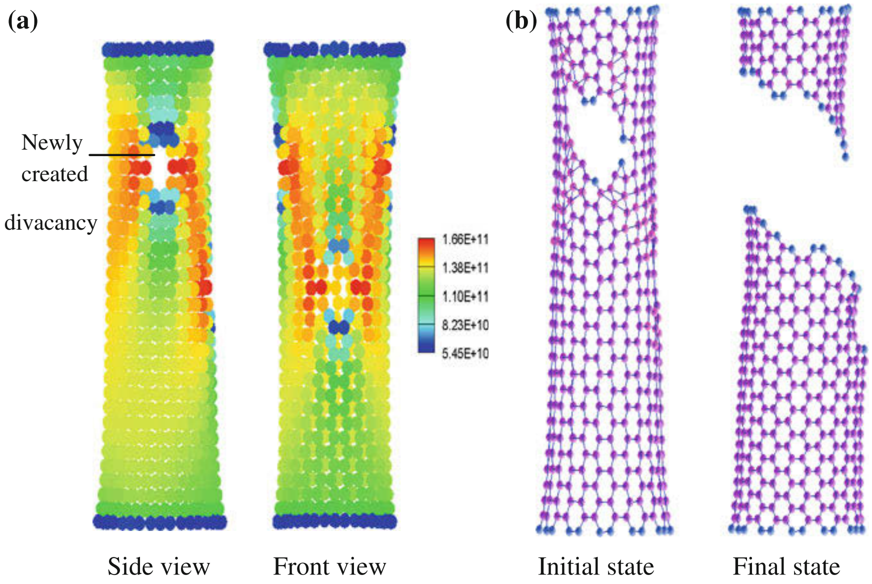

Fig. 33 Atomistic stress distribution before the onset of crack propagation and snapshots of fracture evolution of an armchair SWCNT with three divacancy defects [107]. **a** Atomic stress distribution. **b** Fracture evolution

corresponding atomistic stress distribution right before the onset of crack propagation is shown in Fig. 33a. The figure reveals that high stress concentration also occurs around the two newly created divacancy defects. In addition, two high stress bands can be observed along the lines from the first divacancy defect to the two newly created, respectively. Furthermore, Fig. 33b shows the associated fracture evolution. As can be seen in the figure, crack initiates almost simultaneously from these three divacancy defects, and then propagates quickly toward each other until the entire SWCNT is torn off as the strain attains a critical value.

Thermo-Mechanical Properties of Carbon Fullerenes

The temperature-dependent linear and volumetric CTEs of three typical carbon fullerene molecules, i.e., C_{60}, C_{70} and C_{80}, and also their phase transformation behaviors at temperature below the Debye temperature and atmospheric pressure condition are investigated herein. To achieve the goal, canonical MD simulation using the standard NH, massive NH chain (MNHC) and modified NH thermostat methods are applied in the study. The influences of the sampling methods in MD simulation on the calculated thermodynamic properties, in particular the CTE of carbon fullerenes at temperature below the Debye temperature, are first explored. The major causes behind the large difference in the predicted thermodynamic behaviors of carbon fullerenes are also investigated. The limitations of the standard NH thermostat method and its variants, including the NHC and MNHC, and also the advantages of the modified NH thermostat method are addressed. The simulation results by the modified NH thermostat method are compared with those calculated by the standard NH and MNHC thermostat method and also with the literature experimental and theoretical data. At last, the phase transformation behaviors (e.g., melting point, sublimation point) of C_{60} fullerene molecule at atmospheric pressure are explored. Besides, the investigation attempts to find out whether C_{60} fullerene under the thermodynamic conditions will be converted into gaseous carbon atoms, just like graphite [94–96] or liquid carbon, as well reported in the literature.

In the MD simulation, a time step $\Delta t = 5 \times 10^{-16}$ s and a total of simulation time steps 2×10^6 are used. Basically, the number of equilibrating time steps is much larger than those used in Kim and Tománek [33] and Fang and Chang [97] to ensure the equilibrium of the molecular system. In addition, to statistically extract characteristic values from the MD simulation, three different types of sampling approaches, namely the random, systematic [98] and average [30], are utilized. As soon as the system reaches equilibrium, simulation results are sampled from every 1×10^3, 5×10^4 and 1×10^5 time steps using these three sampling approaches, which are briefly termed “sampling steps” in the work. According to Tuckerman and Parrinello [58], the effective mass Q for the standard and modified NH thermostat is determined by

$$Q = 3N\kappa_B T_s \tau^2, \tag{78}$$

and according to Tobias et al. [23], that for the MNHC thermostat is given by

$$Q_i = \frac{m_i}{m_H} \kappa_B T_s \tau^2, \tag{79}$$

where m_H is the mass of a hydrogen atom. The characteristic time scale τ is selected to be 0.5 ps.

The calculated temperature-dependent volume change ratios of C_{60} fullerene using the standard NH thermostat are shown in Fig. 34. The associated calculation results by the three sampling approaches are also illustrated in the figure, together with those obtained from the General Utility Lattice Program (GULP) [99], as implemented in the Materials Studio™ package, where the force field between two carbon atoms is modeled with the Tersoff-Brenner (TB) potential and Berendsen thermostat method [18] is employed for constant temperature MD simulation. The systematic sampling method is applied to statistically gather the characteristic values from the MD simulation. It is shown that both the random and systematic sampling approaches yield a very consistent result regardless of the number of time steps (i.e., time step size) used for taking a sample. More importantly, only these two results can resemble those calculated by the GULP module. It is more surprising to find that the simulation results calculated from the average sampling approach show a strong dependence on the number of time steps for taking a sample, where a larger sampling step size tends to cause a smaller or even negative volume change of the C_{60} fullerene. For example, as a sample is taken out of every 5×10^4 time steps by using the average sampling approach, a negative volume change or CTE is derived in the range of 0–250 K.

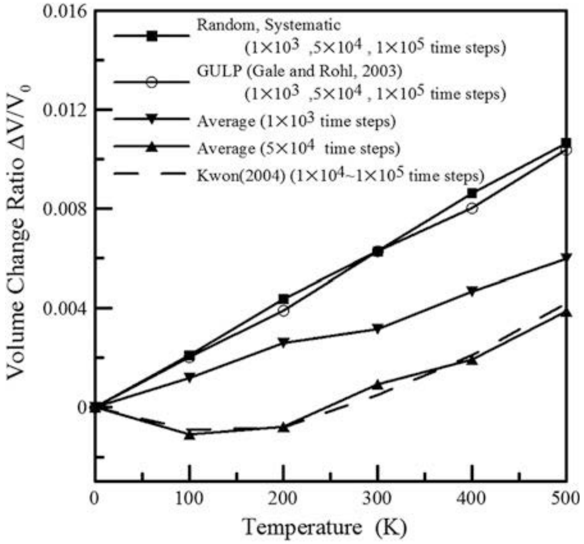

Fig. 34 Temperature effects on C_{60} volume change ratio through the standard NH thermostat using different sampling methods [108]

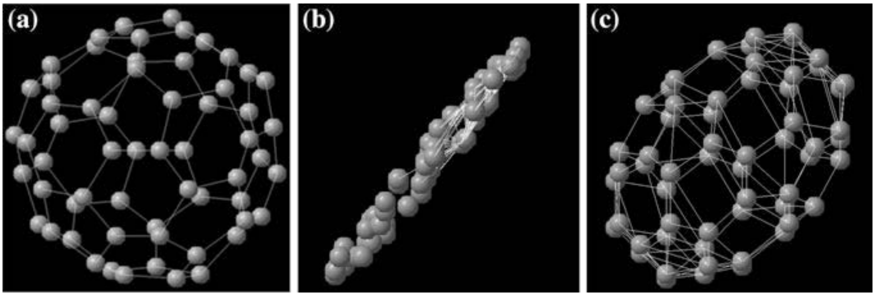

Fig. 35 Geometry prediction of C_{60} molecule structure by three different sampling step sizes [108]. **a** 1×10^3 Δt. **b** 5×10^4 Δt. **c** 1×10^5 Δt

The result trend agrees well with that of Kwon et al. [30]. Furthermore, Fig. 35 gives the resulting geometries of the C_{60} molecule structure at 300 K calculated using the average sampling approach associated with three different numbers of sampling steps for taking a sample, i.e., 1×10^3, 5×10^4 and 1×10^5. We find that the increase of the sampling steps tends to make the C_{60} molecule structure undergo contraction along two of the three major axes, thus gradually being a slender ellipsoid. As the sampling step sizes increase up to 1×10^5 (see Fig. 35c), the C_{60} structure becomes fully compressed into a line. This unanticipated phenomenon is mainly a consequence of the technical limitation of the average sampling approach. From the statistical viewpoint, the calculated properties should be independent of the sampling approaches and also time step sizes for taking a sample as long as the sample number is suitably large. This indicates that the Kwon et al.'s results are just a special-case solution of the average sampling approach.

The line change ratio of C_{60} fullerene as a function of temperature is presented in Fig. 36a, associated with the three thermostat methods. Clearly, there is a linear dependence between the line change of C_{60} fullerene and temperature throughout the temperature range for both the standard NH and MNHC thermostat methods, while showing a nonlinear proportion at temperature below the Debye temperature for the modified NH thermostat. Moreover, both the standard NH and MNHC thermostat methods would yield a larger volume change than the modified NH thermostat. By further taking the first derivative of the line (volume) change ratio with respect to temperature, the linear (volumetric) CTE α (β) can be derived, and the results are shown in Fig. 36b. In principle, the linear CTE for an isotropic material shall be equivalent to one-third of the volumetric CTE. It shows that the calculated linear and volumetric CTEs of C_{60} fullerene at low temperature by the modified NH thermostat tend to lessen with a decreasing temperature, and become a negative value as temperature approaches to absolute zero, while those by the standard NH and MNHC thermostats are not dependent on the temperature. Some studies have been carried out in literature on this issue through experimental and theoretical approaches. For instance, Gugenberger et al. [100] and Aleksandrovskii et al. [101] conducted measurement of the volumetric CTE of C_{60} fullerene at very

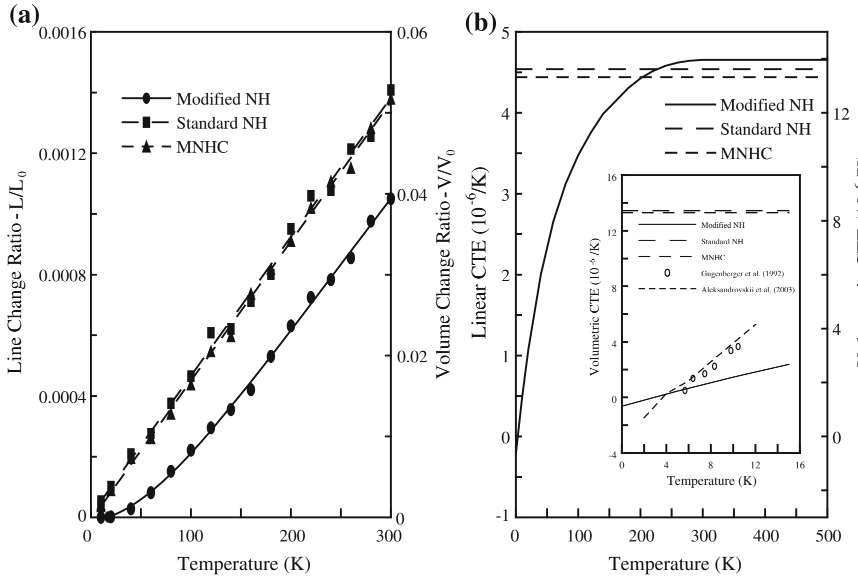

Fig. 36 Temperature-dependent line/volume change ratio and linear/volumetric CTEs of C_{60} fullerene by different thermostats [108]. **a** Line/volume change ratio. **b** Linear/volumetric CTEs

low temperature (<12 K). Their results are also illustrated in Fig. 36b for comparison. The experimental results demonstrate that the CTE of C_{60} fullerene at low temperature would also decrease with the reduction of temperature, and most importantly, tends to become negative at temperature below 5 K. The result trend is in a great consistency with that of the modified NH method, as shown in the figure. In addition, at room temperature, Hamanaka et al. [102] utilized a high-resolution dilatometry to perform measurement of the linear CTE of C_{60} fullerene, in which they reported that the linear CTE is roughly 5.0×10^{-6} K^{-1}. Zubov et al. [103] theoretically explored the relation between the linear CTE of C_{60} fullerene and pressure, and found that it tends to reach a converged value of 4.8×10^{-6} K^{-1} at pressure equal to one atmosphere. By comparing them with the present estimates, it is found that the modified NH thermostat method (i.e., 4.61×10^{-6} K^{-1}) can be in a better agreement with the measurement data than the standard NH (i.e., 4.43×10^{-6} K^{-1}) and MNHC thermostat (i.e., 4.48×10^{-6} K^{-1}). The temperature-dependent linear and volumetric CTEs of C_{70} and C_{80} fullerenes at temperature 0–500 K are also explored by the modified NH thermostat method, and the calculation results are shown in Fig. 37, together with those of C_{60} fullerene. Likewise, negative CTEs occur at temperature approaching to absolute zero. At temperature 300 K and beyond, the CTE of C_{60} (e.g., the linear CTE 4.65×10^{-6} K^{-1}) tends to be larger than those of C_{70} (4.53×10^{-6} K^{-1}) and C_{80} (4.38×10^{-6} K^{-1}).

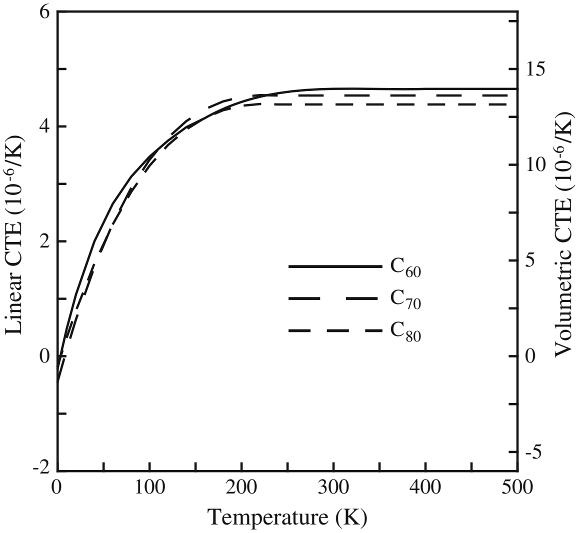

Fig. 37 Temperature-dependent linear/volumetric CTEs of C_{60}, C_{70} and C_{80} fullerenes by the modified NH thermostat [108]

Phase Transformation Behavior of C_{60} Fullerene

The calculatedatomic structures of C_{60} fullerene at different temperatures using both the standard and the modified NH thermostats are presented in Fig. 36. It should be noted that the results calculated by the standard NH thermostat resemble those of the MNHC, and thus are not demonstrated herein. No distinguishable shape change can be observed in the C_{60} atomic structure when $T \leq 300$ K for the NH thermostat and $T \leq 2{,}000$ K for the modified NH thermostat. As shown in Fig. 38a, the result of the standard NH thermostat shows that the C_{60} structure remains intact despite that the structural deformation would increase slightly with the increase of temperature as the temperature is up to 2,000 K, and the C_{60} structure is regarded as the solid-phase fullerene. However, that of the modified NH thermostat reveals that not until the temperature attains 4,000 K will the C_{60} structure undergo any significant structural deformation (see, e.g., Fig. 38c). As the temperature increases beyond the threshold temperature aforementioned, the fullerene will undergo a much more significant structural deformation. It becomes a non-axisymmetric or aspherical shape, as shown in Fig. 38b, d, and develops a gradual onset of the floppy phase. No bond fracture occurs in the C_{60} structure even though there is a significant structural deformation. In essence, the floppy phase of the fullerene structure remains a solid. The phase transition point of C_{60} fullerene from solid to floppy by the standard NH thermostat is 2,000 K, which is comparable to that of Kim and Tománek (1994) (i.e., 2,400 K). However, they all significantly deviate from the result of the modified NH thermostat (i.e., 4,000 K). As the temperature approaches to 2,900 ± 50 K for the standard NH thermostat and 4,350 ± 20 K for the modified NH thermostat, a dramatic transition to a vapor phase is observed, where the fullerene structure will soon turn into a full rupture once a chemical bond starts to break.

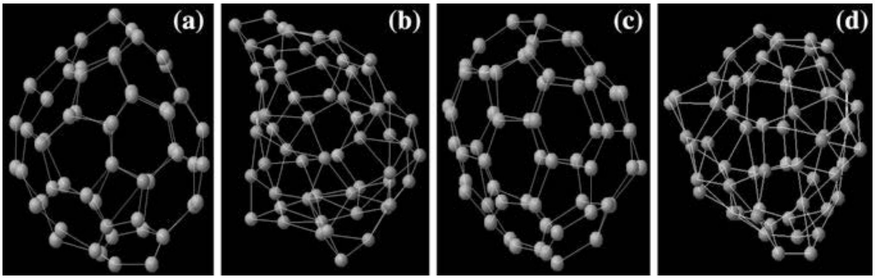

Fig. 38 C_{60} molecule structures predicted by different thermostats [108]. **a** T = 2,000 K (NH). **b** T = 2,800 K (NH). **c** T = 4,000 K (modified NH). **d** T = 4,300 K (modified NH)

Snapshots of the vaporization process of the C_{60} structure at 4,350 ± 20 K at different times calculated by using the modified NH thermostat are presented in Fig. 39. Besides a floppy phase, several other phases prior to attaining a gas phase were also reported by Kim and Tománek (1994), namely pretzel, linked chain and fragment phases. It is, however, believed that these exclusive phases were derived because transient simulation, instead of the commonly-used quasi-static simulation, was carried out in their MD simulation, in which the temperature of heat bath is increased with a temperature increment $\Delta T = 400$ K and 800 time steps for each temperature increment. Since this is a transient simulation, the results calculated are a transient solution rather than a steady-state solution. For example, in their simulation, the linked chain phase occurs at 5,000 K and the fragment phases at 5,400 K, suggesting that the linked chain phase can only exist in a 400 femtosecond (fs) time. It is, thus, believed that the system has not yet attained equilibration. These exclusive phases are, however, not observed in the present investigation using the standard and modified NH thermostats. Due to that only a very small amount of bond fractures takes place in the graphite lattice during melting, the molecules of the liquid phase are considered to be graphite-like fragments [104]. Thus, the linked chain and fragment phases are deemed as liquid. The lack of these two phases may indicate that C_{60} fullerene would sublimate rather than melt when heated under atmospheric pressure. The current result is in a good agreement with

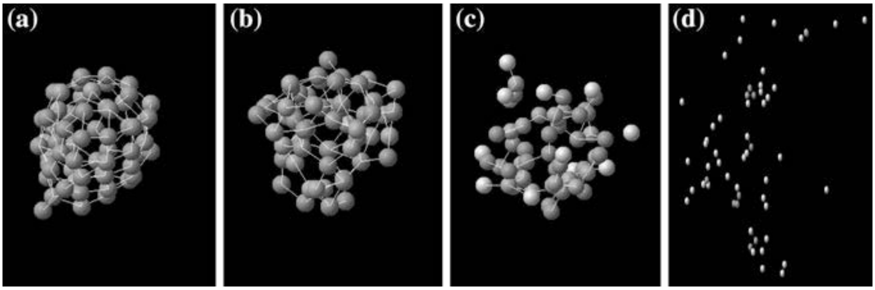

Fig. 39 Snapshots of the vaporization process of C_{60} fullerene [108]. **a** 0.1 ps, **b** 0.2 ps, **c** 0.3 ps, **d** 0.4 ps

the well-known nature of solid graphite, where it would directly turn into gaseous carbon atoms, without going through a liquid state, at high temperature and atmospheric pressure or pressure less than 10 MPa [94–96]. The phase transition point of C_{60} fullerene predicted using the standard NH thermostat under the atmospheric pressure condition is 2,900 ± 50 K, which is much smaller than that of the modified NH thermostat (4,350 ± 20 K) and the literature findings for graphite, i.e., 4,000–4,500 K [94–96]. By contrast, the estimated sublimation point of C_{60} fullerene by the modified NH thermostat (4,350 ± 20 K) is resided within the reported temperature range, i.e., 4,000–4,500 K, of the sublimation point of graphite.

One may deduce, based on the above evidences, that both the C_{60} structure and graphite hold a similar thermodynamic behavior at least at the atmospheric pressure condition. Chelikowsky [105] found that C_{60} fullerene would directly transform from hot carbon plasma to solid fullerene at about 4,000–5,000 K without invoking a preexisting nucleation subunit under atmospheric pressure. His prediction is basically comparable to not only the present investigation but also the phase transformation behaviors of graphite, in which the fullerene would sublimate rather than melt at the threshold temperature and atmospheric pressure.

Acknowledgments The authors would like to express their appreciation to the National Science Council, Taiwan, ROC, for the financial support under grants NSC95-2221-E-007-013-MY3, NSC98-2221-E-007-016-MY3, NSC100-2221-E-035-036-MY3 and NSC101-2221-E-007-009-MY3. Great thanks are also conveyed to our former graduate students: Dr. Yu-Chen Hsu and Dr. Chun-Hung Wu at Taiwan Semiconductor Manufacturing Co., Hsinchu, Taiwan, ROC, and Dr. Yang-Lun Liu at Industrial Technology Research Institute, Hsinchu, Taiwan, ROC, for their great contribution to the work. The authors are also grateful to their graduate student, Mr. Ching-Feng Yu, revision and corrections as well as colleagues [109–111].

References

1. S. Iijima, Helical microtubules of graphitic carbon. Nature **354**, 56–58 (1991)
2. Rodney S. Ruoff, J. Tersoff, C. Lorents, S. Subramoney, B. Chan, Radial deformation of carbon nanotubes by van der Waals forces. Nature **364**, 514–516 (1993)
3. M.M.J. Treacy, T.W. Ebbesen, J.M. Gibson, Exceptionally high Young's modulus observed for individual carbon nanotubes. Nature **381**, 678–680 (1996)
4. M.F. Yu, T. Kowalewski, R.S. Ruoff, Investigation of the radial deformability of individual carbon nanotubes under controlled indentation force. Phys. Rev. Lett. **85**, 1456–1459 (2000)
5. M. Fujii, X. Zhang, H. Xie, K. Takahashi, T. Ikuta, H. Abe, T. Shimizu, Measuring the thermal conductivity of a single carbon nanotube. Phys. Rev. Lett. **95**, 065502 (2005)
6. J.F. Waters, P.R. Guduru, J.M. Xu, Nanotubes mechanics– recent progress in shell buckling mechanics and quantum electromechanical coupling. Compos. Sci. Technol. **66**, 1141–1150 (2006)
7. Z.R. Abrams, Y. Hanein, Radial deformation measurements of isolated pair of single-walled carbon nanotubes. Carbon **45**, 738–743 (2007)
8. S. Wei, C. Li, M.Y. Chou, Ab initio calculation of thermodynamic properties of silicon. Phys. Rev. B **50**, 14587 (1994)

9. J.P. Lu, Elastic properties of carbon nanotubes and nano-ropes. Phys. Rev. Lett. **79**, 1297–1300 (1997)
10. E. Hernandez, C. Goze, P. Bernier, A. Rubio, Elastic properties of C and $B_xC_yN_z$ composite nanotubes. Phys. Rev. Lett. **80**, 4502–4505 (1998)
11. G.H. Gao, T. Cagin, W.A. Goddard III, Energetic, structure, mechanical and vibrational properties of single-walled carbon nanotubes. Nanotechnology **9**, 184–191 (1998)
12. G.V. Lier, C.V. Alsenoy, V.V. Doran, P. Geerlings, Ab initio study of the elastic properties of single-walled carbon nano-tubes and grapheme. Chem. Phys. Lett. **326**, 181–185 (2000)
13. G.Q. Xie, S.Y. Long, Elastic vibration behaviors of carbon nanotubes based on micropolar mechanics. Comput. Mater. Continua **4**, 11–20 (2006)
14. X. Ling, S.N. Atluri, A lattice-based cell model for calculating thermal capacity and expansion of single wall carbon nanotubes. Comput. Model. Eng. Sci. **14**, 91–100 (2006)
15. L.V. Woodcock, Isothermal molecular dynamics calculations for liquid salts. Chem. Phys. Lett. **10**, 257–261 (1971)
16. F.F. Abraham, S.W. Koch, R.C. Desai, Computer-simulation dynamics of an unstable two-dimensional fluid: time-dependent morphology and scaling. Phys. Rev. Lett. **49**, 923–926 (1982)
17. H.C. Andersen, Molecular dynamics simulations at constant pressure and/or temperature. J. Chem. Phys. **72**, 2384 (1980)
18. H.J.C. Berendsen, J.P.M. Postma, W.F. van Gunsteren, A. Dinola, J.R. Haak, Molecular dynamics with coupling to an external bath. J. Chem. Phys. **81**, 3684 (1984)
19. S. Nosé, A molecular dynamics method for simulations in the canonical ensemble. Mol. Phys. **52**, 255–268 (1984)
20. W.G. Hoover, Canonical dynamics: equilibrium phase-space distributions. Phys. Rev. A **31**, 1695–1697 (1985)
21. D.J. Evans, B.L. Holian, The Nose-Hoover thermostat. J. Chem. Phys. **83**, 4069 (1985)
22. G.J. Martyna, M.E. Tuckerman, M.L. Klein, Nosé–Hoover chains: the canonical ensemble via continuous dynamics. J. Chem. Phys. **97**, 2635–2643 (1992)
23. D.J. Tobias, G.J. Martyna, M.L. Klein, Molecular dynamics simulations of a protein in the canonical ensemble. J. Phys. Chem. **97**(49), 12959–12966 (1993)
24. S.D. Bond, B.J. Leimkuhler, B.B. Laird, The Nosé-Poincaré method for constant temperature molecular dynamics. J. Comput. Phys. **151**, 114–134 (1999)
25. K. Zare, V. Szebehely, Time transformations in the extended phase-space. Celest. Mech. **11**, 469–482 (1975)
26. M.E. Tuckerman, C.J. Mundy, G.J. Martyna, On the classical statistical mechanics of non-Hamiltonian systems. Europhys. Lett. **45**, 149–155 (1999)
27. I. László, Formation of cage-like C_{60} clusters in molecular-dynamics simulations. Europhys. Lett. **44**, 741–746 (1998)
28. N.R. Raravikar, P. Keblinski, A.M. Rao, M.S. Dresselhaus, L.S. Schadler, Temperature dependence of radial breathing mode Raman frequency of single-walled carbon nanotubes. Phys. Rev. B **66**, 235424 (2002)
29. P.K. Schelling, P. Keblinski, Thermal expansion of carbon structures. Phys. Rev. B **68**, 035425 (2003)
30. Y.K. Kwon, S. Berber, D. Tomanek, Thermal contraction of carbon fullerenes and nanotubes. Phys. Rev. Lett. **92**, 015901 (2004)
31. D.A. Mcquarie, *Statistical Mechanics*. (Harper & Row Publishers, New York, 1976)
32. E. Lomba, D. Molina, M. Alvarez, Hubbard corrections in a tight-binding Hamiltonian for Se: effects on the band structure, local order, and dynamics. Phys. Rev. B **61**, 9314–9321 (2000)
33. S.G. Kim, D. Tománek, Melting the fullerenes: a molecular dynamics study. Phys. Rev. Lett. **72**, 2418–2421 (1994)
34. G.M. Odegard, T.S. Gates, L.M. Nicholson, K.E. Wise, Equivalent-continuum modeling of nano-structured materials. Compos. Sci. Technol. **62**, 1869–1880 (2002)

35. B.I. Yakobson, C.J. Brabec, J. Bernholc, Nanomechanics of carbon tubes: instabilities beyond linear response. Phys. Rev. Lett. **76**, 2511 (1996)
36. V.M. Harik, Mechanics of carbon nanotubes: applicability of the continuum-beam models. Comput. Mater. Sci. **24**(3), 328–342 (2002)
37. C.Y. Wang, C.Q. Ru, A. Mioduchowski, Axially compressed buckling of pressured multiwall carbon nanotubes. Int. J. Solids Struct. **40**, 3893–3911 (2003)
38. A.N. Sohi, R. Naghdabadi, Torsional buckling of carbon nanopeapods. Carbon **45**, 952–957 (2007)
39. C.J. Wu, C.Y. Chou, C.N. Han, K.N. Chiang, Estimation and validation of elastic modulus of carbon nanotubes using nano-Scale tensile and vibrational analysis. Comput. Model. Eng. Sci. **41**, 49–68 (2009)
40. C.Y. Li, T.W. Chou, A structural mechanics approach for the analysis of carbon nanotubes. Int. J. Solid Struct. **40**, 2487–2499 (2003)
41. C.Y. Li, T.W. Chou, Elastic moduli of multi-walled carbon nanotubes and the effect of van der Waals forces. Compos. Sci. Technol. **63**, 1517–1524 (2003)
42. N.A. Kasti, Zigzag carbon nanotubes-molecular/structural mechanics and finite element method. Int. J. Solid Struct. **44**, 6914–6929 (2007)
43. H.W. Kroto, J.R. Heath, S.C. O'Brien, R.F. Curl, R.E. Smalley, R.E, C_{60} : buckminster fullerene. Nature **318**, 162–163 (1985)
44. R. Saito, M. Fujita, G. Dresselhaus, M.S. Dresselhaus, Electronic structure of chiral graphene tubules. Appl. Phys. Lett. **60**, 2204–2206 (1992)
45. W.-H. Chen, C.-H. Wu, H.C. Cheng, Modified Nosé-Hoover thermostat for solid state for constant temperature molecular dynamics simulation. J. Comput. Phys. **230**, 6354–6366 (2011a)
46. A. Maiti, G.D. Mahan, S.T. Pantelides, Dynamical simulations of nonequilibrium processes-heat flow and the Kapitza resistance across grain boundaries. Solid State Commun. **102**, 51 (1997)
47. W.-H. Chen, H.C. Cheng, Y.L. Liu, Radial mechanical properties of single-walled carbon nanotubes using modified molecular structure mechanics. Comput. Mater. Sci. **47**, 985–993 (2010)
48. J.B. Marion, S.T. Thornton, *Classical Dynamics of Particles and Systems*, 5th edn. (Brooks/Cole, Belmont, 2004)
49. J. Tersoff, New empirical approach for the structure and energy of covalent systems. Phys. Rev. B **37**, 6991–7000 (1988)
50. D.W. Brenner, Empirical potential for hydrocarbons for use in simulating the chemical vapor deposition of diamond films. Phys. Rev. B **42**, 9458–9471 (1990)
51. L.A. Girifalco, V.G. Weizer, Application of the morse potential function to cubic metals. Phys. Rev. **114**, 687–690 (1959)
52. S. Maruyama, Molecular dynamics method for microscale heat transfer. Adv. Numer. Heat Trans. **2**, 189–226 (2000)
53. J.E. Lennard-Jones, The determination of molecular fields. I. from the variation of the viscosity of a gas with temperature. Proc. Royal Soc. (Lond.) **106A**, 441 (1924)
54. L. Battezzatti, C. Pisani, F. Ricca, Equilibrium conformation and surface motion of hydrocarbon molecules physisorbed on graphite. J. Chem. Soc. Faraday Trans. 2: Mol. Chem. Phys. **71**, 1629–1639 (1975)
55. J. Beeler, Displacement spikes in cubic metals. I. alpha-iron, copper, and tungsten. Phys. Rev. **150**, 470–487 (1966)
56. L. Verlet, Computer experiments on classical fluids. I. thermodynamical properties of Lennard–Jones molecules. Phys. Rev. **159**, 98–103 (1967)
57. C. Kittel, *Introduction to Solid State Physics*, 7th edn. (Wiley, New York, 1996)
58. M.E. Tuckerman, M. Parrinello, Integrating the Car-Parrinello equations. I. basic integration techniques. J. Chem. Phys. **101**, 1302–1315 (1994)

59. M.E. Tuckerman, Y. Liu, G. Ciccotti, G.J. Martyna, Non-Hamiltonian molecular dynamics: generalizing Hamiltonian phase space principles to non-Hamiltonian systems. J. Chem. Phys. **115**, 1678–1702 (2001)
60. R. Clausius, On a mechanical theory applicable to heat. Phil. Mag. **40**, 122–127 (1870)
61. Z.S. Basinski, M.S. Duesbery, R. Taylor, Influence of shear stress on screw dislocations in a model sodium lattice. Can. J. Phys. **49**, 2160–2180 (1971)
62. S. Shen, S.N. Atluri, Atomic-level stress calculation and continuum-molecular system equivalence. Comput. Model. Eng. Sci. **6**, 91–104 (2004)
63. W.D. Cornell, P. Cieplak, C.I. Bayly, I.R. Gould, K.M. Merz Jr, D.M. Ferguson, D.C. Spellmeyer, T. Fox, J.W. Caldwell, P.A. Kollman, A second generation force field for the simulation of proteins, nucleic acids, and organic molecules. J. Am. Chem. Soc. **117**, 5179–5197 (1995)
64. T.C. Chang, H.J. Gao, Size-dependent elastic properties of a single-walled carbon nanotube via a molecular mechanics model. J. Mech. Phys. Solids **51**, 1059–1074 (2003)
65. R.M. Badger, A relation between internuclear distances and bond force constants. J. Chem. Phys. **2**, 128–131 (1934)
66. W. Shen, B. Jiang, B.S. Han, S.-S. Xie, Investigation of the radial compression of carbon nanotubes with a scanning probe microscope. Phys. Rev. Lett. **84**, 3634–3637 (2000)
67. C.Y. Li, T.W. Chou, Elastic properties of single-walled carbon nanotubes in transverse directions. Phys. Rev. B **69**, 073401 (2004)
68. C.Y. Li, T.W. Chou, Modeling of elastic buckling of carbon nanotubes by molecular structural mechanics approach. Mech. Mater. **36**, 1047–1055 (2004)
69. L. Muthaswami, Y. Zheng, R. Vajtai, G. Shehkawat, P. Ajayan, R.E. Geer, Variation of radial elasticity in multiwalled carbon nanotubes. Nano Lett. **7**, 3891–3894 (2007)
70. X.-F. Wang, Z.-J. Xu, Z.-Y. Zhu, Reversible mechanical bistability of carbon nanotubes under radial compression. Chem. Phys. **334**, 144–147 (2007)
71. V.N. Popov, V.E. Van Doren, M. Balkamski, Elastic properties of single-walled carbon nanotubes. Phys. Rev. B **61**, 3078–3084 (2000)
72. W.-H. Chen, H.C. Cheng, Y.-C. Hsu, Mechanical properties of carbon nanotubes using molecular dynamics simulations with the inlayer van der Waals interactions. Comput. Model. Eng. Sci. **20**, 123–145 (2007)
73. M. Milnera, J. Kürti, M. Hulman, H. Kuzmany, Periodic resonance excitation and intertube interaction from quasicontinuous distributed helicities in single-wall carbon nanotubes. Phys. Rev. Lett. **84**, 1324–1327 (2000)
74. A. Jorio, R. Saito, J.H. Hafner, C.M. Lieber, M. Hunter, T. McClure, G. Dresselhaus, M.S. Dresselhaus, Structural (n, m) determination of isolated single-wall carbon nanotubes by resonant Raman scattering. Phys. Rev. Lett. **86**, 1118–1121 (2001)
75. J. Kürti, V. Zólyomi, M. Kertesz, G.Y. Sun, The geometry and the radial breathing mode of carbon nanotubes: beyond the ideal behaviour. New J. Phys. **5**, 125.1–125.12 (2003)
76. A.G. Souza Filho, S.G. Chou, G.G. Samsonidze, G. Dresselhaus, M.S. Dresselhaus, L. An, J. Liu, A.K. Swan, M.S. Ünlü, B.B. Goldberg, A. Jorio, A. Grüneis, R. Saito, Stokes and anti-stokes Raman spectra of small diameter isolated carbon nanotubes. Phys. Rev. B **69**, 115428 (2004)
77. M. Damnjanović, E. Dobardžić, I. Miloŝević, Chirality dependence of the radial breathing mode: a simple model. J. Phys. Condens. Matter **16**, L505–L508 (2004)
78. J. Maultzsch, H. Telg, S. Reich, C. Thomsen, Radial breathing mode of single-walled carbon nanotubes: optical transition energies and chiral-index assignment. Phys. Rev. B **72**, 205438 (2005)
79. H.C. Cheng, Y.-L. Liu, C.-H. Wu, W.-H. Chen, On radial breathing vibration of carbon nanotubes. Comput. Methods Appl. Mech. Eng. **199**, 2820–2827 (2010)
80. Y.C. Zhang, X. Chen, X. Wang, Effect of temperature on mechanical properties of multi-walled carbon nanotubes. Compos. Sci. Technol. **68**, 572 (2008)
81. H. Jiang, B. Liu, Y. Huang, K.C. Hwang, Thermal expansion of single-wall carbon nanotubes. J. Eng. Mater. Technol. **126**, 265–270 (2004)

82. G. Cao, X. Chen, J.W. Kysar, contraction of single-walled carbon nanotubes. J. Mech. Phys. Solids **54**, 1206–1236 (2006)
83. P. Poncharal, Z.L. Wang, D. Ugarte, Electrostatic deflections and electromechanical resonances of carbon nanotubes. Science **283**, 1513–1516 (1999)
84. S.S. Rao, *Mechanical Vibrations*, 4th edn. (Addison Wesley, USA, 2004)
85. W.C. Liu, Y.D. Kuang, F.Y. Meng, S.Q. Shi, Temperature effects on mechanical properties of the (3,3) carbon nanotube X-junctions. Comput. Mater. Sci. **49**, 916–919 (2011)
86. G. Zhou, W. Duan, B. Gu, Electronic structure and field-emission characteristics of open-ended single-walled carbon nanotubes. Phys. Rev. Lett. **87**, 095504 (2001)
87. H.C. Cheng, Y.-L. Liu, Y.-C. Hsu, W.-H. Chen, Atomistic-continuum modeling for mechanical properties of single-walled carbon nanotubes. Int. J. Solid Struct. **46**, 1695–1704 (2009)
88. B.I. Yakobson, G. Samsonidze, G.G. Samsonidze, Atomistic theory of mechanical relaxation in fullerene nanotubes. Carbon **38**, 1675–1680 (2000)
89. A. Hashimoto, K. Suennaga, A. Gloter, K. Urita, S. Iijima, Direct evidence for atomic defects in graphene layers. Nature **430**, 870–873 (2004)
90. S.L. Mielke, D. Troya, S. Zhang, J.L. Li, S. Xiao, R. Car, R.S. Ruoff, G.C. Schatz, T. Belytschko, The role of vacancy defects and holes in the fracture of carbon nanotubes. Chem. Phys. Lett. **390**, 413–420 (2004)
91. M. Yu, O. Lourie, M. Dyer, K. Moloni, T. Kelly, R. Ruoff, Strength and breaking mechanism of multiwalled carbon nano-tubes under tensile load. Science **287**, 637–640 (2000)
92. T. Belytschko, S.P. Xiao, G.C. Schatz, R.S. Ruoff, Atomistic simulations of nanotube fracture. Phys. Rev. B **65**, 235430 (2002)
93. K.I. Tserpes, P. Papanikos, S.A. Tsirkas, A progressive fracture model for carbon nanotubes. Compos. B **37**, 662–669 (2006)
94. J. Steinbeck, G. Braunstein, M.S. Dresselhaus, T. Venkatesan, D.C. Jacobson, A model for pulsed laser melting of graphite. J. Appl. Phys. **58**, 4374–4382 (1985)
95. F.P. Bundy, Pressure-temperature phase diagram of elemental carbon. Phys. A **156**, 169–178 (1989)
96. J.M. Zazula, CERN LHC Project Note 78 (1997)
97. T.H. Fang, W.J. Chang, Phase transformation of fullerenes using molecular dynamics simulation. Microelectron. J. **35**, 581–583 (2004)
98. J.M. Haile, *Molecular Dynamics Simulation*. (Wiley, New York, 1997)
99. J.D. Gale, A.L. Rohl, The general utility lattice program. Mol. Simul. **29**, 291 (2003)
100. F. Gugenberger, R. Heid, C. Meingast, P. Adelmann, M. Braun, H. Wuhl, M. Haluska, H. Kuzmany, Glass transition in single-crystal C60 studied by high-resolution dilatometry. Phys. Rev. Lett. **69**, 3774–3777 (1992)
101. A.N. Aleksandrovskii, A.V. Dolbin, V.B. Esel'son, V.G. Gavrilko, V.G. Manzhelii, B.G. Udovidchenko, A.S. Bakai, G.E. Gadd, S. Moricca, B. Sundqvist, Low-temperature thermal expansion of pure and inert-gas-doped fullerite C_{60}. Low Temp. Phys. **29**, 324–332 (2003)
102. T. Hamanaka, R. Yamamoto, A. Onuki, Molecular dynamics simulation of heat conduction in near-critical fluids. Phys. Rev. E **71**, 011507 (2005)
103. V.I. Zubov, J.F. Sanchez, N.P. Tretjakov, A.A. Caparica, I.V. Zubov, Isotherms, thermodynamic properties and stability of the FCC phase of the C_{60} fullerite: A theoretical study. Carbon **35**, 729–734 (1997)
104. F.P. Bundy, Melting of graphite at very high pressure. J. Chem. Phys. **38**, 618–630 (1963)
105. J.R. Chelikowsky, Nucleation of C_{60} clusters. Phys. Rev. Lett. **67**, 2970–2973 (1991)
106. W.-H. Chen, Y.-L. Liu, C.-H. Wu, H.C. Cheng, A theoretical investigation of thermal effects on vibrational behaviors of single-walled carbon nanotubes. Comput. Mater. Sci. **53**, 226–233 (2012)
107. H.C. Cheng, Y.-C. Hsu, W.-H. Chen, The Influence of Structural Defect on Mechanical Properties and Fracture Behaviors of Carbon Nanotubes. J. Comput. Mater. Continua **11**, 127–146 (2009)

108. W.-H. Chen, C.-H. Wu, H.C. Cheng, Temperature-dependent thermodynamic behaviors of carbon fullerene molecules at atmospheric pressure. J. Comput. Mater. Continua **25**, 195–214 (2011)
109. T. Hertel, R.E. Walkup, P. Avouris, Deformation of carbon nanotubes by surface van der Waals forces. Phys. Rev. B **58**, 13870–13873 (1998)
110. E. Dobardžić, I. Milošević, B. Nikolić, T. Vuković, M. Damnjanović, Single-wall carbon nanotubes phonon spectra: symmetry-based calculations. Phys. Rev. B **68**, 045408 (2003)
111. V.M. Harik, Ranges of applicability for the continuum beam model in the mechanics of carbon nanotubes and nanorods. Solid State Commun. **120**(7–8), 331–335 (2001)

Retracted: Nanomechanics: Physics Between Engineering and Chemistry

Boris I. Yakobson and Traian Dumitrică

Abstract Mechanics at nanometer scale involves physical factors often entirely different from the familiar concepts in macroscopic mechanical engineering (elastic moduli, contact forces, friction etc.). These new features are often of chemical nature: intermolecular forces, thermal fluctuations, chemical bonds. The general aspects and issues of nanomechanics are illustrated by an overview of the properties of nanotubes: linear elastic parameters, nonlinear elastic instabilities and buckling, inelastic relaxation, yield strength and fracture mechanisms, and their kinetic theory. Atomistic scenarios of coalescence-welding and the role of non- covalent forces (supra-molecular interactions) between the nanotubes are also discussed due to their significance in potential applications. A discussion of theoretical and computational work is supplemented by brief summaries of experimental results, for the entire range of the deformation amplitudes.

Introduction

A relatively new area of study that concerns itself with the mechanical properties and behavior of small *nanoscale* materials systems can be called nanomechanics. A size of several nanometers in two dimensions (wires, rods etc.) or all three (clusters, particles

---

Editor's note: Nanomechanics is an area of nanoscale mechanics studying mechanical phenomena, mechanical, material properties, mechanical and electro-mechanical behavior of nanoscale material systems or nanostructures of 100 nm or less in size.

An erratum of the original chapter can be found under DOI 10.1007/978-94-017-9263-9_11

B.I. Yakobson (✉) · T. Dumitrică
Department of Mechanical Engineering and Materials Science, and Center for Nanoscale Science and Technology, Rice University, Houston, TEXAS 77005, USA
e-mail: biy@rice.edu

T. Dumitrică
Now at University of Minnesota, Minneapolis, USA
e-mail: td@me.umn.edu

V. Harik (ed.), *Trends in Nanoscale Mechanics*, DOI 10.1007/978-94-017-9263-9_4

etc.) is a simplistic criterion for a system to be considered "nano". This formally may exclude the rich and established science of *surfaces* and interfaces, which are small in only one dimension. One can also argue that a *dislocation* is not a nano-object: while it formally meets the criterion it is never isolated from a crystal lattice and as such has long been a subject of research in solid state physics. To distinguish itself from the well-established dynamics of molecules, nanomechanics relies heavily on the heuristics and methods of mechanical engineering and structural mechanics. It mainly deals with objects of distinct geometrical shape and function: rods, beams, shells, plates, membranes, etc. At the same time, due to the small length scale nanomechanics also relies on physics, specifically, inter-atomic and molecular forces, methods of quantum chemistry, solid state physics, and statistical mechanics. With these approaches come a variety of numerical and computational methods (molecular dynamics, Monte Carlo simulations, classical empirical interatomic potentials, tight-binding approximation, density functional theory, etc.). This cross-disciplinary aspect makes this area both complex and exciting for research and education.

Macroscopic mechanics mainly deals with continuum representation of material, neglecting the underlying atomic structure, which manifests itself primarily at a smaller scale. In this context it is interesting to realize that continuum model of a finite object is not self-contained and inevitably leads to a notion of atom as discrete building block. Indeed, elastic response of continuum is quantified by its moduli, e.g. Young's modulus Y (J/m^3). A boundary surface of a material piece of finite size L must be associated with certain extra energy, surface energy γ (J/m^2). A combination γ/Y is dimensional (m) and constitutes a length not contained within such finite continuum model, which points to some other inherent parameter of the material, a certain size *a*. The surface energy is the additional work to "overstretch"-tear apart an elastic continuum. Such work equals to the energy of the formed boundary (two boundaries), that is a Y/2 ≈ 2γ, and thus a ≈ 4γ/Y. With typical Y = 50 GPa, and γ = 1 J/m^2 one gets *a* = 0.1 nm, a reasonably accurate atomic size [1, 2]. The notion of "indivisibles" was well familiar since Democritus and therefore a simple mechanical measurement could yield an estimate of atomic size much earlier than more sophisticated Brownian motion theory. This discussion also shows that for an object of nanometer scale its grainy, atomistic structure comes inevitably into the picture of its mechanics and that atomistic or hybrid-multiscale methods are necessary.[1]

---

[1] Editor's notes: B. Yakobson and his colleagues were among the first to perform theoretical modeling of carbon nanotubes, i.e.,

1993/94—R.S. Ruoff and J. Tersoff team at IBM has done first theoretical modeling of carbon nanotubes and carbon nanotube crystals.

1996—M.M.J. Treacy, T.W. Ebbesen and J.M. Gibson have carried out first experimental testing of carbon nanotubes with the atomic force microscope (AFM).

1996—B.I. Yakobson, C.J. Brabec and J. Bernholc have performed molecular dynamics (MD) simulation of the axial buckling and twisting of carbon nanotubes. They have shown the shell-like behavior of carbon nanotubes.

1997—C.M. Lieber and his team at Harvard University have done similar experimental testing of vibrating carbon nanotubes.

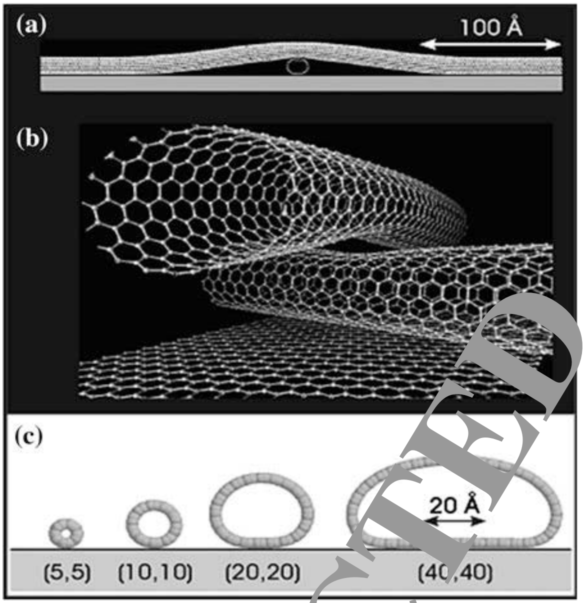

Fig. 1 Molecular mechanics calculations on the axial and radial deformation of single-wall carbon nanotubes. **a** Axial deformation resulting from the crossing of two (10,10) nanotubes. **b** Perspective close up of the same crossing showing that both tubes are deformed near the contact region. **c** Computed radial deformations of single-wall nanotubes adsorbed on graphite. (Adapted from Ph. Avouris et al., Phys. Rev. B, 58, 13870, 1998.). Editor's note: Research group of Dr. Avouris (IBM Research Center) was among the first to perform theoretical modeling of carbon nanotubes and take into account the van der Waals forces and their effect on their quasi-static radial deformation.

Among the numerous subjects of nanomechanics research (tips, contact-junctions, pores, whiskers etc.), carbon nanotubes (CNTs) [3] have earned a special place, receiving much attention. Their molecularly precise structure, elongated and hollow shape, effective absence of a surface (which is no different than the bulk, at least for the single-walled cylinders, SWNTs), and superlative covalent bond strength are among the traits that put CNTs (Fig. 1) in the focus of nanomechanics. Discussion of numerous other objects as well as details of the multiscale methods involved in nanomechanics (for example, see recent monograph [4]) is far beyond the scope of this chapter.

It is noteworthy that the term *resilient* has been first applied not to nanotubes but to smaller fullerene cages, in the study of high-energy collisions of C_{60}, C_{70}, and C_{84} bouncing from a solid wall of H-terminated diamond. The absence of any fragmentation or other irreversible atomic rearrangement in the rebounding cages was somewhat surprising and indicated the ability of fullerenes to sustain great elastic distortion. The very same property of resilience becomes more significant in case of carbon nanotubes, since their elongated shape, with the aspect ratio close to a thousand, makes the mechanical properties especially interesting and important due to potential structural applications. An accurate simulation (with realistic interatomic and van der Waals forces) in Fig. 1 [5] vividly illustrates the appeal of CNT's as a nanomechanical object: well defined cylindrical shape, compliance to external forces, and an expected type of response qualitatively analogous to a common macroscopic behavior puts these objects between molecular chemical physics, elasticity theory and mechanical engineering.

The utility of nanotubes as elements in nanoscale devices or composite materials remains a powerful motivation for the research in this area. While the feasibility of the practical realization of these applications is currently unknown, another incentive comes from the fundamental materials physics. There is an interesting duality in the nanotubes. CNT's possess simultaneously molecular size and morphology as well as sufficient translational symmetry to perform as very small (nano) crystals with well-defined primitive cell, surface, possibility of transport, etc. Moreover, in many respects they can be studied as well defined as engineering structures and many properties can be discussed in traditional terms of moduli, stiffness or compliance, or geometric size and shape. The mesoscopic dimension (a nanometer diameter) combined with the regular, almost translation-invariant morphology along the micrometer lengths (unlike other polymers, usually coiled), make nanotubes a unique and attractive object of study, including the study of mechanical properties and fracture in particular.

Indeed, fracture of materials is a complex phenomenon whose theory generally requires a multiscale description involving microscopic, mesoscopic and macroscopic modeling. Numerous traditional approaches are based on a macroscopic continuum picture that provides an appropriate model except at the region of actual failure where a detailed atomistic description (involving chemical bond breaking) is needed. Nanotubes, due to their relative simplicity and atomically precise morphology, offer the opportunity of addressing the validity of different macroscopic and microscopic models of fracture and mechanical response. Contrary to crystalline solids where the structure and evolution of ever-present surfaces, grain-boundaries, and dislocations under applied stress determine the plasticity and fracture of the material, nanotubes possess simpler structure while still can show rich mechanical behavior within elastic or inelastic brittle or ductile domain. This second, theoretical-heuristic value of nanotube research supplements their import due to anticipated practical applications. A morphological similarity of fullerenes and nanotubes to their macroscopic counterparts, like geodesic domes and towers, makes it compelling to test the laws and intuition of macromechanics in the scale ten orders of magnitude smaller.

In the following, section "Molecular Dynamics Methods in Nanomechanics" gives a brief overview of the molecular dynamics methods employed in nanoscale simulations. Section "Linear Elastic Properties" discusses theoretical linear elasticity and results for the elastic moduli, compared wherever possible with the experimental data. The nonlinear elastic behavior, buckling instabilities and shell model are presented in section "Nonlinear Elasticity and Shell Model", with mentioning of experimental evidence parallel to theoretical results. Yield and failure mechanisms in tensile load are presented in section "Atomic Relaxation and Failure Mechanisms", with the emphasis on the combined dislocation theory and computational approach. More recent results of kinetic theory of fracture and strength evaluation in application to CNTs are briefly presented in section "Kinetic Theory of Strength". Fast molecular tension tests are recalled in the context of kinetic theory. Section "Coalescence of Nanotubes as a Reversed Failure" presents some of the most recent result on CNT "welding", a process essentially reverse to fracture. In section "Persistence Length, Coils and Random Fuzz-Balls of Nanotubes" we also briefly discuss the large-scale mechanical deformation of nanotubes caused by their attraction to each other, and the relation between nanomechanics and statistical persistence length of CNT in a thermodynamic suspension. Throughout the discussion we do not attempt to provide a comprehensive review of broad activities in the field. Presentation is mainly based on the author's research started at North Carolina State University and continued at Rice University. Broader or a more comprehensive discussion can be found in other relatively recent reviews by the author [6, 7].

Molecular Dynamics Methods in Nanomechanics

Molecular dynamics is a simulation technique in which the time-evolution of a set of interacting particles is obtained by directly integrating the equations of motion, which are derived from Newton's law,[2]

$$\mathbf{F}_i = m_i \mathbf{a}_i, \tag{1}$$

applied to each atom i in a system containing N atoms. Here m_i is the atom mass, $\mathbf{a_i}$ the acceleration, and $\mathbf{F_i}$ the force acting upon atom i due to the interaction with other atoms. Most commonly, the time- integration is performed with the velocity Verlet algorithm, where positions, velocities, and accelerations at time t + Δt are obtained from the same quantities at time t:

$$\mathbf{r}_i(t+\Delta t) = \mathbf{r}_i(t) + \mathbf{v}_i(t)\Delta t + (1/2)\mathbf{a}_i(t)\Delta t^2$$
$$\mathbf{v}_i(t+\Delta t) = \mathbf{v}_i(t) + (1/2)[\mathbf{a}_i(t+\Delta t) + \mathbf{a}_i(t)]\Delta t. \tag{2}$$

Because we are integrating Newton's equation, the acceleration $\mathbf{a}_i$(t) is just the force divided by mass. In turn, the force is obtained as the gradient of a potential energy function depending explicitly on the positions of all particles:

$$\mathbf{a}_i(t) = -(1/m_i)\nabla_{\mathbf{r}_i} V(\mathbf{r}_1, .., \mathbf{r}_N). \tag{3}$$

The time step here is denoted by Δt. Since the atomic vibrations are on a time scale of approximately 100 fs, a time step smaller than that is required, typically of 2 fs.

---

[2] Editor's notes in words of Leonardo da Vinci [about his notes on science]: "… I believe that before I am at the end of this I shall have to repeat [some of] the same things; and therefore, O reader, blame me not, because the subjects are many…" and it is important to encourage the reader.

Equations (2) and (3) describe the natural time evolution of a classical system in microcanonical ensemble since the total energy E is a constant of motion. In practice it is useful to compute it at each time step in order to check if it is indeed constant in time. There could be small fluctuations in a typical amount of one part in 10^4 or less, which are due to the errors in the time integration. These errors can be reduced either by decreasing the time step (which implies a longer simulation time) or by employing higher-order evolution algorithms [8].

From Eq. (3) it becomes transparent that the problem of modeling a material is essentially that of finding the potential V that reproduces the behavior of the material under the conditions at which the simulation is run. Depending on the origin of the potential, there are three main varieties of molecular dynamics techniques—*empirical, tight-binding*, and *first principles*.

The empirical methods employ classical potentials, which can be constructed by various techniques. For example, the dependence of the energy on the nuclei position can be extracted from a first principle description. Another choice is to fit the potential to experimental data. In all cases, potentials are valid in physical situations not far from those in which they are fitted and the desired ability of a potential to work properly in different environments (molecule, surface, or bulk) is called *transferability*. It is therefore important to recognize that potentials are always designed with a range of applicability and, when using a potential one should be always familiar with its transferability properties.

The simplest decomposition of the many-body potential is a sum of pairwise terms, with the energy of a pair depending on their relative distance r_{ij}:

$$V(r_1,\ldots,r_N) = (1/2)\sum_{i\neq j}\varphi(r_{ij})$$

Unfortunately, the class of materials that can be realistically modeled using this approach is limited to rare gases, where electronic bonding is absent and atoms are interacting through the weak van der Waals forces.

The potential for metals must incorporate the quantum mechanical effect of bond weakening as the local environment becomes more "crowded" (a consequence of Pauli principle). Several scheme were developed based on the analytical form:

$$V = (1/2)\sum_{i\neq j}\varphi(r_{ij}) + \sum_{i} U(n_i).$$

As before φ is a two-body part whereas U is a function giving the energy of an atom as a function of its coordination n_i. Belonging to this scheme are the glue model [9], the embedded atom method [10], and the Finnis-Sinclair potentials [11], which differ in the choice of the function φ and U. Similarly, the description of covalent semiconductors [12] and hydrocarbons [13] can be achieved by accounting for the variation of the bond strength with environment. The employed analytical form is:

$$V = (1/2)\left[\sum_{i \neq j} \varphi_R(r_{ij}) + \sum_{i \neq j} B_{ij}\varphi_A(r_{ij})\right],$$

where A and R stand or attractive and repulsive. The function B_{ij} is strongly dependent on environment (coordination) and has the effect of weakening the ij bond in the presence of other bonds involving atom i. It also contains an angular dependence and a cutoff, which restricts the pair potential to its nearest neighbors.

In general, the classical potentials for metals and semiconductors are designed from the start with a cutoff radius, which often limits the interaction to only the nearest neighbor atoms. Several subtleties have to be addressed when using a cutoff. If an abrupt truncation in the form of step function is employed, the energy and its derivative are no longer continuous functions of the atomic coordinates and there will be jumps in the energy as atoms move in and out of each other's cutoff distance. This can disrupt a minimization process or lead to unwanted effects (such as heating) in a dynamic simulation. A better choice is to use a smoothing function that tapers the interaction to zero at a given distance. For example, the Brenner potential for carbon [13] employed a switch type function:

$$G(r) = \begin{cases} 1, r < r_1 \\ (1/2)\left\{1 + \cos\left[\frac{\pi(r-r_1)}{(r_2-r_1)}\right]\right\}, r_1 \leq r \leq r_2, \\ 0, r > r_2 \end{cases}$$

which has the property of leaving the interaction unchanged for distances less than the inner cutoff distance r_1 = 1.7 Å and is smoothed to zero at the second cutoff r_2 = 2 Å. Additionally, the first derivative is continuous on the full range, which avoids problems in minimization and dynamic simulations.

Caution must be exercised in nanomechanics simulations, since this cutoff choice is not appropriate if the C–C bonds are stretched beyond 1.7 Å. The artificial forces that arise in the (r_1, r_2) interval have a negligible effect if simulations are performed at high temperatures, but they have a higher influence at lower temperatures, and may lead to unphysical behaviors. For instance, atomistic fracture simulations at room temperature indicated a very high failure strain of polycrystalline diamond, and the 1.7 Å cutoff radius had to be adjusted to a higher value [14].

By employing the Car-Parinello scheme [15] one can perform molecular dynamics from the first principles. In this method the potentials are not required and the forces on ions are obtained directly from the electronic structure, solved by means of density functional theory (local density approximation). Typically, solution of the time-independent Schrodinger equation involves a lengthy iterative process, which has to be repeated at any new atomic configuration. This direct procedure is unpractical for most cases, and constitutes a bottleneck for ab initio molecular dynamics. The difficulty is overcome in the Car-Parinello method. Through an extended Lagrangian approach, this scheme succeeds in keeping the electronic states at optimal values, although not exactly in the electronic ground states.

Another choice to avoid the lengthy self-consistent electronic structure calculations is to employ the tight-binding approximation, and perform semi-empirical tight-binding molecular dynamics [16]. The chemistry is taken into account into a natural way because in tight-binding scheme the electronic states are built from the atomic like orbitals, which are localized on atomic sites. The accuracy depends on the choice of the basis function and on the accuracy with which the tight-binding parameters are fitted. With the proper choice of this input one can obtain a good description of many electronic properties like the density of states, band structure, and Fermi energy. In this respect, tight-binding molecular dynamics represents a semi-empirical approach and lies between empirical and first-principles methods. Computations within the scheme are a few orders of magnitude faster than the ab initio ones. The method must be applied cautiously because of transferability problems.

It is also possible to carry out simulations in ensembles other than microcanonic, such as at constant pressure, at constant stress, or at constant temperature. These approaches are dynamical in origin and the basic idea is to reformulate the Lagrangian equations of motion such that the phase space of desired ensemble is reproduced. There are many areas of applicability. For instance, simulations at finite temperature, which are achieved by introducing into equations of motion a time-dependent frictional term [17], can find applications in optimizing to a true minima (global, as opposed to numerous local minima) or in searching the lowest-energy defects of a nanomechanical system.

Indeed, temperature provides a way to jump over the barriers[3] and at large T the system "senses" the simultaneous existence of many different minima, and states with energy E are obtained with the probability exp(-E/k_BT). Consequently, the system spends more time in deeper states. By slowly decreasing T to 0 there is a high probability that the system will land in the desired true minimum configuration. Alternatively, starting from the perfect structure, a slow temperature increase would make accessible the lowest energy defect state. If the corresponding energy barrier to such a state is large compared to k_BT, the occurrence of new configuration is infrequent until a thermal fluctuation would trigger the event. These considerations are the basis of *simulated annealing* methods, where the system is equilibrated at a certain temperature and then slowly cooled or heated. While these procedures do not guarantee absolute success, they often give good results. They are particularly useful when the desired structures are hard to predict by intuition, as for example in the case of identifying the lowest dislocation dipole in BN systems, discussed in section "Atomic Relaxation and Failure Mechanisms".

All methods discussed above, including the Car-Parinello scheme, assume the Born-Oppenheimer approximation, i.e., the electronic system is assumed in the ground state and adiabatically follows the nuclear motion. This approximation is

---

[3] Editor's notes: "Movement is created by heat and cold." Leonardo da Vinci, Philosophy, p. 79, in *The Notebooks of Leonardo da Vinci* (edited by E. MacCurdy, Konecky and Konecky printing, Duckworth and Co., London, 1906).

valid in most cases, but there are physical situations when such approximation is no longer appropriate. For instance, when studying the response of matter to intense laser pulses, a non-negligible fraction of electrons are situated into the excited states. For these situations one must perform excited-states molecular dynamics and such schemes were formulated from an extended Lagrangian approach in the tight-binding or ab initio context [18]. In this generalization, the forces on the atoms are obtained from the electronic states that satisfy the time-dependent Schrodinger equation. However, these physical phenomena are beyond the scope of nanomechanics, mainly discussed in this chapter.

Linear Elastic Properties

Numerous theoretical calculations are dedicated to linear elastic properties, when displacements (strain) are proportional to forces (stress). We recently revisited [19] this issue in order to compare within the same method the elasticity of three different materials: pure carbon (C), boron-nitride (BN), and fluorinated carbon (C_2F). Due to obvious uncertainty in definition of a nanotube "cross-section", the results should be represented by the values of in-plane stiffness, C (J/m^2). The values computed with Gaussian-based density functional theory are C = 345, 271, and 328 N/m for C, BN, and C_2F respectively. These values in ab initio calculations are almost independent of nanotube diameter and chirality (consistent with the isotropic elasticity of a hexagonal 2D lattice), somewhat in contrast to previous reports based on tight-binding or classical empirical approximations. Notably, substantial fluorination causes almost no change in the in-plane stiffness, because the bonding involves mainly π-system while the stiffness is largely due to in-plane σ-system. For "material" property assessments, the values of bulk moduli (based on a graphite-type 0.34 nm spacing of layers) yield 1,029, 810, and 979 GPa—all very high. Knowing the elastic shell parameter C immediately leads to accurate calculation of a nanotube-beam bending stiffness K (proportional to the cube of diameter, $\sim d^3$) as discussed later in sections "Nonlinear Elasticity and Shell Model" and "Persistence Length, Coils and Random Fuzz-Balls of Nanotubes". It also allowed us to compute vibration frequencies of the tubules, e.g. symmetric breathing mode frequency, $f \sim 1/d$ [illegible], detectable in Raman spectroscopy.

An unexpected feature discovered in the course of that study [19] is the localized strain induced by the attachment of fluorine. This shifts the energy minimum of the C_2F shell lattice from an "unstrained" sheet towards the highly curved polygonal cylinders (for C_2F composition of a near square shape, Figs. 1, 2). Equilibrium free angle is ~72°.

Theoretical values agree reasonably well with experimental values of the Young's modulus. It was first estimated [20] by measuring freestanding room-temperature vibrations in a transmission electron microscope (TEM). The motion of a vibrating cantilever is governed by the known fourth-order wave equation, $y_{tttt} = -(YI/\rho A)y_{xxxx}$, where A is the cross sectional area, ρ is the density of the rod

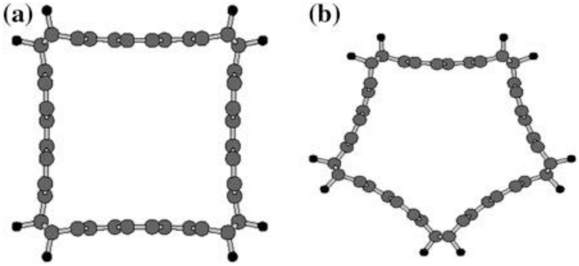

Fig. 2 Geometries of the polygonal fluorinated carbon tubes: **a** square F_4−(10,10) and **b** pentagonal F_5−(10,10). (From K.N. Kudin et al., Phys. Rev. B, 64, 235406 (2001.)

material. For a clamped rod the boundary conditions are such that the function and its first derivative are zero at the origin and the second and third derivative are zero at the end of the rod. Thermal nanotube vibrations are essentially elastic relaxed phonons in equilibrium with the environment; therefore the amplitude of vibration changes stochastically with time. The amplitude of those oscillations was defined by means of careful TEM observations of a number of CNTs and yield the values of moduli within a range near 1 TPa.

Another way to probe the mechanical properties of nanotubes is to use the tip of an AFM (atomic force microscope) to bend an anchored CNT while simultaneously recording the force exerted by the tube as a function of the displacement from its equilibrium position [21]. Obtained values [illegible] vary from sample to sample but generally are close to Y = 1 TPa. Similar values have been obtained in [22] with yet another accurate technique based on a resonant electrostatic deflection of a multi-wall carbon nanotube under an external ac-field. The detected decrease in stiffness must be related to the emergence of a different bending mode for the nanotube. In fact, this corresponds to a wavelike distortion-buckling of the inner side of the CNT. Nonlinear behavior is discussed in more detail in the next section. Although experimental data on elastic modulus are not very uniform, it corresponds to the values of in-plane rigidity C = 340−440 N/m, to the values Y = 1.0−1.3 GPa for multiwall tubules, and to Y = 4C/d = (1.36−1.76) TPa nm/d for SWNTs of diameter d.

Nonlinear Elasticity and Shell Model

Almost any molecular structure can sustain very large deformations (Fig. 3), compared to the range common in macroscopic mechanics. A less obvious property of CNTs is that the specific features of large nonlinear strain can be understood and predicted in terms of continuum theories. One of the outstanding features of nanotubes is their hollow structure; built of atoms densely packed along a closed surface that defines the overall shape. This also manifests itself in dynamic properties of molecules, resembling so much the macroscopic objects of continuum elasticity known as *shells.*

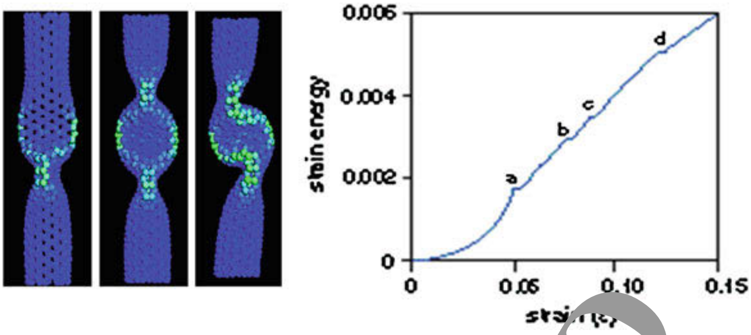

Fig. 3 Simulation of a (7, 7) nanotube exposed to axial compression, L [illegible] nm. The strain energy *a* displays four singularities corresponding to shape changes. At $\varepsilon_1 = 0.05$ the cylinder buckles into the pattern *b*, displaying two identical flattening–"fins" perpendicular to each other. Further increase of ε enhances this pattern gradually until at $\varepsilon_2 = 0.07$ the tube switches to a three-fin pattern *c*. In a buckling sideways at $\varepsilon_3 = 0.09$ the flattenings serve as hinges, and only a plane of symmetry is preserved *d*. At $\varepsilon_4 = 0.13$ an entirely squashed asymmetric configuration forms *e*. (From B.I. Yakobson et al., Phys. Rev. Lett., 76, 2511, [illegible])

Macroscopic shells and rods have long been of interest: the first study dates back to Euler, who discovered the elastic instability. A rod subject to longitudinal compression remains straight but shortens by some fraction *ε*, proportional to the force, until a critical value (the Euler force) is reached. It then becomes unstable and buckles sideways at $\varepsilon > \varepsilon_{cr}$, while the force almost does not vary. For hollow tubules there is also a possibility of local buckling in addition to buckling as a whole. Therefore, more than one bifurcation can be observed, thus causing an overall nonlinear response to the [illegible] deforming forces (note that local mechanics of the constituent shells may well still remain within the elastic domain).

In nanomechanics, the theory of shells was first applied in our early analysis of buckling and since then serves as a useful guide [23–26]. Its relevance for a covalent-bonded system of only a few atoms in diameter was far from being obvious. MD simulations seem better suited for objects that small.[4] Figure 3 shows a simulated nanotube exposed to *axial compression*. The atomic interaction was modeled by the Tersoff-Brenner potential, which reproduces the lattice constants and binding energies of graphite and diamond. The end atoms were shifted along the axis by small steps and the whole tube was relaxed by conjugate-gradient method while keeping the ends constrained. At small strains the total energy (Fig. 3a) grows as $E(\varepsilon) = 1/2\ E''\cdot\varepsilon^2$. The presence of four singularities at higher strains was quite a striking feature and the patterns (b)–(e) illustrate the corresponding morphological changes. The shading indicates strain energy per atom, equally spaced from below 0.5 eV (brightest) to above 1.5 eV (darkest). The sequence of singularities in E(ε)

---

[4] Editor's notes: "Therefore O students study mathematics and do not build without foundations." Leonardo da Vinci, Philosophy, p. 82, in *The Notebooks of Leonardo da Vinci* (edited by E. MacCurdy, Konecky and Konecky printing, Duckworth and Co., London, 1906).

corresponds to a loss of molecular symmetry from $D_{\infty h}$ to S_4, $D_{2h,}$ C_{2h} and C_1. This evolution of the molecular structure can be put in the framework of continuum elasticity.

The intrinsic symmetry of a graphite sheet is hexagonal, and the elastic properties of two-dimensional hexagonal structure are isotropic. A curved sheet can also be approximated by a uniform shell with only two elastic parameters: flexural rigidity D, and its in-plane stiffness, C. The energy of a shell is given by a surface integral of the quadratic form of local deformation,

$$\mathrm{E}\ = \frac{1}{2}\iint\{\mathrm{D}\left[\left(\kappa_{\mathrm{x}}+\kappa_{\mathrm{y}}\right)^2 - 2(1-\nu)\left(\kappa_{\mathrm{x}}\kappa_{\mathrm{y}}-\kappa_{\mathrm{xy}}^2\right)\right]+ \frac{C}{(1-\nu^2)}[(\varepsilon_{\mathrm{x}}+\varepsilon_{\mathrm{y}})^2-2(1-\nu)(\varepsilon_{\mathrm{x}}\varepsilon_{\mathrm{y}}-\varepsilon_{\mathrm{xy}}^2)]\}\mathrm{dS},$$

where κ is the curvature variation, ε is the in-plane strain (and x and y are local coordinates). In order to adapt this formalism to a graphitic tubule, the values of D and C can be identified by comparison with the detailed ab initio and semi-empirical studies of nanotube energetics at small strains. Indeed, the second derivative of total energy with respect to axial strain corresponds to the in-plane rigidity C (cf. section "Linear Elastic Properties"). Similarly, the strain energy as a function of tube diameter d corresponds to D/d^2 in the equation above. Using recent ab initio calculations [19], one obtains C = 56 eV/atom = 340 J/m^2, and D = 1.46 eV. The Poisson ratio ν = [illegible] extracted from a reduction of the diameter of a tube stretched in simulations. A similar value is obtained from experimental elastic constants of single crystal graphite. One can make a further step towards a more tangible picture of a tube as having wall thickness h and Young modulus Y_s. Using the standard relations $D = Yh^3/12(1-\nu^2)$ and $C = Y_s h$, one finds Y_s = 3.9 TPa and h = 0.089 nm.[5] With these parameters, linear stability analysis allows one to assess the nanotube behavior under strain (Fig. 4).

To illustrate the efficiency of the shell model, consider briefly the case of imposed axial compression. A trial perturbation of a cylinder has a form of Fourier harmonics, with M azimuthal lobes and N half waves along the tube (Fig. 4, inset), i.e. sines and cosines of arguments 2My/d and Nπx/L. At a critical level of the imposed strain, $\varepsilon_c(M, N)$, the energy variation vanishes for this shape disturbance. The cylinder becomes unstable and lowers its energy by assuming an (M, N)-pattern. For tubes of d = 1 nm with the shell parameters identified above, the critical strain is shown in Fig. 4.

---

[5] Editor's notes: "He who blames the supreme certainty of mathematics feeds on confusion, and will never impose silence upon the contradictions of the sophistical sciences, which occasion a perpetual clamor." Leonardo da Vinci, Philosophy, p. 83, in *The Notebooks of Leonardo da Vinci* (edited by E. MacCurdy, Konecky and Konecky printing, Duckworth and Co., London, 1906). .

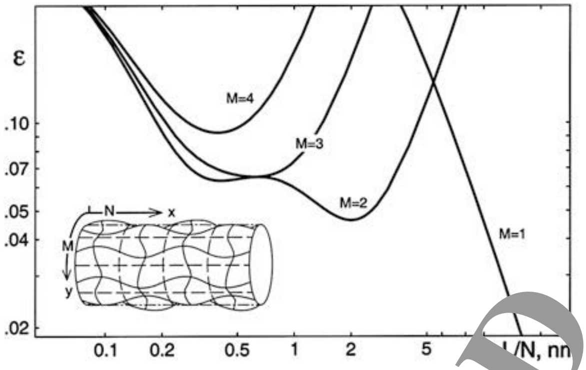

Fig. 4 The critical strains for a 1 nm wide shell-tube as a function of its scaled length L/N. Buckling (M, N) is defined by the number of halfwaves 2M and N in y and x directions, respectively, e.g., a (4,4)-pattern is shown in the inset. The effective moduli and thickness are fit to graphene. (From B.I. Yakobson et al., Phys. Rev. Lett., 76, 2511, 1996.)

According to these plots, for a tube with L > 10 nm the bifurcation is first attained for M = 1, N = 1. The tube preserves its circular cross section and buckles sideways as a whole; the critical strain is close to that for a simple rod,

$$\varepsilon_c = 1/2(\pi d/L)^2, \tag{4}$$

or four times less for a tube with hinged (unclamped) ends. For a shorter tube the situation is different. The lowest critical strain occurs for M = 2 (and N ≥ 1, see Fig. 4), with a few separated flattenings in directions perpendicular to each other, while the axis remains straight. For such a local buckling, in contrast to (4), the critical strain depends little on length and estimates to $\varepsilon_c = 4\sqrt{D/C}\ d^{-1} = (2/\sqrt{3})(1-\nu^2)^{-1/2}\ h\cdot d^{-1}$ in the so-called *Lorenz* limit. For a nanotube one finds,

$$\varepsilon_c = 0.1\ \mathrm{nm}/d. \tag{5}$$

Specifically, for the 1 nm wide tube of length L = 6 nm, the lowest critical strains occur for the M = 2 and N = 2 or 3 (Fig. 4). This is in accord with the two- and three-fin patterns seen in Fig. 3b, c. Higher singularities cannot be quantified by the linear analysis, but they look like a sideways beam buckling, which at this stage becomes a non-uniform object.

Axially compressed tubes of greater length and/or tubes simulated with hinged ends (equivalent to a doubled length) first buckle sideways as a whole at a strain consistent with the above expression for the strain energy. After that the compression at the ends results in bending and a local buckling inward. This illustrates the importance of the "beam-bending" mode, the softest for a long molecule and most likely to attain significant amplitudes due to either thermal vibrations or environmental forces. In simulations of *bending*, a torque rather than force is applied at the ends and the bending angle θ increases stepwise. While a notch in the energy plot can be mistaken for numerical noise, its derivative dE/dθ drops significantly. This unambiguously shows an increase in tube compliance—a signature of a buckling event. In bending, only one side of a tube is compressed and thus can buckle. Assuming that it buckles when its local strain, $\varepsilon = \kappa d/2$, where κ is the local curvature, is close to that in axial compression, Eq. (5), we estimate the critical curvature as

$$\kappa_c = 0.2\ \mathrm{nm/d^2}.$$

In simulation of *torsion*, the increase of azimuthal angle ϕ between the tube ends results in abrupt changes of energy and morphology [23, 24, 27]. In continuum model, the analysis based on the aforementioned equation for energy is similar to that outlined above, except that it involves skew harmonics of arguments like Nπx/L ± 2My/d. For overall beam-buckling (M = 1),

$$\phi_c = 2(1 + \nu)\pi$$

and for the cylinder-helix flattening (M = 2),

$$\phi_c = 0.06\ \mathrm{nm}^{3/2}\mathrm{L/d^{5/2}} \tag{6}$$

The latter should occur first for $L < 140\ d^{5/2}$ nm, which is true for all tubes we simulated. However, in simulations it occurs later than predicted by Eq. (6). The ends, kept circular in simulation, which is physically justifiable, by a presence of rigid caps on normally closed ends of a molecule, deter the thorough flattening necessary for the helix to form (unlike the local flattening in the case of an axial load).

Experimental evidence provides sufficient support to the notion of high resilience of SWNT. An early observation of noticeable flattening of the walls in a close contact of two MWNT has been attributed to van der Walls forces pressing the cylinders to each other [28]. Collapsed forms of the nanotube ("nanoribbons"), also caused by van der Waals attraction, have been observed in experiment, and their stability can be explained by the competition between the van der Waals and elastic energies [29]. Any additional torsional strain imposed on a tube in experimental environment also favors flattening [23, 24] and facilitates the collapse. Graphically more striking evidence of resilience is provided by bent structures [30], as well as the more detailed observations that actually stimulated our research in nanomechanics [31]. An accurate measurement with the atomic force microscope (AFM) tip detects the "failure" of a multiwall tubule in bending [21], which essentially represents nonlinear buckling on the compressive side of the bent tube. The estimated measured local stress is 15–28 GPa, very close to the calculated value [32, 33]. Buckling and ripple of the outmost layers in a dynamic resonant bending has been directly observed and is responsible for the apparent softening of MWNT of larger diameters [7, 34].

Atomic Relaxation and Failure Mechanisms

The important issue of ultimate tensile strength of CNTs is inherently related with the atomic relaxation in the lattice under high strain. This thermally activated process was first predicted to consist of a sequence of individual bond rotations in the approach based on dislocation theory [32, 33, 36]. Careful computer simulations demonstrate feasibility of this mechanism and allowed us to quantify important energy aspects [37, 38]. It has been shown that in a crystal lattice such as the wall of a CNT, a yield to deformation must begin with a homogeneous nucleation of a slip by the shear stress present. The non-basal edge dislocations emerging in such slip have a well-defined core, a pentagon-heptagon pair, 5/7. Therefore the prime dipole is equivalent to the Stone-Wales (SW) defect. The nucleation of this prime dislocation dipole "unlocks" the nanotube for further relaxation: either brittle cleavage or a plastic flow. Remarkably, the latter corresponds to motion of dislocations along the helical paths (glide "planes") within the nanotube wall. This causes a stepwise (quantized) necking, when the domains of different chiral symmetry, and therefore different electronic structure are formed, thus coupling the mechanical and electrical properties [32, 35, 36]. It has further been shown [32, 33, 35, 38–40] that the energy of such nucleation explicitly depends on CNT helicity (chirality).

Below, we deduce starting with dislocation theory, the atomistics of mechanical relaxation under extreme tension.[6] Locally, the wall of a nanotube differs little from a single graphene sheet, a two-dimensional crystal of carbon. When a uniaxial tension σ (N/m for the two-dimensional wall, it is convenient to use force per unit length of its circumference) is applied it can be represented as a sum of expansion (locally isotropic within the wall) and a shear of a magnitude σ/2 (directed at ± 45° with respect to tension). Generally, in a macroscopic crystal the shear stress relaxes by a movement of *dislocations*, the edges of the atomic extra-planes. Burgers vector **b** quantifies the mismatch in the lattice due to a dislocation. Its glide requires only local atomic rearrangements and presents the easiest way for strain release, provided sufficient thermal agitation. In an initially *perfect* lattice such as the wall of a nanotube, a yield to a great axial tension begins with a homogeneous *nucleation* of a slip, when a dipole of dislocations (a tiny loop in three-dimensional case) first has to form. The formation and further glide are driven by the reduction of the applied-stress energy, as characterized by the elastic Peach-Koehler force on a dislocation. The force component along **b** is proportional to the shear in this direction and thus depends on the angle between the Burgers vector and the circumference of the tube,

$$\mathrm{fb} = -{}^{1}\!/_{2}\sigma|\mathrm{b}| \sin 2\theta,$$

---

[6] Editor's notes: "Let no one read me who is not mathematician in my beginnings." Leonardo da Vinci, Philosophy, p. 85, in *The Notebooks of Leonardo da Vinci* (edited by E. MacCurdy, Konecky and Konecky printing, Duckworth and Co., London, 1906).

The max $|f_b|$ is attained on two ± 45° lines, which mark the directions of a slip in an isotropic material under tension.

The graphene wall of the nanotube is not isotropic, its hexagonal symmetry governs the three glide planes—the three lines of closest zigzag atomic packing, oriented at 120° to each other (corresponding to the $\{10\bar{1}l\}$ set of planes in three-dimensional graphite). At non-zero shear these directions are prone to slip. The corresponding c-axis edge dislocations involved in such slip are indeed known in graphite. The six possible Burgers vectors $1/3a <2\bar{1}\bar{1}0>$ have a magnitude b = a = 0.246 nm (lattice constant), and the dislocation core is identified as a 5/7 pentagon-heptagon pair in the honeycomb lattice of hexagons. Therefore, the primary nucleated dipole must have a 5/7/7/5 configuration (a 5/7 attached to an inverted 7/5 core). This configuration is obtained in the perfect lattice (or a nanotube wall) by a 90° rotation of a single C–C bond, well known in fullerene science as a Stone-Wales diatomic interchange. One is led to conclude that the SW transformation is equivalent to the smallest slip in a hexagonal lattice and must play a key role in the nanotube relaxation under external force.

The preferred glide is the closest to the maximum-shear ± 45° lines, and depends on how the graphene strip is rolled-up into a cylinder. This depends on nanotube helicity specified by the chiral indices (c_1, c_2) or a chiral angle θ indicating how far the circumference departs from the leading zigzag motif $\mathbf{a}_1$. The max $|f_b|$ is attained for the dislocations with $\mathbf{b} = \pm$ (0,1) and their glide reduces the strain energy,

$$Eg = -|fba| = -Ca^2/2\cdot\sin(2\theta+60^\circ)\cdot\varepsilon, \qquad (7)$$

per one displacement, *a*. Here ε is the applied strain, and C = Yh = 342 N/m can be derived from the Young modulus of Y = 1,020 GPa and the interlayer spacing h = 0.335 nm in graphite; one then obtains $Ca^2/2 = 64.5$ eV. The Eq. 7 allows one to compare different CNTs (assuming similar amount of pre-existing dislocations): the more energetically favorable is the glide in a tube, the earlier it must yield to applied strain.

In a pristine nanotube-molecule, the 5/7 dislocations have to first emerge as a dipole, by a prime SW transformation. Topologically, the SW defect is equivalent to either one of the two dipoles, each formed by a ∼*a*/2 slip. Applying Eq. 7 to each of the slips one finds

$$E_{SW} = E_o - A\cdot\varepsilon - B\cdot\sin(2\theta+30^\circ)\cdot\varepsilon.$$

The first two terms, the zero-strain formation energy and possible isotropic dilation, do not depend on chiral symmetry. The symmetry-dependent third term, which can also be derived as a leading term in the Fourier series, describes the fact that SW rotation gains more energy in an armchair (θ = 30°) CNT, making it thermodynamically the weakest and most inclined to SW nucleation of the dislocations, in contrast to the zigzag (θ = 0) where the nucleation is least favorable.

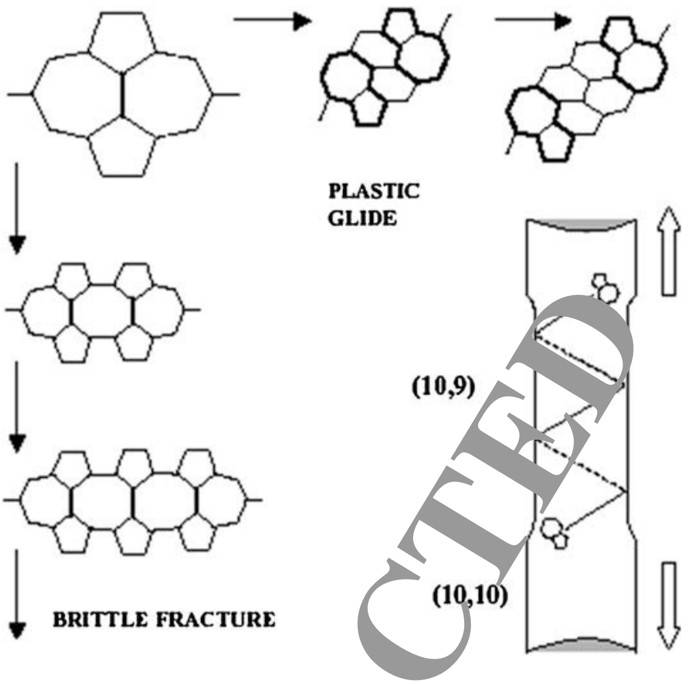

Fig. 5 SW-transformations of an equatorially oriented bond into a vertical position create a nucleus of relaxation (*top left corner*). It evolves [illegible] as either a crack—brittle fracture route, left column—or as a couple of dislocations gliding away along the spiral slip "plane" (plastic yield, *top row*). In both cases only SW rotations are required as elementary steps. The stepwise change of the nanotube diameter reflects the change of chirality, bottom right image, causing the corresponding variations of electrical properties. (Adapted from B.I. Yakobson, Appl. Phys. Lett., 72, 918, 1998.)

Consider for example a ([illegible]) armchair CNT as a typical representative (we will also see below that this armchair type can undergo a more general scenario of relaxation). The initial stress-induced SW rotation creates a geometry that can be viewed as either a dislocation dipole or a tiny crack along the equator. Once "unlocked", the SW defect can ease further relaxation. At this stage, both brittle (dislocation pileup and crack extension) or plastic (separation of dislocations and their glide away from each other) routes are possible, the former usually at larger stress and the latter [illegible] higher temperatures.

Formally, both routes correspond to a further sequence of SW-switches. The 90° rotation of the bonds at the "crack tip" (Fig. 5, left column) will result in a 7/8/7 flaw and then 7/8/8/7 etc. This further strains the bonds-partitions between the larger polygons, leading eventually to their breakage, with the formation of greater openings like 7/14/7 etc. If the crack, represented by this sequence, surpasses the critical Griffith size, it cleaves the tubule.

In a more interesting distinct alternative, the SW rotation of another bond (Fig. 5, top row) divides the 5/7 and 7/5, as they become two dislocation cores separated by a single row of hexagons. A next similar SW switch results in a double-row separated pair of the 5/7's, and so on. This corresponds, at very high temperatures, to a plastic flow *inside* the nanotube-molecule, when the 5/7 and 7/5 twins glide away from each other driven by the elastic forces, thus reducing the total strain energy [cf. Eq. (7)]. One remarkable feature of such glide is due to mere cylindrical geometry: the glide "planes" in case of nanotubes are actually spirals, and the slow thermally-activated Brownian walk of the dislocations proceeds along these well-defined trajectories. Similarly, their extra-planes are just the rows of atoms also curved into the helices.

A nanotube with a 5/7 defect in its wall loses axial symmetry and has a bent equilibrium shape; the calculations show [41] the junction angles <15°. Interestingly then, an exposure of an even achiral nanotube to the axially symmetric tension generates two 5/7 dislocations, and when the tension is removed, the tube "freezes" in an asymmetric configuration, S-shaped or C-shaped, depending on the distance of glide, that is time of exposure. This seemingly "symmetry violating" mechanical test is a truly nanoscale phenomenon. Of course the symmetry is conserved statistically, since many different shapes form under identical conditions.

When the dislocations sweep a noticeable distance, they leave behind a tube segment changed strictly following the topological rules of dislocation theory. By considering a planar development of the tube segment containing a 5/7, for the new chirality vector **c'** one finds,

$$(c_1', c_2') = (c_1, c_2) - (b_1, b_2),$$

with the corresponding reduction of diameter, d. While the dislocations of the first dipole glide away, a generation of another dipole results, in further narrowing and proportional elongation under stress and thus forming a neck as shown above. The orientation of a generated dislocation dipole is determined every time by the Burgers vector closest to the lines of maximum shear (± 45° cross at the end-point of the current circumference-vector **c**). The evolution of a (c,c) tube will be: (c, c) → (c, c−1) → (c, c−2) → … (c, 0) → (c−1, 1) or (c, −1)] → (c−1, 0) → (c−2, 1) or (c−1, −1)] → (c−2, 0) → [(c−3, 1) or (c−2, −1)] → (c−3, 0) etc. It abandons the armchair (c,c) type entirely, but then oscillates in the vicinity of zigzag (c, 0) kind, which appears a peculiar attractor. Correspondingly, the diameter for a (10,10) tube changes stepwise, d = 1.36, 1.29, 1.22, 1.16 nm, etc., the local stress grows in proportion and this quantized necking can be terminated by a cleave at late stages. Interestingly, such plastic flow is accompanied by the change of electronic structure of the emerging domains, governed by the vector (c_1, c_2): The armchair tubes are metallic, others are semiconducting with the different band gap values. The 5/7 pair separating two domains of different chirality has been discussed as a pure-carbon heterojunction, is argued to cause the current rectification detected in a nanotube nanodevice [42] and can be used to modify, in a controlled way, the electronic structure of the tube. Here we see how this electronic heterogeneity can arise from a mechanical relaxation at high temperature: if the initial tube was armchair-metallic, the plastic dilation transforms it into a semiconducting type irreversibly [35, 36, 43].

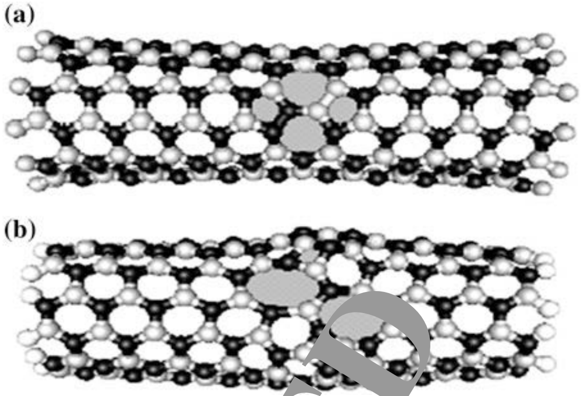

Fig. 6 The geometries of (5, 5) BN tubule with (**a**) 5/7/7/5 defect emerging at high tension and temperature, and (**b**) 4/8/8/4 dislocation dipole. (From H.F. Bettinger et al., Phys. Rev. B, 65, 041406, 2002.)

While the above analysis is based on atomic picture (structure and interactions), recent developments [44] offer an approach where the fracture nucleation can be described rather elegantly within nonlinear continuum mechanics (based on classical interatomic forces for carbon). Whether this approach can describe change in chirality, temperature dependence or temporal aspects of relaxation should yet be explored.

The dislocation theory allows one to expand the approach to other materials, and we have recently applied it to boron nitride (BN) nanotubes [45]. While the binding energy in BN is lower than in CNT, the formation of 5/7/7/5 defect can be more costly due to Coulomb repulsion between emerging BB and NN pairs, Fig. 6a (bonding in BN is partially ionic with strong preference to chemical neighbor alternation in the lattice). Another dislocation pair 4/8/8/4 that preserves the alternation must be considered, Fig. 6b.

It turns out that the quantitative results are sensitive to the level of theory accuracy. Tight binding approximation [46] underestimates the repulsion by almost 3 eV [45]. Ab initio DFT calculations show that 5/7/7/5 is metastable lowest energy defect in BN, and its formation energy 5.5 eV is higher than 3.0 eV in carbon [45], thus suggesting higher thermodynamic stability of BN under tensile load. Relaxation under compression is different as it involves skin-type buckling also investigated recently [47].

Kinetic Theory of Strength

Computer simulations have provided a compelling evidence of the mechanisms discussed above. By carefully tuning a *quasi-static* tension in the tubule and gradually elevating its temperature, with extensive periods of MD annealing, the first stages of the mechanical yield of CNT have been observed, Fig. 7 [37, 38]. In simulation of tensile load the novel patterns in plasticity and breakage, just as described above, clearly emerge. At very *high strain* rate the details of primary

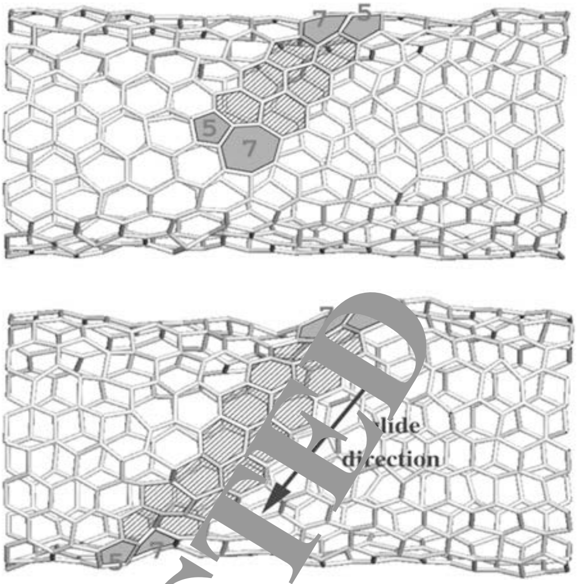

Fig. 7 $T = 3{,}000$ K, strain 3 %, plastic flow behavior (about 2.5 ns). The shaded area indicates the migration path of the 5/7 edge dislocation. (Adapted from M. Nardelli et al., Phys. Rev. Lett., 81, 4656, 1998.)

defects cannot be seen and they only begin [illegible] emerge at higher strain level, giving impression of exceedingly high breaking strain [27].

Fracture, of course, is a *kinetic* process, where time is an important parameter. Even a small tension, as any non-hydrostatic stress, makes material thermodynamically meta-stable and a generation of defects energetically favorable. Thus the important issue of strength remains beyond the defect formation energy and its reduction with the applied tension. Recently we developed kinetic theory in application to CNT [40, 48]. In this approach we evaluate conditions (strain ε, temperature T) when the probability P of defect formation becomes significant within laboratory test time Δt,

$$P \approx \nu\, \Delta t\, N_B/3 \sum_m \exp[-E_m(\varepsilon, \chi)/k_bT] \sim 1.$$

Here n = k_bT/h is the usual attempt frequency and N_B is the number of bonds in the sample. Activation barrier $E_m(\varepsilon, \chi)$ must be computed as a function of strain and chirality χ of the tube, and then the solution of this equation with respect to ε gives the breaking strain values.

This approach has involved substantial computational work in finding the saddle points and energies (Fig. 8a) for a variety of conditions and for several transition state modes (index m in the summation above). Obtained yield strain near 17 % (Fig. 8b, [40, 48]) is in reasonable agreement with the series of experimental reports. We currently are implementing similar approach with ab initio level of saddle point barriers calculations [49]. Preliminary data shows higher 8–9 eV barriers but their reduction with tension is also faster.

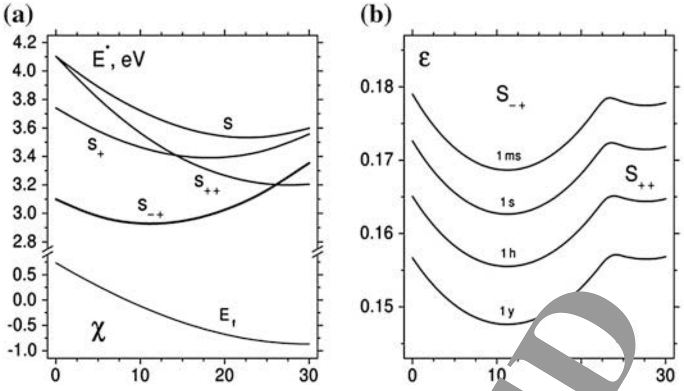

Fig. 8 Activation barrier values (here computed within classical multi-body potential) **a** serve as input to the rate equation and the calculation of the yield strain as a function of time (here from 1 ms), **b** temperature (here 300 K) and chiral symmetry (χ). (From Ge. G. Samsonidze et al., Phys. Rev. Lett., 88, 065501, 2002.)

Previously performed high strain rate simulations have shown temperature dependence of breaking strain [24, 27], consistent with the kinetic theory [40]. In a constant strain rate arrangement (when the ends of the sample are pulled from the equilibrium with certain rate), the rate equation is slightly modified to its integral form. However the main contribution comes from the vicinity of the upper limit,

$$P = \nu\, N_B/3 \int \sum_m \exp\{-E_m[\varepsilon(t), \chi]/k_b T\} dt \sim 1,$$

Simple analysis reveals certain invariant T × log(νΔt) of the time of failure and temperature (provided the constant strain). Detailed simulations could shed additional light on this aspect [50].

Coalescence of Nanotubes as a Reversed Failure

Understanding the details of failure mechanism has lead us recently [51] to investigate an opposite process, a coalescence of nanoscale clusters analogous to macroscopic sintering or welding. Fusion of smaller components into a larger whole is a ubiquitous process in condensed matter. In molecular scale it corresponds to chemical synthesis, where exact rearrangement of atoms can be recognized. Coalescence or sintering of macroscopic parts are usually driven by the well-defined thermodynamic forces (frequently, surface energy reduction), but the atomic evolution path is redundant and its exact identification is irrelevant. Exploring a possibility of the two particles merging with atomic precision becomes compelling in nanometer scale, where one aspires to "arrange the atoms one by one". Are the initial and final states connected by a feasible path of atomic movements, or separated by insurmountable barriers? Direct molecular dynamics (MD) investigation is usually hampered by energy landscape traps and beyond very few atomic steps needs to be augmented with additional analysis.

An example of very small particles is offered by fullerene cages and CNTs. Fusion of fullerenes has been previously reported and the lateral merging (diameter-doubling) of CNT have been observed and simulated [52, 53]. In contrast, head-to-head coalescence of CNT segments remained unexplored and of particular theoretical and practical interest: Is it permitted by rigorous topology rules to eliminate all the pentagons always present in the CNT ends and thus dissolve the caps completely? Can this occur through a series of well-defined elementary steps (Fig. 9) and what is overall energy change if the system evolves through the intermediate disordered states to the final purely hexagonal lattice of continuous tubule? If feasible, such "welding" can lead to increase of connectivity in CNT arrays in bundles/ropes and crystals, and thus significantly improve the mechanical, thermal and electrical properties of material. In addition, determining the atomistic steps of small-diameter tubes coalescence (with the end-caps identical to half-buckyball) can shed light on the underlying mechanism of condensed phase conversion or CNT synthesis from C_{60} components.

In [51] we have reported for the first time atomically precise routes for complete coalescence of generic fullerene cages: cap-to-cap CNT and C_{60} merging together to form defectless final structure. The entire process is reduced to sequence of Stone-Wales bond switches and therefore is likely the lowest energy path of transformation. Several other examples of merging follow immediately as special cases: coalescence of buckyballs in peapod, joining of the two (5,5) tubes as in Fig. 9, "welding" the (10,10) to (10,10) following Fig. 10, etc. The approach remains valid for arbitrary tubes with the important constraint of unavoidable grain-boundary for the tubes of different chirality.[7] The junction of (n,m) and (n`,m`) must contain 5/7 dislocations or their equivalent of (n−n`,m−m`) total Burgers vector [35]. The proposed mechanism [51] has important implications for nanotube material (crystals, ropes) processing and property enhancement, engineering of nanoscale junctions of various types, possible growth mechanisms with the C60 and other nanoparticles as feedstock. In the context of nanomechanics an interesting feature of the later stages of coalescence is the annealing and annihilation of 5/7 pairs in a process exactly reverse to the formation and glide of these dislocation cores in the course of yield and failure under tension.

---

[7] Editor's notes: "Inequality is the cause of all local movements." Leonardo da Vinci, Aphorisms, p. 89, in *The Notebooks of Leonardo da Vinci* (edited by E. MacCurdy, Konecky and Konecky printing, Duckworth and Co., London, 1906).

Fig. 9 2D geodesic projection (*left*) and the actual 3D structures (*right*) show the transformations from a pair of separate (5,5) tubes (**a**) to a single defect-free nanotube. Primary "polymerization" links form as two other bonds break (**b**, *dashed lines*). The π/2-rotations of the links (the bonds subject to such SW-flip are dotted) and the SW-flips of the four other bonds in (**c**) produce a (5,0) neck (**d**). It widens by means of another ten SW-rotations, forming a perfect single (5,5) tubule (not shown). (From Y. Zhao et al., Phys. Rev. Lett., 88, 185501, 2002.)

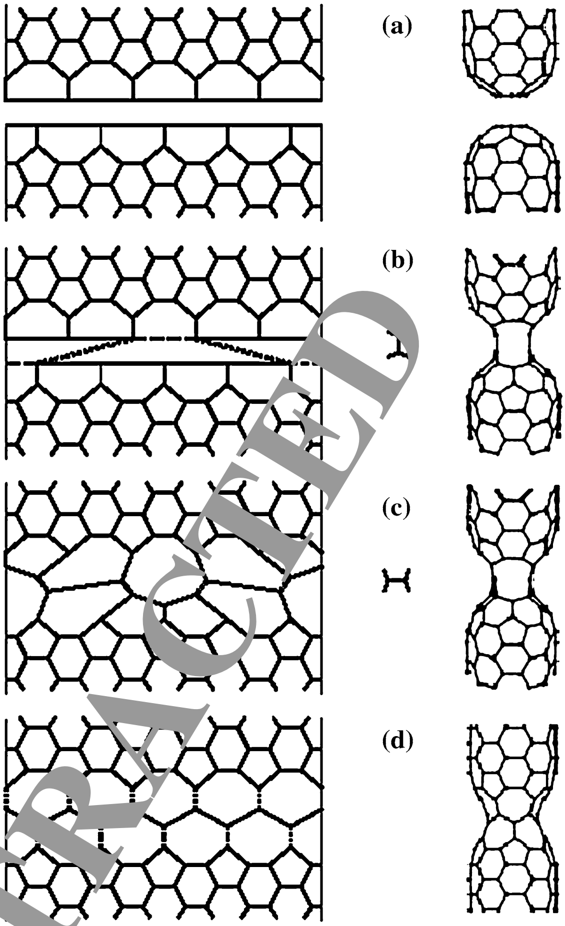

Persistence Length, Coils and Random Fuzz-Balls of Nanotubes

Van der Waals forces play an important role not only in the interaction of the nanotubes with the substrate but also in their mutual interaction. The different shells of a MWNT interact primarily by van der Waals forces; single-wall tubes form ropes for the same reason. A different manifestation of van der Waals interactions involves the self-interaction between two segments of the same single-wall CNT to produce a closed ring (loop) [54]. SWNT rings were first observed in trace amounts in the products of laser ablation of graphite and assigned a toroidal structure. More recently, rings of SWNTs were synthesized with large yields (~ 50 %) from straight nanotube segments. These rings were shown to be loops not tori [54]. The synthesis involves the irradiation of raw SWNTs in a sulfuric acid-hydrogen peroxide

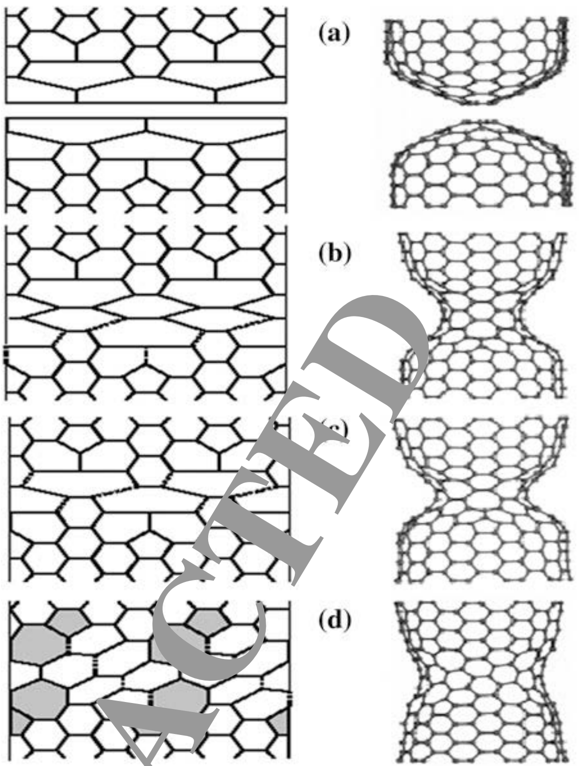

Fig. 10 2D-projections (*left*) and the computed 3D intermediate structures (*right*) in the coalescence of the two (10,10) nanotubes: separate caps (**a**) in a sequence similar to Fig. 8 develop a (5,5) junction (**b**), which then shortens (**c**) and widens into a (10,5) neck (**d**). Glide of the shaded 5/7-dislocations completes the annealing into a perfect (10,10) CNT (not shown). Due to the fifth-fold symmetry, only two cells are displayed. (From Y. Zhao et al., Phys. Rev. Lett., 88, 185501, 2002.)

solution by ultrasound. This treatment both etches the CNTs, shortening their length to about 3–4 μm, and induces ring formation.

The formation of coils by CNTs is particularly intriguing. While coils of biomolecules and polymers are well known structures, they are stabilized by a number of interactions that include hydrogen bonds and ionic interactions. On the other hand, the formation of nanotubes coils is surprising given the high flexural rigidity (K = Young's modulus times areal moment of inertia) of CNTs and the fact that CNT coils can only be stabilized by van der Waals forces. However, estimates based on continuum mechanics show that in fact it is easy to compensate for the strain energy induced by the coiling process through the strong adhesion between tube segments in the coil. Details of this analysis can be found in the original reports [54] or in our recent review [7]. Here we will outline briefly a different and more common situation where the competition of elastic energy and the intertubular linkage is important. Following our recent work [55], we will discuss the connection between the nanomechanics of CNTs and their *random* curling in a suspension or a raw synthesized material of buckypaper.

SWNT are often compared with polymer chains or beams [56] as having very high rigidity, and therefore large persistence length. In order to quantify this argument we note that a defectless CNT has almost no static flexing, although 5/7 defects for example introduce small kink-angle 5–15° and could cause some static curvature, but their energies are high and concentration is usually negligible. Only dynamic elastic flexibility should be considered. If **u**(s) is a unit direction vector tangent to the CNT at contour length point s, and the bending stiffness is K, then statistical probability of certain shape **u**(s) is,

$$P[\mathbf{u}(s)] = \exp[-{}^{1}\!/_{2}(K/k_bT)\textstyle\int(\partial\mathbf{u}/\partial s)^2 ds] = \exp[-{}^{1}\!/_{2}\, L\textstyle\int(\partial\mathbf{u}/\partial s)^2 ds].$$

Here persistence length is $L = (K/k_bT)$. For a (10,10) SWNT of radius $R = 0.7$ nm and the effective wall thickness $h = 0.09$ nm (see sections "Linear Elastic Properties" and "Nonlinear Elasticity and Shell Model"), the bending stiffness is very close to $K = \pi CR^3$ ($C = 345$ N/m is the in-plane shall stiffness, based on ab initio calculations). Persistence length at room temperature therefore is $L_1[(10, 10), 293\ K] \sim 0.1$ mm, in the macroscopic range much greater than for most polymer molecules. The result can be generalized for a single SWNT of radius R,

$$L_1 = (30\ K/T)(R/0.7\ nm)^3 mm,$$

or N times more for a bundle of N tubes (assuming additive stiffness for the case of weak lateral cohesion of the constituent SWNTs). For example for a smallest close packed bundle of seven (one surrounded by six neighbors) this yields $L_7 = 1$ mm. Such incoherent bundle and a solid-coherent bundle with perfect lateral adhesion provide the lower and upper limits for the persistence length, $NL_1 < L_N < N^2L_1$.

Remarkably, these calculations show that the true thermodynamic persistence length of small CNT bundles or even an individual SWNT is in the macroscopic range from a fraction of a millimeter and greater. This means that highly curved structures often observed in bucky paper mats (Fig. 11) are attributed not to

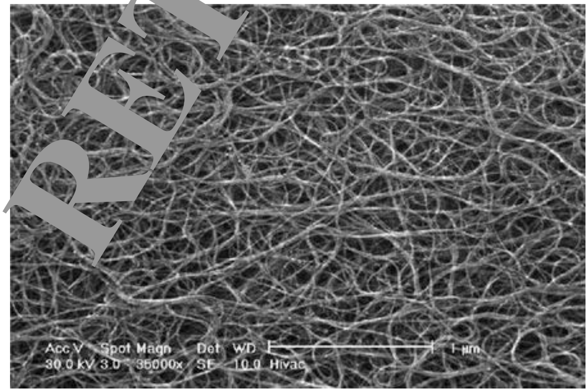

Fig. 11 Raw-produced SWNTs often form ropes-bundles entangled bent into a rubbery structure called "buckypaper". The length scale of bends is much smaller than the persistence length for the constituent filaments. Shown here is such material produced by HiPco (high pressure CO) synthesis method (Adapted from M.J. O'Connell et al., Chem. Phys. Lett., 342, 265, 2001.)

thermodynamic fluctuations but rather to residual mechanical forces preventing these coils from unfolding. Elastic energy of a typical micron size (r ∼ 1 m) curl-arc is much greater than thermal, $U_{curl} \sim k_bT(L/r)^2 >> k_bT$ [55]. At the same time, a force required to maintain this shape $F_{curl} \sim K/r^2 = N$ pN, several picoNewtons, where N is the number of SWNTs in each bundle. This is much less than a force per single chemical bond (∼1 nN), and therefore any occasional lateral bonding between the tubules can be sufficient to prevent them from disentanglement.

References

1. B.I. Yakobson, Morphology and rate of fracture in chemical decomposition of solids. Phys. Rev. Lett. **67**(12), 1590–1593 (1991)
2. B.I. Yakobson, Stress-promoted interface diffusion as a precursor of fracture. J. Chem. Phys. **99**(9), 6923–6934 (1993)
3. S. Iijima, Helical microtubules of graphitic carbon. Nature **354**, 5[illegible]–58 (1991)
4. R.B. Phillips, *Crystals, Defects and Microstructures*. (Cambridge University Press, Cambridge, 2001), p. 780
5. T. Hertel, R.E. Walkup, P. Avouris, Deformation of carbon nanotubes by surface van der Waals forces. Phys. Rev. B **58**(20), 13870–13873 (1998)
6. B.I. Yakobson, R.E. Smalley, Fullerene nanotubes: $C_{1,000,000}$ and beyond. Am. Scien. **85**(4), 324–337 (1997)
7. B.I. Yakobson, P. Avouris, in *Mechanical Properties of Carbon Nanotubes*, ed. by M.S. Dresselhaus, G. Dresselhaus, P. Avouris, Carbon Nanotubes (Springer, Berlin, 2001), pp. 287–327
8. S.A. Chin, Symplectic integrators from composite operator factorizations. Phys. Lett. A **226** (6), 344–348 (1997)
9. F. Ercolessi, M. Parinello, E. Tosatti, Simulation of gold in the glue model. Philos. Mag. A **58** (1), 213–226 (1988)
10. M.S. Daw, Model of metallic cohesion[illegible] the embedded-atom method. Phys. Rev. B **39**(11), 7441–7452 (1989)
11. M.W. Finnis, J.E. Sinclair, A simple empirical N-body potential for transition-metals. Philos. Mag. A **50**(1), 45–55 (1984)
12. J. Tersoff, New empirical approach for the structure and energy of covalent systems. Phys. Rev. B **37**(12), 6991–7000 (1988)
13. D.W. Brenner, Empirical potential for hydrocarbons for use in simulating the chemical vapor-deposition of diamond films. Phys. Rev. B **42**(15), 9458–9471 (1990)
14. O.A. Shenderova, [illegible]W. Brenner, A. Omeltchenko, X. Su, L.H. Yang, Atomistic modeling of the fracture of polycrystalline diamond. Phys. Rev. B **61**(6), 3877–3888 (2000)
15. R. Car, M. Parrinello, Unified approach for molecular dynamics and density-functional theory. Phys. Rev. Lett. **55**(2[illegible]), 2471–2474 (1985)
16. O.F. Sankey, R.E. Allen, Atomic forces from electronic energies via the Hellmann-Feynman theorem, with application to semiconductor (110) surface relaxation. Phys. Rev. B **33**(10), 7164–7171 (1986); O.F. Sankey, D.J. Niklewski, Ab initio multicenter tight-binding model for molecular-dynamics simulations and other applications in covalent systems. Phys. Rev. B **40** (6), 3979–3995 (1989); C.M. Goringe, D.R. Bowler, E. Hernandez, Tight-binding modeling of materials. Rep. Prog. Phys. **60,** 1447–1512 (1997)
17. S. Nose, A molecular dynamics method for simulations in the canonical ensemble. Mol. Phys. **52**(2), 255–268 (1984); W. G. Hoover, Canonical dynamics: equilibrium phase-space distributions. Phys. Rev. A **31**(3), 1695–1697 (1985)

18. R.E. Allen, Electron-ion dynamics: a technique for simulating both electronic transitions and ionic motion in molecules and materials. Phys. Rev. B **50**(24), 18629–18632 (1994); R.E. Allen, T. Dumitrica, B. Torralva, in *Electronic and Structural Response of Materials to Fast Intense Laser Pulses*, ed. by K.T. Tsen, Ultrafast Physical Processes in Semiconductors (Academic, New York, 2001), pp. 315–388
19. K.N. Kudin, G.E. Scuseria, B.I. Yakobson, C_2F, BN and C nano-shell elasticity by ab initio computations. Phys. Rev. B **64**, 235406 (2001)
20. M.M.J. Treacy, T.W. Ebbesen, J.M. Gibson, Exceptionally high Young's modulus observed for individual carbon nanotubes. Nature **381**, 678–680 (1996)
21. E.W. Wong, P.E. Sheehan, C.M. Lieber, Nanobeam mechanics: elasticity, strength and toughness of nanorods and nanotubes. Science **277**, 1971–1975 (1997)
22. P. Poncharal, Z.L. Wang, D. Ugarte, W.A. Heer, Electrostatic deflections and electromechanical resonances of carbon nanotubes. Science **283**, 1513–1[illegible]6 (1999)
23. B.I. Yakobson, C.J. Brabec, J. Bernholc, Nanomechanics of carbon nanotubes: instabilities beyond the linear response. Phys. Rev. Lett. **76**(14), 2511–2514 (1996)
24. B.I. Yakobson, C.J. Brabec, J. Bernholc, Structural mechanics of carbon nanotubes: from continuum elasticity to atomistic fracture. J. Comput. Aided Mater. Des. **3**, 173–182 (1996)
25. A. Garg, J. Han, S.B. Sinnott, Interactions of carbon-nanotube proximal probe tips with diamond and graphite. Phys. Rev. Lett. **81**(11), 2260–2263 (1998)
26. D. Srivastava, M. Menon, K. Cho, Nanoplasticity of single-wall carbon nanotubes under uniaxial compression. Phys. Rev. Lett. **83**(15), 297[illegible]–297[illegible] (1999)
27. B.I. Yakobson, M.P. Campbell, C.J. Brabec, J. Bernholc, High strain rate fracture and C-Chain unraveling in carbon nanotubes. Comput. Mater. Sci. **8**, 341–348 (1997)
28. R.S. Ruoff et al., Radial deformation of carbon nanotubes by van der Waals forces. Nature **364**, 514–516 (1993)
29. N.G. Chopra et al., Fully collapsed carbon nanotubes. Nature **377**, 135–138 (1995)
30. J.F. Despres, E. Daguerre, K. Lafdi, Flexibility of graphene layers in carbon nanotubes. Carbon **33**(1), 87–92 (1995)
31. S. Iijima, C.J. Brabec, A. Maiti, J. Bernholc, Structural flexibility of carbon nanotubes. J. Chem. Phys. **104**(5), 2089–2092 ([illegible]96)
32. B.I. Yakobson, in *Dynamic Topology and Yield Strength of Carbon Nanotubes*. Fullerenes, Electrochemical Society (ECS, [illegible] Pennington, 1997)
33. R.E. Smalley, B.I. Yakobson, The future of the fullerenes. Solid State Commun. **107**(11), 597–606 (1998)
34. J.Z. Liu, Q. Zheng, Q. Jiang, Effect of a rippling mode on resonances of carbon nanotubes. Phy. Rev. Lett. **86**, 4843–4846 (20[illegible])
35. B.I. Yakobson, Mechanical relaxation and 'intramolecular plasticity' in carbon nanotubes. Appl. Phys. Lett. **72**([illegible]), 9[illegible]–92[illegible] (1998)
36. B.I. Yakobson, Physical Property Modification of Nanotubes. U.S. Patent 6,280,677 B1, 2001
37. M.B. Nardelli, B.I. Yakobson, J. Bernholc, Mechanism of strain release in carbon nanotubes. Phys. Rev. B **57**, R[illegible]77 (1998)
38. M.B. Nardelli, B.I. Yakobson, J. Bernholc, Brittle and ductile behavior in carbon nanotubes. Phys. Rev. Lett. [illegible]), 4656–4659 (1998)
39. B.I. Yakobson, G. Samsonidze, G.G. Samsonidze, Atomistic theory of mechanical relaxation in fullerene nanotubes. Carbon **38**, 1675 (2000)
40. G.G. Samsonidze, G.G. Samsonidze, B.I. Yakobson, Kinetic theory of symmetry-dependent strength in carbon nanotubes. Phys. Rev. Lett. **88**, 065501 (2002)
41. L. Chico et al., Pure carbon nanoscale devices: nanotube heterojunctions. Phys. Rev. Lett. **76** (6), 971–974 (1996)
42. P.G. Collins et al., Nanotube nanodevice. Science **278**, 100–103 (1997)
43. D. Tekleab, D.L. Carroll, G.G. Samsonidze, B.I. Yakobson, Strain-induced electronic property heterogeneity of a carbon nanotube. Phys. Rev. B **64**, 035419 (2001)

44. P. Zhang, Y. Huang, H. Gao, K.C. Hwang, Fracture nucleation in SWNT under tension: a continuum analysis incorporating interatomic potential. ASME Trans. J. Appl. Mech. (2002) (in press)
45. H. Bettinger, T. Dumitrica, G.E. Scuseria, B.I. Yakobson, Mechanically induced defects and strength of BN nanotubes. Phys. Rev. B **65**(Rapid Comm.), 041406 (2002)
46. P. Zhang, V.H. Crespi, Plastic deformations of boron-nitride nanotubes: an unexpected weakness. Phys. Rev. B **62**, 11050 (2000)
47. D. Srivastava, M. Menon, K.J. Cho, Anisotropic nanomechanics of boron nitride nanotubes: nanostructured “skin” effect. Phys. Rev. B **63**, 195413 (2001)
48. G.G. Samsonidze, G.G. Samsonidze, B.I. Yakobson, Energetics of Stone-Wales defects in deformations of monoatomic hexagonal layers. Comp. Mater. Sci. **23**, 62–72 (2000)
49. T. Dumitrica, H. Bettinger, B.I. Yakobson, Stone-Wales barriers and kinetic theory of strength for nanotubes. (2002) (in progress)
50. C. Wei, K.J. Cho, D. Srivastava, private communication. xxx.lanl.gov/abs/cond-mat/0202513
51. Y. Zhao, B.I. Yakobson, R.E. Smalley, Dynamic topology of fullerene coalescence. Phys. Rev. Lett. **88**, 185501 (2002)
52. P. Nikolaev et al., Diameter doubling of single-wall nanotubes. Chem. Phys. Lett. **266**, 422 (1997)
53. M. Terrones et al., Coelescence of single-walled carbon nanotubes. Science **288**, 1226–1229 (2000)
54. R. Martel, H.R. Shea, P. Avouris, Rings of single-wall carbon nanotubes. Nature **398**, 582 (1999)
55. B.I. Yakobson, L.S. Couchman. Persistence length and nanomechanics of random coils and bundles of nanotubes. (2002) (submitted)
56. V.M. Harik, Ranges of applicability of the continuum beam models in the mechanics of carbon nanotubes. Solid State Comm. **120**, 331 (2001)

Part II
Modeling and Analysis of Graphene, Nanocomposites and Biomedical Problems

New Trends in Nanoscale Mechanics of Nanostructures, Graphene Sheets and Nanocomposites

Editor's Notes

Vasyl Harik

Abstract Editor's notes first introduce special examples of nanostructures to illustrate a useful nanoscale homogenization criterion. Later editor's notes introduce chapters on graphene sheets, nanocomposites, molecular modeling of nanocomposites and new analysis of safety of carbon nanotubes along with reviews of new studies and applications. A review of a new registry matrix analysis and a nanoscale analog of the Newton's friction law are presented in chapter "Nanomechanics of Graphene Sheets: Registry Matrix Analysis and Interfacial Sliding" along with examples of interfacial sliding of the adjacent graphene sheets. Enhancement of material properties of nanocomposites and their molecular modeling analysis are lucidly presented in chapter "Molecular Mechanics of Polymer Nanocomposites". A new parametric map for geometric parameters of carbon nanotubes and different types of phagocytosis is presented to improve understanding of safety issues in nanotechnology (see chapter "Carbon Nanotubes and Safety," which points out the growing importance of safety in nanotechnology).

Dr. V. Harik, Principal Scientist at Nanodesigns Consulting, a former ICASE Staff Scientist at the NASA Langley Research Center (Hampton, VA), author of a monograph and a short course entitled "*Mechanics of Carbon Nanotubes*" © (2001) presented at the ASME Annual Congress (2001 & 2004) and a co-editor of two Kluwer volumes: "*Trends in Nanoscale Mechanics*" (2003) and "*Micromechanics and Nanoscale Effects*" (2004).

Nanodesigns Consulting is a 2004 spin-off from the NASA Langley Research Center, Hampton, Virginia. Its Staff consulted for the Princeton-based NASA-funded URETI Institute for Nanostructured Bio-inspired Materials (http://bimat.org), National Institute of Aerospace (Hampton, VA), University Space Research Association (USRA) and NASA NAIC (Atlanta, GA).

V. Harik (✉)
Nanodesigns Consulting, P.O. Box 5303, Wilmington, DE 19808-5303, USA
e-mail: Harik@nanodesignconsult.com

V. Harik (ed.), *Trends in Nanoscale Mechanics*, DOI 10.1007/978-94-017-9263-9_5

Introduction

Nanostructured materials such as graphene sheets and nanocomposites are important materials for the latest developments in nanotechnology. This part of the edited volume introduces some novel applications of graphene sheets (see chapter "Nanomechanics of Graphene Sheets: Registry Matrix Analysis and Interfacial Sliding") and the carbon nanotube based polymer composites (see chapter "Molecular Mechanics of Polymer Nanocomposites"). Advances in nanomechanics of graphene sheets (Fig. 1) are illustrated in chapter "Nanomechanics of Graphene Sheets: Registry Matrix Analysis and Interfacial Sliding" by reviewing new methods to control nanoscale sliding of graphene sheets through the registry matrix analysis of interfacial sliding of graphene sheets and a nanoscale analog of the Newton's friction law. The new *effect of the spatial exclusion of electrons (SEE)* during interaction between the spatially-distributed π–π electrons between the adjacent graphene sheets [1] is also reviewed in chapter "Nanomechanics of Graphene Sheets: Registry Matrix Analysis and Interfacial Sliding".

Material properties of graphene sheets have been discussed along with the nanoscale homogenization criterion for graphene sheets, carbon nanotubes and other nanostructures. The data of Fig. 2 can be used to illustrate this *homogenization criteria* [1], *which requires at least ten smallest structural elements for the material properties to reach an invariant size-independent value, i.e., the macroscopic value*. This figure demonstrates that stability of nanorods increases along with their size. It also can be inferred from the data presented that the stability of such nanorods reaches its highest value as soon as their nanoscale structure becomes large enough to include the structural edge cell $(\mathrm{SEC})_{10}$ boundary characterized by a homogenization parameter $X_{10}(E)$. Here, $X_{10}(E) = 0.99$ indicating that a material property (i.e. formation energy) reaches the 99 % of its macroscopic value on the edge of a material consisting of 10 structural elements. The graphene flakes shown in Fig. 1 have not reached the critical size at which their material properties are independent of their size. This illustrates *the intrinsic nanoscale size dependence* of material properties below *the critical size of the ten structural elements or so*.

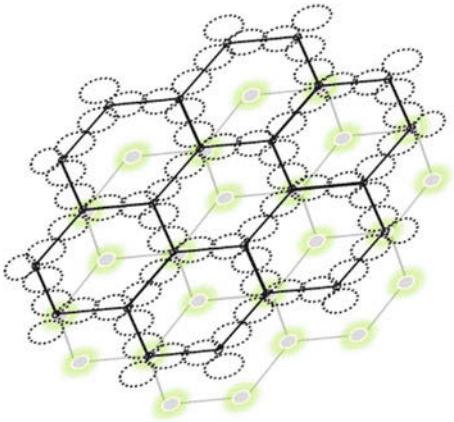

Fig. 1 Schematic of the two graphene lattices in a typical AAA stacking sliding from the incommensurate lattice-lattice registry (after [1])

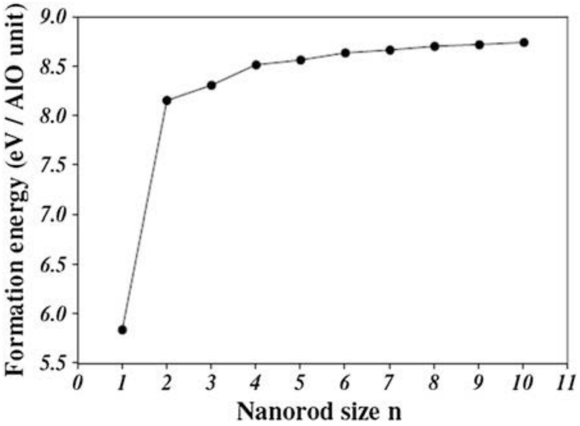

Fig. 2 Dependence of the formation energies of the nanorods as a function of the number of the so called $(AlO)_n$ units [2]. The limiting value of the formation energies is reached after 10 $(AlO)_n$ units on the structural edge boundary with a homogenization parameter $X_{10}(E) = 0.99$, which indicates the 99 % of the macroscopic value for the formation energy

Different materials with the distinct structural elements of varying intrinsic nanoscale properties have a unique $X_{10}(M)$ parameter for each material property, M. Hence, all material properties of a nanostructured material can be characterized by a set of homogenization parameters: $X_{10}(M_1)$, $X_{10}(M_2)$, $X_{10}(M_3)$ or by $X_9(M_1)$, $X_{12}(M_2)$, $X_{11}(M_3)$ and so on. Ideally, each nanostructured material should be characterized by pairs of homogenization parameters, $(X_{10}(M_1), X_{11}(M_1))$, $(X_{10}(M_2), X_{12}(M_2))$ or $(X_{10}(M_3), X_{14}(M_3))$ and so on, where the value of the second homogenization parameter must be always unity, while the number of structural elements may vary for different materials and distinct material properties.

Nanoscale materials, which require less than 10 units to reach the macroscopic value of their material properties, exhibit strong intrinsic tendency to poses those properties. If a number of the minimum structural elements, which is required to reach the macroscopic value of material properties, is greater than 10 than a nanoscale material exhibits a weak intrinsic tendency to poses those properties. In Fig. 2 it is shown that nanorods exhibit intrinsic tendency for the formation energies, which is close to normal since $X_{10}(E) = 0.99$. When nanostructured materials include regions of the size, which is less that *the critical size* associated with the macroscopic properties (see Fig. 3), the material properties of these regions are highly dependent on their local dimensions and the ability to measure the size of distinct local material phases before the process of homogenization (i.e., volume averaging) or the local structural analysis with further multiscale analysis. Meng and Voyiadjis [3] have demonstrated such local regions along with very interesting laminar formations of the so called crystalline ZrN/AlN multilayer (Fig. 3).

The multiscale analysis of complex material systems shown in Fig. 3 can be quite challenging if the nanoscale measurements are not detailed enough or the

Fig. 3 A single crystalline ZrN/AlN multilayer grown on a heteroepitaxial AlN buffer layer. The composition modulation wavelength is 3.4 nm. The dark and bright layers are respectively ZrN and AlN (after Meng and Voyiadjis [3])

subsequent characterization of local and macroscopic material properties is lacking a coherent framework of scaling parameters accompanied by appropriate ranges of applicability of the local models used. In Fig. 3 the nanoscale scale of 2 nm has been provided along with the modulation wavelength of material composition. In Fig. 4 an example of multiscale modeling is presented for a material system of the Si/Si_3N_4 nanopixel with the use of molecular dynamic (MD) modeling and the finite element analysis (FEA), where the MD modeling region represents both atoms and atomic bonds. Note that the MD region involving a graphene sheet is smaller than the critical size of 10 structural elements consisting of carbon rings. Such material system configuration may occur either by a necessity or as a result of manufacturing (as in Fig. 3), which requires multiscale analysis such as shown in Fig. 4.

The multiscale modeling of interfacial regions in nanoscale material systems is also very important for the carbon nanotube based nanocomposites. The use of MD modeling region shown in Fig. 4 is important around embedded nanoscale fibers and thick carbon nanotubes (Fig. 5). Chapter “Molecular Mechanics of Polymer Nanocomposites” presents yet another method for multiscale modeling, i.e., Monte Carlo based molecular mechanics modeling, which takes into account complex molecular structure of interfacial regions in polymer nanocomposites with various inclusions. Carbon nanotube based polymer nanocomposites represent an important group of nanocomposites. The following editor’s notes and chapter “Molecular Mechanics of Polymer Nanocomposites” review some of the latest developments in the nanoscale analysis of nanocomposites.

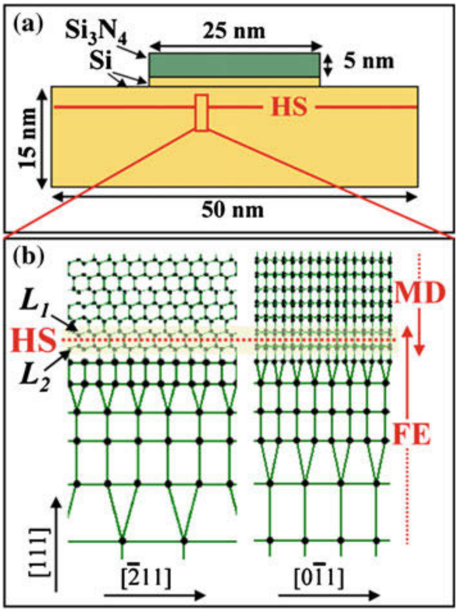

Fig. 4 **a** A schematic of the Si/Si_3N_4 nanopixel. The two dimensional projections shows Si_3N_4 and Si in *green* and *yellow*, respectively. Above and bellow the hand shake (HS) region (denoted by the *red line*), MD and FE apply respectively. **b** Close-up of the HS region and its surroundings in the Si substrate showing 2D views from two different directions. On the *top* is the MD region (*spheres* and *lines* represent atoms and atomic bonds), and on the *bottom* is the FE region (*spheres* and *lines* represent nodes and element boundaries). The *yellow box* marks the HS region in which particles are hybrid nodes/atoms, and the *red dotted line* marks the HS surface (after Voyiadjis, Aifantis and Weber [4])

Fig. 5 Axial stress distribution in polymer matrix: **a** perfect bonding, isostrain, **b** van der Waals bonding, isostrain (after Li and Chou [7])

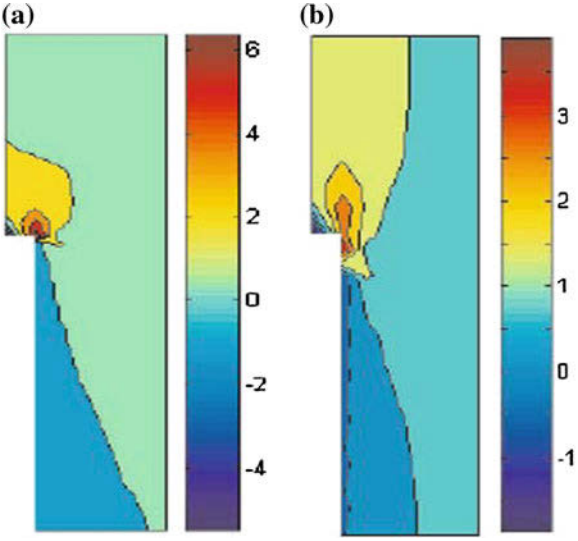

Carbon Inclusions in Polymer Matrix Nanocomposites

Polymer matrix nanocomposites are typically reinforced by carbon fibers, carbon nanotubes [5], graphene multilayers [6], flakes of graphene layers (Fig. 1), carbon nanofibers and other carbon inclusions. Chapter "Molecular Mechanics of Polymer Nanocomposites" shows examples of complex interface regions in polymer matrix nanocomposites, which may include gradients in material properties near interfaces, complex polymer networks and even interphases. In material systems, where there are small or insignificant gradients in material properties near interfacial surfaces, it is important to consider two limiting cases of a classical perfect interfacial bonding and a weak interfacial bonding [8] or the nanoscale weak bonding by van der Waals forces [7, 8]. For these types of cases Li and Chou [7] have used the so called structural molecular mechanics approach for the nanoscale finite element analysis of carbon nanotube polymer matrix composites (Fig. 5). In their study the stress distributions have been examined in the unit cell having the width, w, such that $w/R = 5$, where R is the radius of inclusion, R. They have shown that the stress concentration near the nanoscale inclusions with van der Waals bonding is lower than that near the perfectly bonded inclusions.

It should be mentioned that at nanoscale level there is no 100 % perfect bonding. There is a very strong covalent bonding between nanoscale inclusions and the structural elements of a matrix material. The covalent bonding or rather the high density covalent bonding is a close approximation for the perfect bonding in the classical sense. In practice, however, it is very hard to achieve the high density covalent bonding (Fig. 6). The density of covalent density at the interfaces depends on a number of factors such processing methods, chemical systems involved, local stoichiometry and the processing conditions. Nevertheless, the assumption of the perfect bonding is a very important and useful limiting case in the multiscale analysis of nanostructured materials.

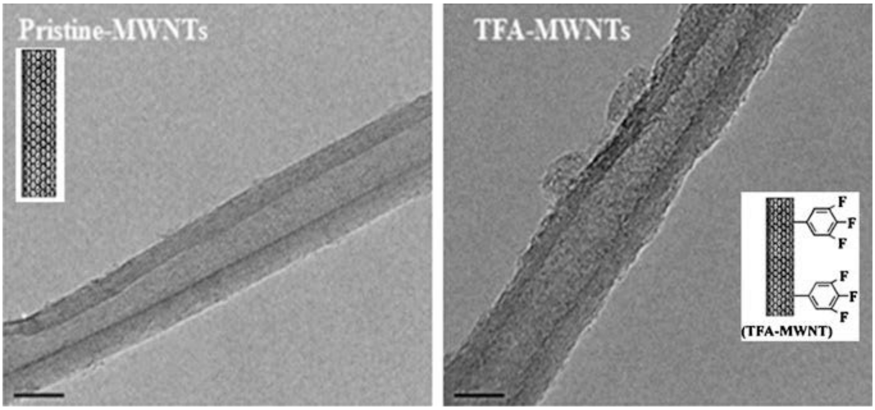

Fig. 6 Images of pristine and functionalized multiwall carbon nanotubes (MWNTs) by Trifluoroaniline (after [9]). Images are obtained by transmission electron microscope (TEM)

Nanoscale finite element analysis of Li and Chou [7] can also serve as a useful albeit limited guide (Fig. 5) for the case of nanocomposites with the semi-rectangular graphene platelets as reinforcing inclusions. One should remember the differences between the more confined case of cylindrical symmetry and the more open two-dimensional geometry. Chapter "Nanomechanics of Graphene Sheets: Registry Matrix Analysis and Interfacial Sliding" presents new results on interfacial properties of graphene sheets and the phenomena associated with the shearing deformation of graphene platelets of semi-rectangular form. Shearing deformation of nanoscale inclusions depends on nanoscale interfacial sliding between adjacent graphene sheets. Reinforcement of material properties in nanocomposites, which is reviewed in chapter "Molecular Mechanics of Polymer Nanocomposites", is affected by the interfacial properties and the molecular structure in the interfacial region near nanoscale inclusions. Interfacial phenomena are further discussed below and in all of the following chapters: for graphene sheets in chapter "Nanomechanics of Graphene Sheets: Registry Matrix Analysis and Interfacial Sliding", for polymer nanocomposites in chapter "Molecular Mechanics of Polymer Nanocomposites" and for the engulfment of carbon nanotubes in macrophages in chapter "Carbon Nanotubes and Safety". Safety of Nanotechnology is very important.

Carbon Nanotube/Polymer Interfaces in Nanocomposites

The nanotube/polymer interface plays an important role in the stress transfer in nanocomposites. The strength of interfacial adhesion depends on the surface area of the nanotube/polymer interface (see chapter "Molecular Mechanics of Polymer Nanocomposites"), its roughness (Fig. 6), interlocking of asperities and molecular bonding of the nanoscale interface [1, 8, 9]. Carbon nanotube surface can be modified by surfactants, nanoscale particles (e.g., oxide and nitride ceramics or graphene flakes) and the molecular chains capable of covalent bonding or van der Waals bonding by the aromatic units composed of carbon rings. Mechanical property measurements [10] of ceramic nanocomposites after the addition of 0.1 wt% of carbon nanotubes (CNTs) in the alumina have shown the increased fracture toughness by about 1.6 times from 3.7 to 4.9 MPa $m^{1/2}$. For 1 wt% CNTs/$BaTiO_3$ composite [10], the toughness value (1.65 MPa·$m^{1/2}$) is about 2.4 times than that of pure $BaTiO_3$ (0.68 MPa·$m^{1/2}$) (Fig. 7). Chapter "Nanomechanics of Graphene Sheets: Registry Matrix Analysis and Interfacial Sliding" presents a review of nanoscale sliding properties of graphene flakes, which also can improve toughness properties of the fiber-reinforced ceramic matrix nanocomposites by tailoring their layered interfacial properties.

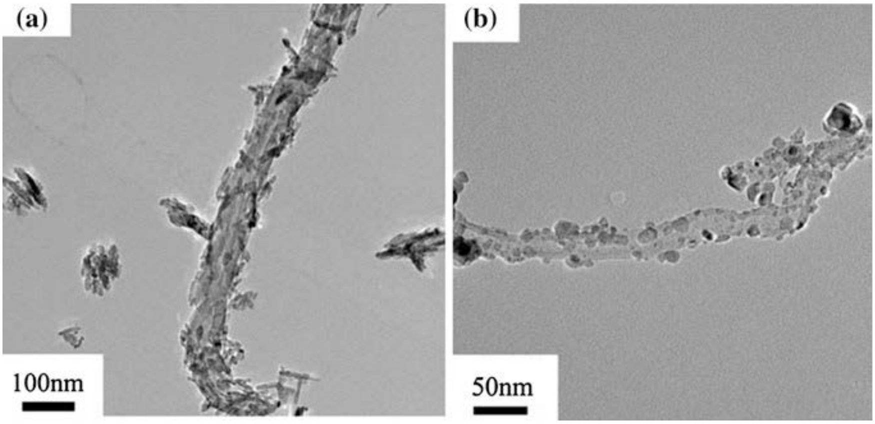

Fig. 7 TEM image of **a** rod-like TiO_2 nanoparticles on a carbon nanotube (CNT) and **b** tiny TiO_2 nanoparticles on CNTs (after [10])

Molecular Modeling of the Carbon Nanotube/Polymer Interfaces

Molecular modeling of the carbon nanotube/polymer interfaces allows to examine nanoscale surface interactions at more details. Chapter "Nanomechanics of Graphene Sheets: Registry Matrix Analysis and Interfacial Sliding" introduces new results in nanomechanics of graphene sheets, which are used both for nanoscale electronic devices and for nanocomposites with polymer and ceramic matrices. The following examples of novel methods to tailor interfacial properties on molecular level are presented here to motivate both chapters "Nanomechanics of Graphene Sheets: Registry Matrix Analysis and Interfacial Sliding" and "Molecular Mechanics of Polymer Nanocomposites", where molecular modeling is used to enhance material properties of nanocomposites. Figures 8 and 9 illustrate molecular modeling of the non-covalent and covalent adsorption of alanine and alanine radicals onto the surface of a (5, 0) zig-zag single-walled carbon nanotube using the first principles calculations [11]. The π-electron interactions have been shown to play a significant role in the non-covalent absorption with the functional group close to the carbon nanotube surface naturally has a significant influence on the binding strength and the associated interactions.

Results of non-covalent functionalization of carbon nanotubes with alanine have shown that such functionalization enhances the conductivity of a (5, 0) zig-zag nanotube [11]. In the case of covalent adsorption of alanine radicals onto the surface of a carbon nanotube, the alanine-nanotube binding energy depends on the local lattice configuration at an adsorption site and on the type of electronegative atom (e.g., a strong amine group) that binds with the nanotube. Chapter "Nanomechanics of Graphene Sheets: Registry Matrix Analysis and Interfacial Sliding" presents other methods of analysis of different lattice configurations in the surface-surface sliding

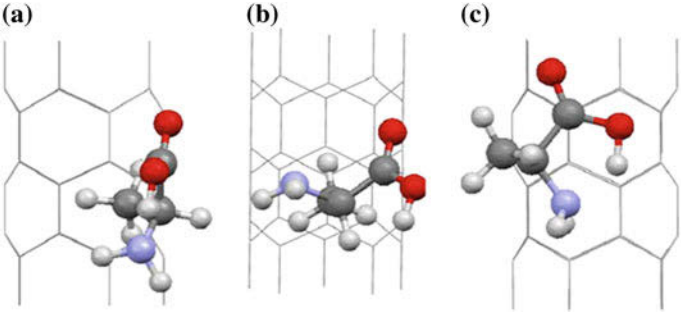

Fig. 8 Noncovalent adsorption of alanine on a (5, 0) zig-zag carbon nanotube (CNT): **a** $C_{50}ACH_3$-I, **b** $C_{50}ACH_3$-II and **c** $C_{50}ANH_2$-I (after [11])

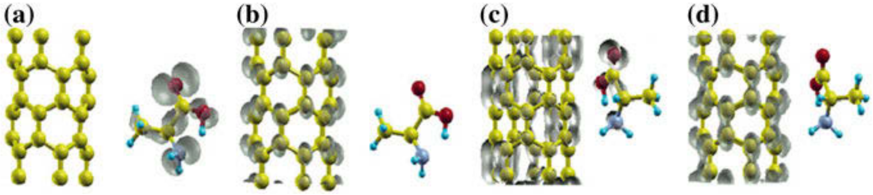

Fig. 9 Molecular modeling of interfacial interactions with a (5, 0) CNT [11]: **a** Highest occupied molecular orbital (HOMO) of a conformer $C_{50}ACH_3$-I (E = −0.12 eV). **b** Lowest unoccupied molecular orbital (LUMO) of a conformer $C_{50}ACH_3$-I (E = 0.38 eV). **c** The HOMO of a conformer $C_{50}ANH_2$-II (E = −0.23 eV). **d** The LUMO of a conformer $C_{50}ANH_2$-II (E = 0.25 eV)

interactions within the framework of registry potentials and the registry matrix analysis. Non-covalent interactions in the absorption of alanine onto a zig-zag (5, 0) carbon nanotube also occur within the lattice registry potentials, however, they are analyzed by the charge density analysis. In the highest occupied molecular orbital (HOMO) of the conformer $C_{50}ACH_3$-I (Fig. 9a), the charge is distributed over the alanine homogeneously. The resulting electrostatic interaction with carbon nanotube is one of the most stable among the conformers.

The covalent bonding illustrated in Fig. 10 [11] is associated with the so called perfect bonding or perfect adhesion in the classic micromechanics of composite

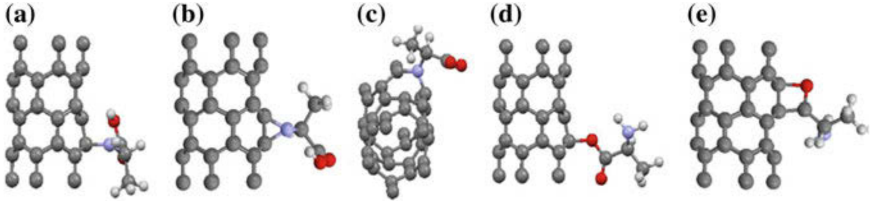

Fig. 10 Molecular modeling of covalent absorption [11]: **a**–**e** Covalent adsorption of alanine radicals onto a (5, 0) zig-zag carbon nanotube with **a** $C_{50}ANH$-I, **b** $C_{50}AN$-I, **c** $C_{50}AN$-II, **d** $C_{50}ACOO$-I and **e** $C_{50}ACO$-I

materials [1], which is examined in great details in chapter "Molecular Mechanics of Polymer Nanocomposites" of this edited volume. Molecular modeling, which is shown in Figs. 8, 9 and 10, and the examples included in the earlier editor's notes provide good illustrations for the molecular mechanics modeling of polymer nanocomposites [12–14] presented in chapter "Molecular Mechanics of Polymer Nanocomposites". The modeling techniques and the new research reviewed in chapter "Molecular Mechanics of Polymer Nanocomposites" are based on the powerful Monte Carlo methods.

References

1. V.M. Harik, *Mechanics of Carbon Nanotubes* (Nanodesigns Press, Newark, 2011)
2. X. Song, Q. Ge, S.C. Yen, An ab-initio study of mechanical behavior for $(AIO)_n$ nanorods, ed. by T. J. Chuang et al., in *Nanomechanics of Materials and Structures* (Springer, Berlin, 2006), pp. 23–32
3. W.J. Meng, G.Z. Voyiadjis, Structure and mechanical properties of ceramic nanocomposite coatings, Chapter 4 in *Trends in Nanoscale Mechanics* ed. by V.M. Harik, M.D. Salas (Kluwer Academic Publishers, The Netherlands, 2003), pp. 89–120
4. G.Z. Voyiadjis, E.C. Aifantis, G.Weber, Constitutive modeling of plasticity in nanostructured materials, Chapter 5 in *Trends in Nanoscale Mechanics* ed. by V.M. Harik, M.D. Salas (Kluwer Academic Publishers, The Netherlands, 2003), pp. 123–146
5. Z. Ounaies, C. Park, K.F. Wise, E.J. Siochi, J.S. Harrison, Electrical properties of single wall carbon nanotube reinforced polyimide composites. Compos. Sci. Technol. **63**, 1637–1646 (2003)
6. S. Stankovich, D.A. Dikin, G.H.B. Dommett, K.M. Kohlhaas, E.J. Zimney, E.A. Stach, R.D. Piner, S.B.T. Nguyen, R.S. Ruoff, Graphene-based composite materials. Nature **442**(20), 282–286 (2006)
7. C.Y. Li,T.-W. Chou, Multiscale modeling of the interfacial load transfer in carbon nanotube/polymer composites, J. Nanosci. Nanotech. **3**, 423–430 (2004)
8. S.J.V. Frankland, V.M. Harik, Surf. Sci. Lett. **525**, L103–L108 (2003)
9. S.K. Yadav, S.S. Mahapatra, J.W. Cho, H.C. Park, J.Y. Lee, Fibers Polym. **10**(6), 756–760 (2009)
10. L. Gao, L. Jiang, J. Sun, J. Electroceram. **17**, 51–55 (2006)
11. M. Rajarajeswari, K. Iyakutti, Y. Kawazoe, J. Mol. Model. **18**, 771–781 (2012)
12. C.Y. Li, T.-W. Chou, Modeling of carbon nanotubes and their composites, in *Nanomechanics of Materials and Structures*, ed. by T.J. Chuang et al. (Springer, Berlin, 2006), pp. 55–65
13. S.J.V. Frankland, V.M. Harik, Mat. Res. Soc. Symp. Proc. **733 E**, T6.2.1 (2002)
14. V.M. Harik, R.A. Cairncross, Mech. Mater. **32**, 807 (2000)

Nanomechanics of Graphene Sheets

Registry Matrix Analysis and Interfacial Sliding

Vasyl Harik

Abstract This chapter reviews basic structure of graphene sheets, interfacial sliding between adjacent graphene sheets, a nanoscale analog of the Newton's friction law, registry effects between adjacent graphene sheets and their atomic lattices, registry matrices to describe interfacial registry in graphene stacking and the registry matrix analysis for the sliding of graphene sheets in nanoscale electronic devices. Interfacial sliding of graphene sheets depends on the interfacial registry potentials and the so called *effect of the spatial exclusion of electrons (ESEE)* at the interface of two graphene sheets, which can be viewed as the nanoscale analog of *Pauli's exclusion principle*. Understanding of nanoscale sliding phenomena is critical for improving manufacturing technology for the single layer graphene sheets in nanoelectronic devices. Interfacial sliding between adjacent graphene sheets has been also described by a nanoscale analog of the Newton's friction law for the nanoscale surface sliding mechanics and the associated stiction effects. Understanding of nanoscale sliding helps nanoscale cleaning and safety.

Dr. V. Harik, f. ICASE Staff Scientist at the NASA Langley Research Center (Hampton, VA), Principal Scientist at Nanodesign Consulting, author of a monograph and a short course entitled "*Mechanics of Carbon Nanotubes*" © (2001) presented at the Annual ASME Congress (2001 and 2004) and a co-editor of Kluwer volumes: "*Trends in Nanoscale Mechanics*" (2003) and "*Micromechanics and Nanoscale Effects*" (2004).

Nanodesigns Consulting is a 2004 spin-off from the NASA Langley Research Center, Hampton, Virginia. Its Staff consulted for the Princeton-based NASA-funded URETI Institute for Nanostructured Bio-inspired Materials (http://bimat.org), National Institute of Aerospace (Hampton, VA), University Space Research Association (USRA) and NASA NAIC (Atlanta, GA). Nanodesigns Consulting also works on safety of nanotechnology.

V. Harik (✉)
Nanodesigns Consulting, P.O. Box 5303, Wilmington, DE 19808-5303, USA
e-mail: Harik@nanodesignconsult.com

V. Harik (ed.), *Trends in Nanoscale Mechanics*, DOI 10.1007/978-94-017-9263-9_6

Introduction

Graphene sheets have periodic hexagonal structure made of carbon atoms arranged into hexagonal carbon rings (Fig. 1). Stacks of graphene sheets are a part of commonly used pencils, which are sometimes wrongfully called lead pencils. Exfoliation of graphite has been a long challenge [1, 2]. Graphene has exceptional properties in the form of single-layer graphene sheets, which are similar to the properties of carbon nanotubes with their lattice structure made of carbon rings. Single graphene sheets have remarkable electronic properties, for example, the unique quantum Hall effect [1–4] and the noteworthy band gap-width dependence [5, 6]. Graphene properties such as electric conductivity and Young's modulus depend on the minimum length or size of graphene sheets, i.e., the minimum number of carbon rings along its length as was noted for carbon nanotubes [7, 10]. The lattice structure of graphene sheets can be described and analyzed with respect to its structural characteristics by using the scaling analysis, which is based on examination of the physical length scales and the structure of edges of graphene nanoribbons (Fig. 1).

Size Effects in the Material Properties of Graphene Sheets

The uniqueness of average material properties of graphene sheets depends on the size of graphene sheets. The uniqueness of averaging (or nanoscale homogenization) of material properties over an extended surface requires that the size of a graphene sheet, L, is much greater than the size of the carbon ring, its smallest structural element, $a = 2.46\ \mathring{A}$ [7–10], i.e.

$$L \gg a, \quad or \quad L/a \gg 1. \tag{1}$$

The nanoscale homogenization of graphene properties depends on the minimum length at which the size-invariant value is reached (i.e., the minimum number of carbon rings along its length as has been noted for the carbon nanotubes [7, 10]). Note that a graphene sheet can satisfy the homogenization criterion (1) for the uniquely-defined material properties in longitudinal dimension and be transversely smaller than the minimum length: L_{min} In general, the scaling dependence for the uniquely-defined size-invariant value, P_h, of a material property, P, is given by the nanoscale re-normalization relation:

$$P = P_h(1 \pm \frac{a}{L_h - L}), \quad \text{or} \quad P = P_h\left[1 \pm \left(\frac{L_h}{a} - \frac{L}{a}\right)^{-1}\right] \tag{2}$$

where a is an atomic lattice constant or the smallest structural element of a nanostructured material and L_h ($L_h \approx L_{min}$) is the size of a homogenized material at

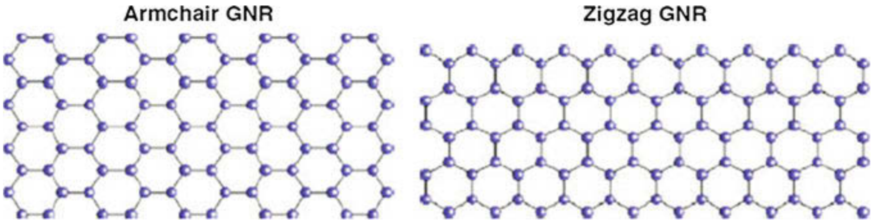

Fig. 1 Lattice structure of graphene sheets with the armchair and zig-zag edges and graphene nano-ribbons (GNR) (after [5])

which the size-invariant value, P_h of the volume-or the surface-averaged material property is reached (or the 95 % of its value, 0.95 P_h, at the minimum size: $L_{min} < L_h$ from below: "–" sign, or from above: "+" sign). The nanoscale re-normalization formula (2) can be written for various material properties [7–16].

The atomic lattice structure of the graphene sheets can be described by the (n,m) nomenclature illustrated in Fig. 2. The two unit vectors, $\boldsymbol{a_1}$ and $\boldsymbol{a_2}$, are defined at the origin (0, 0). The width of a graphene sheet along the unit vector, $\boldsymbol{a_1}$, can be measured in the units of the carbon ring size, $a = 2.46\ \AA$, i.e., $L = 2.5a$ for the graphene flake shown in Fig. 2. In the orientation of the unit vector, $\boldsymbol{a_1}$, the shown graphene flake has the so called *zig-zag* configuration. In the orientation perpendicular to the unit vector, $\boldsymbol{a_2}$, the shown graphene flake has the so called *armchair* configuration and the size, $L = 3a$.

Fig. 2 Schematic of the graphene sheet made of the carbon rings of six carbon atoms with the σ-electrons along the C–C bonds of length, $l_{C\text{–}C} = 1.42\ \AA$. The (n, m) nomenclature is defined by the two unit vectors, $\boldsymbol{a_1}$ and $\boldsymbol{a_2}$, at the origin (0, 0)

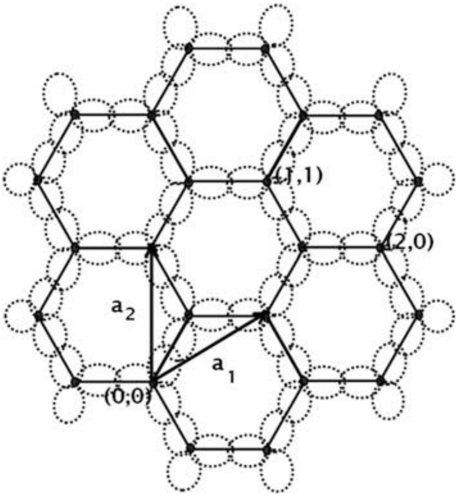

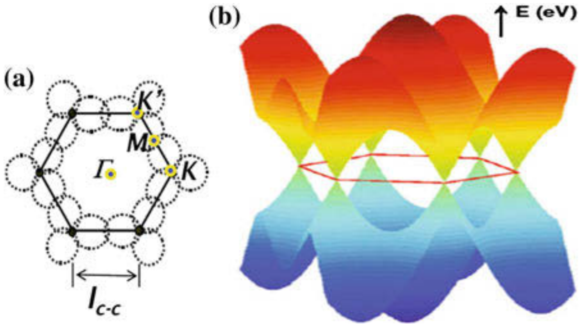

Fig. 3 Schematic of the carbon ring of six carbon atoms with the schematically-shown σ-electrons **a** with the approximate size of the spatial energy distribution of the π-electrons **b** distributed over covalent C–C bonds and the interior of a carbon ring (after [5]). (H. Raza (ed.), *Graphene Nanoelectronics*, NanoScience and Technology, Springer, 2012)

Electron Energy and the Registry Potentials of Graphene Lattice

The atomic lattice structure of graphene nano-ribbons shown in Fig. 2 is made of the carbon rings of six carbon atoms in the sp^2 bonding between σ-electrons schematically shown in Fig. 3a. The spatially distributed electrons cover the entire surface area of the carbon rings, with the σ-electrons forming the elastic C–C bonds and the out-of-plane π-electrons distributed over the C–C bonds and the interior area of carbon rings (Fig. 3b). Distribution of the energy of states for the out-of-plane π-electrons has its high points right above the midpoint of each C–C bond (i.e., M-point of the so called *Brillouin zone*,[1] which is marked by the ΓK′K area of the carbon ring, Fig. 3a). The highest value of the energy of states is in the center of the carbon ring (i.e., the Γ-point of the Brillouin zone) and its lowest zero-points are at the position of each carbon atom (i.e., the K-point of the Brillouin zone, Fig. 3a):

Distribution of the energy of states $E_G(k)$ for electrons in graphene shown in Fig. 3b can be described by

$$E_{\mathrm{G}}(k) = \pm t\sqrt{1 + 4\cos\left(\frac{3k_x a_{\mathrm{cc}}}{2}\right)\cos\left(\frac{\sqrt{3}k_y a_{\mathrm{cc}}}{2}\right) + 4\cos^2\left(\frac{\sqrt{3}k_y a_{\mathrm{cc}}}{2}\right)},$$

where k_x and k_y are the x- and y-components of the wave vector k, a_{cc} is the length of the C–C bond and t is the first nearest-neighbor tight binding parameter [17]. The concave top of the π-electrons energy of states distribution is deformed into the 6-

---

[1] The so called Brillouin zone is used to schematically represent the energy dispersion relation for the energy of states of the graphene lattice vibration waves, i.e., *phonons*, and the energy of states of the oscillating electrons.

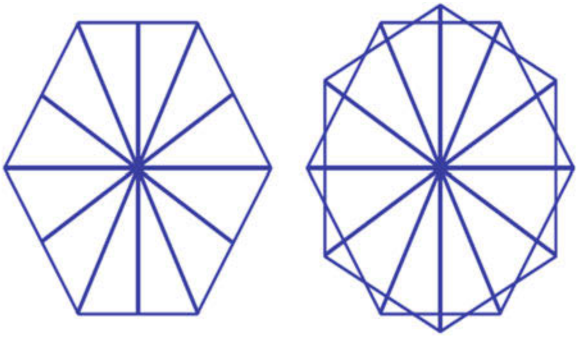

Fig. 4 Schematic of the geometric symmetry of the six Brillouin zones within the carbon ring (*left*) and a schematic of the 6-fold dome (or the B-modulation dome) of the approximate experimental energy distribution of the π-electron states (i.e., the π-electrons density) with the 12 radial modulation toward the six K and the six M points around the center of the carbon ring (*right*), which is the **Γ** point of all six Brillouin zones (after [23])

fold dome by the 12 radius modulations pointing toward the six K- and the six M-points with the *π/6* period of the π-electron density modulation around the center of the carbon ring (Fig. 4), which contributes to the registry potential.

The energy of states for the *π*-electrons distributed over the center of the carbon ring (the *Γ*-point) scales with the energy for the near-neighbor hoping, E_h, (the M-point) as 88/33 or 2.6(6) with respect to the Fermi free energy, E_F, and as 2.93 or ∼3 with respect to the Dirac energy, E_D. The angular modulation of the *π*-electrons energy of states has lower values along the directions pointing toward the six M-points with the energy level of 3.3 *eV* (i.e., the six-fold dome with the angular period of *π/6* for the *π*-electron density modulation around the center of the carbon ring).

Lattice Registry Configurations for Graphene Sheets

Atomic lattice structure of graphene typically involves the so called AAA or ABA stacking of graphene sheets [5, 23] as well as other types of registries between two atomic lattices of graphene sheets:

- the Φ- and the Θ-registry (Figs. 5a and b) between a C–C bond and a carbon ring akin to the O-registry of a carbon atom;
- the Y-registry of a carbon atom and three C–C bonds and the opposite carbon ring, i.e., the complete Y-O registry is the symmetric rhombic registry (Fig. 5c).

A typical ABA stacking of the commensurate graphene sheets consists of the adjacent graphene lattices arranged so that a carbon atom of one graphene sheet is positioned right over the center of the opposite carbon ring (i.e., the C-atom/C-ring registry or the Y-O registry, Fig. 5c). In the Y-O registry, the three carbon atoms are positioned right above the carbon atoms of the opposite graphene sheet in the

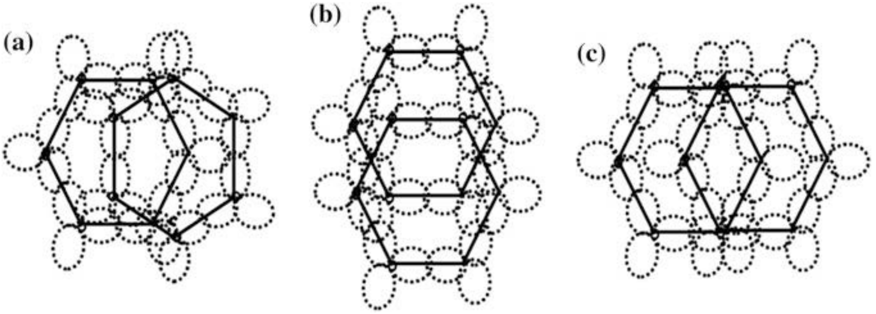

Fig. 5 Schematics of the Φ-registry (**a**) and the Θ-registry (**b**) between the C–C bond of two carbon atoms and a carbon ring of six carbon atoms and the rhombic registry (**c**), i.e. complete Y-O registry of the ABA stacking, and the incomplete companion Y-registry next to the Φ-registry **a** between a carbon atom and a carbon ring (i.e., the C-atom/C-ring registry; after [23])

incommensurate positions and the other three carbon atoms are positioned above the centers of carbon rings as asperities.

In the case of incommensurate AAA stacking of the graphene sheets, all six carbon atoms are positioned right above their counterparts in the full ring-ring registry (or the O-O registry) with the opposite carbon rings being a little further from the opposite atomic lattice as compared to the ABA stacking. The projections of the C–C bonds between the adjacent graphene lattices of the AAA stacking coincide in the O-O registry unlike in the case of the ABA stacking of the commensurate graphene sheets.

Note that the in-plane distance between the two carbon atoms and the nearest C–C bond in the Φ-registry (Fig. 5a) is slightly less than the Bohr radius,[2] $a_0 = 0.529$ *Å*. The typical van der Waals distance between two adjacent graphene sheets is *3.35 Å*. The distance between two carbon atoms and the carbon atom on the two sides in the Θ-registry (Fig. 5b) is exactly one half of the elastic C–C bond, $l_{C-C}/2$, i.e., *0.71 Å*. The distance between these two atoms and the nearest C–C bond is exactly *a/2* or *1.23 Å*. The companion complete Y-O registry (Fig. 5c) is the most stable. The energy barrier for a π-electron to pass through the X-registry (Figs. 5b and 6c) between an electron and the opposite C–C bond is about *3.3 eV* at the M-point of the so called *Brillouin zone* for the energy of states in a carbon ring.[3] The X-registries are unstable.

---

[2] The Bohr radius, $a_0 = 0.529$ *Å* is the most probable distance between a proton and an electron in the Hydrogen atom according to the Bohr's planetary model of an atom.

[3] The onset of the Ψ-registry configuration (Fig. 6a) is associated with the need of a π-electron to overcome the registry potential of the C–C bond and the associated Coulomb repulsion within the electron spatial exclusion (ESE) zone (see Harik [16]). The size of the ESE zone depends on the local atomic lattice configuration, the registry potential barriers, the nanoscale Coulomb repulsion proportional to $1/r^2$, and the nanoscale repulsion proportional to $1/r^{12}$. The combined effect results in the so called *SEE effect*. The nanoscale analog of Pauli exclusion of electrons is similar to the quantum Pauli principle for the identical particles with the spin ½ (*fermions*); the two identical

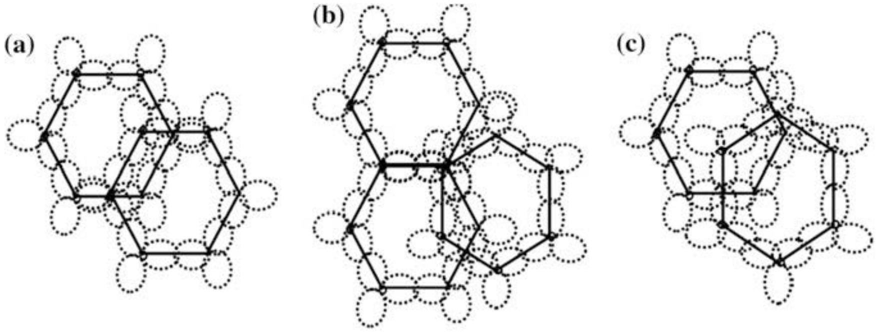

Fig. 6 Schematics of the ψ-registry (**a**) between a carbon atom and the C–C bond, an incomplete Y-registry (**a**), (**b**) and (**c**) between a carbon atom and the C-ring and the X- or the "+" registry (**c**) between two elastic C–C bonds of the two carbon rings (after [23])

The in-plane distance between all carbon atoms in the ψ-registry (Fig. 6a) along the C–C bonds is exactly one half of the elastic C–C bond, $l_{C-C}/2$. The same is true for all atoms involved in the X- or the "+" registry between two C–C bonds (Fig. 6c). In the X-registry between two C–C bonds, two out of six carbon atoms are positioned in the incomplete Y-registry, i.e., the opposite carbon atoms of the two graphene sheets are located almost above each other in the incomplete incommensurate positions as opposed to the O-O registry of the AAA stacking and the Y-O registry of the ABA stacking with the six and three carbon atoms in the incommensurate locations (i.e., the complete Y-registry). The full (six-six) and the partial incommensurate atom configurations of Y-registries are prone to sliding as they are less stable than the complete Y-O registry.

Matrix Analysis for the Lattice Registry of Graphene Sheets

Theatomic lattice structure of graphene sheets consists of carbon rings of six carbon atoms, which can be identified by six indices with the top left carbon atom being the first (Fig. 7), the top right carbon atom being the second in the top C–C bond, the third and the sixth carbon atoms are below on the right and on the left, and the forth and the fifth carbon atoms are in the bottom C–C bond. The lattice registry of two adjacent carbon rings can be described as follows [23]. When the two carbon rings with the corresponding atoms are directly on top of each other in the O-O registry of the AAA stacking, then the O-O lattice registry of their atoms can be described by

---

(Footnote 3 continued)
particles cannot occupy the same energy state, as their combined wave function, ψ, is anti-symmetric. The nanoscale Coulomb repulsion, the nanoscale SEE repulsion and the quantum Pauli principle for the electrons all affect precise dimensions of the ESE zone.

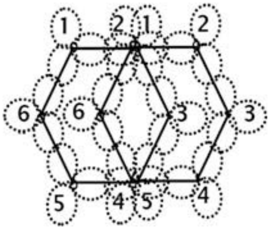

Fig. 7 Schematic of the Y-O registry of two carbon rings described by the integer indices identifying carbon atoms in clockwise direction along the C–C bonds and the corresponding locations in the registry matrix R_{YO} (after [23])

the pairs of indices (1,1), (2,2), (3,3), (4,4), (5,5) and (6,6). These pairs of indices can form a registry matrix for the O-O lattice registry with the presence of a carbon atom in a certain position of the lattice registry described by a pair of indices is indicated by a unity, 1. For the O-O lattice registry, the corresponding registry matrix R_{OO} for two graphene sheets will have 2 for the two carbon atoms being in the same registry position on top of each other and the bond registry coefficient b for the C–C bonds in the (1,2) and (2,1), (2,3) and (3,2), (3,4) and (4,3), (4,5) and (5,4), (5,6) and (6,5) registry positions [23]:

$$R_{OO} \equiv \begin{pmatrix} 2 & b & 0 & 0 & 0 & 0 \\ b & 2 & b & 0 & 0 & 0 \\ 0 & b & 2 & b & 0 & 0 \\ 0 & 0 & b & 2 & b & 0 \\ 0 & 0 & 0 & b & 2 & b \\ 0 & 0 & 0 & 0 & b & 2 \end{pmatrix}$$

forming a well-structured diagonal registry matrix for the O-O lattice registry.

The registry matrix for the Y-O lattice registry of the atomic lattices of graphene sheets in the ABA stacking is formed in a similar way [23]. The lattice registry positions identified by the pairs of indices (1,1), (2,2), (3,3), (4,4), (5,5), (6,6) and the corresponding terms in the registry matrix identified by the same pairs of indices describe the presence of one carbon atom by a unity, 1. In the Y-O lattice registry of the ABA stacking the C–C bonds do not have overlapping registry. Therefore, the registry matrix R_{YO} does not include the bond registry coefficient b. This registry matrix has a partial diagonal structure. A unity in the registry matrix position identified by the pair of indices (6,1) means that over the registry location of the sixth atom of a carbon ring in the bottom graphene sheets there is the first carbon atom from the top graphene sheet. Similarly, the pairs of indices (2,1) and (4,5) identify the pairs of carbon atoms in the lattice registry. The pairs of indices identify both the position in the registry matrix and the indices of carbon atoms from the two adjacent graphene sheets that are in that lattice registry [23]:

$$R_{YO} \equiv \begin{pmatrix} 1 & 0 & 0 & 0 & 0 & 0 \\ 1 & 1 & 0 & 0 & 0 & 0 \\ 0 & 0 & 1 & 0 & 0 & 0 \\ 0 & 0 & 0 & 1 & 1 & 0 \\ 0 & 0 & 0 & 0 & 1 & 0 \\ 1 & 0 & 0 & 0 & 0 & 1 \end{pmatrix}$$

A sum of the registry matrix row elements gives the number of carbon atoms that are in the lattice registry positions. A single unity in a row means that there is no registry with that particular carbon atom, which is identified by a unity. The presence of the bond registry coefficient b in the registry matrix R_{OO} indicates that the C–C bonds have overlapping registry. The registry matrix R_{ψ} has the partial bond registry coefficient b_{ψ} and the atom-bond registry described by the sum of unity and the atom-bond registry coefficient a_{ψ} [23]:

$$R_{\Psi} \equiv \begin{pmatrix} 1 + a_{\Psi}b_{\Psi} & b_{\Psi} & 0 & 0 & 0 & 0 \\ b_{\Psi} & 1 & 0 & 0 & 0 & 0 \\ 0 & 0 & 1 + a_{\Psi}b_{\Psi} & 0 & 0 & 0 \\ 0 & 0 & 0 & 1 & b_{\Psi} & 0 \\ 0 & 0 & 0 & b_{\Psi} & 1 + a_{\Psi}b_{\Psi} & 0 \\ 0 & 0 & 0 & 0 & 0 & 1 \end{pmatrix}.$$

The registry matrix R_{Θ} for the Θ-registry (Fig. 5b) has the following form [23]:

$$R_{\Theta} \equiv \begin{pmatrix} 1 & 0 & 0 & 0 & 0 & b_{\Theta} \\ 0 & 1 & b_{\Theta} & 0 & 0 & 0 \\ 0 & b_{\Theta} & 1 & b_{\Theta} & 0 & 0 \\ 0 & 0 & b_{\Theta} & 1 & 0 & 0 \\ 0 & 0 & 0 & 0 & 1 & b_{\Theta} \\ b_{\Theta} & 0 & 0 & 0 & b_{\Theta} & 1 \end{pmatrix},$$

where the bond overlap coefficient b_{Θ} denotes the bond overlap registry between two carbon rings of the two adjacent graphene sheets.

Matrix Analysis of the Inter-Registry Sliding in Graphene

Graphene sheets can easily slide off one another as in graphite pencils. Understanding of nanoscale details of the sliding process for individual graphene sheets and their parts can be achieved by examining the lattice registry of individual carbon rings and their sliding from one lattice registry to another. The inter-registry sliding of a graphene sheet on the graphene surface between two lattice registries can be described by the inter-registry matrices, which link one registry matrix with another matrix and its lattice registry through an operation of the matrix addition, e. g., $R_{\Theta} + \Delta R_{\Theta,OO} = R_{OO}$, where the inter-registry matrix $\Delta R_{\Theta,OO}$ is given by

$$\Delta R_{\Theta,OO} \equiv \begin{pmatrix} 1 & b & 0 & 0 & 0 & -b_{\Theta} \\ b & 1 & b-b_{\Theta} & 0 & 0 & 0 \\ 0 & b-b_{\Theta} & 1 & b-b_{\Theta} & 0 & 0 \\ 0 & 0 & b-b_{\Theta} & 1 & b & 0 \\ 0 & 0 & 0 & b & 1 & b-b_{\Theta} \\ -b_{\Theta} & 0 & 0 & 0 & b-b_{\Theta} & 1 \end{pmatrix}$$

with the aforementioned bond registry coefficient b and the partial bond registry coefficient b_{Θ} [23]. The O-O lattice registry of two carbon rings in the AAA stacking is easily perturbed into the Θ-registry through the inter-registry sliding described by the inter-registry matrix $\Delta R_{\Theta,OO}$ and the inter-registry sliding equation:

$$R_{OO} - R_{\Theta,OO} = R_{\Theta},$$

The Ψ-registry of two graphene sheets can be easily achieved from the O-O lattice registry through the inter-registry sliding described by the inter-registry matrix $\Delta R_{OO,\Psi}$ [23]:

$$\Delta R_{OO,\Psi} \equiv \begin{pmatrix} -1+a_{\Psi}b_{\Psi} & b_{\Psi}-b & 0 & 0 & 0 & b_{\Psi} \\ b_{\Psi}-b & -1 & -b & 0 & 0 & 0 \\ 0 & -b & -1+a_{\Psi}b_{\Psi} & -b & 0 & 0 \\ 0 & 0 & -b & -1 & b_{\Psi}-b & 0 \\ 0 & 0 & 0 & b_{\Psi}-b & -1+a_{\Psi}b_{\Psi} & -b \\ b_{\Psi} & 0 & 0 & 0 & -b & -1 \end{pmatrix}.$$

These inter-registry sliding processes can be very useful in the design of the graphene based electronic devices.

Nanoscale Friction and Interfacial Sliding of Graphene Sheets

At the nanoscale level, the fundamental origins of sliding friction involve surface-to-surface interactions such as the interlocking and registry effects [17–26] between the adjacent graphene sheets (Fig. 8), the sliding induced excitation of the atomic lattice vibrations, i.e., *phonons* [22], interaction of phonons [27] propagating along the sliding surfaces [28, 29], electrostatic interactions and interactions of electrons including but not limited to the $\pi - \pi$ bonding interactions [30–32], especially, those involving aromatic ring structures. Some of these interfacial friction mechanisms have been studied by a quartz-crystal microbalance [33, 34], scanning force microscopy [35–37], AFM experiments [38–42] and theoretical modeling [43, 44]

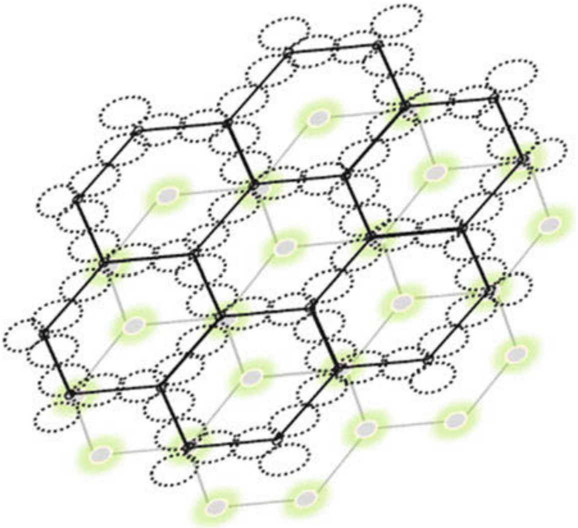

Fig. 8 Schematic of a typical AAA stacking of the incommensurate graphene sheets with the carbon rings of the adjacent atomic lattices positioned right above the opposite carbon rings and their C–C bonds between carbon atoms (after [23])

including molecular dynamics (MD) simulations [18–23, 30–32, 45–48]. The coupling of two or more interfacial interaction mechanisms such as strong registry effects, asperity interlocking and a non-standard stick-slip behavior with generation of lattice phonons is particularly challenging [17, 19–23]

A Nanoscale Analog of the Newton's Friction Law

The nanoscale sliding of two graphene sheets and surface cleaning from graphene flakes depends on the local lattice registry, the applied force and other interfacial interactions mechanisms mentioned above. The frictional sliding between two graphene lattices can be modeled on the length-scale level larger than a few carbon rings in a particular registry configuration (Fig. 8). Multiple lengths of carbon rings have to be considered for the meaningful averaging of the graphene lattice sliding. Dimensions of a graphene sheet, e.g., the length, L, should be sufficiently long, that is, $L/a > 10$ [7–10], where a is the width of a carbon ring.

The relative sliding of two graphene sheets (Fig. 8) takes place from the energetically less favorable position to another with the applied forces that may allow a sliding sheet to overcome some registry-induced potential barriers. At the length-scale larger than a carbon ring, a nanoscale friction can be analyzed as follows. The average shear stress, $<\tau_{xz}>$, for the sliding interactions between two graphene sheets can be defined as $<\tau_{xz}> \approx <f>_{pull}/A_{ss})$, where $<f>_{pull}$ is the average force applied to the sliding graphene sheet and A_{ss} is the common interfacial area during steady sliding between the two lattices separated by the van der Waals forces with the energy of interactions illustrated in Fig. 9.

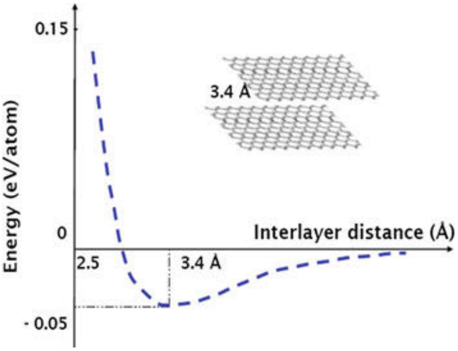

Fig. 9 The energy of interfacial interactions associated with the van der Waals forces between the adjacent graphene lattices (with the graphene-based equilibrium distance of *3.4 Å*)

The average strain rate, $<\dot{\gamma}>$, of interfacial sliding can be estimated as $<\dot{\gamma}> \approx \frac{\partial < V_{sliding} >}{\partial z}$, where $<V_{sliding}>$ is the average velocity of the graphene sheet in the axial x-direction and z is the distance between the two graphene sheets. Then, a nanoscale analog of the Newton's law for the steady interfacial sliding can be written as

$$< \tau_{xz} > = \mu_{eff} \frac{\partial < V_{sliding} >}{\partial z}, \tag{3}$$

where μ_{eff} is an effective viscosity for the graphene-graphene interfacial sliding. As a result, an interfacial friction model for the entire sheet-sliding process can be developed for the total shear stress, $<\tau_{xz}>_{\text{pull}}$, which, in addition to the sliding component $<\tau_{xz}>$, includes an initial threshold pull-out stress, τ_0:

$$< \tau_{xz} >_{pull} = \tau_0 + \mu_{eff} \frac{\partial < V_{sliding} >}{\partial z}. \tag{4}$$

After approximating the change in velocity across the interfacial separation, h_{VdW}, as the average sliding velocity, $<V_{sliding}>$, Eq. (4) can be rewritten as

$$< \tau_{xz} >_{pull} = \tau_0 + \mu_{eff} \frac{< V_{sliding} >}{h_{VdW}}, \tag{5}$$

where the strain rate is $\frac{\partial < V_{sliding} >}{\partial z} \approx \frac{< V_{sliding} >}{h_{VdW}}$.

In order to complete the description of the interface model, the effective viscosity, μ_{eff}, should be described. The interfacial sliding velocity is, on average, linearly related to the average applied force, $<f>$ [23], and the slope, χ_{eff}, can be determined. The resulting force-velocity dependence

$$< f > \; = \chi_{eff} < V_{sliding} > \tag{6}$$

is a nanoscale analog of the Newton's friction law.[4] The applied force, <*f*>, in Eq. (6) is related to the shear stress in Eq. (5) by the force balance: $< f > \; = \; < \tau_{xz} > A_{ss}$. Therefore, the viscosity coefficient, χ_{eff}, can be related [23] to the effective viscosity μ_{eff} as follows

$$\mu_{eff} = \frac{1}{w}\frac{h_{vdW}}{L}\chi_{eff}. \tag{7}$$

The effective viscosity of the spatially-distributed electrons, $\mu_{eff,}$ has the 1/w dependence, which is similar to some other property relations for graphene sheets. The viscosity of electrons is higher for higher densities of π-electrons and the associated greater values of the van der Waals separation, h_{VdW}. Then, the interfacial friction model for the entire sheet-sliding process is

$$< f >_{pull} = f_0 + \chi_{eff} < V_{sliding} > , \tag{8}$$

where f_0 is the critical force.

An Estimate of the Intrinsic Viscosity of the Spatially-Distributed Electrons Along the Graphene-Graphene Interface

Evaluations of the effective interfacial "viscosity" of the graphene-graphene interface and other surface-surface interfaces are important for the understanding of stiction and the dominant influence of the surface area at the nanoscale. The intrinsic sliding viscosity of the spatially-distributed electrons can be evaluated by using the molecular dynamics (MD) simulations data for the force-velocity dependence at the low temperature of 10 K [49] and the above nanoscale analog of the Newton's friction law [19–21, 23], where the effective viscosity coefficient χ_{eff} is estimated to be about *5 nN ps)/Å*) and the intrinsic sliding viscosity of the spatially-distributed electrons, μ_e, is estimated by Harik [23] to be on the order of *1 cP*, (i.e., centi-Poise).

---

[4] This fundamental research was partially supported by the Princeton-based NASA-funded URETI Institute (http://bimat.org) for the Bio-inspired Nanostructured Multifunctional Materials (award No. NCC-1-02037).

Deformation of Graphene Sheets and Phonons

At the nanoscale level, oscillations of the graphene lattice are inherent in most physical settings due to thermodynamic motion of carbon atoms [50]. Such continuous oscillations of the graphene lattice are associated with the constant thermal vibrations of the atomic lattice, and stochastic appearance and scattering of small low energy phonons (i.e., border value phonons [23]). The nature of these border value (BV) phonons of frequency, ω_i, and vector, k_i, is associated with the stochastic thermal vibrations of the atomic lattice, exchanges between different vibrational energies including electromagnetic effects and the random emergence of the small-scale stochastic order [23].

Conclusions

In this chapter the basic structure of graphene sheets has been examined along with its effects on the interfacial sliding between the adjacent graphene layers. A nanoscale analog of the Newton's friction law has been presented to describe the nanoscale sliding between the adjacent graphene sheets. The registry effects between adjacent graphene lattices has been analyzed by the so called registry matrices, which are used to describe the interfacial registry in graphene stacking and develop a new registry matrix analysis for the sliding of graphene sheets.[5] The new registry matrix analysis is very useful for the design of nanoscale electronic devices. Understanding of nanoscale sliding helps nanoscale cleaning and safety. Focus on individual nanocomponents also improves safety.

It has been also shown that interfacial sliding of graphene sheets depends on the interfacial registry potentials and the so called *effect of the spatial exclusion of electrons (ESEE)* at the interface of two graphene sheets, which can be viewed as the nanoscale analog of *Pauli's exclusion principle*. Understanding of the nanoscale sliding phenomena between graphene sheets and other surfaces is critical for improving manufacturing technology for the graphene based nanoelectronic devices and their dynamics.[6]

---

[5] In the late 15th century Leonardo da Vinci had identified the three important parts of friction as follows. "Friction is divided into three parts: these are simple, compound and disordered." Simple friction is due to the motion and dragging; the compound friction is "between two immovable things" and the irregular friction is associated with the "corners of different sides." For more details see the notebooks of Leonardo da Vinci [51], p. 527, and the following footnote.

[6] The momentum of moving "things" has been also analyzed by Leonardo da Vinci [51], p. 543: "No impulse can end immediately but proceeds to consume itself through stages of movement."

References

1. A.K. Geim, K.S. Novoselov, The rise of graphene. Nature **6**, 183 (2007)
2. A. Bostwick, T. Ohta, T. Seyller, K. Horn, E. Rotenberg, Nature **3**, 36 (2006)
3. H. Raza, J. Phys.: Condens. Matter, **23**, 382203 (2011)
4. S. Ihnatsenka, I.V. Zozoulenko, G. Kirczenow, Phys. Rev. B **80**, 155415 (2009)
5. H. Raza, *Graphene Nanoelectronics: Metrology, Synthesis, Properties and Applications* (Springer, Berlin, 2011)
6. V.M. Harik, Solid State Comm. **120**(7–8), 331 (2001)
7. V.M. Harik, *Ranges of Applicability for the Continuum- Beam Model in the Constitutive Analysis of Carbon Nanotubes: Nanotubes or Nano-beams? (NASA/CR-2001-211013, NASA Langley Research Center)* (Hampton, Virginia, 2001)
8. V.M. Harik, *Mechanics of Carbon Nanotubes (A Short Course Notes)* (ASME Education Institute, American Society of Mechanical Engineers, New York, 2001)
9. V.M. Harik, Computational Mater. Sci. **24**(3), 328 (2002)
10. V.M. Harik, M. Salas (eds.), *Trends in Nanoscale Mechanics* (Kluwer Academic Publishers, The Netherlands, 2003)
11. A.N. Cleland, *Foundations of Nanomechanics* (Springer, Berlin, 2003)
12. V.M. Harik, L.-S. Luo (eds.), *Micromechanics and Nanoscale Effects* (Kluwer Academic Publishers, The Netherlands, 2004)
13. A.N. Kolmogorov, V.H. Crespi, Phys. Rev. Lett. **85**(22), 4727 (2000)
14. K. Liao, S. Li, Appl. Phys. Lett. **79**(25), 4225 (2001)
15. A.N. Kolmogorov, V.H. Crespi, Phys. Rev. B **71**, 235415 (2005)
16. N. Marom, J. Bernstein, J. Garel, A. Tkatchenko, E. Joselevich, L. Kronik, O. Hod, Phys. Rev. Lett. **105**, 046801 (2010)
17. R. Saito, G. Dresselhaus, M.S. Dresselhaus, *Physical Properties of Carbon Nanotubes* (Imperial College Press, London, 1998)

13. S.J.V. Frankland, A. Caglar, D.W. Brenner, M. Griebel, J. Phys. Chem. B **106**, 3046 (2002)

19. S.J.V. Frankland, V.M. Harik, Surf. Sci. Lett. **525**, L103 (2003)
20. S.J.V. Frankland, V.M. Harik, Mat. Res. Soc. Symp. Proc. **733** E, T6.2.1 (2002)
21. V.M. Harik, R.A. Cairncross, Mech. Mater. **32**, 807 (2000)
22. S.J.V. Frankland, V.M. Harik, Mat. Res. Soc. Symp. Proc. **740**, I12.1.1 (2002)
23. V.M. Harik, *Mechanics of Carbon Nanotubes* (Nanodesigns Press, Newark, Delaware, 2011)
24. B.N.J. Persson, *Sliding Friction: Physical Principles and Applications* (Springer, Berlin, 1999)
25. B.N.J. Persson, Surf. Sci. Reports, **33**, 83 (1999)
26. Q.Y. Li, K.-S. Kim, Proc. Roy. Soc. A **464**, 1319 (2008)
27. M.S. Dresselhaus, P.C. Eklund, Adv. Phys. **49**(6), 705 (2000)
28. P. Tangney, M.L. Cohen, S.G. Louie, Phys. Rev. Lett. **97**(19), 195901 (2006)
29. X.H. Zhang, G.E. Santoro, U. Tartaglino, E. Tosatti, Phys. Rev. Lett. **102**(12), 125502 (2009)
30. M.J. Yang, V. Koutsos, M. Zaiser, J. Phys. Chem. B **109**, 10009 (2005)
31. Q.B. Zheng, Q.Z. Xue, K.Y. Yan, L.Z. Hao, Q. Li, X.L. Gao, J. Phys. Chem. C **111**, 4628 (2007)
32. M. Foroutan, A.T. Nasrabadi, J. Phys. Chem. B **114**, 5320 (2010)
33. J. Krim, A. Widom, Phys. Rev. B **38**, 12184 (1998)
34. C. Daly, J. Krim, Phys. Rev. Lett. **76**, 803 (1996)
35. S. Morita, S. Fujisawa, Y. Sugawara, Surf. Sci. Reports **23**, 1 (1996)
36. S. Okita, M. Ishikawa, K. Miura, Surf. Sci. **442**, L959 (1999)
37. M.R. Falvo, R.M. Taylor, A. Helser, V. Chi, F.P. Brooks, S. Washburn, S. Superfine, Nature **397**, 236 (1999)
38. H.D. Wagner, O. Lourie, Y. Feldman, R. Tenne, Appl. Phys. Lett. **72**, 188 (1998)
39. P.M. Ajayan, L.S. Schadler, C. Giannaris, A. Rubio, Adv. Mater. **12**, 750 (1998)
40. A.H. Barber, S.R. Cohen, H.D. Wagner, Phys. Rev. Lett. **92**, 186103 (2004)

41. A. Kis, K. Jensen, S. Aloni, W. Mickelson, A. Zettl, Phys. Rev. Lett. **97**(2), 025501 (2006)
42. B. Bhushan, J. Phys.: Condens. Matter. **20**, 365214 (2008)
43. J. Servantie, P. Gaspard, Phys. Rev. Lett. **91**, 185503 (2003)
44. J. Servantie, P. Gaspard, Phys. Rev. B **73**, 125428 (2006)
45. Z. Xia, W.A. Curtin, Phys. Rev. B **69**, 233408 (2004)
46. L. Li, Z.H. Xia, W.A. Curtin, Y.Q. Yang, Am. Ceram. Soc. **92**(10), 2331 (2009)
47. A. Garg, S.B. Sinnott, Chem. Phys. Lett. **295**, 273 (1998)
48. S.-J. Heo, S.B. Sinnott, J. Appl. Phys. **102**, 064307 (2007)
49. L. Xu, T.-B. Ma, Y.-Z. Hu, H. Wang, Nanotechnology **22**, 285708 (2011)
50. M.S. Dresselhaus, P.C. Eklund, Adv. Phys. **49**(6), 705 (2000)
51. E. MacCurdy (ed.), *The Notebooks of Leonardo Da Vinci* (Konecky and Konecky printing, Duckworth & Co., London, 1906)

Molecular Mechanics of Polymer Nanocomposites

Enhancement of Macroscopic Properties

R. Catalin Picu

Abstract Polymer nanocomposites have been a central theme in nanotechnology over the last decade. This activity was determined primarily by expectations generated by early experiments showing significant property enhancement associated with the addition of a small fraction of nano-fillers in thermoplastics. A large number of experimental, numerical and theoretical investigations of the physical basis of these enhancements followed. Today it is generally accepted that, while the fillers do not modify chemically the matrix material, the mechanical properties of the polymer are nevertheless altered. This chapter reviews some of the numerical and experimental works aimed at developing this basic understanding. We focus on modifications of the chain structure and relaxation time in the vicinity of impenetrable fillers, the residence time of polymeric chains on filler surfaces in melts, and the formation of a network of chains connecting fillers. This molecular-scale physics has been incorporated in rheological models aimed at predicting the macroscopic response of the composite. One such model is presented here. Despite not reviewing the entire, large literature produced to date on this subject, the discussion provides insight into the essential physics of these systems, and a starting point for future investigations.

Introduction

Today, polymeric materials are ubiquitous. They are used in the solid and liquid phase, as structural components, base materials for various liquids and emulsions, additives in many products and, in general, are present in almost all engineering applications and perform functions which cannot be performed by other types of material.

R.C. Picu (✉)
Department of Mechanical, Aerospace and Nuclear Engineering, Rensselaer Polytechnic Institute, Troy, NY 12180, USA
e-mail: picuc@rpi.edu

V. Harik (ed.), *Trends in Nanoscale Mechanics*, DOI 10.1007/978-94-017-9263-9_7

Viewed from the molecular scale, dense polymer melts and solids are multi-body systems of polymeric chains. The chains may be monodisperse, i.e. all of the same length, or polydisperse. In practice, it is difficult to ensure that a given system is monodisperse, so the vast majority of such materials are polydisperse. The simplest systems contain linear chains, but many polymers of practical importance have more complex architecture, e.g. are branched, form combs, stars or rings. A given chain may contain a single type of mer (repeat unit), or multiple chemical compounds (co-polymers). Another interesting class of polymers is represented by networks. These are formed by cross-linking polymeric chains, which can be performed either by using groups already present along the chain (e.g. in telechelic polymers) or by adding a cross-linking agent (e.g. as in epoxy). Polymeric networks have unique properties and are encountered in both the engineering and living worlds as gels, tissue constructs, rubber etc.

The mechanical properties of polymers are diverse and are tunable by controlling the chain architecture, crystallinity, chain size and cross-link density (in networks). Thermosets, which have network architecture, when tested below their glass transition temperature, have low ductility and toughness, and relatively high strength. Other networks, such as rubber, which are above the glass transition temperature in ambient conditions, exhibit large deformations, non-linear elasticity and stiffening at large strains. Themoplastics as well as polymeric melts which do not form networks, are viscoelastic/viscoplastic materials characterized by complex relaxation spectra and exhibiting significant strain rate and temperature dependence of their mechanical behavior. This broad range of properties justifies the widespread use of this class of materials.

To focus the discussion, the modeling work presented in this chapter considers linear monodisperse uncrosslinked homopolymers. However, experimental results obtained with thermoplastics as well as thermosets are reviewed.

In many engineering applications polymers are used as composites. Fillers can be particles or fibers with characteristic dimensions of tens of micrometers or larger. Their addition to the polymeric base leads to a dramatic enhancement of the strength and toughness. Very common materials of this type are (chopped) fiber glass-filled epoxies and continuous fiber reinforced polymers, which are used as structural materials. The field of polymer composites is broad and has evolved significantly over the last few decades.

Polymer nanocomposites form a relatively newer class of materials, in which fillers have at least one characteristic dimension smaller than 100 nm. Probably the oldest man-made nanocomposite is carbon black rubber [1–3]. The addition of carbon black has increased the toughness and strength of rubber to levels which allow its use in automobile tires. With the advent of nanotechnology at the end of the 1990s, filling of many other polymers has been attempted, often with positive results in terms of improving mechanical properties. A major difference between the older carbon black-filled rubber and the newer nanocomposites is that the filling fraction in the newer materials is kept very small (usually smaller than few percent).

Another major difference between the older and newer nanocomposites is with respect to the molecular-scale mechanisms leading to property enhancement. Let us consider the fillers to be nanoparticles with approximately spherical shape. As the particle radius decreases while keeping the volume fraction constant, the number of particles per unit volume increases and hence, the average distance between them decreases. If one assumes good dispersion, when fillers become small enough, most of the polymer matrix chains are within few chain gyration radii from a filler surface. The structure and dynamics of the chains next to an impenetrable interface are different from those in the neat bulk polymer. Hence, the simple presence of fillers modifies the properties of the matrix. The composite contains a matrix with the same chemistry as the respective bulk polymer, but with modified mechanical properties. This is an interesting new concept. Furthermore, as the filler wall-to-wall distance decreases, the probability of formation of a network of chains that connect multiple neighboring nanoparticles increases. One envisions that a rubbery state may result, with nanoparticles playing the role of (high coordination) cross-links. It should be observed that this may happen in semi-crystalline polymers even without the addition of fillers, when the crystallites have nanometer dimensions. Several major polymer manufacturers market polyolefin materials with nanocrystals which play the role of the nanoparticles discussed here. These materials are not filled, but form large scale molecular networks and exhibit excellent non-linear elastic behavior and resistance to creep, just like regular rubbers.

Additional effects produced by fillers have been described and studied. Functionalizing the filler surface by tethering short or long molecules makes mixing more efficient (improves dispersion) and may improve the quality of the filler-matrix interface. Short surface groups chemically bond fillers to the surrounding matrix chains, while long chains tethered to the surface of fillers entangle with the matrix chains. The filler surface may promote crystallization in semi-crystalline polymers, and may modify the cross-link density in the case of filled networks. All these modifications have significant effects on the mechanical behavior observed at the macroscopic scale.

In this chapter we do not attempt a review of the complex effects associated with all these modifications. Rather, the scope is limited to describing the effect of the presence of spherical, impenetrable fillers on the structure and dynamics of linear chains located in the vicinity of nanoparticles. The issues of interest are:

(a) considering an isolated particle embedded in the polymer, what is the range over which its presence modifies the structure and dynamics of the polymer?
(b) what is the magnitude of this perturbation?
(c) in the case in which particles are close enough to each other for a network of chains connecting multiple fillers to form, what is the structure of this network? The incorporation of these effects in molecular rheology models describing the macroscopic mechanical behavior of the mixture is of interest for material processing. An example of such model is provided and the calibration of its parameters based on molecular-scale models is discussed. Both for exemplification and motivation purposes, several experimental results obtained with various nanocomposite systems, both thermosets and thermoplastics, are presented at the beginning of the chapter.

Experimental Results

Three examples of enhancement of macroscopic properties by the addition of nanofillers to polymers are reviewed in this section. The first is a thermoplastic (PMMA) filled with ceramic nanoparticles (silica). The second is a thermoset (epoxy) filed with carbon nanotubes (both single, SWCNT, and multiwall, MWCNT). The third example refers to epoxy filled with graphene platelets (GPL). As discussed below, the ductility increases dramatically without loosing strength in the first example. This is due to a nano-cavitation process which is enabled by nanoparticles with weak particle-matrix interfaces. In the second example, the thermoset deforms by crazing in the vicinity of the crack tip; a deformation mode seen at the macroscopic scale only in thermoplastics. This happens only when the CNT-epoxy interface is strong. In the third example, all material properties measurable in a monotonic text, modulus, strength and ductility, remain largely unaffected by the addition of GPL, but the creep resistance increases.

It can be immediately remarked that no single mechanism can explain all these effects. Part of the molecular scale physics introduced or just modified by the presence of nanofillers is discussed in section "Modeling Results: Understanding the Molecular Scale Physics" of this chapter. Let us begin by reviewing the experimental facts.

Strength and Ductility Enhancement

Improvements of the elastic response (modulus), yield, strength and ductility have been reported for many nanocomposite systems and several reviews have been published on this subject [e.g. 4, 5].

Improvement of the elastic modulus, to various degrees, was reported in most systems. As an example of a thermosetting polymer, the addition of only 0.4 vol.% of layered silicate in epoxy was shown to increase the modulus by 58 % relative to the pristine epoxy, in the glassy state [6]. Also, in case of thermoplastics, 0.1 wt% single-walled carbon nanotubes (SWNT)/poly(methyl methacrylate) (PMMA) nanocomposite has 10 % higher elastic modulus comparing to the unfilled polymer [7].

One of the attractive features of these results is that one may improve one property without compromising the other, as is usually the case in material development. As well-known, increasing strength usually leads to a decrease of ductility. In some nanocomposite systems, simultaneous increase of these properties has been reported.

Ash et al. [8] studied PMMA filled with silica nanoparticles. In this work, the nanoparticles have their surface treated with either methyl methacrylate (MMA) monomer in order to improve the compatibility with the polymer, or with 3-glycidoxypropyltrimethoxysilane coupling agent (GPS). The MMA coating facilitates the dispersion of fillers in the matrix but the interface remains rather weak. The

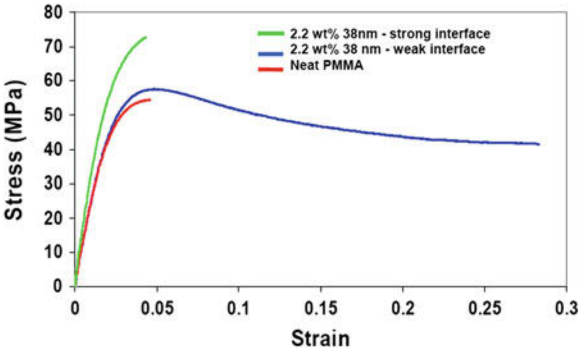

Fig. 1 Uniaxial mechanical behavior of PMMA filled with 2.2 wt% silica nanoparticles of 38 nm average diameter. Results are shown for the neat polymer, and for the composite with functionalized nanoparticles with weak (MMA functionalization) and strong (GPS functionalization) interfaces. Adapted from [8]

other coating produces strong interfaces with PMMA. The results of uniaxial tests are shown in Fig. 1. The three curves correspond to the unfilled PMMA and the two filler surface functionalization mentioned. When the interface is strong, the strength of the composite increases but the strain at failure remains equal to that of the neat polymer (and rather small). However, the composite with weak interfaces (the MMA coating) exhibits a dramatic increase of ductility, with the strength remaining close to that of the unfilled polymer. This phenomenon requires both sufficient chain mobility and the ability to release the normal component of the stress at nanoscale interfaces. It is conjectured that similar brittle-to-ductile transitions may be observed in other brittle polymers filled with nanoparticles having weak interfaces with the matrix.

Toughness and Fatigue Resistance Enhancement

An example of toughening of epoxy by the addition of nanofillers is described in this section. Epoxy is typically toughened by the addition of fibers with micron-scale diameter which increase resistance to crack propagation by crack bridging. Specifically, crack opening is possible only after either debonding along the fiber-matrix interface or fiber fracture has happened. These processes dissipate energy, which produces the toughening effect. The micromechanics of this process has been studied three decades ago [e.g., 9].

It is important to observe that in fiber-composites the matrix properties are not different from those of the unfilled polymer. What is the expected toughening mechanism if the polymer is filled with nanoparticles or nanotubes instead? When attempting to answer this question one should keep in mind the fact that the typical plastic zone size at the crack tip is many times larger than any nanoscale inclusion even in a relatively brittle thermoset, such as epoxy. Hence, it is unlikely that the fillers alone dramatically increase the plastic dissipation in front of the crack to a level comparable to the dissipation associated with fiber pull-out in a regular (micro) composite. Some degree of crack bridging may take place in the case of nanotubes, but due to the small length of these “nano-fibers”, the effect should be rather limited. As shown next, toughening still takes place and is substantial, and this appears to be due to the fact that the mechanical behavior of the polymeric matrix is modified relative to the unfilled polymer case [10].

Much work has been done on understanding the mechanisms of fatigue in both polymers [11, 12] and polymer composites [13–15]. Some recent studies [16–18] with nanoparticle fillers such as SiO2, TiO2, and Al2O3 embedded in polymer matrices suggested that nanoparticles cause crack defection, plastic deformation, as well as crack pinning, which increase the fracture toughness. In [10], significant crack growth rate reduction, up to an order of magnitude, has been observed in epoxy filled with less than 0.5 wt% carbon nanotubes. Both single and multiwall carbon nanotubes were used in this study and in [19, 20] and the effect is similar: the crack growth rate is reduced at small amplitudes of the cycle, while at large amplitudes no improvement is observed.

Figure 2 shows test data for the crack propagation rate as a function of the applied stress intensity factor amplitude for the epoxy/MWCNT and epoxy/SWCNT systems, respectively. Results for the baseline epoxy without nanotube additives are also shown for comparison. For epoxy/MWCNT composites at nanotube loading fractions of 0.5, 1,000 % reduction in the crack growth rate in the low stress intensity factor amplitude range is observed. The reduction of the crack growth rate became more pronounced with increasing weight fraction of the nanotube additives. The same trends are also observed for epoxy/SWCNT composites. At low weight fraction, e.g., in the 0.1–0.25 % range, SWCNT are more effective than MWCNT; however, at higher weight fractions the MWCNT offer improved reduction in the crack growth rate. We attribute this to the degradation of the dispersion quality of the SWCNT at the higher weight fractions [21].

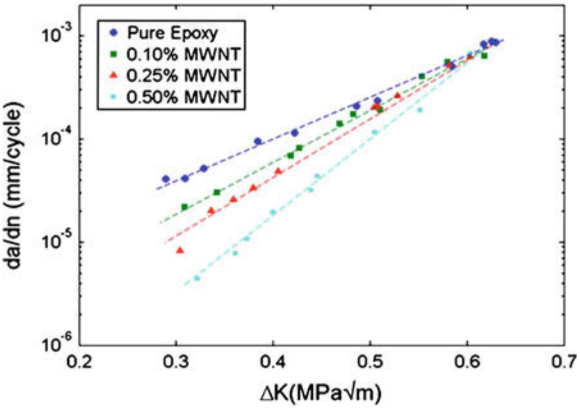

Fig. 2 Fatigue crack growth rate of pure epoxy and MWNCT-epoxy composite samples with 0.1, 0.25, and 0.5 wt% fraction of MWCNT additives plotted versus the applied stress intensity factor. Reproduced from [10]

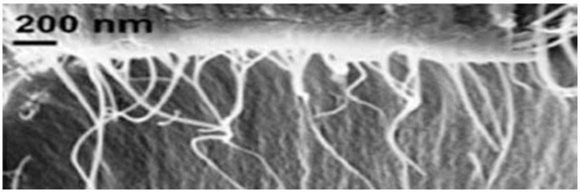

Fig. 3 Scanning electron microscopy (SEM) image of the side view of a fatigue crack. Carbon nanotubes are bridging the crack close to the crack tip, and are being pulled out as the crack opens. Reproduced from [10]

Direct observations of the crack tip region indicate that the reduction of the crack growth rate is associated with crack bridging. A crack bridging model similar to that in Ref. [22] was used to interpret the data and the match is adequate. Figure 3 shows an SEM image of nanotubes being pulled-out from one of the crack faces, which confirms the mechanism suggested by modeling.

In the sequel of the work in [10, 20], composites with functionalized nanotubes were considered. Pristine MWNTs were functionalized with amido-amine ($NHCH_2CH_2NH_2$) groups and were dispersed in a bisphenol-A based epoxy [19]. The amine used for functionalization is also a central component of the hardener used to cross-link the epoxy resin. Hence, the procedure provides good bonding between nanofillers and the matrix. The results of the fatigue tests are shown in Fig. 4. Two of the curves in Fig. 2 are reproduced in Fig. 4, for reference. The crack

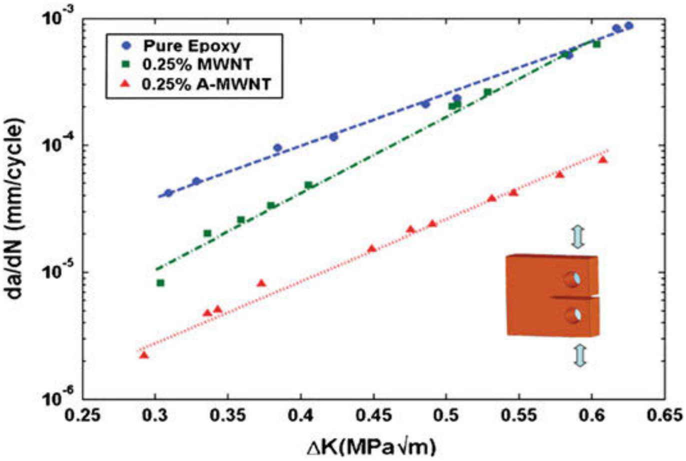

Fig. 4 Fatigue crack propagation data showing crack growth rate (da/dN) plotted as a function of the stress intensity factor amplitude (ΔK). The inset shows a schematic of the compact tension samples and loading mode used. Reproduced from [19]

growth rate decreases dramatically in the functionalized CNT case, by approximately one order of magnitude, at all stress intensity factors considered. Obviously, the main gain relative to the unfunctionalized filler case is the crack growth rate reduction at large loads.

An interesting observation made in these experiments is related to the mechanism controlling the large toughening observed in the functionalized CNT case. Direct observations of the region close to the crack tip indicate no nanotube pull-out as observed in the pristine CNT case (Fig. 3). Rather, a dense population of fibrils connecting the two crack faces is observed. The bridging of cracks by such fibrils is an important mechanism for energy dissipation and toughening in thermoplastic polymers. However, crazing is not observed [13, 15] in thermosetting polymers such as epoxies due to the high crosslinking density of the epoxy chains. Figure 5 shows fibrils forming close to the crack tip. In order to insure that these are not carbon nanotubes, the sensitivity to heating has been probed by attempting to cut the fibrils with the electron beam of the electron microscope. These can be easily sectioned, which should not happen if the fibrils are carbon structures. The observation indicates that fibrils are made from pure polymer. Therefore, interestingly, the presence of fillers which are well bonded to the matrix enables a deformation mode which is not observed in thermosets. The detailed molecular mechanisms that make this possible are not fully understood at present.

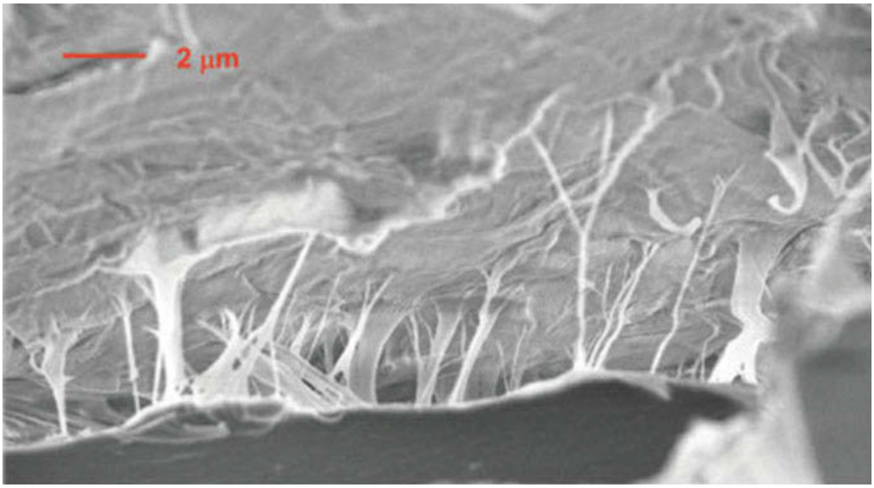

Fig. 5 Fractography analysis for the functionalized MWNT/epoxy nanocomposite. The SEM micrograph shows crack bridging in the vicinity of the crack tip (on the *left* of this frame). The diameter of bridging fibrils is in the 100–1,000 nm range. Reproduced from [19]

Creep Resistance Enhancement

A graphene-epoxy system is considered in this section. Graphene, a single layer of carbon atoms sp2 bonded in a hexagonal array, has attracted attention recently due to its interesting mechanical and transport properties [23, 24]. Its use as filler material in polymer nanocomposites, mostly in the form of graphene platelets (GPL), was also studied [25]. The results discussed to date indicate that graphene does not modify significantly the monotonic mechanical properties of the polymer, the strength, stiffness and ductility of the composite being close to those of the base epoxy. It has been reported that the fracture properties, both the fracture toughness and the fatigue crack growth rate are more sensitive to the presence of graphene than the monotonic properties.

In [26], GPL at small volume fractions (0.1–0.5 wt%) was added to epoxy. The processing conditions are described in detail in Refs. [27, 28]. Consistent with previous work using graphene, it was observed that the monotonic mechanical properties are not modified relative to the unfilled epoxy. In fact, although the strength remains the same, strain localization (necking) in the filled material is more difficult and hence post-critical deformation is smaller, which leads to a smaller apparent ductility.

Quite different results are obtained when these materials are tested for creep. Figure 6 shows the creep strain (total strain minus the elastic strain corresponding to the creep load) versus time for the unfilled epoxy and for three GPL-epoxy systems, with 0.1, 0.3 and 0.5 wt% GPL. Two families of curves are shown, corresponding to 20 and 40 MPa creep stress.

The creep behavior is essentially identical for filled and pristine epoxy at the small load (20 MPa). However, at the larger stress (40 MPa) the four materials respond differently. The smallest creep strain is measured in the nanocomposite with 0.1 wt% GPL, which deforms significantly less than pristine epoxy in the same time. The strain rate at the end of the hold period (after 37.5 h) is much smaller in the 0.1 wt% GPL composite than in pristine epoxy. The other composites (0.3 and 0.5 wt% GPL) creep more than the unfilled polymer.

Interestingly, similar behavior is observed when creep is probed at the nanoscale, by nanoindentation. Indentation was performed with a flat punch of 50 μm diameter and a constant load of 2 mN was applied. The advantage of using a flat, cylindrical indenter is that the variation in time of the displacement measured in this experiment is proportional to the creep compliance, J(t), which would be measured macroscopically if one would have a large sample with the same microstructure as that of the volume of material located under the indenter.

Figure 7 shows the indentation displacement versus creep time for pristine epoxy and the 0.1 wt% GPL nanocomposite. Each curve represents the mean of 10 indentation measurements and the error bars indicate variability from indentation site to indentation site.

The nanocomposite creeps less compared to the pristine epoxy, as also seen in macroscopic tests. It is also interesting to observe that, although epoxy is generally

Fig. 6 Creep strain versus time for neat epoxy and GPL/epoxy with different filler contents and at stresses of 20 and 40 MPa, at room temperature. Reproduced from [26]

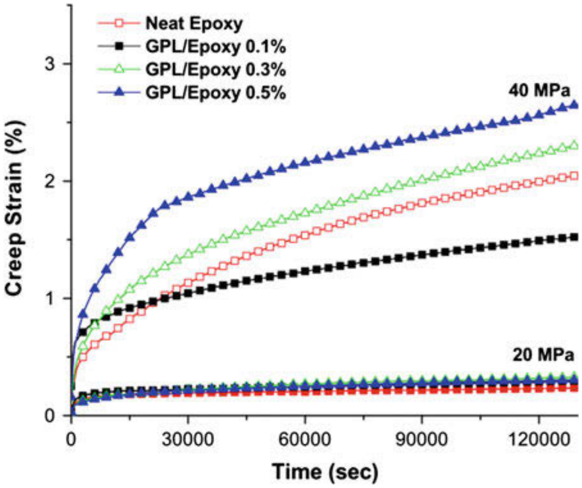

Fig. 7 Creep displacement versus time in indentation experiments using a 50 μm flat punch. Reproduced from [26]

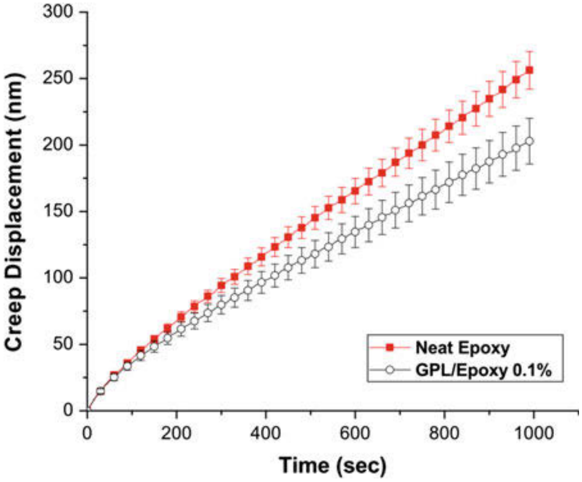

considered to be homogeneous down to the smallest scales (~ 10 nm), the indentation data indicate some spatial variability of mechanical properties.

These findings demonstrate that nanofillers lead to modifications of the mechanical behavior of the surrounding polymer which are unique and cannot be obtained by other means. The diversity of effects observed in experiments is impressive and clearly, no single molecular mechanism can explain all of them. This indicates that we are still far from having discovered all possible ways in which we can improve the mechanical properties of nanocomposites and therefore, structural optimization for desired macroscopic behavior is not achievable at this time. It is encouraging though that these systems maintain a great promise.

Modeling Results: Understanding the Molecular Scale Physics

Molecular modeling is a convenient way to investigate aspects of the nanoscale physics that controls the mechanical behavior of nanocomposites on large scales. Results relevant for polymers filled with nanoparticles are discussed in this section.

Several generic considerations can be made before discussing the details. The structure and dynamics of confined chains is controlled by energetic and entropic interactions. The entropic forces arise from the constraint imposed by the presence of impenetrable fillers to chain motion and the number of conformations these can take. This leads to a thermodynamic force driving the chains away from the filler surface. When several fillers are close to each other, this entropic effect drives the polymer located in-between fillers away from the confined space, which leads to particle agglomeration. The energetic interactions have an opposite effect, creating a bonded polymer layer on the surface of fillers. The chains belonging to this layer have long residence time at the interface. This issue is discussed in detail later. If the interaction with the filler surface is strong, the chains in contact with the filler have essentially infinite residence time, i.e. they are tethered. In this case, the filler is surrounded by a polydisperse brush which is penetrated by the surrounding chains. This brush has reduced dynamics and its interaction with the free chains in its vicinity leads to slower dynamics in a broader range, larger than the thickness of the brush. This effect is also discussed in below. Finally, when the filler number density is large (note that this does not imply a large filler volume fraction!) and the distance between fillers becomes comparable with the chain radius of gyration, R_g, one expects that there exist chains that connect multiple neighboring fillers forming a “network.” This network is expected to play a significant role in the mechanics of the composite. However, the percolation of this network throughout the composite material volume requires a close-to-perfect distribution of fillers, which is difficult to be achieved. The structure of such network is discussed later.

Some Modeling Details

Various coarse grained models have been used in this work to represent the filled polymeric system. The finest scale model employed is of bead-spring type. The polymers are represented as chains of spherical beads which interact through Lennard-Jones potentials of well depth wp. The beads belonging to given chain are held together by “bonded interactions” represented by linear springs. These springs are stiff enough to insure that the chains do not cross. The unit of length is the length parameter, σ, of the Lennard-Jones potential. This model has been used extensively in polymer physics [e.g. 29, 30]. It provides a coarse grained representation of the system since each bead stands for either a repeat unit, including the side groups, or for an entire Kuhn segment.

The nanoparticles are represented as spheres which are impenetrable for the polymers. The interaction between nanoparticles and polymeric beads is modeled with a Lennard-Jones potential with adjustable well depth, *wnp*. If $\left|w_{np}\right| > \left|w_p\right|$, the polymer-filler interaction is attractive. The other two cases, $\left|w_{np}\right| = \left|w_p\right|$ and $\left|w_{np}\right| < \left|w_p\right|$, are denoted as neutral and repulsive, respectively. It is useful to introduce an affinity parameter, $w = w_{np}/w_p$, which captures the chemical bonding between fillers and matrix. In separate simulations, a subpopulation of chains was tethered to the filler and this tether interaction was represented by a stiff linear spring (a covalent bond).

The filler is considered smooth in these simulations. The atomic scale roughness of the filler appears to be important in the dynamics of bonding-debonding [31, 32], but it is rather inconsequential for the polymer structure.

The interaction between fillers, other than the excluded volume, is not considered in this work. This approximation is justified by the small volume fraction of fillers and by the fact that the filler surface is always covered with polymeric beads. Filler agglomeration driven by entropic and energetic effects was studied by molecular dynamics in other works [33, 34].

The system of chains is evolved either with molecular dynamics or with a lattice Monte Carlo procedure. Simulations with one or multiple fillers per unit cell were performed. The filler diameter and the unit cell size determine the filler volume fraction and the average wall-to-wall distance between fillers. Periodic boundary conditions are used for the unit cell.

Another model used for this system is a coarse-grained rotational isomeric state (RIS) model, where the chains were represented on a high coordination lattice [35, 36] and evolved using a Metropolis Monte Carlo algorithm. The coarse-graining was achieved by combining every two carbon and associated hydrogen atoms on the polyethylene (PE) chain into a bead that was located on a second nearest neighbor diamond (SNND) lattice. The SNND lattice was created by removing every other site from a diamond lattice resulting in a lattice structure that, when a random walk was taken, the path closely approximated the actual angles between carbon atoms belonging to the backbone of a vinyl polymer chain. The RIS model was incorporated into the simulation to calculate the short-range intramolecular conformational potential energy of polyethylene (PE) chains. The long-range intramolecular and intermolecular interaction potential energies were calculated using a lattice based approximation of the Lennard-Jones potential between monomers, and between monomers and filler particle beads. This simulation method has been incrementally improved over the years [36–38] and widely used to investigate the properties of PE and other vinyl polymers including their bulk dynamics [38, 39] mixing of polypropylene and PE [40].

Structure of Chains in the Vicinity of Filler Surfaces

The structure of linear monodisperse polymeric chains in the vicinity of flat surfaces was studied by analytical means and computer simulations [41–50] and experimentally [51, 52]. A review is provided in [53]. It has been found that chains do not distort even when they are confined in films as thin as *Rg*. Rather, they orient with their long axis (chains have, in average, an elongated ellipsoidal shape) parallel to the surfaces such to minimize any conformational distortion. In contrast to these established ideas, recent studies on the conformation of polymer chains in the presence of curved nanoparticles are controversial. Mark and collaborators [54, 55] performed simulations of phantom (or Gaussian) chains in the presence of a prescribed volume fraction of impenetrable spheres. The chains are found to either stretch or compress, depending on the ratio of the chain dimension and the mean wall-to-wall distance. Experimental results published by Nakatani et al. [56] appear to support these conclusions. However, recent Monte Carlo [32, 57–59] and molecular dynamics [31] simulations of melts of self-avoiding chains in the presence of impenetrable fillers show that chain dimensions are always smaller compared to the bulk dimensions at high and moderate filler volume fractions. At low filler volume fractions the chains are not distorted, consistent with results obtained for polymer melts near flat surfaces. Vacatello argues [57] that the assumption of non-interacting chains made in [54, 55] is not valid for filled systems, and that melts of self-avoiding chains at proper densities have to be modeled if a clear understanding of chain conformations is desired.

Using a model of interacting chains and fillers occupying a regular cubic lattice it may be concluded [58, 59] the following. If the filler diameter, *D*, is much smaller than the chain radius of gyration, *Rg*, the chain structure is not affected by the presence of fillers. The statistics of segment lengths is identical to that in the bulk, unfilled polymer. This conclusion is independent of the value of the filler-polymer affinity, *wnp*. If the filler diameter is larger than approximately 5*Rg*, the interaction with the chains is similar to that between the polymer and a flat surface. As mentioned above, the chains do not distort significantly, rather tend to rotate in order to align their large semi-axis (which is also approximately parallel to the end-to-end vector) with the direction tangent to the filler surface.

A transition between these two extreme cases takes place in the approximate interval $R_g/2 \leq D \leq 5R_g$. Interestingly, this is also the range for which most experimental studies report improvements of mechanical properties.

Let us consider systems in which the filler size is comparable with the polymer chains size, and the affinity parameter $w = w_{np}/w_p$ is varied. Figure 8 shows the variation of the three eigenvalues of the chain gyration tensor with the distance between the chain center of mass and the wall, for the case in which fillers are far apart. The filler size is $R = D/2 = 2\sigma$ and 8σ in separate simulations. In the bulk, the three semi-axes (for these chains of $N = 101$ beads) are $\langle\lambda 1\rangle = 3.89$, $\langle\lambda 2\rangle = 1.84$, $\langle\lambda 3\rangle = 1.14$ (in units of σ), which defines a flattened ellipsoid. For these chains $Rg = 4.4\sigma$.

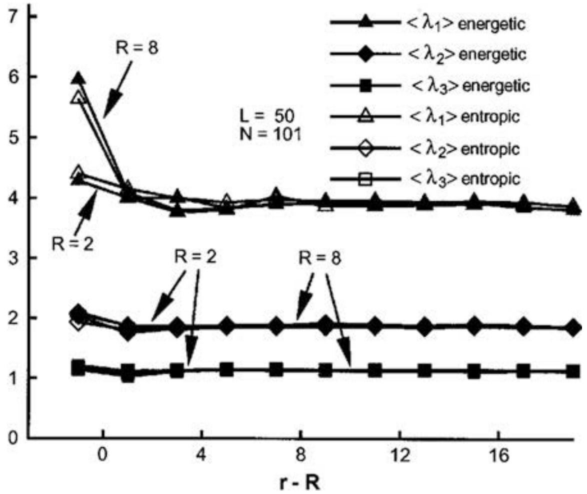

Fig. 8 Variation of the three eigenvalues of the gyration tensor of chains with the distance between the chain center of mass and the wall, for the case in which fillers are far apart. *L* stands for the size of the cubic unit cell used in the simulation (values are indicated in units of length, σ), which contains one spherical filler. The chain is composed from $N = 101$ beads and the density is 0.8, i.e. it corresponds to a melt. Reproduced from [59]

The chain size and shape is unperturbed by the presence of the filler even when the center of mass is within $<\lambda_3>$ from the wall. A small number of chains wrap around the filler and distort. These chains have their center of mass within the filler ($r - R < 0$). The distortion is most pronounced along the large semi-axis of the ellipsoidal coil. An entropic model, in which no energetic interactions are taken into account, but the excluded volume and chain uncrossability condition are enforced at all times, and an energetic model in which long-range attractive and repulsive interactions are included are compared in the figure. The entropic and energetic cases are essentially identical, within the accuracy of the present simulations. As long as the filler radius is larger than the radius of gyration, the chain shape and size are independent of the filler size, i.e. the limit of the flat wall is reached in these systems.

The structure on the chain scale is also weakly influenced by the attractive potential. The chains remain undistorted even for $w = w_{np}/w_p$ as large as 12 [59]. This value corresponds roughly to hydrogen bonding between filler and polymers. Chains having their center of mass as close as $<\lambda_3>$ from the wall have essentially the same dimensions with those in the bulk.

Further insight into the chain structure may be obtained by computing $\langle P_2^c \rangle$. This measure shows preferential orientation of the eigenvector associated with the largest eigenvalue of the chain gyration tensor, i.e. the large semi-axis of the ellipsoidal coil. A negative value shows preferential orientation in the direction tangential to the filler, with $\langle P_2^c \rangle = -0.5$ denoting total orientation. $\langle P_2^c \rangle = 0$ indicates random orientation of coils. Figure 9 shows this measure as a function of the distance

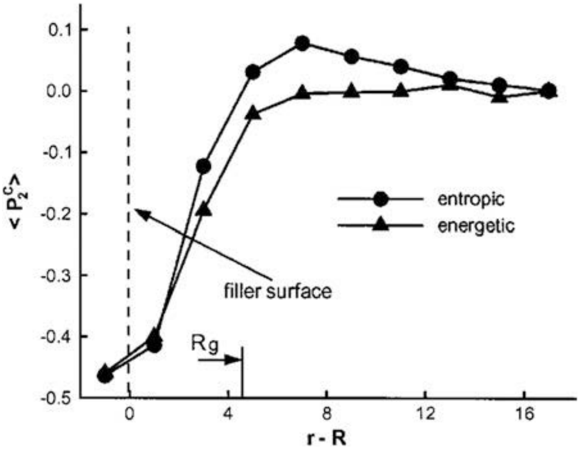

Fig. 9 Variation of the orientation factor $\langle P_2^c \rangle$ with the distance between the chain center of mass and the wall, for the case in which fillers are far apart ($N = 100$, $L = 50\sigma$). Coils are oriented with their large semi-axis in the direction tangential to the filler when their centers of mass are within $2 < \lambda_1 >$ from the wall

between the chain center of mass and the filler surface. The entropic result for this system is reproduced from [58] for reference. The data suggest that, once the center of mass is within about 2<λ1> (a chain size) to the wall, the coils rotate in the tangential direction. The chains undergo a "docking" transition as also observed in the flat wall case [60, 61]. Chain distortion, which would require a large decrease of the entropy, is avoided. Chain distortion was reported in the literature when a driving force for chain collapse in the interface exists [62].

Secondary Network Formation

Let us discuss now the structure of chains that participate in the polymer mediated transient network that forms between filler particles. The situation envisioned is shown schematically in Fig. 10 [63]. Here, a representative chain forms bridges between fillers, loops (segments that start and end on the surface of the same filler) and dangling ends. It should be noted that this structure evolves due to thermal fluctuations. The destruction and creation of segments is a stochastic, reversible process. The internal structure has a transient topology and its dynamics is controlled by the rate of the attachment and detachment process as discussed later. The results presented below are statistically representative for the steady state of this stationary dynamic process.

We consider systems with three different filler volume fractions (≤27 %) as representative of experimentally studied nanocomposites. The wall-to-wall distance is selected to be on the order of the chain size ($0.5R_g$, R_g and 2 R_g), while the radius of the spherical fillers is taken to be $\sim R_g$.

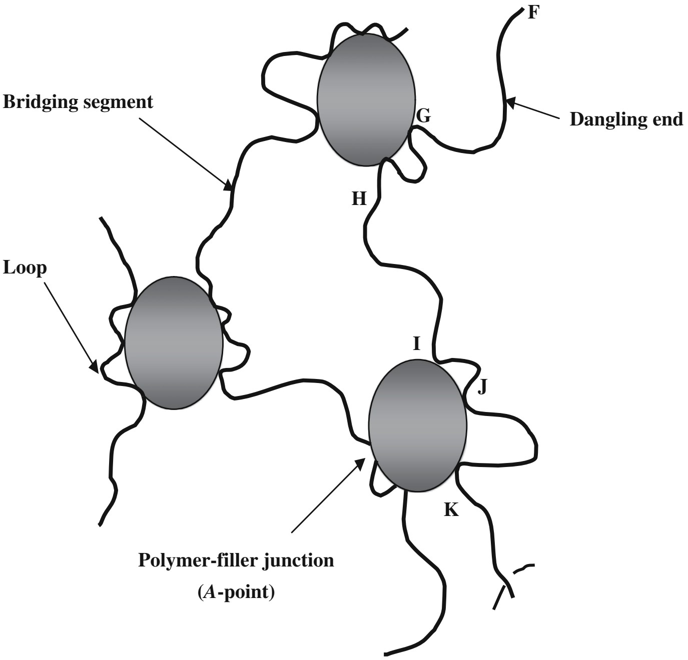

Fig. 10 Schematic representation of the molecular scale structure. The macromolecules form bridging segments, loops and dangling ends

Bridges

The importance of bridges derives from the fact that they are central to the formation of a transient particle network. Additionally, if the lifetime of this network is long enough, the stiffness of the composite should increase dramatically. Figure 11 shows the distribution of the number of monomers in a bridge. There are three sets of curves, corresponding to wall to wall distance $d = 0.5\ Rg$, Rg, and $2\ Rg$, respectively. For each given d value (say Rg), the ratios d/Rg and d/particle size are chosen to be independent of the chain length, N. The effect of the affinity parameter, w, that describes the strength of the polymer-filler attraction (w = 10kT, 2kT, 0.2kT) is weak in this context; w perturbs the local polymer configuration, in the vicinity of the wall, but not the longer range structure. Thus, both the mean number of monomers in a bridge and the end-to-end distance are hardly affected by w. Similar results are also found for tails, loops and trains. However, it is emphasized that the filler-polymer bond strength is known to be a primary variable in determining the reinforcement levels [64] and the recovery kinetics of modulus following large strain deformation [65].

The total number of bridging segments per filler depends strongly on the wall-to-wall distance, d. For N = 100, we find for d = Rg that 8 % of lattice sites on a particle surface are associated with polymer bridges. When the wall-to-wall distance d increases to $2Rg$, the total number of bridging segments per filler decreases to 17 (2 % of the available sites on the filler surface).

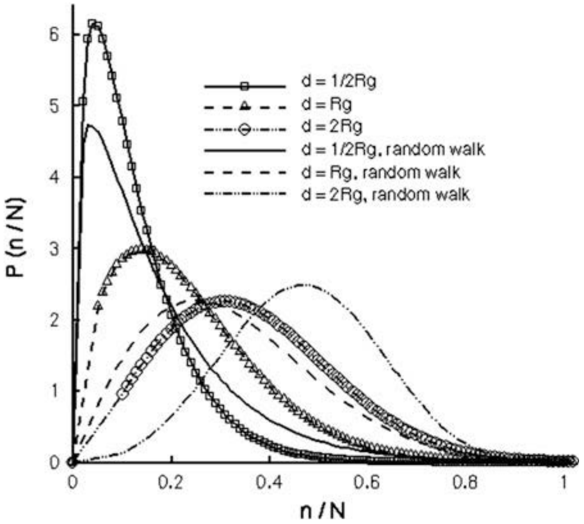

Fig. 11 Probability distribution function of the normalized number of bonds in a bridging segment, *n*, for systems with wall-to-wall distance d = $0.5R_g$, R_g and $2R_g$, $w = 2$ and chain length $N = 100$. The distribution of the normalized number of bonds in a bridge segment is independent of the chain length *N*. Data from self-avoiding random walk chains are shown in this plot

The figure includes data for simple random walks which do not take into account the presence of fillers. As shown in Fig. 11, there is a higher probability for these random walks to have a larger number of links, *n*, than the bridges.

Dangling Segments (Tails)

A large number of dangling segments are attached to each filler. As in the case of bridges, an attachment point is defined when a bead resides in a layer of unit thickness at the surface of the filler. About 10 % of the filler surface sites are occupied by dangling segments. The probability distribution function of the number of bonds in a dangling segment is shown in Fig. 12 for $d = 0.5R_g$, R_g and $2R_g$. With decreasing *d* there are more short segments, due to the fact that when the wall-to-wall distance is a small fraction of the chain size, dangling segments become bridges.

Loops

A dense population of loops exists on the surface of each filler. Loop ends occupy about 37 % of the available surface sites. The total number of loops per filler and therefore their surface coverage are independent of *d*. The distribution of the number of bonds in a loop is shown in Fig. 13. The most important observation here is that most of the loops are very short, and that, to first order, the loop distribution (plotted against *n* rather than *n/N*) is independent of *d* and chain length.

Fig. 12 Probability density distribution function of the normalized number of bonds in a dangling segment for systems with wall-to-wall distance $d = 0.5R_g$, R_g and $2R_g$, respectively, with chain length $N = 100$

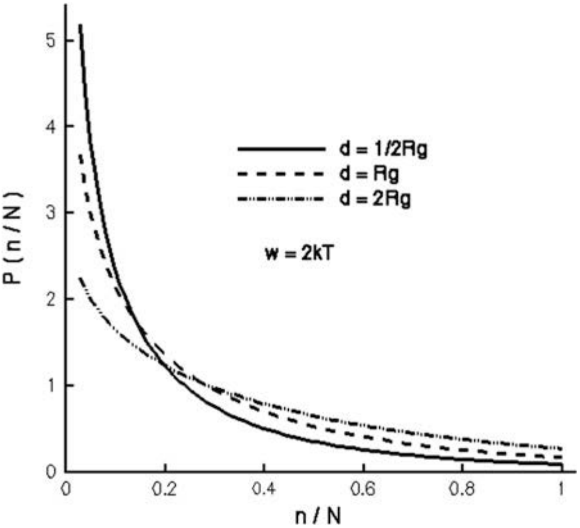

Fig. 13 Probability density distribution function of the number of bonds in a loop segment for systems with $d = 0.5R_g$, R_g and $2R_g$, $N = 100$

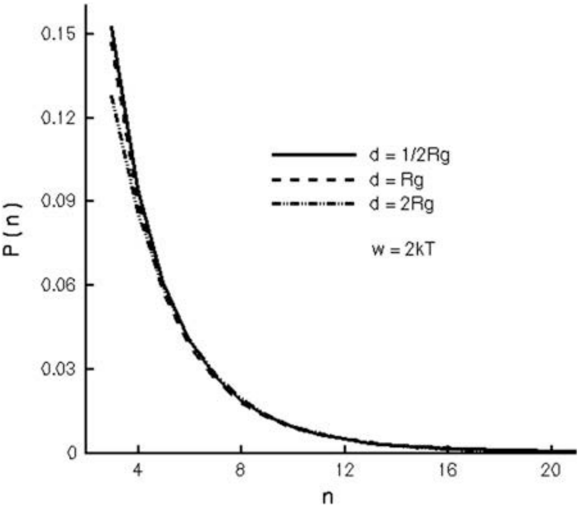

Trains

A large number of train segments exist. These are chain segments longer than one bond length that are snaking on the surface of the filler without a single monomer leaving the surface. The trains are essentially inactive in stress production. Their importance is associated with the chain detachment process. During deformation, when a chain segment is pulled from the wall, the presence of a long train makes it harder to detach this segment. The lifetime of these trains increases due to this synergy. The trains may be as long as 10 bonds, although the probability of such entities is small. Most trains are 2–4 bonds in length. The average train length is not a function of chain length, or of the wall-to-wall distance, d.

Dynamics of Chains in the Vicinity of Filler Surfaces

The presence of fillers is expected to influence more the dynamics of chains than their structure. The chain dynamics controls macroscopic relaxation rates, such as creep, mechanical and dielectric relaxation, and other macroscopic rate effects. Here we present results outlined in [35] regarding the modification of the average relaxation time due to the presence of nanofillers, and in [66] regarding the dependence of the residence time of chains contacting fillers on the polymer-filler affinity parameter, w (Fig. 14).

Rouse Modes [35]

The dynamics of chains is investigated by examining the Rouse modes and the mean-square displacement of the chain center of mass, $g_3(t)$, as a function of time. The coarse grained RIS model of PE chains described earlier was used for this purpose and hence the physical time is replaced by the number of Monte Carlo steps (MCS). The characteristic relaxation times of the system are determined in the usual way by computing the autocorrelation function of the normal modes. Figure 14 shows the autocorrelation function of the first Rouse mode ($p = 1$) for various systems. Figure 14a shows the effect of confinement by comparing systems with the same R_g and different filler wall-to-wall distances, d, for which $w = 1$. As long as d is larger than $\sim 1.5R_g$, confinement is too weak to influence relaxation. Slowing down is seen in the system with $d = 1.2R_g$. The relaxation of the neat system (labeled S1 in Fig. 14) is shown for reference. The effect of the affinity parameter w is shown in Fig. 14b in which both the wall-to-wall distance and R_g are held constant. As expected, increasing the polymer-filler affinity leads to an additional slowdown.

Diffusion [35]

The chain dynamics is further analyzed by evaluating the mean-square displacement (MSD) of the chain center of mass, $g_3(t)$, where time, t, is interpreted again as the number of Monte Carlo steps. The results are shown in Fig. 15. The horizontal axis is normalized by the Rouse time in the neat system. This choice of normalization constant is possible since the Rouse time of the various filled systems considered is only slightly different from the value in the neat polymer.

Fig. 14 Autocorrelation function for the first (p = 1) Rouse mode normal coordinate, **a** dependence on confinement, d, **b** dependence on polymer-filler affinity, w. Reproduced from [35]

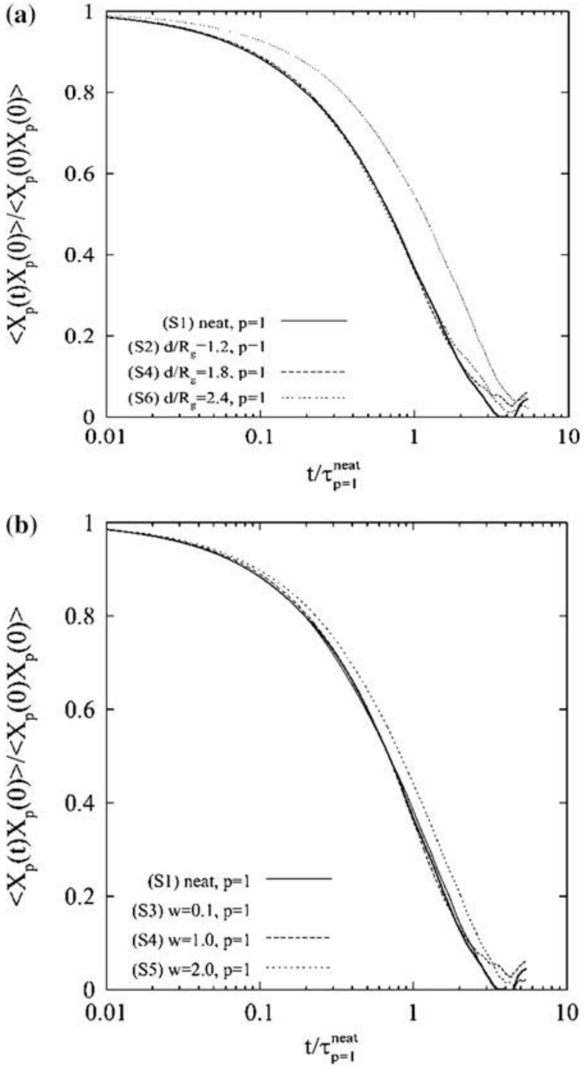

Figure 15a demonstrates the effect of confinement (w = 1 in all cases). The conclusion is similar to that obtained from the Rouse analysis: confinement slows down dynamics. The various g_3 curves are parallel, which indicates that confinement preserves the nature of diffusion, but changes the diffusivity.

Figure 15b shows the effect of the filler-polymer affinity parameter, w. The curve corresponding to neutral interactions (w = 1) has slope 1 at times larger than the Rouse time, i.e. normal diffusion dynamics prevails. The system with repulsive interaction (w = 0.1) is super-diffusive, while the one with attractive interaction (w = 2) is sub-diffusive (slope smaller than 1).

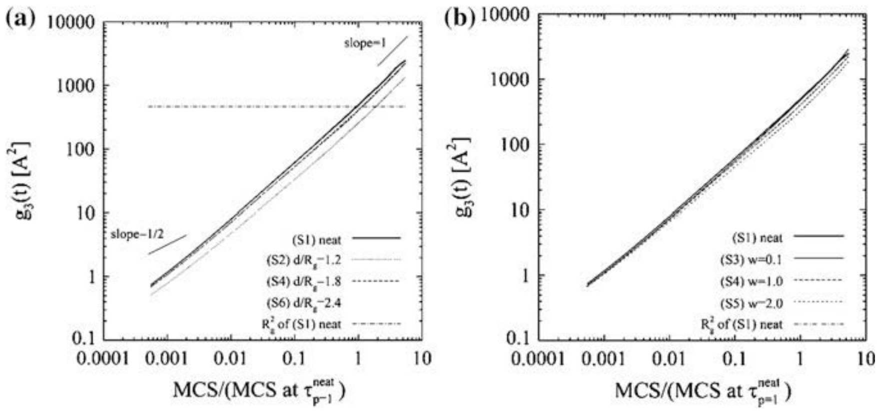

Fig. 15 Mean-squared displacement of the chain center of mass vs. time (MCS), **a** dependence on confinement, *d*, **b** dependence on polymer-filler affinity, *w*. Reproduced from [35]

Residence Time [66]

The number of adsorbed beads per chain N_a at any time controls the probability of desorption of that chain. The value of N_a is determined by counting the number of polymer beads per chain located within an adsorption zone around the filler particle at given time. These beads are said to be in contact with the filler. The adsorption zone is defined by the range of the polymer-filler potential and contains roughly three layers of closely packed polymer beads at the filler surface. A chain may come in contact with the filler, build up contacts, and then diffuse away from the filler. This lower frequency process is of interest here. An adsorption-desorption event is defined as a span of the simulation in which N_a is continuously greater than zero. The duration of the adsorption-desorption event is equal to the residence time of that chain, τ_{ad}. From these data, it is possible to estimate the average, $\overline{N}_a = \frac{1}{n_{ad}} \sum_{j=1}^{n_{ad}} \frac{1}{\tau_{ad}} \sum_{i=1}^{\tau_{ad}} N_a(t_i)$, where n_{ad} is the number of adsorption-desorption events whose duration is equal to τ_{ad}, and $N_a(t_i)$ stands for the number of adsorbed beads per chain at time t_i. This quantity is a function of the residence time τ_{ad} and indicates the mean number of beads per chain remaining in contact with the filler a time τ_{ad} (Fig. 16).

The function $\overline{N_a}(\tau_{ad})$ is shown in Fig. 16. The adsorption time is normalized here by the Rouse relaxation time in the neat polymer, τ_R^{neat}. The function may be represented over a broad range of τ_{ad} by a power function of exponent 0.25. Also, it is observed that the curves shift downward as the polymer-particle interaction parameter, w, increases. At long residence times, a transition to a plateau is observed.

More interestingly, the relationship between the system average attachment lifetime and the polymer-filler affinity parameter, w, can be determined. This relation is shown in Fig. 17 in a semi-log plot. An Arrhenius dependence of the

Fig. 16 Variation of the mean number of beads per chain in contact with filler function of their residence time

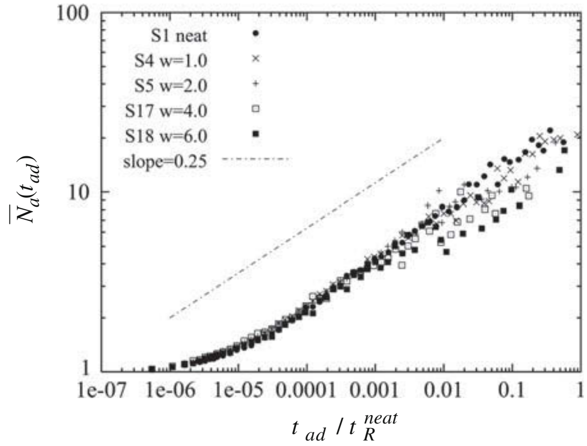

Fig. 17 Characteristic residence time as a function of the polymer-particle energetic interaction parameter, *w*. Reproduced from [66]

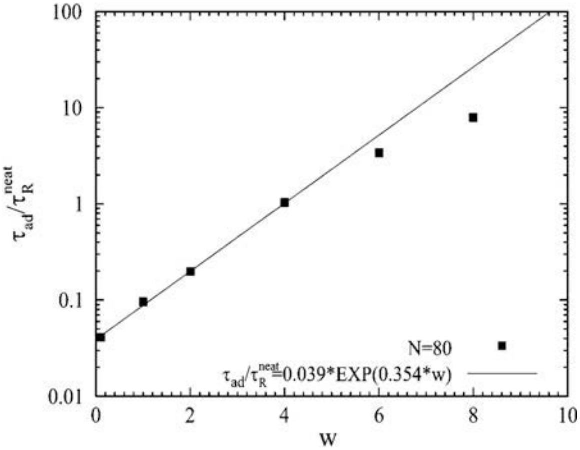

form $\tau_{ad}(w) = c_1 e^{c_2 w}$ can be fitted to the data. The information about the geometry and the chain size is contained in the pre-exponential constant c_1. The constant c_2 is inversely proportional to the temperature, as observed from simulations performed at various temperatures.

Long Range Effects on Chain Dynamics

As discussed above, the presence of fillers embedded in a polymeric matrix leads to the modification of the dynamics of the chains in their vicinity. An important question which arises refers to the range of this effect: consider an isolated spherical filler—how far into the bulk polymer is the dynamics of chains perturbed?

Attempting to find an answer to this question, two systems were considered in [67]: a regular filled material in which the filler-polymer affinity is controlled, and a system in which the beads in contact with the filler at the beginning of the production phase of the simulation are tethered to the filler surface. This second system represents the limit case of long polymer-filler attachment time. In this case attention is focused on the free chains of the melt.

In the filled system uniform slowing down for all Rouse modes is observed. The effect varies monotonically with the filer-polymer affinity. Let us consider the Rouse behavior of polymer chains in this filled system. The chains have a finite residence time on the surface of the filler, residence time that depends on the polymer-filler affinity parameter, w. The Rouse modes are computed from all chains in the system. The results are shown in Fig. 18, where the open squares represent the neat melt, while the filled circles represent the Rouse times of the filled system with $w = 1$. It is observed that modes corresponding to $p \leq 4$ are stretched in both neat and filled systems, with a stretch exponent 0.81 (the value of the stretch exponent is independent of w). Stretching is expected in the case of chains significantly longer than the entanglement length. Comparing the Rouse times of the filled and neat systems, it is observed that all modes of the filled system are slowed down by approximately the same amount for all p (the filled system has $\tau_p p^2/N^2$ approximately 11 % larger than the neat system). Similar conclusions have been obtained previously, for example, in the work of Smith et al. [68] who studied short chains in contact with fillers, Pryamitsyn and Ganesan [69] who performed extensive MD simulations of filled systems and Dionne et al. [35] who used lattice Monte Carlo to study the same model material.

In the system with grafted chains one follows the dynamics of the free chains which interact with the grafted chains, but do not interact with fillers directly. The free chain Rouse dynamics is identical to that in the neat material at high frequencies (high order modes), while the lower index modes are slower than in the neat polymer (Fig. 18). The slowing down of the free chains is due to the interaction

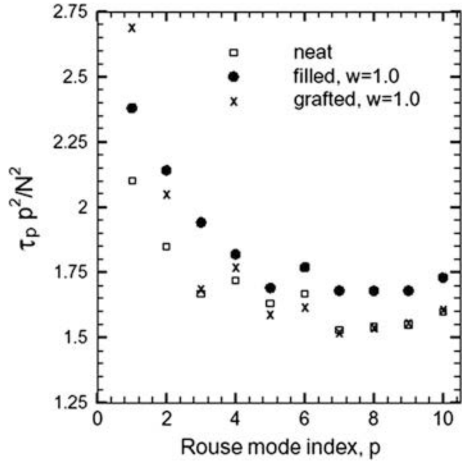

Fig. 18 Normalized rouse times corresponding to the first 10 modes of the neat polymer, filled and grafted systems with $w = 1$

with the slower chains of the brush. This effect can be captured only in part by classical models with a modified tube diameter.

The data in [67] also show that the dynamics of the free chains is controlled by *w* even though these chains do not interact directly with the filler. The short range polymer-filler interaction influences the structure of the brush which, in turn, affects the dynamics of the free chains in contact with it. Specifically, for small *w*, the brush is less compact and more free chains may intercalate. These free chains are significantly slowed down. As *w* increases, the brush gets compacted, “squeezing out” the free chains. The dynamics of the free chains in this case is comparable to that of the neat polymer. Hence, one concludes that the range of the effect of fillers on the dynamics of the surrounding matrix varies non-monotonically with *w*. An optimal *w* exists, for which the range is largest. A side conclusion is that making a polymeric brush poly-disperse postpones the de-wetting transition usually observed at large grafting densities.

The dynamics of chains residing at distances from filler surfaces larger than about $2R_g$ is indirectly modified by the presence of fillers. Their relaxation is slower than in the neat melt, but significantly faster than the relaxation of chains that come in direct contact with the filler or the region of density fluctuations next to its surface. The distance from the filler surface over which this effect persists could not be determined by direct simulations of such long-chain systems due to computing power limitations. However, based on our current understanding of this model, we estimate the range to be on the order of four or five R_g.

A Molecular Rheological Model of Nanocomposite Melts

Constitutive models are required in order to represent the deformation of the composite in continuum-scale simulations. Ideally, these models reflect the physics taking place on the molecular scale. Unfortunately, despite the vast literature dedicated to developing molecular rheology models, only relatively simple systems can be considered today. In this section we present an example referring to melts of linear chains interacting with spherical nanoparticles. This discussion is included in this chapter in order to demonstrate how one can link molecular simulations and rheological modeling, isolating essential physical processes observed in discrete-level simulations.

A set of constitutive equations that take into account the formation of a network of chains connecting fillers has been developed in Ref. [70]. To test the validity of this reinforcement mechanism, we investigate whether this network may lead to features akin to those observed in experiments. The situation envisioned is shown schematically in Fig. 10. A representative chain forms bridges between fillers, loops and dangling ends. The objective is to homogenize this system, i.e. to find constitutive equations describing the response of the ensemble. In absence of topological entanglements, the molecular structure is modeled using a combination of classical network theory and the elastic dumbbell model for poly-dispersed polymer segments and localized junctions. A junction represents an adsorbed polymer-filler attachment (A-point). A-points are reversible junctions and their time evolution is due primarily to the applied deformation, but fluctuations are possible in equilibrium. Hence, the destruction and creation of segments is a stochastic reversible process. The internal structure has a transient topology and its dynamics is controlled by the rate of the attachment and detachment process and depends on the applied deformation.

Let us consider an arbitrary representative volume element. The end-to-end vector for a typical bridging or dangling segment is denoted by $\mathbf{R}$. $\psi_i^j(R,t)$ is the distribution function of chain segments of type j. Here $j = B$ or $j = D$, where B stands for bridging segments and D refers to the dangling ends and loops. A loop of $2n$ monomers is visualized as two separate dangling segments each of length n. i represents the number of "beads" (Kuhn segments) in the respective chain segment. Hence, $\psi_i^j(R,t)\,\mathrm{d}R$ represents the number density of strands of type j composed of i beads, having end-to-end vectors in the range d$\mathbf{R}$ about $\mathbf{R}$. The total number density of this type of segments at time t is given by $N_i^j(t) = \int \Psi_i^j(\mathbf{R},t)\,\mathrm{d}\mathbf{R}$, where the integration is performed over the end-to-end vector configuration space.

Using the principle of local action, the time evolution of the distribution function for bridging segments is represented by the convection equation [71]

$$\frac{\partial \Psi_i^B}{\partial t} = -\frac{\partial}{\partial \mathbf{R}} \cdot (\Psi_i^B\,\dot{\mathbf{R}}) + G_i(\mathbf{R},t) - D_i(\mathbf{R},t), \tag{1}$$

where $G_i(\mathbf{R},t)$ and $D_i(\mathbf{R},t)$ represent the rate of generation and destruction of bridging segments per unit volume, respectively.

In general, there is no explicit form for the rate of generation and destruction functions in Eq. (1). These are described here by phenomenological relations based on the linear response theory. For example, the bridge destruction function is often taken to be proportional to the current distribution, i.e. [72]

$$D_i(R,t) = d_i(\mathrm{R})\psi_i^B(\mathrm{R},t) \tag{2}$$

where $d_i(\mathrm{R})$ is the detachment probability for A-points, and therefore the probability of failure of bridging segments per unit time.

The physical picture of the bridge formation rate is less obvious. The effect of flow is accounted for by including a term proportional to ψ_i^B in the equation for the rate of bridge formation:

$$G_i(\mathbf{R},t) = g_i(\mathrm{R})\Big(\lambda_i^B\,\Psi_{i,eq}^B(\mathbf{R}) - \Psi_i^B(\mathbf{R},t)\Big), \tag{3}$$

where $g_i(\mathrm{R})$ is the rate of A-point formation, and $\Psi_{i,eq}^B(\mathbf{R}) = \Psi_i^B(\mathbf{R},0)$. λ_i^B is a dimensionless constant to be determined, which is included in order to keep the formulation consistent at time $t = 0$ (in equilibrium). The functional form of $d_i(\mathrm{R})$ and $g_i(\mathrm{R})$ is Arrhenius. Detachment depends on an activation energy which is proportional to the energy of interaction between polymers and fillers and on the force pulling the respective strand from the surface (in non-equilibrium). Attachment occurs at all times when an empty spot exists on the surface, since sticky fillers surfaces are always saturated.

Equations 1–3 define the evolution of the distribution function $\Psi_i^B(\mathbf{R}, t)$ of bridging segments. A similar equation can be written for dangling ends. Its derivation is not presented here, but is given in full in [70].

Neglecting the contribution of entanglements, the total stress may be expressed as a superposition of contributions from bridging and dangling segments as:

$$\mathbf{T} = \sum_i (\mathbf{T}_i^B + \mathbf{T}_i^D), \tag{4}$$

where $\mathbf{T}_i^B$ and $\mathbf{T}_i^D$ represent the stress contribution of bridging and dangling strands of length i Kuhn units, respectively. These quantities are evaluated using the virial equation as $\mathbf{T}_i^B = \langle \mathbf{F}_i^B \, \mathbf{R} \rangle_B$ and $\mathbf{T}_i^D = \langle \mathbf{F}_i^D \, \mathbf{R} \rangle_D$. The brackets denote averaging over the respective configuration space. Substituting the expression of the entropic force using the Warner approximation to the inverse Langevin function, the stress tensor reads:

$$\mathbf{T} = \sum_i \frac{3k_B T}{il^2} \frac{\mathbf{B}_i}{1 - \frac{1}{(il)^2} \frac{Tr\,\mathbf{B}_i}{N_i^B}} + \frac{3k_B T}{il^2} \frac{\mathbf{D}_i}{1 - \frac{1}{(il)^2} \frac{Tr\,\mathbf{D}_i}{N_i^D}}, \tag{5}$$

where

$$\mathbf{B}_i(t) = \int \Psi_i^B \, \mathbf{RR} \, \mathrm{d}\mathbf{R}, \; \mathbf{D}_i(t) = \int \Psi_i^D \, \mathbf{RR} \, \mathrm{d}\mathbf{R} \tag{6}$$

and the end-to-end length of a Kuhn segment is denoted by l.

Equations (1)–(6) form a full set defining the constitutive model. The model requires the integration of the evolution Eq. (1) for the distribution functions of bridging and dangling segments of all lengths (all i), $\Psi_i^B(t)$ and $\Psi_i^D(t)$. These are functions of time and depend on the motion of fillers. The fillers are assumed to move affinely with the macro-deformation, $\dot{\mathbf{R}} = \mathbf{L} \cdot \mathbf{R}$ (although in MD simulations one observes thermal diffusion of fillers [67]), where $\mathbf{L}(t)$ is the macroscopic velocity gradient tensor (the tensor satisfies the incompressibility condition, $\mathrm{tr}\,\mathbf{L} = 0$). Hence, knowing $\mathbf{L}$ and with appropriate initial conditions for the distribution functions, one computes $\Psi_i^B(t)$ and $\Psi_i^D(t)$, and the total stress tensor $\mathbf{T}$(t).

In order to calibrate the model, one needs to evaluate using discrete models the number of bridging, dangling and loop segments and the details of the chain-filler attachment/detachment process. These issues are discussed in earlier sections of this chapter, respectively. The main conclusions, rephrased to conform with the notation of the model here are:

- A wide distribution of polydisperse bridging segments $\Psi^{B}_{i,eq}(\mathbf{R})$ exists (Fig. 11). The total number of bridging segments per filler decreases dramatically with the wall-to-wall distance, essentially vanishing when this parameter equals $2R_g$.
- Dangling ends form a wide distribution $\Psi^{D}_{i,eq}(\mathbf{R})$ including long and short segments (Fig. 12). The dangling segments follow approximately a Gaussian distribution of their end-to-end vectors at given i. The distribution depends on the wall-to-wall distance since as the fillers approach each other, part of the long dangling segments become bridges.
- A large number of loop segments form on the surface of each filler. Their distribution is rather narrow (Fig. 13) and the loops are short (relative to the other segment types). Their number per filler is independent of the filler wall-to-wall distance and is largely independent of the intensity and range of the attraction between polymers and fillers. The dense population of loops increases the effective filler radius, hence enhancing the hydrodynamic interaction between fillers and matrix at large deformations rates.
- It was observed that varying the affinity between polymers and fillers has no qualitative and little quantitative effect on the previous conclusions (regarding the polymer structure). The affinity has a strong effect on polymer dynamics.
- The attachment time of chains to fillers scales exponentially with the affinity parameter, w (Fig. 17).

Some results of this atomistically-informed constitutive model are shown in Fig. 19. The figure shows the storage and loss moduli of the composite (just the contribution from the transient network is represented) for systems with filler volume fraction of 6 and 12 %. The model predicts a feature usually seen in experiments performed with filled polymer melts: the appearance of a secondary quasi-plateau in G’ at low frequencies. This is the effect of the network of chains connecting fillers. The curve is continuously decreasing (not exactly horizontal)

Fig. 19 Storage moduls, G’, of nanocomposites with filling volume fraction 6 and 12 % versus frequency. Reproduced from [70]

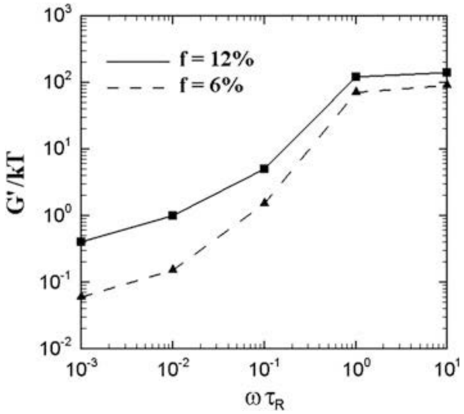

because the network is transient. G' is higher in the system with larger filling fraction due to the fact that the network is better defined when the filler wall-to-wall distance is small.

This discussion exemplifies how physical insight into the molecular scale behavior, as well as information obtained directly from fine scale models, can be used to develop and calibrate constitutive laws and hence to predict macroscopic properties of the material.

Closure

The macroscopic mechanical behavior of polymer-based nanocomposites is determined by a variety of physical processes taking place on multiple scales. Its understanding requires multiscale modeling and multiscale experimentation. This Chapter presents results from modeling and experimental works pertinent for various composite systems: matrix thermoplastic and thermoset materials, and fillers ranging from nanoparticles to carbon nanotubes and graphene. These systems exhibit very diverse properties and are characterized by diverse physics. This review makes no attempt to exhaustively summarize all aspects of the problem; rather it is aimed at outlining a number of possible approaches and several general guiding principles which may be useful in future targeted studies.

References

1. A.M. Bueche, J. Poly. Sci. **25**, 139 (1957)
2. M. Sumita, T. Shizuma, K. Miyasaka, K. Shikawa, J. Sci. Macromolec. **B22**, 601 (1983)
3. B. Kuriakose, S.K. De, S.S. Bhagawan, R. Sivaramkrishnan, S.K. Athithan, J. Appl. Poly. Sci. **32**, 5509 (1986)
4. P.M. Ajayan, L.S. Schadler, P.V. Braun (eds.), *Nanocomposites Science and Technology* (Wiley, New York, 2003)
5. E. Manias, Nat. Mater. **6**, 9 (2007)
6. P.B. Messersmith, E.P. Giannelis, Chem. Matls. **6**, 1719 (1994)
7. K.W. Putz, C. Mitchell, R. Krishnamoorti, P.F. Green, J. Sci. Poly. **B42**, 2286 (2004)
8. B.J. Ash, R.W. Siegel, L.S. Schadler, Macromolecules **37**, 1358 (2004)
9. D. Hull and T.W. Clyne, *An Introduction to Composite Materials* (Cambridge University Press, Cambridge, 1996)
10. W. Zhang, R.C. Picu, N. Koratkar, Appl. Phys. Lett. **91**, 193109 (2007)
11. J.C. Radon, Int. J. Fract. **16**, 553 (1980)
12. M.D. Skibo, R.W. Hertzberg, J.A. Manson, S.L. Kim, J. Mater. Sci. **12**, 531 (1977)
13. L. Becu, A. Maazouz, H. Sautereau, J.F. Gerard, J. Appl. Polym. Sci. **65**, 2419 (1997)
14. L. Rey, N. Poisson, A. Maazouz, H. Sautereau, J. Mater. Sci. **34**, 1775 (1999)
15. H.R. Azimi, R.A. Pearson, R.W. Hertzberg, Polym. Eng. Sci. **36**, 2352 (1996)
16. B.B. Johnsen, A.J. Kinlock, R.D. Mohammed, A.C. Taylor, S. Sprenger, Polymer **48**, 530 (2007)
17. A.J. Kinlock, R.D. Mohammed, A.C. Taylor, C. Eger, S. Sprenger, D. Egan, J. Mater. Sci. **40**, 5083 (2005)

18. B. Wetzel, P. Rosso, F. Haupert, K. Friedrich, Eng. Fract. Mech. **73**, 2375 (2006)
19. W. Zhang, I. Srivastava, Y.-F. Zhu, R.C. Picu, N. Koratkar, Small **5**, 1403 (2009)
20. W. Zhang, R.C. Picu, N. Koratkar, Nanotechnology **19**, 285709 (2008)
21. N. Koratkar, J. Suhr, A. Joshi, R. Kane, L.S. Schadler, P.M. Ajayan, S. Bartolucci, Appl. Phys. Lett. **87**, 063102 (2005)
22. F. Erdogan, P.F. Joseph, J. Am. Ceram. Soc. **72**, 262 (1989)
23. A.K. Geim, K.S. Novoselov, Nat. Mater. **6**, 183–191 (2007)
24. C.O. Compton, S.T. Nguyen, Small **6**, 711 (2010)
25. M.J. McAllister, Chem. Mater. **19**, 4396 (2007)
26. A. Zandiatashbar, R.C. Picu and N. Koratkar, Small, DOI: 10.1002/smll.201102686 (2012) in press
27. H.C. Schniepp, J.-L. Li, M.J. McAllister, H. Sai, M. Herrera-Alonso, D.H. Adamson, R.K. Prud'homme, R. Car, D.A. Saville, I.A. Aksay, J. Chem. Phys. **B110**, 8535 (2006)
28. M.A. Rafiee, J. Rafiee, I. Srivastava, Z. Wang, H. Song, Z.-Z. Yu, N. Koratkar, Small **6**, 179 (2010)
29. K. Kremer, G. Grest, J. Chem. Phys. **92**, 5057 (1990)
30. R.C. Picu, M.C. Pavel, Macromolecules **36**, 9205 (2003)
31. F.W. Starr, T.B. Schroder, S.C. Glotzer, Macromolecules **35**, 4481 (2002)
32. M. Vacatello, Macromolecules **34**, 1946 (2001)
33. M. Goswami, B.G. Sumpter, J. Chem. Phys. **130**, 134910 (2009)
34. F.W. Starr, J.F. Douglas, S.C. Glotzer, J. Chem. Phys. **119**, 1777 (2003)
35. P.J. Dionne, R.C. Picu, R. Ozisik, Macromolecules **38**, 9351 (2005)
36. R.F. Rapold, W.L. Mattice, Macromolecules **29**, 2457 (1996)
37. J. Cho, W.L. Mattice, Macromolecules **30**, 637 (1997)
38. P. Doruker, W.L. Mattice, Macromol. Theor. Simul. **8**, 463 (1999)
39. R. Ozisik, P. Doruker, W.L. Mattice, E.D. von Meerwall, Comput. Theor. Polym. Sci. **10**, 411 (2000)
40. T.C. Clancy, M. Putz, J.D. Weinhold, J.G. Curro, W.L. Mattice, Macromolecules **9**, 452 (2000)
41. S. Sen, J.M. Cohen, J.D. McCoy, J.G. Curro, J. Chem. Phys. **101**, 9010 (1994)
42. P.G. de Gennes, Adv. Colloid Interface Sci. **27**, 189 (1987)
43. J.M.H.M. Scheutjens, G.J. Fleer, J. Phys. Chem. **83**, 1619 (1979)
44. J.M.H.M. Scheutjens, G.J. Fleer, Macromolecules **18**, 1882 (1985)
45. Y. Zhan, W.L. Mattice, Macromolecules **27**, 7056 (1994)
46. K.F. Mansfield, D.N. Theodorou, Macromolecules **24**, 6283 (1991)
47. S.K. Kumar, M. Vacatello, D.Y. Yoon, Macromolecules **23**, 2189 (1990)
48. A. Yethiraj, J. Chem. Phys. **101**, 2489 (1994)
49. E. Eisenriegler, K. Kremer, K. Binder, J. Chem. Phys. **77**, 6296 (1982)
50. I.A. Bitanis, G. ten Brinke, J. Chem. Phys. **99**, 3100 (1993)
51. R.L. Jones, S.K. Kumar, D.L. Ho, R.M. Briber, T.P. Russell, Nature **400**, 146 (1999)
52. J. Kraus, P. Muller-Buschbaum, T. Kuhlman, D.W. Schubert, M. Stamm, Europhys. Lett. **49**, 210 (2000)
53. G. Allegra, G. Raos, M. Vacatello, Prog. Polym. Sci. **33**, 683 (2008)
54. A. Kloczkowski, M.A. Sharaf, J.E. Mark, Chem. Eng. Sci. **49**, 2889 (1994)
55. Q.W. Yuan, A. Kloczkowski, J.E. Mark and M.A. Sharaf, J. Poly. Sci. Poly. Phys. **34**, 1647 (1996)
56. A.I. Nakatani, W. Chen, R.G. Schmidt, G.W. Gordon, C.C. Han, Polymer **42**, 3713 (2001)
57. M. Vacatello, Macromolecules **35**, 8191 (2002)
58. M.S. Ozmusul, R.C. Picu, Polymer **43**, 4657 (2002)
59. R.C. Picu, M.S. Ozmusul, J. Chem. Phys. **118**, 11239 (2003)
60. T. Pakula, J. Chem. Phys. **95**, 4685 (1991)
61. E.B. Zhulina, T. Pakula, Macromolecules **25**, 754 (1992)
62. T.C. Clancy, S.E. Webber, Macromolecules **26**, 628 (1993)
63. M.S. Ozmusul, R.C. Picu, S.S. Sternstein, S. Kumar, Macromolecules **38**, 4495 (2005)

64. S.S. Sternstein, A.J. Zhu, Macromolecules **35**, 7262 (2002)
65. A. Zhu, S.S. Sternstein, Compos. Sci. Technol. **63**, 1113 (2003)
66. P.J. Dionne, R.C. Picu, R. Ozisik, Macromolecules **39**, 3089 (2006)
67. R.C. Picu, A. Rakshit, J. Chem. Phys. **126**, 144909 (2007)
68. G.D. Smith, D. Bedrov, L. Li, O. Byutner, J. Chem. Phys. **117**, 9478 (2002)
69. V. Pryamitsyn, V. Ganesan, Macromolecules **39**, 844 (2006)
70. A.S. Sarvestani, R.C. Picu, Polymer **45**, 7779 (2004)
71. R.B. Bird, R.C. Armstrong, O. Hassager, *Dynamics of Polymeric Liquids* (Wiley, New York, 1987)
72. N. Phan Thien, R.I. Tanner, J. Non-Newtonian Fluid Mech. **2**, 353 (1977)

Carbon Nanotubes and Safety

Classification of Carbon Nanotubes, Size Effects and Potential Toxicity of the High-Aspect Ratio Nanotubes

Vasyl Harik

Abstract This chapter reviews geometry of different classes of carbon nanotubes and examines similarities between carbon nanotubes and asbestos fibers. Geometric parameters of carbon nanotubes are characterized by the aspect ratios and other critical scaling parameters related to the inhalability of carbon nanotubes and their engulfment by macrophages in phagocytosis. Geometric and scaling parameters are used to present a conceptual framework and a parametric map for the extrapolation of potential toxic effects resulting from the inhalation of carbon nanotubes. Similarities between carbon nanotubes and asbestos fibers are also examined by using the Cook's criteria for the asbestos-like pathologies that can be also caused by microscopic fibers. Scaling parameters for the size effects associated with carbon nanotubes and a new parametric map for the efficiency of phagocytosis are used to evaluate the potential toxicological effects of the inhaled carbon nanotubes from the point of view of the Cook's criteria for asbestos fibers and other research.

Dr. V.M. Harik, f. ICASE Staff Scientist at the NASA Langley Research Center (Hampton, VA), Principal Scientist at Nanodesign Consulting, author of a monograph and a short course entitled "*Mechanics of Carbon Nanotubes*" © (2001) presented at the Annual ASME Congress (2001 & 2004) and a co-editor of Kluwer volumes: "*Trends in Nanoscale Mechanics*" (2003) and "*Micromechanics and Nanoscale Effects*" (2004).

Nanodesigns Consulting is a 2004 spin-off from the NASA Langley Research Center, Hampton, Virginia. Its Staff consulted for the Princeton-based NASA-funded URETI Institute for Nanostructured Bio-inspired Materials (http://bimat.org), National Institute of Aerospace (Hampton, VA), University Space Research Association (USRA) and NASA NAIC (Atlanta, GA).

V. Harik (✉)
Nanodesigns Consulting, P.O. Box 5303, Wilmington, DE 19808-5303, USA
e-mail: Harik@nanodesignconsult.com

V. Harik (ed.), *Trends in Nanoscale Mechanics*, DOI 10.1007/978-94-017-9263-9_8

Introduction

Microscopic particles such as commercial powders, various aerosols, airborne particulate pollutants, exhaust particulates and allergens have been a part of industrial and natural air pollution for a long time. However, the mechanical and physical properties of individual microparticles have never aroused so much interest as in the case of carbon nanotubes. Nanotechnology of carbon nanotubes has been widely expected to result in significant advances in miniaturization, efficiency and complexity of various products (Table 1) and materials, especially, in electronics, multifunctional materials and healthcare industries. However, nanoscale particles and carbon nanotubes, in particular, are also a cause for serious safety concerns. In 2013 a large German corporation, Bayers, has evaluated the mounting potential health and safety risks as well as financial costs of the production and the use of carbon nanotubes and decided to stop its company-wide utilization of these nanoparticles. Even earlier NASA Langley Research Center in Hampton, Virginia, has shifted its focus away from carbon nanotubes as a significant component of new advanced materials systems.

Concerns about safety of new nanoscale particles have nothing to do with the so called "nano-myths" about the dangerous "gray goo" or nano-robots. The British Royal Academy of Engineering, the British Royal Society [1] and others have pointed out the evidence that "at least some manufactured nanoparticles are more toxic than the same chemical in its larger form." This report was among the first to point out that "size matters". The toxicity of ultrafine powders is known to increase with the larger surface area and, hence, higher surface reactivity [1]. These further details suggest that the "size matters" because the surface area does, especially, at the nanoscale level. The impact of nanoparticle toxicity on human health, safety regulations and manufacturing environment can be enormous. For years small pollutant particles from vehicle exhaust and industrial emissions have been linked to a rise in heart and lung problems. Nanoparticles, in fact, are so small that they become easily airborne and may be inhaled and absorbed with unforeseen bad health consequences. The most plausible consequences are irritation and low-level

Table 1 Potential industrial applications of carbon nanotubes

Electronic applications	Nanodevices and probes	Other applications[a]
Nanoscale circuits	NEMS, MEMS, nano-tools	Multifunctional materials
Nanoscale electrodes	Nanoscale resonators	Polymer nanocomposites
Nano-transistors, nano-chips	Energy conversion devices	Nanostructured adhesives
Nanoscale capacitors	Photovoltaic elements	EM absorption/shielding
Nanoscale lithography	Lithium-battery anodes	Nanotube composites
Electron field emitters	Nano-probes: STM, AFM	Nanotube covered fibers
Cathode ray lighting elements	Nano-sensors, actuators	Hydrogen storage
Superconductors	Nanoscale strain sensors	Drug delivery, implants
Flat panel displays	Novel super-capacitors	Hazardous waste cleaners

[a] For more details on applications of carbon nanotubes see www.nanodesignconsult.com

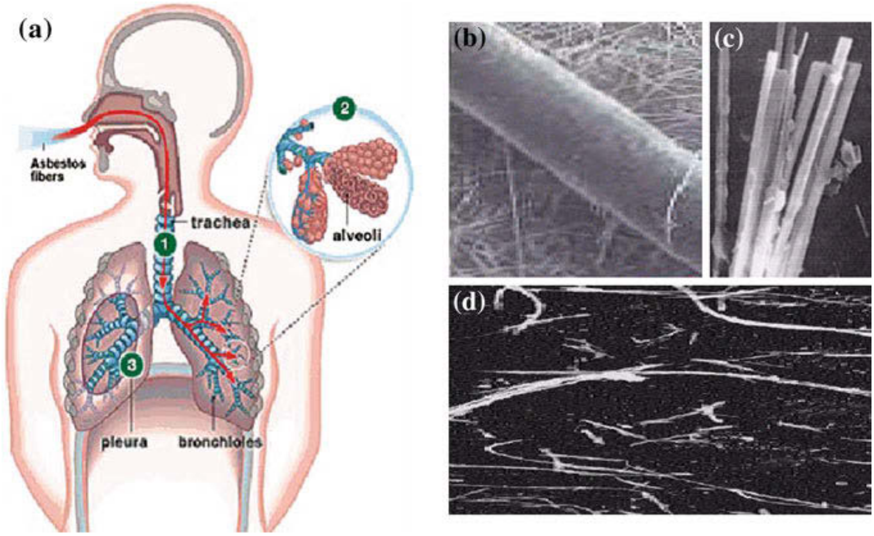

Fig. 1 A schematic of asbestos transport (**a**) in the human lungs with (*1*) trachea, (*2*) alveoli and (*3*) pleura. Amosite asbestos fibers (**b**) are shown below a human hair, next to a bundle of rod-like crocidolite asbestos fibers (**c**) along with the bundles (**d**) and fibrils of chrysotile asbestos fibers (After Cook [2]). "When you represent the lung make it perforated so that it may not obstruct what is behind it, and let the perforation be all the ramifications of the trachea and the veins of the artery (aorta) and of the vena cava and then outside these draw a contour line round about them to show the true shape, position and extent of this lung." Leonardo da Vinci (1452–1519), Anatomy, p. 173, *The Notebooks of Leonardo da Vinci* (edited by E. MacCurdy, Konecky and Konecky printing, Duckworth and Co., London, 1906)

inflammatory processes that may be detrimental to human health, especially, with longer exposures.

Hazardous properties of microscopic fibrous particles such as asbestos have been known for decades [2, 3]. Inhalation of these particles (see Fig. 1) has been shown to cause different diseases of the lung and its lining tissue. Most of these diseases prove to be fatal, as the harmful particles reach the gas-exchanging part of the lung and most of them cannot be readily removed by macrophages. Human immune system has no defenses against such hazards. Natural or man-made fibers do not have to be asbestos to be toxic. High toxicity is due to larger surface area, higher surface reactivity and potential absorption of other chemicals. Safety concerns can become even higher when toxicity of some nanoparticles is significantly increased by the absorption of other harmful chemicals. The ability of carbon nanotubes to absorb various chemicals on their surface is proportional to their geometric size or the surface area. Therefore, potential toxic effects of carbon nanotubes can be analyzed by using scaling analysis and the scaling parameters based on their geometric size [4–7] or their surface area [8–10].

It is worth mentioning that carbon nanotubes and carbon particles, in general, are highly porous, and they are specifically used now in protective masks to absorb hazardous gases. While the porosity of nanoparticles such as carbon nanotubes could be beneficial for hydrogen storage, say, their toxicity may be exceptionally dangerous when they are treated with various acids and other corrosive chemicals. Porosity of carbon nanotubes is also proportional to their geometric size or, more importantly, to their volume. Therefore, potential toxic effects of carbon nanotubes can be analyzed as was mentioned earlier by using again the scaling parameters based on their geometric parameters.

The size of surface area of car bon nanotubes and their volume both depend on their geometric parameters, i.e., radius, R_{NT}, or diameter, d_{NT}, and the length, L_{NT}. In 2004 Cook from the National Health and Environmental Effects Research Laboratory in Duluth, Minnesota, was first to propose using the “size and shape” of microscopic fibers and their total “surface area” in his criteria for the asbestos-like pathologies [2]:

- size and shape of particles that allow respiration and retention in lungs;
- size and shape of particles that allow translocation to pleura;
- durability of fibers, persistent contact in tissues;
- reactive surfaces, ability to induce oxidative stresses;
- high collective surface area; and
- propensity to split into thin fibers in vivo.

In his report, he also referred to the similarities between carbon nanotubes and asbestos fibers. In 2005 the conceptual framework of dimensional analysis [3–7], its scaling parameters and the laws of similitude have been used to more rigorously demonstrate the geometric similarities between asbestos fibers and carbon nanotubes as well as between their properties associated with the ability to cause potentially toxic effects [3]. The quantitative characteristics of the “size and shape” of carbon nanotubes have been employed in the scaling analysis and its results have been utilized for the development of methodology for extrapolation of the potential toxic effects associated with the inhaled nanotube (NT) shells [3].

The early toxicological studies on mammals [11–14] can also benefit from a methodology for the extrapolation of their assessment of nanotube toxicity in lung tissues of rats and human cells to other similar cases as defined by the scaling analysis and the so called laws of similitude [4–7]. In studies carried out at NIOSH [15], Du Pont and NASA [11–14] nanotubes were instilled rather than inhaled in a natural manner. Nevertheless, these *studies clearly demonstrate that carbon nanotubes are indeed toxic*, thus, confirming earlier extrapolations [1–3]. In some of these studies, entanglement of nanotubes has resulted in large clusters/clumps and a blockage of airways and intra-airway fibrosis. As was mentioned earlier, inhalation of small clumps or bundles may also lead to problems for normal lung defenses, including the possibility of increasing surface area during separation of single nanotubes or smaller bundles by the action of lung surfactants or cellular mechanisms.

In 2006 Stone and Donaldson [16, 17] and, especially, Kostarelos from the School of Pharmacy of the University of London have shown in 2008 that the “size does matters” in his study of “the long and short carbon nanotubes toxicity” [16, 17] and the engulfment of various nanotubes by macrophages in phagocytosis in lungs. In this chapter we show that the process of phagocytosis in lungs and its effectiveness can be analyzed by using scaling analysis [3–7] and a scaling parameter based on the length of carbon nanotubes and the size of macrophages. This method provides a quantitative framework to analyze experiments on phagocytosis of engulfed nanoparticles such as carbon nanotubes or other particles in the macrophages. The effectiveness of phagocytosis, the rate of engulfing process and the probability of complete phagocytosis can be characterized within the framework of such scaling analysis.

In 2009 Jaurand et al. [18] have examined the size effects on the toxicity of multiwall carbon nanotubes (MWCNTs) and their similarities with asbestos fibers and demonstrated that the size of carbon nanotubes, especially, their length, affects the initiation of inflammation in lungs. In 2008 Poland et al. [19] have shown that the length of carbon nanotubes is linked to the asbestos like pathologies in mice. Later the same team Donaldson et al. [20] have confirmed these results in toxicological studies for pleura and attributed them to the so called structure-activity paradigm for the length-dependent toxicity of microscopic fibers. In 2010 Yamashita et al. [21] have also demonstrated that the long MWCNTs cause the most inflammation and DNA damage, as opposed to the short and thin MWCNTs. It should be noted that the larger length of carbon nanotubes increases their surface area and, hence, the area of interaction between deposited nanotubes and biological tissues. Interactions between the surface of a foreign material particle may have chemical, bio-chemical, dynamic and mechanical nature. It turns out that geometric parameters of microscopic fibers and carbon nanotubes affects the degree of harmful interactions with biological tissues. In this chapter, scaling parameters for the normalization of surface area and nanotube length (i.e., aspect ratio) are discussed in the conceptual framework for the extrapolation of potential toxic effects of the inhaled carbon nanotubes.

Geometry of Carbon Nanotubes and Potential Toxic Effects

The structure-activity paradigm [20] for the toxicological studies of carbon nanotubes can benefit from better understanding of the structural properties of carbon nanotubes and their dependence on geometric parameters of these nanoscale fibers. In 2001 shortly after the National Nanotechnology Initiative was introduced a research study [4–7] performed at the NASA Langley Research Center in Hampton, Virginia, has presented the first *classification of carbon nanotubes* into four classes: *thin and thick lattice shells, long high-aspect-ratio nanotubes and beam-like carbon nanotube crystals of small radii* (Fig. 2), where a modified classification of carbon nanotubes is shown to explicitly specify a sub-class of the long high-aspect-ratio nanotubes, i.e., the extra-long carbon nanotubes (the fifth class of the X-long NT shells).

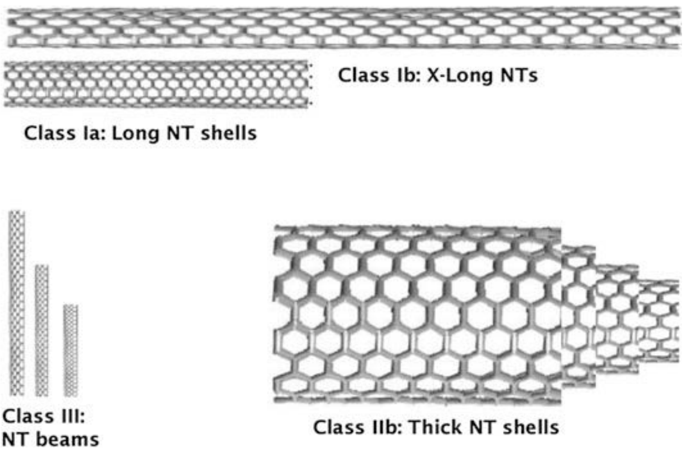

Fig. 2 The modified 2001 classification of carbon nanotubes (C_{NT}) into different classes (after [16–19]): *the long* C_{NT} *shells* (Class Ia, i.e., the high aspect ratio C_{NT} shells), *the extra-long high aspect ratio* C_{NT} *shells* (Class Ib), *the thick* C_{NT} *shells* (Class IIb, while *the thin* C_{NT} *shells* form Class IIa), and the C_{NT} *nano-beams* (Class III)

Carbon nanotubes with large values of radius, R_{NT}, have larger surface area, i.e., $A_{NT} = 2\pi R_{NT} L_{NT}/a^2$, where it is normalized [4–10] by the size of a carbon ring, a. Since the ring size a is about $2.46\ \mathring{A}$, i.e., the smallest structural element of a carbon nanotube lattice, the long carbon nanotubes ($L_{NT}/a >> 1$) and the thick carbon nanotubes ($R_{NT}/a >> 1$) also tend to have larger surface area. Note that the normalized surface area includes the product of two non-dimensional scaling parameters: the normalized nanotube length, L_{NT}/a, and the normalized radius, R_{NT}/a. It should be noted that Yamashita et al. [21] have shown that the long and thick MWCNTs results in more inflammation, as opposed to the short and thin MWCNTs. The large surface area of the engulfed carbon nanotubes needed to be covered by the macrophages in phagocytosis results in the oxidative stress and inflammation (see Table 2, where L_{NT} can be up to 500 µm).

Donaldson et al. [20] have conducted toxicological studies for pleura and stressed the importance of the structure-activity relations and the high aspect ratios in the length- and the aspect-ratio-dependent toxicity of various fibers. Table 2 presents a summary of different toxicological studies [18, 19] in the form demonstrating the role of aspect ratios on the initiation of inflammation during in vivo experiments. Donaldson et al. [20] have also emphasized the ability of the high aspect ratio particles (HARP) to cause toxic effects (e.g., the extra-long high aspect ratio carbon nanotubes or (HARCNT), see Fig. 2). All these studies show that the long and relatively thick carbon nanotubes (class Ib), especially, with the aspect ratios above 100, are likely to cause inflammation and potentially toxic effects. Propensity of the long high aspect ratio carbon nanotubes to split in vivo and

Table 2 Size of carbon nanotubes and their potential health effects (in vivo studies)[a]

Aspect ratio, d_{NT}/L_{NT}	Dose and exposure	Resulting effects
Between 1/12500–1/8	1–7 mg/kg (1–90 days)	Inflammation
Between 1/35–1/14	2 mg/rat (3 and 60 days)	Inflammation (3 days) granulomas (60 days)
About 1/20	40 g/mouse (4 h)	Inflammation
Between 1/1250–1/83	50 mg/mouse (24 days)	Inflammation, oxidative stress, coagulation
Between 1/606–1/121	50 mg/mouse (24 h, 7 days)	Inflammation
Between 1/250–1/125	40 mg/mouse (4 h)	Inflammation, oxidative stress, coagulation
Between 1/470–1/388	50 mg/mouse (24 h, 7 days)	Inflammation

[a] This Table is based on the summary information presented in [12, 13] without the aspect ratios

behave similarly to microscopic asbestos fibers has been also pointed out in the extrapolation methodology based on the scaling analysis of nanotube geometry [3].

The inhaled nanoscale particles belonging to the class of short or thin carbon nanotubes (e.g., the class III) are easily engulfed by macrophages and cleared from the lungs through the lymphatic system [11, 14]. Kostarelos [16, 17] and Donaldson et al. [20] have shown that the "size does matters" both for the ability and for inability of macrophages to engulf and process various nanotubes as illustrated in Fig. 3. A non-dimensional scaling parameter, M_{ph}, based on the ratio of the nanotube length, L_{NT}, and the average size of macrophages, L_m, i.e., $M_{ph} = L_m/L_{NT}$, can be used to evaluate the ability of macrophages to perform an effective phagocytosis in lungs. If $M_{ph} > 1$ then the length of carbon nanotubes is such that macrophages are able to clear these nanoparticles from the lungs or the probability of the effective phagocytosis is being greater than 1. If carbon nanotubes have very high aspect ratios then $M_{ph} < 1$ and the probability of the effective phagocytosis is less than unity (see Fig. 3). A distribution of carbon nanotube sizes or lengths can provide a distribution of probabilities for the effective phagocytosis in different parts of the lungs depending on where different nanotubes settle according to their length, local penetrability and transport processes.

It is understandable that Donaldson et al. [20] have found that the high aspect ratio particles (HARP) or the extra-long high aspect ratio carbon nanotubes (HARCNT) may cause potentially toxic effects. Note that the non-dimensional scaling parameter, M_{ph}, for such nanoparticles is very small, i.e., $M_{ph} << 1$, so the probability of the effective phagocytosis is much less than unity. These nanoparticles belong to the class Ib nanotubes (Fig. 3). For smaller nanotubes, probability of the effective phagocytosis for the class III nanotubes, say (Fig. 2), is greater than unity, because the scaling parameter, M_{ph}, is such that $M_{ph} > 1$. The process of phagocytosis of these nanotubes is illustrated in Fig. 3. The thick carbon nanotubes belonging to the class IIb may also result in the incomplete phagocytosis and cause oxidative stresses (Fig. 3). In these cases, a scaling parameter, $M_{ph\text{-}R} = L_m L_m/$

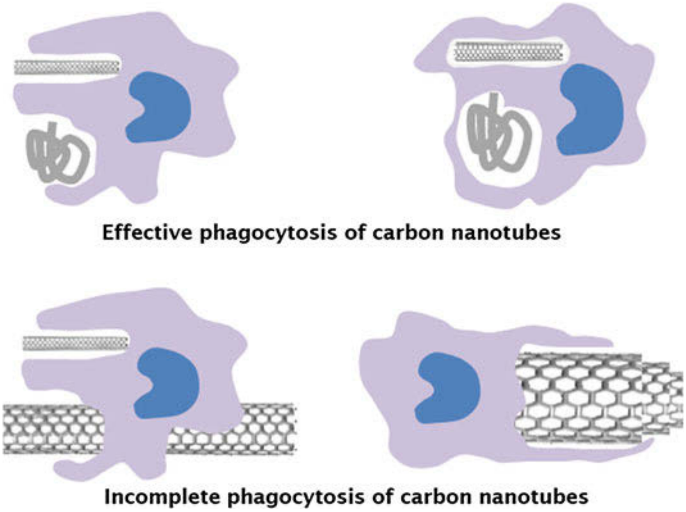

Fig. 3 Illustration of successful engulfment of short and the curled carbon nanotubes or their bundles in the process of effective phagocytosis in macrophages and incomplete phagocytosis of the thick and the long high aspect ratio carbon nanotubes

$R_{NT}L_{NT}$, can be used. It is based on both the radial and longitudinal sizes of carbon nanotubes and represents a non-dimensional ratio of the surface area of macrophages and that of carbon nanotubes. Note that the process of phagocytosis satisfies the law of the conservation of mass, which is reflected in the illustrations of Fig. 3. The relevance of non-dimensional scaling parameter, $M_{ph\text{-}R}$, to the process of engulfment of carbon nanotubes is also connected to the law of the conservation of mass as it characterizes a relation between the merging surface areas.

The long and very thin carbon nanotubes are prone to the spontaneous buckling [22] and coiling, which may limit their linear size and result in a better phagocytosis than originally expected (see Fig. 4). In such cases, the scaling parameter, M_{ph}, should be based on the effective size of the newly formed nanotube bundles and not on their original total length. Nanotube bundles may deform in vivo as long nanotubes have to adjust and often buckle under the ambient pressure and surface interactions, which depend on the type of biological cells and tissues being present. The value of the scaling parameter, M_{ph}, is also indicative of the rate of phagocytosis and the rate of engulfing carbon nanotubes depending on their size, i.e., the smaller the parameter M_{ph} the lower rate of the process of engulfing and, hence, the lower rater of phagocytosis. The size and the vitality of the local cells in the lung tissue directly affect the rate of phagocytosis. Moreover, in different parts of the lungs with distinct nanotube sizes being settled there the rate of phagocytosis will be different. Therefore, the map of the values of parameter M_{ph} is useful for representing variations of the rate of phagocytosis across the lungs with different regions of biological tissues and varying sizes of cells.

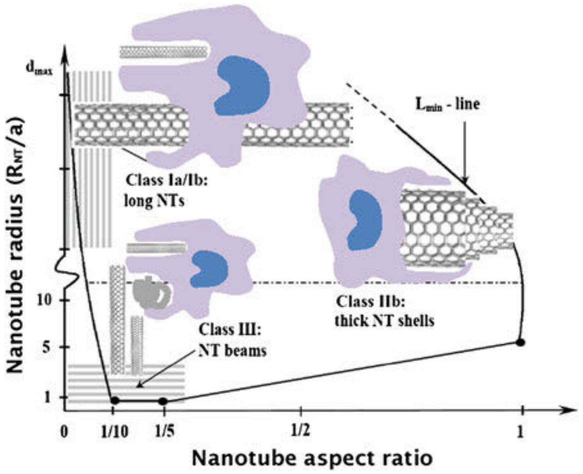

Fig. 4 A map of carbon nanotube parameters showing different classes of carbon nanotubes (after [19]) and the corresponding type of incomplete or effective phagocytosis. The engulfment of carbon nanotubes of distinct sizes and shapes by the macrophages is illustrated

According to the laws of similitude the research results on one type of phagocytosis for a group of similar carbon nanotubes extends to the entire class of carbon nanotubes (Fig. 2) to which that group belongs. Different carbon nanotube geometries in one class and the corresponding type of phagocytosis (Fig. 3) can be described by a set of geometric parameters and be represented on a parametric map (Fig. 4). It is not surprising that the region on the (R_{NT}/a)-(d_{NT}/L_{NT}) parametric map corresponding to the long high aspect ratio and thick carbon nanotubes shows the most ineffective phagocytosis (see Fig. 4 for the region, where R_{NT}/a and $(d_{NT}/L_{NT})^{-1}$ are large). Distribution of carbon nanotube sizes also may result in the bundles of different shapes and sizes, which undergo varying processes of phagocytosis. Hence, different parts of a bundle may take part in distinct types of phagocytosis. If the long high aspect ratio carbon nanotubes are surrounded by short and thin nanotubes then the ineffective phagocytosis will become even more difficult. This is a consequence of the law for the conservation of mass of macrophages during phagocytosis. It should be also noted that the high concentration of long nanotubes impedes even the basic fluid transport as demonstrated in Fig. 5.

The Concepts of Dose and Exposure at the Nanoscale Level

The concept of *hazard* is defined as the potential of a substance to cause harm. The content of this and other concepts, their meaning as well as the mechanisms of causing harm may, in fact, change at nanoscale. A more quantitative analysis, which is capable to take into account different scales as in the scaling analysis, is

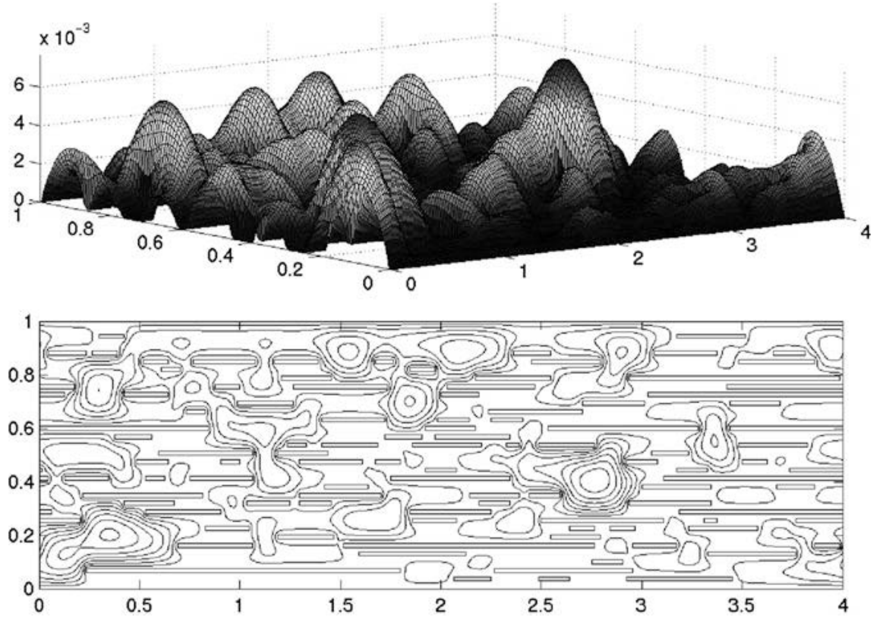

Fig. 5 Viscous fluid flow with the velocity distribution (*above*) and the stream lines (*below*) around numerous microscopic particles distributed in a viscous flow under a small axial pressure gradient. Velocity is vanishing along the *upper* and *lower* walls. The *left* and *right* boundaries are open to the flow (numerical simulations by Diskin and Harik [23])

needed. From the viewpoint of the scaling analysis, nanoparticles indeed have higher total area of the surface contact and reactions with biological tissues than their microscopic counterparts and greater ability to pierce or penetrate through the cells and membranes. The greater area for the surface contacts and material interactions in the body results in an increased ability of nanoparticles to take part in reactions with cells, including the tissue-damaging reactions. For example, surface of the quartz crystal is highly reactive. It generates free radicals (reactive atoms), which lead to oxidative damage to the defensive cells [1].

It should be noted that non-reactive surfaces can also generate oxidative stresses on the cells. Some investigations have shown that, weight for weight, finely divided particles of a material, such as titanium dioxide or carbon black, have been more toxic than larger particles of the same material. Surface area and its reactivity seem to be fundamental to the toxicity of particles and nanoparticles, in particular. Precise measurements of the surface area at the nanoscale level depend on the definition of the effective radius of curved nanoscale structures (see [22]).

Exposure to a hazardous material is defined as the *concentration* of the substance in the relevant medium (air, food, water or tissue) multiplied by the duration of contact [1]. *Concentration* of particles is the number of particle per unit volume (see Fig. 5). At the same weight, the number of nanoparticles is much greater than that of microscopic particles, and, hence, their concentration would be considerably higher for the same weight-to-bio-volume ratio. Higher concentration of microscopic particles also impedes even the basic transport of viscous fluid around long or short but dense microparticles in either biological or non-biological setting (as shown in Fig. 5).

Different batches of carbon nanotubes having the same weight but different geometries corresponding to distinct class of nanotubes will have varying concentrations for the same weight-to-volume ratio. This ratio defines a dose; a *dose* is the amount of a substance that will reach a specific biological system or an organ. Consequently, the exposure and a dose will be both higher for nanoscale particles. Both the exposure and the dose will vary from one distribution of carbon nanotube sizes to another. Therefore, the parametric map shown in Fig. 4 can be also used to characterize variation of the exposure and the dose resulting from different classes of carbon nanotubes. The exposure may be further increased by the ability of nanoparticles to have a better interfacial contact and higher surface energy of adherence, and, hence, the longer duration of contact.

Surface Interactions of Carbon Nanotubes

Other nanoscale carbon fibers similar to carbon nanotubes as well as some functionalized carbon nanotubes may induce considerable inflammation and oxidative stresses when they are inhaled and deposited into lungs. Numerous studies [1] of air pollutants, dusts of mineral particles and pharmaceutical powders indicate that the toxicity of various nanoparticles within the structure-activity paradigm [20] depends on

- the total particle-surface area presented to a target organ;
- the chemical reactivity of the entire surface with absorbents; and
- the longitudinal time or duration of bio-contact.

In the previous section, a brief discussion is presented on how the nanoscale increases in the nanoparticle-surface area affect the concepts of dose, concentration and exposure. The role of chemical reactivity of the nanotube surface has to be addressed as well. It should be mentioned, for example, that in the lab-scale manufacturing, purification and handling, carbon nanotubes are often accompanied by small particles of amorphous carbon, graphite and various catalysts (Fe, Ni, Co, etc.). Treatment of carbon nanotubes by various chemical solvents and surfactants may also result in absorbed additives, which may dramatically alter the surface properties of nanotubes to allow degradation (Fig. 6) as well as increase or decrease their potential toxic effects.

It is safe to assume that the surface reactivity of carbon nanotubes is often modified by the catalytic transition metals and the process-induced coatings. As a result, the ability of such modified surfaces to take part in oxidative reactions that release free radicals or other reactions is beyond any doubts. For example, carboxylate-functionalized single wall carbon nanotubes (SWNTs) can degrade during

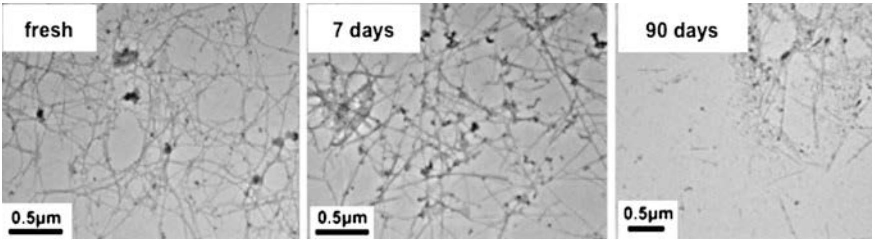

Fig. 6 Biological response to carboxylate-functionalized single wall carbon nanotubes involving degradation of carbon nanotubes during 90 days in phagolysosomal simulant fluid (Shown by Robert Hurt, Brown University) ("When you represent the lung make it perforated so that it may not obstruct what is behind it, and let the perforation be all the ramifications of the trachea and the veins of the artery (aorta) and of the vena cava and then outside these draw a contour line round about them to show the true shape, position and extent of this lung." Leonardo da Vinci (1452–1519), Anatomy, p. 173, *The Notebooks of Leonardo da Vinci* (edited by E. MacCurdy, Konecky and Konecky printing, Duckworth and Co., London, 1906))

90 days in phagolysosomal simulant fluid as shown by Hurt[1] of Brown University (Fig. 6). The size of carbon nanotubes, as was noted before, affects their total surface area, which takes part in the reactions with the surrounding fluid.

The carcinogenic toxicity depends on the inhalation, deposition and absorption of a large number of carbon nanotubes into the lungs. While inhalation of a small number of various nanoparticles is unlikely to represent a significant risk, *the longitudinal time-history of the at-organ environment* should be considered to assess the carcinogenic toxicity dose of specific nanoparticles. For example, the presence of various pro-inflammatory agents and fermentation promoting bacteria would enhance pre-carcinogenic processes. The negative health effects associated with the inhalation of a very large number of carbon nanotubes and other nanoparticles in manufacturing processes, can be controlled by federal regulations, along with other industrial components of the workplace safety.

Physical dimensions of nanoparticles, which are used in industry, affect their interactions with other materials, their aerodynamic properties and behavior, clustering and their ability to be suspended in the air and become inhaled. The transport of nanotubes in the inhalation flows through the airways determines what proportion of nanotubes reaches the deep lungs and where they are deposited in the lungs. The small size of carbon nanotubes (diameter of 1 nm or more; length of 100 nm or more) allows a high portion of these particles to be inhaled from the air, transported and deposited in the deep lung. The nanoscale size of nanotubes and their bundles may increase their transportability and penetrability, and, hence, the direct impact of the at-organ concentration and exposure as well as the toxicity of carbon nanotubes. The nanoscale size of nanotubes may also influence their uptake into various cells and, thus, the duration of toxic bio-contact. Therefore, *the nanoscale size of*

---

[1] R. Hurt, Which material properties/features determine the biological response to carbon nanotubes? Brown University, Providence, Rhode Island, 2011.

nanotubes is one of the critical factors in their toxicity, as it intrinsically affects the overall concentration and the total surface area per unit mass (i.e. the dose) along with the cell damage and the duration of bio-contact.

Conclusions

Geometry of different classes of carbon nanotubes has been characterized by the aspect ratios and other critical scaling parameters related to the efficiency of their engulfment by the macrophages in phagocytosis. Geometric and scaling parameters have been used to present a conceptual framework and a parametric map for the extrapolation of potential toxic effects resulting from the inhalation of carbon nanotubes. Similarities between carbon nanotubes and asbestos fibers are also noted within the framework of the Cook's criteria for the asbestos-like pathologies. Scaling parameters for the size effects associated with carbon nanotubes and a new parametric map for the efficiency of phagocytosis are used to evaluate the potential toxicological effects of the inhaled carbon nanotubes from the point of view of the Cook's criteria for asbestos fibers and other research. In 2007 Salvador-Morales has concluded with colleagues [24] that

> Currently, it is important to point out that regardless of the inaccuracy of the methodology used to investigate the pulmonary toxicity of carbon nanotubes, the major conclusion is that [the high aspect ratio] carbon nanotubes are toxic to some extent. This is based not only in the trend that can be observed in all the most recent papers in this area but also on the analogies that exists in the toxicity (size and morphology) with other well-characterized toxic materials such as asbestos and carbon black.

This conclusion still reflects the current state of toxicological research, although methodologies for toxicological studies do improve and refine this statement as indicated by the parenthesis. Methodologies for the safer handling of carbon nanotubes and safe nanoscale manufacturing also improve.

Smart processing of nanoparticles with the ability to control processing [23] of carbon nanotubes, their use in manufacturing processes and their ability to become airborne can improve safety of nanotechnology and the safety of carbon nanotube based microelectronics and computer manufacturing. Smart processing of nanoscale particles [23], *microscopically controlled* manufacturing, *microscopically controlled* nanostructured processing flows and microscopically tailored nanostructured materials are emerging areas of modern manufacturing, which will not only improve the safety of nanotechnology-based manufacturing, but will also lead the industry toward highly sophisticated microscopic and nanoscale manufacturing of very complex materials systems and uniquely manufactured products. Safety of carbon nanotubes is critical for the stable development of nanotechnologies without the asbestos-like health problems and the long or high cost litigations, which can bury some unsafe nanotechnology-based innovations.innovations.

Acknowledgments This research has been supported in part by the Nanotech Safety Program at Nanodesigns Consulting (www.nanodesignconsult.com), which encourages all researchers to allocate at least 5 % of the research funding for ensuring and improving the safety of nanotechnology in their area of research.

References

1. The Royal Academy of Engineering and the British Royal Society, *Nanoscience and Nanotechnologies: Opportunities and Uncertainties* (Joint Report, the Royal Academy of Engineering and the British Royal Society, London, United Kingdom, August 2004)
2. P.M. Cook, *Asbestos and Related Durable Fibers: Too Ubiquitous, Too Persistent, Too Complex to Put Health Risks to Rest?* (Mid-Continent Ecology Division, National Health and Environmental Effects Research Laboratory, Duluth, Minnesota, 2004)
3. V.M. Harik, *Nanotechnology of Carbon Nanotubes and Safety Issues* (Proceedings of the 20th Technical Conference of American Society for Composites, Philadelphia, Pennsylvania, 7–8 September 2005), p. 44
4. V.M. Harik, *Ranges of Applicability for the Continuum-Beam Model in the Constitutive Analysis of Carbon Nanotubes: Nanotubes or Nano-Beams?* (NASA/CR-2001-211013, NASA Langley Research Center, Hampton, Virginia, USA, June 2001)
5. V.M. Harik, Ranges of applicability of the continuum beam model in the mechanics of carbon nanotubes. Solid State Commun. (Int. J.) **120**, 331–335 (2001)
6. V.M. Harik, *Mechanics of Carbon Nanotubes (A Short Course Notes)* (ASME Education Institute, American Society of Mechanical Engineers, New York, NY, USA, 2001)
7. V.M. Harik, Comput. Mater. Eng. (Int. J.) **24**(3), 328 (2002)
8. S.J.V. Frankland, V.M. Harik, Analysis of carbon nanotube pull-out from a polymer matrix. Surf. Sci. Lett. **525**, L103 (2003)
9. S.J.V. Frankland, V.M. Harik, Mat. Res. Soc. Symp. Proc. **733 E**, T6.2.1 (2002)
10. S.J.V. Frankland, V.M. Harik, Mat. Res. Soc. Symp. Proc. **740**, I12.1.1 (2002)
11. D.B. Warheit, B.R. Laurence, K.L. Reed, D.H. Roach, G.A.M. Reynolds, T.R. Webb, Comparative pulmonary toxicity assessment of single-wall carbon nanotubes in rats. Toxicol. Sci. **77**, 117–125 (2004)
12. C.-W. Lam, J.T. James, R. McCluskey, R.L. Hunter, Pulmonary toxicity of single-wall carbon nanotubes in mice 7 and 90 days after intratracheal instilation. Toxicol. Sci. **77**, 126–134 (2004)
13. J. Muller, F. Huaux, N. Moreau, P. Misson, J.F. Heilier, M. Delos et al., Respiratory toxicity of multi-wall carbon nanotubes. Toxicol. Appl. Pharmacol. **207**(3), 221–31 (2005)
14. L.E. Murr, K.M. Garza, K.F. Soto, A. Carrasco, T.G. Powell, D.A. Ramirez et al., Cytotoxicity assessment of some carbon nanotubes and related carbon nanoparticle aggregates and the implications for anthropogenic carbon nanotube aggregates in the environment. Int. J. Environ. Res. Public Health **2**(1), 31–42 (2005)
15. A.A. Shvedova, V. Castranova, E.R. Kisin, A.R. Murray, D. Schwegler-Berry, V.Z. Gandelsman, A. Maynard, P. Baron. Exposure to nanotube material: assessment of nanotube cytotoxicity using human keratinocyte cells (Multiscale analysis of cells and other materials systems has been presented in V.M. Harik, M. Salas (eds.) *Trends in Nanoscale Mechanics* (Kluwer Academic Publishers, The Netherlands, 2003), while various transport phenomena in ionic fluids have been examined in V.M. Harik, L.-S. Luo (eds.), *Micromechanics and Nanoscale Effects* (Kluwer Academic Publishers, The Netherlands, 2004)). J. Toxicol. Environ. Health **66**, 1901–1918 (2003)
16. V. Stone, K. Donaldson, Signs of stress (“Signs of stress” refers to the situation when 500 μm cell tried to digest carbon nanotubes without success). Nature **1**, 23–24 (2006)

17. K. Kostarelos, The long and short of carbon nanotube toxicity, (The "long and short" sized nanotube toxicity depends on geometric parameters of carbon nanotubes.) Nat. Biotechnol. **28** (7), 774–776 (2008)
18. M.-C.F. Jaurand, A. Renier, J. Daubriac, Mesothelioma: do asbestos and carbon nanotubes pose the same health risk? Part. Fibre Toxicol. **6**(16), 1–14 (2009)
19. C.A. Poland, R. Duffin, I. Kinloch, A. Maynard, W.A. Wallace, A. Seaton, V. Stone, S. Brown, W. Macnee, K. Donaldson, Carbon nanotubes introduced into the abdominal cavity of mice show asbestos like pathogenicity in a pilot study. Nat. Nanotechnol. **3**, 423–428 (2008)
20. K. Donaldson, F.A Murphy, R. Duffin, C.A Poland, Asbestos, carbon nanotubes and the pleural mesothelium: a review of the hypothesis regarding the role of long fibre retention in the parietal pleura, inflammation and mesothelioma. Part. Fibre Toxicol. **7**(5), 1–17 (2010)
21. K. Yamashita, Y. Yoshioka, K. Higashisaka et al., Carbon nanotubes elicit DNA damage and inflammatory response relative to their size and shape. Inflammation **33**(4), 276–280 (2010)
22. V.M. Harik, *Mechanics of Carbon Nanotubes* (Nanodesigns Press, Newark, Delaware, 2011)
23. B. Diskin, V.M. Harik, Efficient multigrid methods for materials processing flows with small particles: effects of particle distribution and processing conditions, Chapter 5, in *Micromechanics and Nanoscale Effects*, ed. by V.M. Harik, L.-S. Luo (Kluwer Academic Publishers, The Netherlands, 2004)
24. C. Salvador-Morales, P. Townsend, E. Flahaut, C. Ve´nien-Bryan, A. Vlandas, M.L.H. Green, R.B. Sim, Binding of pulmonary surfactant proteins to carbon nanotubes; potential for damage to lung immune defense mechanisms. Carbon **45**, 607–617 (2007)

Further Readings

25. D.W. Cugell, D.W. Kamp, Asbestos and the pleura: a review. Chest **125**, 1103–1117 (2004)
26. S.J. Lai-Fook, Pleural mechanics and fluid exchange. Physiol. Rev. **84**, 385–410 (2004)
27. J. Liu, H.L. Wong, J. Moselhy, B. Bowen, X.Y. Wu, M.R. Johnston, Targeting colloidal particulates to thoracic lymph nodes. Lung Cancer **51**, 377–386 (2006)
28. I. Ahmad, G. Hsuan, C. Li, R. Cairncross, Reaction-diffusion model describing antioxidant depletion in polyethylene-clay nanocomposites, in *Abstracts of the 2013 AIChE Annual Meeting on Environmental Aspects, Applications, and Implications of Nanomaterials and Nanotechnology* (San Francisco, CA, 2013)

Trends in Recent Publications on Nanoscale Mechanics

Editor's Notes

Vasyl Harik

Abstract This part of the edited volume highlights trends in recent publications by providing examples of important research papers in different areas of nanoscale mechanics. Research papers on novel applications of carbon nanotubes, nanocomposites, nanodevices, quantum anti-dots, and other nanostructures are noted.

Introduction

Advances in nanoscale mechanics [1–19] are illustrated in this section by recent publications, which are presented as additional references. All papers are divided into sections. Figure 1 brings to light a useful example of nanoscale manipulations [1]. A section on mechanics of carbon nanotubes provides more such examples. A section on nanocomposites presents a list of papers on other useful material applications. This review of bibliography also includes a section on nanodevices.

Publications on Nanoscale Mechanics

Scientists from the emerging world-class research laboratories [1–19] publish new reports on nanoscale devices, quantum dots electronics as well as the so called quantum anti-dots [2]. Holovatsky's group [2] has examined the electron energy spectrum in a semiconducting AlxGa1-xAs/GaAs quantum anti-dot with the donor impurity being placed at the center of a spherical nanostructure. Energies and the

---

V. Harik (✉)
Nanodesigns Consulting, P.O. Box 5303, Wilmington, DE 19808-5303, USA
e-mail: Harik@nanodesignconsult.com

V. Harik (ed.), *Trends in Nanoscale Mechanics*, DOI 10.1007/978-94-017-9263-9_9

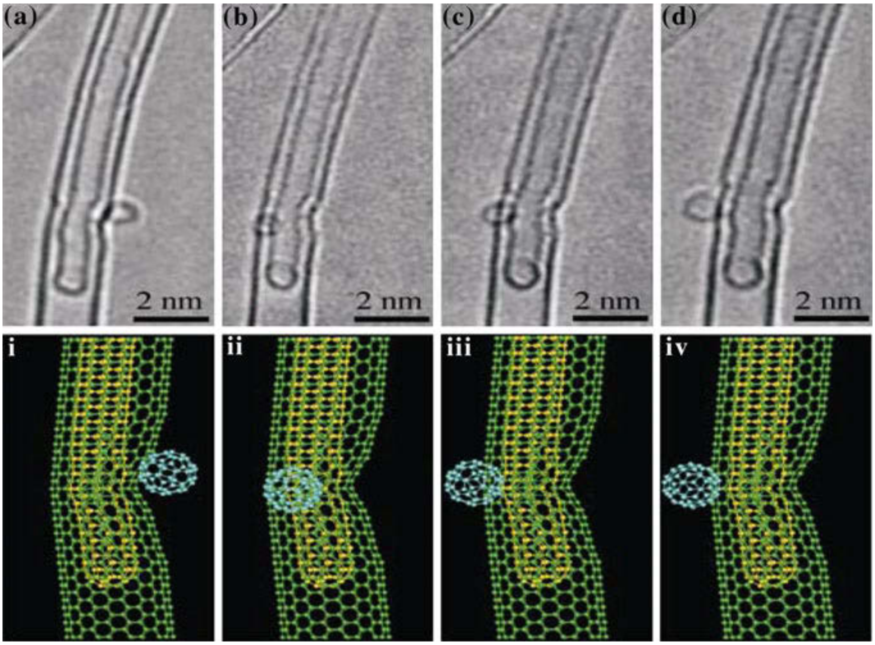

Fig. 1 HRTEM images (**a**–**d**) of a C60 molecule moving around a buckle bend on the surface of a DWNT and a schematic representation (*i*–*iv*) of the observed molecular dynamics [1]

Fig. 2 Distribution of probability density of electron location in nanostructure with central donor impurity [2]

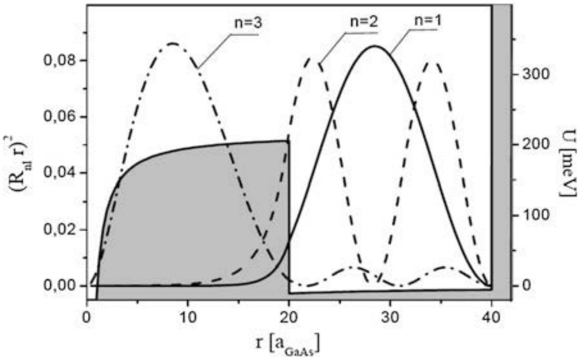

fractions of the width of quasi-stationary states have been defined within the distribution of the probability density function of electron residence in the quantum anti-dot (see Fig. 2). The details of other publications can he obtained from the listed titles, scientific journals and the additional references provided.

References

1. S. Gorantla, S. Avdoshenko, F. Börrnert, A. Bachmatiuk, M. Dimitrakopoulou, F. Schäffel, R. Schönfelder, J. Thomas, T. Gemming, J.H. Warner, G. Cuniberti, J. Eckert, B. Büchner, M.H. Rümmeli, Enhanced π–π interactions between a C60 fullerene and a buckle bend on a double-walled carbon nanotube. Nano Res. **3**, 92–97 (2010)
2. V. Holovatsky, O. Voitsekhivska, I. Bernik, Effect of magnetic field on electron spectrum in spherical nano-structures. Condens. Matter Phys. **17**(1), 13702:1–8 (2014)
3. C.M. Wang, A.N. Roy Chowdhury, S.J.A. Koh, Y.Y. Zhang, Molecular dynamics simulation and continuum shell model for buckling analysis of carbon nanotubes. in *Modeling of Carbon Nanotubes, Graphene and their Composites,* ed. by K.I. Tserpes, N. Silvestre. Springer Ser. Mater. Sci. **188**, 239 (2014)
4. K. Moth-Poulsen, T. Bjornholm, Molecular electronics with single molecules in solid-state devices. Nat. Nanotechnol. **4**, 551–556 (2009)
5. H.-E. Schaefer, *Carbon nanostructures—Tubes, graphene, fullerenes, wave-particle duality, nanoscience* (Springer, Berlin, 2010)
6. X. Xiao, T. Li, Z. Peng, H. Jin, Q. Zhong, Q. Hu, B. Yao, Q. Zhang, Q. Luo, C. Zhang, L. Gong, J. Chen, Y. Gogotsi, J. Zhou, Freestanding functionalized carbon nanotube-based electrode for solid-state asymmetric supercapacitors. Nano Energy **6**, 1–9 (2014)
7. P. Egberts, Z. Ye, X.-Z. Liu, Y. Dong, A. Martini, R.W. Carpick, Environmental dependence of atomic-scale friction at graphite surface steps. Phys. Rev. B **88**, 035409/1-0 (2013)
8. X. Li, W. Qi, D. Mei, M.L. Sushko, I. Aksay, J. Liu, Functionalized graphene sheets as molecular templates for controlled nucleation and self-assembly of metal oxide-graphene nanocomposites. Adv. Mater. **24**, 5136–5141 (2012)
9. M. Xu, J.T. Paci, J. Oswald, T. Belytschko, A constitutive equation for graphene based on density functional theory. Int. J. Solids Struct. **49**, 2582–2589 (2012)
10. J.R. Potts, D.R. Dreyer, C.W. Bielawski, R.S. Ruoff, Graphene-based polymer nanocomposites. Polymer **52**, 5–25 (2011)
11. V.M. Harik, *Mechanics of Carbon Nanotubes* (Nanodesigns Press, Newark, Delaware, 2011)
12. C. Efstathiou, H. Sehitoglu, J. Lambros, Multiscale strain measurements of plastically deforming polycrystalline titanium: role of deformation heterogeneities. Int. J. Plasticity **26**, 93–106 (2010)
13. A.A. Pelegri (Mina), S.D. Tse, B.H. Kear, in *Multifunctional Graphene Composites for Lightning Strike Protection: Structural Mechanics and System Integration* (Rutgers University, Rutgers, 2012). A.A. Pelegri, X. Huang, Nanoindentation on soft film/hard substrate and hard film/soft substrate material systems with finite element analysis. Composites Sci. Techn. **68**(1), 147–155 (2008)
14. Z. Ounaies, C. Park, J. Harrison, P. Lillehei, Evidence of piezoelectricity in SWNT-polyimide and SWNT-PZT-polyimide composites. J. Thermoplas. Compos. Mater. **21**(5), 393–409 (2008)
15. M. Rahmat, P. Hubert, Carbon nanotube–polymer interactions in nanocomposites: a review. Compos. Sci. Techn. **72**, 72–84 (2011)
16. L. Wang, A.K. Prasad, S.G. Advani, Composite membrane based on SiO_2-MWCNTs and nafion for PEMFCs. J. Electrochem. Soc. **159**(8), F490–F493 (2012)
17. T.E. Chang, L.R. Jensen, A. Kisliuk, R.B. Pipes, R. Pyrz, A.P. Sokolov, Microscopic mechanism of reinforcement in single-wall carbon nanotube/polypropylene nanocomposite. Polymer **46**, 439–444 (2005)
18. S.C. Chowdhury, B.Z. Haque(Gama), J.W. Gillespie Jr., R. Hartman, Molecular simulations of pristine and defective carbon nanotubes under monotonic and combined loading. Comput. Mater. Sci., **65**, 133–143 (2012)
19. K.Z. Milowska, J.A. Majewski, Elastic properties of functionalized carbon nanotubes. Phys. Chem. Chem. Phys. **15**, 14303–14309 (2013)

Additional References on Mechanics of Carbon Nanotubes[1]

20. B. Arash, Q. Wang, A review on the application of nonlocal elastic models in modeling of carbon nanotubes and graphenes. Comput. Mater. Sci. **51**, 303–313 (2012)
21. A.H. Korayem, W.H. Duan, X.L. Zhao, C.M. Wang, Buckling behaviour of short multi-walled carbon nanotubes under axial compression loads. Int. J. Struct. Stab. Dyn. **12**, 1250045 (2012)
22. Y. Zheng, X. Lanqing, F. Zheyong, N. Wei, Y. Lu, Z. Huang, Mechanical properties of graphene nanobuds: a molecular dynamics study. Curr. Nanosci. **8**, 89–96 (2012)
23. X. Li, K. Maute, M.L. Dunn, R. Yang, Strain effects on the thermal conductivity of nanostructures. Phys. Rev. B **81**, 245318 (2010)
24. Z. Huang, Z. Tang, J. Yu, S. Bai, Temperature-dependent thermal conductivity of bent carbon nanotubes by molecular dynamics simulation. J. Appl. Phys. **109**, 104316 (2011)
25. Z. Xu, M.J. Buehler, Geometry controls conformation of graphene sheets: membranes, ribbons, and scrolls. ACS Nano. **4**, 3869–3876 (2010)
26. J. Wackerfuß, Molecular mechanics in the context of the finite element method. Int. J. Numer Meth Eng. **77**, 969–997 (2009)
27. S.J. Heo, S.B. Sinnott, Investigation of influence of thermostat configurations on the mechanical properties of carbon nanotubes in molecular dynamics simulations. J. Nanosci. Nanotechnol. **7**, 1518–1524 (2007)
28. R. Li, G.A. Kardomateas, Thermal buckling of multi-walled carbon nanotubes by nonlocal elasticity. J. Appl. Mech. **74**(3), 399–405 (2006)
29. F. Khademolhosseini, N. Rajapakse, A. Nojeh, Application of nonlocal elasticity shell model for axial buckling of single-walled carbon nanotubes. Sens. Trans. **7**, 88–100 (2009)
30. Y. Huang, J. Wu, K. Hwang, Thickness of graphene and single-wall carbon nanotubes. Phys. Rev. B **74**, 245413 (2006)
31. J. Peng, J. Wu, K.C. Hwang, J. Song, Y. Huang, Can a single-wall carbon nanotube be modeled as a thin shell? J. Mech. Phys. Solids **56**, 2213–2224 (2008)
32. K. Chandraseker, S. Mukherjee, Atomistic-continuum and ab initio estimation of the elastic moduli of single-walled carbon nanotubes. Comput. Mater. Sci. **40**, 147–158 (2007)
33. N. Silvestre, Length dependence of critical measures in single-walled carbon nanotubes. Int. J. Solids Struct. **45**, 4902–4920 (2008)
34. B.W. Jeong, J.K. Lim, S.B. Sinnott, Turning stiffness of carbon nanotube systems. Appl. Phys. Lett. **91**, 093102 (2007)
35. C. Lee, X.D. Wei, J.W. Kysar, J. Hone, Measurement of the elastic properties and intrinsic strength of monolayer graphene. Science **321**, 385–388 (2008)
36. D. Wang, P. Song, C. Liu, W. Wu, S. Fan, Highly oriented carbon nanotube papers made of aligned carbon nanotubes. Nanotechnology, **19**, 075609 (2008). C.Y. Li, T.-W. Chou, Single-walled carbon nanotubes as ultrahigh frequency nanomechanical resonators. Phys. Rev. B **68**, 073405/1-4 (2003)
37. Q. Zheng, Q. Jiang, Carbon nanotubes as oscillators. Phys. Rev. Lett. **88**, 045503/1-3 (2002). C.Y. Li, T.-W. Chou, Vibrational behaviors of multi-walled carbon nanotube-based nanomechancial resonators. Appl Phys Lett. **84**, 121–123 (2004)
38. H. Jiang, P. Zhang, B. Liu, Y. Huang, P.H. Geubelle, H. Gao, K.C. Hwang, The effect of nanotube radius on the constitutive model for carbon nanotubes. Comput. Mater. Sci. **28**, 429–442 (2003)

---

[1] More references on Mechanics of Carbon Nanotubes can be found in V. M. Harik, *Mechanics of Carbon Nanotubes* (Nanodesigns Press, Newark, Delaware, 2011). Also in V. M. Harik, *Mechanics of Carbon Nanotubes* (Lecture Notes), ASME CD, ASME Short Course (ASME Educational Institute, New York, New York, 2002). Lecture Notes, ASME Short Course, 2001 ASME Annual Meeting (ASME Educational Institute, New York, New York, 2001)

39. A. Pantano, D.M. Parks, M.C. Boyce, Mechanics of deformation of single- and multi-wall carbon nanotubes. J. Mech. Phys. Solids **52**, 789–821 (2004)
40. X. Wang, H.K. Yang, Bending stability of multiwalled carbon nanotubes. Phys. Rev. B **73**, 085409 (2006)
41. C.M. Wang, V.B.C. Tan, Y.Y. Zhang, Timoshenko beam model for vibration analysis of multi-walled carbon nanotubes. J. Sound Vib. **294**, 1060–1072 (2006)
42. S. Zhang, R. Khare, T. Belytschko, K.J. Hsia, S.L. Mielke, G.C. Schatz, Transition states and minimum energy pathways for the collapse of carbon nanotubes. Phys. Rev. B **73**, 075423 (2006)
43. Y. Shibutani, S. Ogata, Mechanical integrity of carbon nanotubes for bending and torsion. Model. Simul. Mater. Sci. Eng. **12**, 599–610 (2004)
44. A. Kutana, K.P. Giapis, Transient deformation regime in bending of single-walled carbon nanotubes. Phys. Rev. Lett. **97**, 245501 (2006)
45. H.K. Yang, X. Wang, Bending stability of multi-wall carbon nanotubes embedded in an elastic medium. Model. Simul. Mater. Sci. Eng. **14**, 99–116 (2006)
46. O. Liba, D. Kauzlaric, Z.R. Abrams, Y. Hanein, A. Greiner, J.G. Korvink, A dissipative particle dynamics model of carbon nanotubes. Mol. Simul. **34**, 737–748 (2008)
47. Z. Xia, P. Guduru, W. Curtin, Enhancing mechanical properties of multiwall carbon nanotubes via sp3 interwall bridging. Phys. Rev. Lett. **98**, 245501 (2007)

Additional References on Buckling of Carbon Nanotubes

48. A.N. Roy Chowdhury, C.M. Wang, S.J.A. Koh, Continuum shell model for buckling of armchair carbon nanotubes under compression or torsion. Int. J. Appl. Mech. **6**(1) (2014)
49. S.D. Akbarov, Microbuckling of a doublewalled carbon nanotube embedded in an elastic matrix. Int. J. Solids Struct. **50**(1), 2584–2596 (2013)
50. J. Feliciano, C. Chun Tang, Y.Y. Zhang, C.F. Chen, Aspect ratio dependent buckling mode transition in single-walled carbon nanotubes under compression. J. Appl. Phys. **109**, 084323 (2011)
51. A.H. Korayem, W.H. Duan, X.L. Zhao, Investigation on buckling behavior of short MWCNT. Proc. Eng. **14**, 250–255 (2011)
52. C.M. Wang, Z.Y. Tay, A.N.R. Chowdhuary, W.H. Duan, Y.Y. Zhang, N. Silvestre, Examination of cylindrical shell theories for buckling of carbon nanotubes. Int. J. Struct. Stab. Dyn. **11**, 1035–1058 (2011)
53. R. Ansari, S. Rouhi, Atomistic finite element model for axial buckling of single-walled carbon nanotubes. Phys. E **43**, 58–69 (2010)
54. Y.Y. Zhang, C.M. Wang, W.H. Duan, Y. Xiang, Z. Zong, Assessment of continuum mechanics models in predicting buckling strains of single-walled carbon nanotubes. Nanotechnology **20**, 395707 (2009)
55. X. Huang, H.Y. Yuan, K.J. Hsia, S.L. Zhang, Coordinated buckling of thick multi-walled carbon nanotubes under uniaxial compression. Nano Res. **3**, 32–42 (2010)
56. Y.D. Kuang, X.Q. He, C.Y. Chen, G.Q. Li, Buckling of functionalized single- walled nanotubes under axial compression. Carbon **47**, 279–285 (2009)
57. X. Yao, Q. Han, H. Xin, Bending buckling behaviors of single- and multi-walled carbon nanotubes. Comput. Mater. Sci, **43**, 579–590 (2008). H. Xin, Q. Han, X.H. Yao, Buckling and axially compressive properties of perfect and defective single-walled carbon nanotubes. Carbon, **45**, 2486–2495 (2007). Y.Y. Zhang, Y. Xiang, C.M. Wang, Buckling of defective carbon nanotubes. J. Appl. Phys. **106**, 113503 (2009)
58. H.C. Cheng, Y.L. Liu, Y.C. Hsu, W.H. Chen, Atomistic-continuum modeling for mechanical properties of single-walled carbon nanotubes. Int. J. Solids Struct. **46**, 1695–1704 (2009)

59. J. Ma, J.N. Wang, X.X. Wang, Large-diameter and water-dispersible single-walled carbon nanotubes: Synthesis, characterization and applications. J. Mater. Chem. **19**, 3033–3041 (2009)
60. J. Zhu, Z.Y. Pan, Y.X. Wang, L. Zhou, Q. Jiang, The effects of encapsulating C60 fullerenes on the bending flexibility of carbon nanotubes. Nanotechnology **18**, 275702 (2007)
61. T. Chang, J. Hou, Molecular dynamics simulations on buckling of multiwalled carbon nanotubes under bending. *J. Appl. Phys.* **100**:114327 (2006). T.C. Chang, J.Y. Geng, X.M. Guo, Chirality- and size-dependent elastic properties of single-walled carbon nanotubes. Appl. Phys. Lett. **87**(25), 251929 (2005). X. Guo, A.Y.T. Leung, H. Jiang, X.Q. He, Y. Huang, Critical strain of carbon nanotubes: an atomic-scale finite element study. J. Appl. Mech. **74**, 347–351 (2007)
62. A.Y.T. Leung, X. Guo, X.Q. He, H. Jiang, Y. Huang, Postbuckling of carbon nanotubes by atomic-scale finite element. J. Appl. Phys. **99**(12), 124308 (2006)
63. G. Cao, X. Chen, Buckling of single-walled carbon nanotubes upon bending: molecular dynamics and finite element simulations. Phys. Rev. B **73**, 155435 (2006)
64. Y.Y. Zhang, V.B.C. Tan, and C.M. Wang, Effect of chirality on buckling behavior of single-walled carbon nanotubes, J. Appl. Phys., **100**(7):074304 (2006). C.Y. Wang, Y.Y. Zhang, C. M. Wang, V.B.C. Tan, Buckling of carbon nanotubes: A literature survey. *J. Nanosci. Nanotechnol.* **7**:4221–4247 (2007). Y.Y. Zhang, M. Wang, V.B.C. Tan, Examining the effects of wall numbers on buckling behavior and mechanical properties of multiwalled carbon nanotubes via molecular dynamics simulations. *J. Appl. Phys.* **103** 053505 (2008). C. M. Wang, Y.Y. Zhang, Y.Xiang, J.N. Reddy, Recent studies on buckling of carbon nanotubes. *Appl. Mech. Rev.*, **63**:030804 (2010)
65. Q. Wang, K.M. Liew, W.H. Duan, Modeling of the Mechanical Instability of Carbon Nanotubes. Carbon **46**(2), 285–290 (2008)
66. J.F., Waters, P. R. Gudurua, J.M. Xu Nanotube mechanics—Recent progress in shell buckling mechanics and quantum electromechanical coupling. *Compos. Sci. Technol.* **66**, 1141–1150 (2006). J.F. Waters, L. Riester, M. Jouzi, P.R. Guduru, J.M. Xu, Buckling instabilities in multiwalled carbon nanotubes under uniaxial compression. *Appl. Phys. Lett.*, **85**, 1787–1789 (2004). J.F. Waters, P.R. Guduru, M. Jouzi, J.M. Xu, T. Hanlon, S. Suresh, Shell buckling of individual multi-walled carbon nanotubes using nano indentation *Appl. Phys. Lett.*,**87**, 103109 (2005)
67. R.C. Batra, Buckling of multiwalled carbon nanotubes under axial compression.. *Phys. Rev. B* **73** 085410 (2006)
68. B. Ni, S.B. Sinnott, P.T. Mikulski, J.A. Harrison, Compression of carbon nanotubes filled with C60, CH4, or Ne: Predictions from molecular dynamics simulations. Phys. Rev. Lett. **88**, 205505 (2002)
69. M.J. Buehler, J. Kong, H.J. Gao, Deformation mechanism of very long single-wall carbon nanotubes subject to compressive loading. J. Eng. Mater. Technol. **126**, 245–249 (2004)
70. A. Pantano, M.C. Boyce, D.M. Parks, Mechanics of axial compression of single-and multi-wall carbon nanotubes. J. Eng. Mater. Technol. **126**, 279–284 (2004)
71. G. Weick, F. von Oppen, F. Pistolesi, Euler buckling instability and enhanced current blockade in suspended single-electron transistors. Phys. Rev. B **83**, 035420 (2011)
72. H.W. Yap, R.S. Lakes, R.W. Carpick, Mechanical instabilities of individual multiwalled carbon nanotubes under cyclic axial compression. Nano Lett. **7**, 1149–1154 (2007)
73. A. Misra, P.K. Tyagi, P. Rai, D.R. Mahopatra, J. Ghatak, P.V. Satyam, D.K. Avasthi, D.S. Misra, Axial buckling and compressive behavior of nickel-encapsulated multiwalled carbon nanotubes. Phys. Rev. B **76**, 014108 (2007)
74. J. Zhao, M.R. He, S. Dai, J.Q. Huang, F. Wei, J. Zhu, TEM observations of buckling and fracture modes for compressed thick multiwall carbon nanotubes. Carbon **49**, 206–213 (2011)
75. N. Hu, K. Nunoya, D. Pan, T. Okabe, H. Fukunaga, Prediction of buckling characteristics of carbon nanotubes. *Int. J Solids Struct.* **44** 6535–6550 (2007)

76. C.Q. Ru, Column buckling of multiwalled carbon nanotubes with interlayer radial displacements. *Phys. Rev. B*, **62** 16962–16967 (2000). K.N. Kudin, G.E. Scuseria, B.I. Yakobson, C2F, BN, and C nanoshell elasticity from ab initio computations. *Phys. Rev. B* **64** 235406 (2001).
77. H.S. Shen, Postbuckling prediction of double-walled carbon nanotubes under hydrostatic pressure. Int. J. Solids Struct. **41**, 2643–2657 (2004)
78. X.Q. He, S. Kitipornchai, K.M. Liew, Buckling analysis of multi-walled carbon nanotubes: A continuum model accounting for van der Waals interaction. J. Mech. Phys. Solids **53**, 303–326 (2005)
79. D.D.T.K Kulathunga, K.K Ang, J.N. Reddy, Accurate modeling of buckling of single- and double-walled carbon nanotubes based on shell theories. J. Phys. Condens. *Mater*. **21**, 435301 (2009). D.D.T.K. Kulathunga, K.K. Ang, J.N. Reddy, Molecular dynamics analysis on buckling of defective carbon nanotubes. J. Phys. Condens. Mater., **22**:345301 (2010)
80. N. Silvestre, C.M. Wang, Y.Y. Zhang, Y. Xiang, Sanders shell model for buckling of single-walled carbon nanotubes with small aspect ratio. Compos. Struct. **93**, 1683–1691 (2011)
81. J. Wu, K.C. Hwang, Y. Huang, A shell theory for carbon nanotubes based on the interatomic potential and atomic structure, in *Advances in Applied Mechanics*, Chap. 1. Elsevier, 1–68 (2009)
82. J.A. Elliott, L.K.W. Sandler, A.H. Windle, R.J. Young, M.S.P. Shaffer, Collapse of single-wall carbon nanotubes is diameter dependent. Phys. Rev. Lett. **92**, 095501 (2004)
83. Q. Wang, K.M. Liew, X.Q. He, Y. Xiang, Local buckling of carbon nanotubes under bending. Appl. Phys. Lett. **73**, 093128 (2007)
84. X.J. Duan, C. Tang, J. Zhang, W.L. Guo, Z.F. Liu, Two distinct buckling modes in carbon nanotube bending. Nano Lett. **7**, 143–148 (2007)
85. X. Wang, B. Sun, H.K. Yang, Stability of multi-walled carbon nanotubes under combined bending and axial compression loading. *Nanotechnology*. **17**, 815–823 (2006). X.Wang, G. X. Lu, Y.J. Lu, Buckling of embedded multi-walled carbon nanotubes under combined torsion and axial loading. Int. J. Solids Struct. **44**, 336–351 (2007)
86. C.L. Zhang, H.S. Shen, Buckling and postbuckling of single-walled carbon nanotubes under combined axial compression and torsion in thermal environments. Phys. Rev. B **75**, 045408 (2007)

Additional References on Radial Deformation and Torsion of Carbon Nanotubes

87. H.Y. Wang, M. Zhao, S.X. Mao, Radial moduli of individual single-walled carbon nanotubes with and without electric current flow. Appl. Phys. Lett. **89**, 211906 (2006)
88. M. Hasegawa, K. Nishidate, Radial deformation and stability of single-wall carbon nanotubes under hydrostatic pressure. Phys. Rev. B **74**, 115401 (2006)
89. H. Shima, M. Sato, Multiple radial corrugations in multiwall carbon nanotubes under pressure. *Nanotechnology*. **19**, 495705 (2008). *Mater.* **5**, 76 (2012)
90. B.W. Jeong, J.K. Lim, S.B. Sinnott, Tuning the torsional properties of carbon nanotube systems with axial prestress. Appl. Phys. Lett. **92**, 253114 (2008)
91. A.P.M. Barboza, H. Chacham, B.R.A. Neves, Universal response of single-wall carbon nanotubes to radial compression. Phys. Rev. Lett. **102**, 025501 (2009)
92. H. Shima, S. Ghosh, M. Arroyo, K. Iiboshi, M. Sato, Thin-shell theory based analysis of radially pressurized multiwall carbon nanotubes. Comput. Mater. Sci. **52**, 90–94 (2012)
93. Y.H. Yang, W.Z. Li, Radial elasticity of single-walled carbon nanotube measured by atomic force microscopy. Appl. Phys. Lett. **98**, 041901 (2011)
94. X. Huang, W. Liang, S. Zhang, Radial corrugations of multi-walled carbon nanotubes driven by inter-wall nonbonding interactions. Nanoscale Res. Lett. **6**, 53 (2011)

95. B.W. Jeong, J.K. Lim, S.B. Sinnott, Tuning the torsional properties of carbon nanotube systems with axial prestress. Appl. Phys. Lett. **92**, 253114 (2008)
96. H.K. Yang, X.Wang, Torsional buckling of multi-wall carbon nanotubes embedded in an elastic medium. *Compos. Struct.*, **77**:182–192 (2007). *Mater.* **5**, 77 (2012)
97. Y.Y. Zhang, C.M. Wang, Torsional responses of double-walled carbon nanotubes via molecular dynamics simulations. J. Phys. Condens. Mat. **20**, 455214 (2008)
98. Q. Wang, Torsional buckling of double-walled carbon nanotubes. Carbon **46**, 1172–1174 (2008)
99. Q. Wang, Transportation of hydrogen molecules using carbon nanotube in torsion. Carbon **47**, 1870–1873 (2009)
100. B.W. Jeong, S.B. Sinnott, Unique buckling responses of multi-walled carbon nanotubes incorporated as torsion springs. Carbon **48**, 1697–1701 (2010)

Additional References on Nanocomposites

101. E.M. Byrne, M.A. McCarthy, Z. Xia, W.A. Curtin, Multiwall nanotubes can be stronger than single wall nanotubes and implications for nanocomposite design. Phys. Rev. Lett. **103**, 045502 (2009)
102. S.G. Advani, *Processing and properties of nanocomposites* (World Scientific Publishing Co, London, 2007)
103. P.J.F. Harris, Carbon nanotube composites. Int. Mater. Rev. **49**, 31–43 (2004)
104. E.T. Thostenson, Z.F. Ren, T.-W. Chou, Advances in the science and technology of carbon nanotubes and their composites: a review, Comp. Sci. Tech, **61**, 1899–1912 (2001). E. T. Thostenson, T.-W. Chou, Aligned multi-walled carbon nanotube-reinforced composites: processing and mechanical characterization. J. Phys. D: Appl. Phys. **35**(16), L77-L80 (2002). E. T. Thostenson, T.-W. Chou, On the elastic properties of carbon nanotube-based composites: modeling and characterization. J. Phys. D: Appl. Phys. **36**, 573–582 (2003)
105. K.-T. Hsiao, J. Alms, S.G. Advani, Use of epoxy/multiwalled carbon nanotubes as adhesives to join graphite fibre reinforced polymer composites. Nanotechnology **14**, 791 (2003)
106. K.T. Lau, Interfacial bonding characteristics of nanotube/polymer composites. Chem. Phys. Lett. **370**(3–4), 399–405 (2003)
107. V. Lordi, N. Yao, Molecular mechanics of binding in carbon nanotube-polymer composites. J. Materials Res. **15**, 2770–2779 (2000)
108. H.D. Wagner, O. Lourie, Y. Feldman, R. Tenne, Stress-induced fragmentation of multiwall carbon nanotubes in a polymer matrix. Appl. Phys. Lett. **72**, 188–190 (1998)
109. L.S. Schadler, S.C. Giannaris, P.M. Ajayan, Load transfer in carbon nanotube epoxy composites. Appl Phys Lett **73**, 3842–3844 (1998)
110. D. Qian, E.C. Dickey, R. Andrews et al., Load transfer and deformation mechanisms in carbon nanotube-polystyrene composites. Appl. Phys. Lett. **76**, 2868–2870 (2000)

Additional References on Nanodevices

111. I. Elishakoff, D. Pentaras, K. Dujat, C. Versaci, G. Muscolino, J. Storch, S. Bucas, N. Challamel, T. Natsuki, Y. Zhang, C.M. Wang, G. Ghyselinck, *Carbon Nanotubes and Nanosensors: Vibration, Buckling and Ballistic Impact* (ISTE Ltd and Wiley, New York, 2013)
112. V.A. Holovatsky, O.M. Makhanets, O.M. Voitsekhivska, Oscillator strengths of electron quantum transitions in spherical nanosystems with donor impurity in the center, Physica E, **41**:1522–1526 (2009). V. Holovatsky, O. Makhanets and I. Frankiv, Quasi-stationary electron states in spherical anti-dot with donor impurity, *Rom. Journ. Phys.*, **57**(9–10):

1285–1292 (Bucharest, 2012). V. Holovatsky, I. Bernik and O. Voitsekhivska, Oscillator Strengths of Quantum Transitions in Spherical Quantum Dot GaAs/AlxGa1-xAs/GaAs/AlxGa1-xAs with On-Center Donor Impurity. Acta Physica Polonica A **125**(1), 1–5 (2014)

113. R. Yatskiv, J. Grym, V.V. Brus, O. Cernohorsky, P.D. Maryanchuk, C. Bazioti, G.P. Dimitrakopulos, Ph. Komninou, Transport properties of metal–semiconductor junctions on n-type InP prepared by electrophoretic deposition of Pt nanoparticles, Semicond. Sci. Technol. **29:**045017 (1–8) (2014)
114. L. Guangyong, L. Liming, Carbon nanotubes for organic solar cells. Nanotechnology Magazine, IEEE **5**, 18–24 (2011)
115. D.M. Sun, M.Y. Timmermans, Y. Tian, A.G. Nasibulin, E.I. Kauppinen, S. Kishimoto, T. Mizutani, Y. Ohno, Flexible high-performance carbon nanotube integrated circuits. Nat Nanotechnol. **6**, 156–161 (2011)
116. G. Weick, F. Pistolesi, E. Mariani, F. von Oppen, Discontinuous Euler instability in nanoelectromechanical systems. Phys. Rev. B **81**, 121409 (2010)
117. A.K. Naieni, P. Yaghoobi, D.J. Woodsworth, A. Nojeh, Structural deformations and current oscillations in armchair-carbon nanotube cross devices: A theoretical study. J. Phys. D Appl. Phys. **44**, 085402 (2011)
118. A.R. Hall, M.R. Falvo, R. Superfine, S. Washburn, A self-sensing nanomechanical resonator built on a single-walled carbon nanotube. *Nano Lett.*, **8**:3746–3749 (2008). Hall A. R., Falvo M. R., Superfine R., Washburn S., Electromechanical response of single walled carbon nanotubes to torsional strain in a self-contained device. Nat. Nanotechnol. **2**, 413–416 (2007)
119. I. Kang, M.J. Schulz, J.H. Kim, V. Shanov, D. Shi, A Carbon Nanotube Strain Sensor for Structural Health Monitoring. Smart Mater. Struct. **15**(3), 737–748 (2006)
120. X.M.H. Huang, C.A. Zorman, M. Mehregany, M.L. Roukes, Nanodevice motion at microwave frequencies. Nat. **421**, 496 (2003)
121. M. Freitag, M. Radosavljevic, Y. Zhou, A.T. Johnson, W.F. Smith, Controlled creation of a carbon nanotube diode by a scanned gate. Appl. Phys. Lett. **79**, 3326 (2001)

Archival References on Nanoscale Mechanics

122. R.S. Ruoff, J. Tersoff, D.C. Lorents, S. Subramoney, B. Chan, Radial deformation of carbon nanotubes by van der Waals' forces. Nature **364**, 514–516 (1993)
123. B.I. Yakobson, C.J. Brabec, J. Bernholc, Nanomechanics of carbon tubes: instabilities beyond linear response. *Phys. Rev. Lett.*, **76**:2511 (1996). B.I. Yakobson, T. Dimitrica, In: V. M. Harik, M. Salas **by ed.**, Trends in Nanoscale Mechanics. pp. 3–33, Kluwer Academic Publishers, The Netherlands (2003)
124. M.M.J. Treacy, T.W. Ebbesen, J.M. Gibson, *Nature*, **381**:680 (1996). Wong E. W., P. E. Sheehan, C. M. Lieber. Nanobeam Mechanics: Elasticity, Strength, and Toughness of Nanorods and Nanotubes. Science **277**, 1971–1975 (1997)
125. V. M. Harik, Solid State Comm., **120**(7–8):331–335 (2001). V.M. Harik, Mechanics of carbon nanotubes: applicability of the continuum-beam models. *Compt. Mat. Sci.*, **24** (3**)**:328–342 (2002). V.M. Harik, *Ranges of applicability for the continuum-beam model in the constitutive analysis of carbon nanotubes: nanotubes or nano-beams?* NASA/CR-2001–211013 (NASA Langley Research Center, Hampton, Virginia, June (2001)
126. C.Y. Wang, C.Q. Ru, A. Mioduchowski, Elastic buckling of multiwall carbon nanotubes under high pressure. J. Nanosci. Nanotechnol. **3**, 199–208 (2003)
127. C.Y. Li, T.-W. Chou, A structural mechanics approach for the analysis of carbon nanotubes, Int. J. Solids Struct., **40**:2487–2499 (2002). C.Y. Li, T.-W. Chou, Elastic properties of single-walled carbon nanotubes in transverse directions. Phys. Rev. B 69, 073401/1-4 (2004)
128. D. Srivastava, M. Menon, K.J. Cho, Computational Nanotechnology with Carbon Nanotubes and Fullerenes. Comp. Sci. Engng **3**, 42–55 (2001)

129. Qian D., G. J. Wagner, W. K. Liu, M. F. Yu and R. S. Ruoff, Mechanics of carbon nanotubes (The topic of this review paper was requested by Dr. V. M. Harik (ICASE Institute, NASA Langley Research Center), who is the author of a short course "Mechanics of Carbon Nanotubes" © 2001, through Dr. A. Noor (Old Dominion University and NASA Langley Research Center), who was an editor of Applied Mechanics Reviews, for a special volume on Mechanics of Carbon Nanotubes and Nanocomposites designed to address the needs of NASA Langley Research Center (Hampton, Virginia) for the state-of-the-art reviews of research in nanoscale mechanics), Appl. Mech. Rev. 55(6):495–532 (2002)
130. P. Zhang, Y. Huang, P.H. Geubelle, P.A. Klein, K.C. Hwang, The Elastic Modulus of Single-Wall Carbon Nanotubes: A Continuum Analysis Incorporating Interatomic Potentials. Int. J. Solids Structr. **39**, 3893–3906 (2002)
131. M.F. Yu, O. Lourie, M.J. Dyer, K. Moloni, T.F. Kelly, R.S. Ruoff, Strength and Breaking Mechanism of Multiwalled Carbon Nanotubes Under Tensile Load. Science **287**, 637–640 (2000)
132. W.H. Knechtel, G.S. Dusberg, W.J. Blau, E. Hernandez, A. Rubio, Reversible bending of carbon nanotubes using a transmission electron microscope. *Appl. Phys. Lett.*, **73**, 1961–1963 (1998). M.R. Falvo, G.J. Clary, R.M.Taylor, II., V. Chi, F.P. Brooks, Jr., S. Washburn, R. Superfine, Bending and buckling of carbon nanotubes under large strain. *Nat.*, **389**, 582–584 (1997). O. Lourie, D.M. Cox, H.D. Wagner, Buckling and collapse of embedded carbon nanotubes. Phys. Rev. Lett. **81**, 1638–1641 (1998)
133. D.W. Brenner, Empirical potential for hydrocarbons for use in simulating the chemical vapor deposition of diamond films. Phys. Rev. B **42**, 9458–9471 (1990)

Erratam to:
Trends in Nanoscale Mechanics

Vasyl Harik

Erratum to:
V. Harik (ed.), *Trends in Nanoscale Mechanics,*
DOI 10.1007/978-94-017-9263-9

p. vii, par. 3: Chapter “Mechanics of Carbon Nanotubes” should read as Chapter “Molecular Modeling and Simulation of Physical Properties and Behavior of Low-Dimensional Carbon Allotropes”.

The online version of the original book can be found under
DOI 10.1007/978-94-017-9263-9

V. Harik (✉)
Nanodesigns Consulting, Wilmington, DE, USA
e-mail: Harik@nanodesignconsult.com

V. Harik (ed.), *Trends in Nanoscale Mechanics*, DOI 10.1007/978-94-017-9263-9_10

Erratum to: New Trends in Nanoscale Mechanics of Carbon Nanotubes

Vasyl Harik

Erratum to:
Chapter 1 in: V. Harik (ed.), *Trends in Nanoscale Mechanics,*
DOI 10.1007/978-94-017-9263-9_1

p. 5, par. 2: (see chapter "New Trends in Nanoscale Mechanics of Carbon Nanotubes") should read as (see chapter "Mechanics of Carbon Nanotubes").

The online version of the original chapter can be found under
DOI 10.1007/978-94-017-9263-9_1

V. Harik (ed.), *Trends in Nanoscale Mechanics*, DOI 10.1007/978-94-017-9263-9_10

Erratum to: Mechanics of Carbon Nanotubes

Vasyl Harik

p. 20, footnote 2: This research results should read as These research results.

p. 33, 2nd formula for the Lenard-Jones potential should have: r_0 to the 12th and 6th power, respectively.

The online version of the original chapter can be found under
DOI 10.1007/978-94-017-9263-9_2

V. Harik (ed.), *Trends in Nanoscale Mechanics*, DOI 10.1007/978-94-017-9263-9_10

Erratum to: Molecular Modeling and Simulation of Physical Properties and Behavior of Low-Dimensional Carbon Allotropes

Wen-Hwa Chen and Hsien-Chie Cheng

p. 63, 1st sentence in the section "Atomistic Stress": The Cauchytype of stress measure should read as The Cauchy type stress measure.

The online version of the original chapter can be found under
DOI 10.1007/978-94-017-9263-9_3

V. Harik (ed.), *Trends in Nanoscale Mechanics*, DOI 10.1007/978-94-017-9263-9_10

Erratum to: Nanomechanics of Graphene Sheets

Vasyl Harik

p. 163, last paragraph: 5 nN ps)/Å) should read as 5 nN ps/Å).

The online version of the original chapter can be found under
DOI 10.1007/978-94-017-9263-9_6

V. Harik (ed.), *Trends in Nanoscale Mechanics*, DOI 10.1007/978-94-017-9263-9_10

Retraction Note to: Nanomechanics: Physics Between Engineering and Chemistry

Boris I. Yakobson and Traian Dumitrică

Erratum to:
Chapter 4 in: V. Harik (ed.), *Trends in Nanoscale Mechanics*, DOI 10.1007/978-94-017-9263-9_4

This article “Nanomechanics: Physics Between Engineering and Chemistry” has been retracted as it was re-published without the consent of the co-author, Dr. Dumitrică and the publisher.

The online version of the original chapter can be found under
DOI 10.1007/978-94-017-9263-9_4

B.I. Yakobson (✉) · T. Dumitrică
Department of Mechanical Engineering and Materials Science, and Center for Nanoscale Science and Technology, Rice University, Houston, TEXAS 77005, USA
e-mail: biy@rice.edu

T. Dumitrică
Now at University of Minnesota, Minneapolis, USA
e-mail: td@me.umn.edu

V. Harik (ed.), *Trends in Nanoscale Mechanics*, DOI 10.1007/978-94-017-9263-9_11

Index

V. Harik (ed.), *Trends in Nanoscale Mechanics*, DOI 10.1007/978-94-017-9263-9